

**Investigating the role of *ZEB2* in the establishment
of neuroepithelial architecture and axon tract
formation**

Stefano Luca Giandomenico

Homerton College

University of Cambridge

This dissertation is submitted for the degree of Doctor of Philosophy

April 2019

Declaration

The work described here was undertaken in the Cell Biology Division at the MRC Laboratory of Molecular Biology.

I hereby declare that this dissertation is the result of my own work and includes nothing that is the outcome of work done in collaboration except as declared in the Preface and specified in the text.

I further state that my dissertation has not been submitted, or, is being concurrently submitted for any degree or diploma or other qualification at the University of Cambridge or any other University or similar institution.

Finally, it does not exceed the prescribed word limit (60,000 words) for the Biology Degree Committee.

Investigating the role of *ZEB2* in the establishment of neuroepithelial architecture and axon tract formation

Stefano Luca Giandomenico

Abstract

A bioinformatic screen of comparative genomic and transcriptomic datasets identified the transcription factor *ZEB2* as a putative regulator of brain size. In this work we show that in both human brain organoids and mouse embryos *ZEB2* is expressed in telencephalic neuroepithelial cells (NECs) before the switch to radial glia (RGCs). By establishing a human embryonic stem cell (hESC) model of *ZEB2* heterozygous loss-of-function we show that this gene modulates the changes in cell-cell contacts at the transition from NECs to RGCs. Upon partial loss of *ZEB2*, changes in cell adhesion are mirrored by changes in tissue architecture, including thin elongated neuroepithelial buds with densely packed cells. We demonstrate that the secreted growth factor FGF2 is a positive regulator of *ZEB2*, which in turn suppresses *FGF2* expression, thus establishing a link between *ZEB2* and a known regulator of NEC proliferation. Preliminary gain-of-function (GOF) experiments confirm *ZEB2* as a neurogenic driver and pharmacological rescue by dual SMAD inhibition suggests that *ZEB2* may be acting by inhibiting BMP and TGF β at the transition from NECs to RGCs. In an attempt to model also later aspects of the *ZEB2* mutant phenotype we adapt air-liquid interface culture to cerebral organoids. Air-liquid interface cerebral organoids (ALI-COs) develop thick axon tracts with distinct morphologies and hodologies; including long-range projection within and away from the organoid, growth cone turning, decussation and dynamics typical of pioneer and follower axons. Single-cell RNA sequencing on ALI-COs reveals a wide array of cortical cell types and retrograde tracing demonstrates that the tracts established have distinct and accurate molecular identities. ALI-COs develop active neuronal networks and escaping tracts can innervate mouse spinal cord explants and evoke paraspinal muscle contractions. Overall, we establish a novel culture paradigm that allows *in vitro* modeling of axon guidance and network establishment. Lastly, we demonstrate that ALI-COs can be used to study the ultrastructure of navigating axons by cryo-electron tomography.

Preface

My dissertation on “Investigating the role of ZEB2 in the establishment of neuroepithelial architecture and axon tract formation” is divided into five chapters. The first chapter introduces the early stages of human embryonic development, it then focuses on the development of the cerebral cortex and details the molecular and cell biological mechanisms involved in areal patterning, progenitor proliferation, neurogenesis and axon guidance. The chapter ends by presenting the transcription factor *ZEB2*, its known roles in brain development across different model systems and its implication in human disease, and a statement of the research goals of the project. Chapter two describes in details the materials and methods used in the study. Chapter three examines the role of *ZEB2* in human cerebral cortex development using cerebral organoids as a model system. *ZEB2* was identified through a bioinformatics screen of comparative genomic and transcriptomic datasets as a putative regulator of brain size. In humans *ZEB2* heterozygous loss-of-function (LOF) causes Mowat-Wilson syndrome (MWS), a severe condition characterized by a number of central nervous system (CNS) defects. By contrast, heterozygous LOF mice do not show any observable phenotype. These observations underscore the importance of *ZEB2* in human brain development and suggest that humans may have evolved sensitivity to *ZEB2* gene dosage compared to mice. The goal of this chapter was to test gene dosage sensitivity in human brain development and model Mowat-Wilson syndrome in hESC-derived organoids. Chapter four presents an improved culture system implemented to model later neurodevelopmental stages *in vitro*. To model later developmental aspects of MWS we established an air-liquid interface culture paradigm able to recapitulate axon guidance and network establishment. Chapter five discusses the data presented in chapter three and four, highlighting their strengths and limitations, and outlining future experimental directions.

My PhD work started with the establishment of *ZEB2*^{+/-} hESC lines and characterization of the effects of partial loss of *ZEB2* on neuroepithelial architecture. Towards the end of my second year, the research focus shifted to establishing a culture method that would enable us to expand the repertoire of neurodevelopmental events accessible *in vitro*. In fact, a long-standing limitation of *in vitro* 3D neural cultures had been the absence of vascularization, leading to necrosis in the center of organoids and spheroids. Improved culture survival had been achieved by transplanting organoids into the brain of a rodent host, but due to costs and labour this is not a viable solution for routine studies. Thus, we successfully implemented a simple air-liquid interface culture model that improves neural tissue maturation and long-term survival *in vitro*.

Some of the concepts and schematics introduced in chapter one are published in ‘Giandomenico, S.L. & Lancaster, M.A., 2017. Probing human brain evolution and development in organoids. *Current opinion in cell biology*, 44, pp.36–43’ and the majority of the data presented in chapter four are published in ‘Giandomenico, S.L. et al., 2019. Cerebral organoids at the air-liquid interface generate

diverse nerve tracts with functional output. *Nature neuroscience*, 22(4), pp.669–679’, with parts of the publication adapted in the Materials & Methods and figure legends.

It should be noted that the work on Air-Liquid Interface Cerebral Organoids (ALI-COs) was a joint effort and individual contributions are detailed here with specific reference to the data presented. Max Kellner analyzed the scRNA-seq data on embryonic mouse brain and produced figures 16a-d. Madeline A. Lancaster acquired the images shown in Fig. 24, Fig. 34a, b, Fig. 39a, b and performed the analyses shown in Fig. 27, 32 and 33. The MEA recordings shown in Fig. 31a, b, d-f and Fig. 40 were performed by Susanna Mierau and me and analysed by Timothy Sit. The whole-cell patch-clamp recordings shown in Fig. 31g, h and Appendix 2 were performed and analyzed by Laura Masullo under the supervision of Marco Tripodi. The single cell RNA-seq experiment presented in Fig. 36, 37 and 38 was performed and analyzed by George Gibbons, Lea M.D. Wenger and András Lakatos on ALI-COs generated by me. Elizabeth Apsley performed the luciferase reporter experiments presented in Fig. 23a under my supervision. The CTB quantifications shown in Fig. 39c were performed by Magdalena Sutcliffe. Microelectrode stimulation experiments shown in Fig 42 & 43 were performed by Susanna Mierau and me on samples I prepared. The latency shown in Fig. 43e was computed by Jerome Boulanger with help from Emmanuel Derivery. Jerome Boulanger also wrote the ImageJ macro used to analyze muscle contraction of organoid-mouse spinal cord explants. The cryo-CLEM data presented in Figure 44 were acquired and analyzed by Patrick Hoffmann from samples I prepared.

Acknowledgments

Firstly, I want to thank my supervisor Madeline A. Lancaster for her help, support and vision throughout my PhD. Her contribution was instrumental to the success of the project, which I would not have been able to complete without her continuous guidance throughout the years. Her knowledge, drive, curiosity and enthusiasm have made my doctorate a tremendous experience, consolidating my desire to pursue a career in science. I would also like to thank my second and University supervisors, Simon L. Bullock and William A. Harris for their support. I would like to thank present and past members of the lab for contributing to a very friendly and enjoyable working atmosphere – Silvia Benito, Ilaria Chiaradia, Iva Kelava, Max Kellner, Laura Pellegrini, Alex Phillips and Magdalena Sutcliffe. In particular, I want to thank Max for his help analyzing mouse single cell RNA-sequencing datasets and Magda for maintaining the organoids and the ALI-COs, analyzing the CTB tracing experiment and establishing useful tools in the lab.

Secondly, I want to thank all of our collaborators, without whose help the ALI-CO project would not have been possible - Susanna B. Mierau, George M. Gibbons, Lea M. D. Wenger, Laura Masullo, Timothy Sit, Jerome Boulanger, Marco Tripodi, Emmanuel Derivery, Ole Paulsen and András Lakatos. I want to thank the LMB light microscopy facility; Nick Barry, Jonathan Howe and Ben Sutcliffe, for training and helping me on the microscopes, Maria Daly and Fan Zhang of the LMB flow cytometry facility for cell line isolation by FACS sorting. I would like to particularly thank Claire Knox and the animal technicians at the LMB and ARES for organizing the timed matings, taking care of the mice and euthanizing them. The work completed in my PhD would not have been possible without funding from the Medical Research Council (MRC), and I would also like to thank my college, Homerton College, the Federation of European Neuroscience Societies (FENS) and the Company of Biologists for additional support.

I would like to thank my dear friends and fellow LMB PhD students Giulio Valperga, Patrick Hoffmann and Nicholas Ader who contributed to making my PhD a memorable experience. I want to thank Zoe Neuburger for her understanding and emotional support. Special thanks go to members of my family, Edoardo, Cinzia, Uga, Sergio and Piera for their help, advice and support. Last, I thank my mum, Valeria, for believing in me, pushing me to always do my best and helping me to pursue my aspirations.

Table of contents

List of figures	9
List of abbreviations	12
Abstract	16
Chapter 1: Introduction	18
<i>Opening statement</i>	18
<i>The embryonic origin of the human central nervous system (CNS)</i>	20
Fertilisation, cleavage divisions and implantation in humans	20
Formation of the primitive groove, gastrulation and genesis of the notochord	22
Neural induction, neural tube closure and formation of brain vesicles	24
<i>The molecular drivers of neural induction and telencephalic patterning</i>	28
The default model of neural induction and axial patterning in the embryo	28
Telencephalic induction and dorsoventral regionalization	30
Telencephalic organizing centres and patterning	31
<i>Histogenesis of the neocortex</i>	34
Patterning leads to distinct neuroepithelial domains with diverse neurogenic behaviours	34
Cell biology of neuroepithelial cells (NECs)	34
FGF signalling regulates NECs expansion and the timing of neurogenesis	35
Apical radial glia cells (aRGCs) and the onset of neurogenesis	36
Different modes of cell division – direct versus indirect neurogenesis	38
The SVZ – basal radial glia cells (bRGCs) and intermediate progenitor cells (IPCs)	39
From the radial unit hypothesis to the discontinuous scaffold model	42
<i>Specification of cortical projection neurons</i>	44
The inside-out gradient of neurogenesis	44
Cortical axons navigation – molecular guidance cues in the CNS	44
Cell adhesion molecules in axon pathfinding	46
Projection neuron types and molecular identity	47
Molecular determinants of subcerebral projection neurons specification	48
Molecular determinants of CPN specification	50
Evolutionary relevance of layer II/III	51
<i>In vitro 3D models of cortical development</i>	52
An evo-devo approach to neurodevelopmental studies	52
In vitro 2D and 3D neural differentiation	52
Cerebral organoids – a 3D intrinsic neural differentiation model	53
Cerebral organoids: a tractable system for evo-devo and disease studies	54
Advances in genome editing and reprogramming technologies	54

Present limitations of brain organoids as a model system	57
<i>An in silico screen identifies ZEB2 as a putative regulator of neocortical expansion</i>	59
A list of brain evolution candidate genes	59
The transcription factor ZEB2	59
Regulation of TGF β signalling by ZEB2	61
ZEB2 induces neuroectoderm and neural crest fates	62
Zeb2 regulates multiple aspects of cerebral development	63
Zeb2 in glial cell development and myelination	63
In human Zeb2 mutations cause Mowat-Wilson syndrome	64
Neurogenesis as a gradual process of EMT	64
<i>Thesis objectives</i>	66
Chapter 2: Materials & Methods	68
<i>Plasmid constructs</i>	68
<i>Cell culture, transfection and nucleofection</i>	69
<i>Karyotyping</i>	69
<i>Organoid culture</i>	70
<i>Electroporation of cerebral organoids</i>	70
<i>Cholera toxin subunit B (CTB) and emGFP labelling</i>	70
<i>Air-Liquid Interface Cerebral Organoid (ALI-CO) culture</i>	71
<i>ALI-CO live imaging and image analysis</i>	71
<i>Histological and immunohistochemical analysis</i>	72
<i>Immunoblotting</i>	73
<i>Antibodies</i>	73
<i>Whole-cell patch-clamp recordings</i>	74
<i>ChIP-seq data visualization and SUMOylation/ubiquitylation analysis</i>	74
<i>Bioinformatic analysis of scRNA-seq datasets</i>	75
<i>Organoid dissociation for single-cell RNA sequencing (scRNA-seq)</i>	76
<i>scRNA-seq library preparation and sequencing</i>	76
<i>scRNA-seq data analysis</i>	77
<i>Multielectrode array (MEA) recordings</i>	78
<i>Mouse embryos harvesting and mouse spinal cord-ALI-CO co-culture</i>	78
<i>ALI-CO stimulation and axotomy</i>	79
<i>PCR analysis</i>	80
<i>Droplet digital PCR (ddPCR) and RT-ddPCR</i>	80
<i>Luciferase reporter assay</i>	82
<i>Cryo-CLEM on ALI-CO tracts</i>	82
Chapter 3: The zinc-finger transcription factor ZEB2 regulates cell-cell contacts and architecture in the developing neuroepithelium	85

<i>Introduction</i>	85
<i>ZEB2 is highly expressed in early neural progenitor cells</i>	86
<i>At day 6 of the protocol ZEB2 protein is present but not detectable by immunofluorescence</i>	90
<i>Exon IV of ZEB2 contains a putative SUMOylation/ubiquitylation site that controls protein stability</i>	92
<i>ZEB2 is expressed transiently in dorsal telencephalic progenitors and is repressed after the switch from NECs to aRGs</i>	95
<i>ZEB2 has a similar expression pattern in the developing mouse dorsal telencephalon</i>	97
<i>Generation of ZEB2 mutant hESCs for interrogation of ZEB2 function and modelling Mowat-Wilson syndrome in cerebral organoids</i>	100
<i>ZEB2^{+/-} mutants display a ~50% reduction in ZEB2 protein, retain pluripotency, are karyotypically normal but show a structural phenotype upon differentiation</i>	103
<i>ZEB2 heterozygous loss-of-function mutation leads to increased cell adhesion in the neuroepithelium</i>	106
<i>ZEB2^{+/-} organoids display elongated EMX1⁺/TBR2⁺ neuroepithelial buds and reduced numbers of TBR2⁺ intermediate progenitors</i>	109
<i>Evidence suggests that FGF2 and ZEB2 may form a negative feedback loop</i>	111
<i>Preliminary gain-of-function experiments support a neurogenic role of ZEB2</i>	114
<i>Dual SMAD inhibition partially rescues the ZEB2^{+/-} phenotype</i>	117
Chapter 4: Air-Liquid Interface Cerebral Organoids (ALI-COs) display diverse nerve tracts with functional output	121
<i>Introduction</i>	121
<i>Culture of cerebral organoids at the air-liquid interface (ALI) leads to improved tissue morphology</i>	122
<i>ALI-COs display improved neuronal survival compared to whole organoids</i>	124
<i>ALI-COs display higher numbers of both deep- and superficial-layer neurons</i>	125
<i>ALI-COs develop highly directional and coherent tracts</i>	126
<i>Culture at the ALI promotes long-term neuronal survival and astrogenesis</i>	128
<i>ALI-CO neurons acquire complex morphology and display mature synapses</i>	130
<i>Interneurons are present within ALI-COs</i>	133
<i>ALI-COs are electrophysiologically active</i>	135
<i>Early-stage ALI-COs display highly dynamic growth cones</i>	137
<i>More mature axons form robust and directional tracts</i>	138
<i>Organising centres secreting guidance cues are found within ALI-COs</i>	140
<i>scRNA-seq reveals a large array of cortical neuron types in ALI-COs</i>	143
<i>ALI-COs present distinct populations of deep- and superficial-layer neurons with specific projection patterns</i>	148
<i>ALI-COs establish neural networks with functional output</i>	151

<i>Electron cryotomography (ECT) of ALI-CO escaping tracts uncovers elements of ultrastructural organisation of developing axons</i>	158
Chapter 5: Discussion	163
<i>ZEB2 is dynamically expressed in the developing neuroepithelium</i>	163
<i>ZEB2 regulates the cell adhesion properties and architecture of the neuroepithelium</i>	164
<i>ZEB2: future directions and experimental considerations</i>	168
<i>ALI-COs: a novel culture system able to model axon pathfinding and tract formation</i>	169
<i>ALI-CO neurons mature and establish functional networks</i>	170
<i>Cryo-CLEM on ALI-CO escaping axons</i>	172
<i>ALI-COs: future directions and experimental considerations</i>	174
<i>Conclusions</i>	175
Bibliography	177
Appendix 1	201
<i>Table of oligos used in the study</i>	201
Appendix 2	203
<i>Whole-cell patch-clamp recording data</i>	203

List of figures

<i>Figure 1 From a fertilized egg to the bilaminar stage embryo.</i>	21
<i>Figure 2 The process of gastrulation.</i>	23
<i>Figure 3 Development of the central nervous system.</i>	27
<i>Figure 4 The molecular players of neural induction and embryonic axial plan establishment.</i>	30
<i>Figure 5 Telencephalic organisers and areal patterning.</i>	33
<i>Figure 6 The histogenesis of the cerebral cortex and the inside-out gradient of neurogenesis.</i>	37
<i>Figure 7 Changes in pallial tissue architecture across evolutionary and developmental timescales across amniotes.</i>	42
<i>Figure 8 Major classes of projection neurons within the neocortex.</i>	49
<i>Figure 9 Application of cerebral organoids to evo-devo studies.</i>	56
<i>Figure 10 The functional domains of Zeb2.</i>	60
<i>Figure 11 ZEB2 is expressed early in NECs and late in postmitotic neurons.</i>	88
<i>Figure 12 Western blot and RT-ddPCR analyses reveal high ZEB2 expression in day 6 and 11 EBs.</i>	89
<i>Figure 13 ZEB2 protein is expressed in day 6 organoids but is not detected by an antibody against its N-terminus in immunofluorescence.</i>	91
<i>Figure 14 Transcript variant II of ZEB2 contains a putative SUMOylation/ubiquitylation site that leads to longer protein half-life.</i>	93
<i>Figure 15 ZEB2 is expressed transiently in the neuroepithelium prior to the NEC to aRGC switch.</i>	96
<i>Figure 16 scRNA-seq and immunofluorescence analyses confirm a switch in Zeb2 expression from NECs to postmitotic neurons in the mouse dorsal telencephalon.</i>	98
<i>Figure 17 CRISPR-Cas9n targeting of ZEB2 generates two heterozygous loss-of-function mutants and compound heterozygotes with one in-frame deletion.</i>	101
<i>Figure 18 ZEB2^{+/-} H9 hESCs show an approximately 50% reduction in ZEB2 mRNA and protein, retain pluripotency and normal karyotype but present a structural phenotype upon cerebral organoid differentiation.</i>	104
<i>Figure 19 ZEB2 heterozygous loss-of-function mutation leads to changes in the cell adhesion properties of the neuroepithelium.</i>	107
<i>Figure 20 ZEB2^{+/-} organoids display elongated buds and reduced numbers of TBR2⁺ IPCs.</i>	109
<i>Figure 21 FGF2 and ZEB2 show reciprocal regulation.</i>	112
<i>Figure 22 Inducible overexpression of ZEB2 in early stage organoids appears to drive premature neurogenesis and shrinkage of neuroepithelial buds.</i>	115
<i>Figure 23 Dual SMAD inhibition appears to restore normal neuroepithelial architecture and neurogenesis in ZEB2^{+/-} organoids.</i>	119
<i>Figure 24 Air-liquid interface culture cerebral organoids (ALI-COs) display improved morphology.</i>	123
<i>Figure 25 ALI-COs display reduced numbers of TUNEL⁺ cells compared to whole organoids.</i>	124

<i>Figure 26 Culture at the ALI promotes survival of deep- and superficial-layer neurons.</i>	125
<i>Figure 27 ALI-COs develop directional and coherent axon bundles.</i>	127
<i>Figure 28 ALI culture allows for extended survival and maturation of neural tissue in vitro.</i>	129
<i>Figure 29 Neurons in ALI-COs display complex dendritic architectures and mature synapses.</i>	131
<i>Figure 30 Interneurons and GABAergic synapses are found within ALI-COs.</i>	134
<i>Figure 31 ALI-COs display electrophysiological activity.</i>	135
<i>Figure 32 Organoid electroporation and live imaging reveal axon guidance dynamics in ALI-COs.</i>	137
<i>Figure 33 Neurons of ALI-COs exhibit dynamic axon guidance behaviours and form robust bundles.</i>	139
<i>Figure 34 ALI-COs develop robust internal tracts with callosal identity.</i>	140
<i>Figure 35 ALI-COs display foci of secreted guidance cues and axon tracts display specific cell-surface receptors.</i>	141
<i>Figure 36 scRNA-seq of ALI-COs reveals a wide array of cortical cell types.</i>	143
<i>Figure 37 Pseudotime and correlation analyses reveal similar gene-expression profiles in ALI-COs and human fetal brain.</i>	145
<i>Figure 38 scRNA-seq clustering is driven by cell type identity and developmental cell state.</i>	146
<i>Figure 39 Deep- and superficial layer neurons in ALI-COs show immature layering and project into bundles with discrete non-random identities.</i>	149
<i>Figure 40 ALI-COs display specific spatial patterns of connectivity.</i>	151
<i>Figure 41 ALI-COs establish functional connections with mouse spinal cord explants.</i>	153
<i>Figure 42 Stimulation of the tract connecting the ALI-CO to the mouse spinal cord explant elicits contractions that are abolished by axotomy.</i>	155
<i>Figure 43 Displacement of the stimulation electrode and axotomy abolish evoked contractions and contractions display latency.</i>	156
<i>Figure 44 Workflow for cryo-CLEM on ALI-CO-derived axons.</i>	160
<i>Figure 45 ZEB2 is a central regulator of neuroepithelial architecture.</i>	167
<i>Figure 46 Future applications of ALI-COs.</i>	173

List of abbreviations

a/bRGCs: apical/basal radial glia cells
aa: amino acid
AA: Antibiotic-Antimycotic
ALI-CO: Air-Liquid Interface Cerebral Organoid
AME: axial mesoderm
ANR: anterior neural ridge
AP: antero-posterior
BMP: bone morphogenic protein
bPCs: basal progenitor cells
CCA: canonical correlation analysis
CDL: cell dense layer
cDNA: complementary DNA
ChIP-seq: chromatin immunoprecipitation-sequencing
CID: CtB interaction domain
CLEM: correlative light-electron microscopy
CNS: central nervous system
CP: cortical plate
CPN: callosal projection neurons
CRC: Cajal-Retzius cell
CRISPR: clustered regularly interspaced short palindromic repeats
CSF: cerebrospinal fluid
CSPMNs: cortico
CtBP: C-terminal binding protein
CuO: cumate
DBL: dorsal blastopore lip
ddPCR: droplet digital PCR
DL: deep-layer
dLGE: dorso-lateral ganglionic eminence
DP: dorsal pallium
DRG: dorsal root ganglia
DV: dorso-ventral
EBs: embryoid bodies
ECM: extracellular matrix
ECT: electron cryo-tomography
EGF: epidermal growth factor
emGFP: Emerald GFP

EMT: epithelial-mesenchymal transition
 EPL: external plexiform layer
 ER: endoplasmic reticulum
 ESCs: embryonic stem cells
 FDR: false discovery rate
 FGF: fibroblast growth factor
 fGFP: farnesyl-GFP
 gDNA: genomic DNA
 GECIs: genetically encoded calcium indicators
 GFP: green fluorescent protein
 GOF: gain-of-function
 GW: gestational week
 H&E: Hematoxylin & Eosin
 HAR: human accelerated region
 HAT: histone acetyltransferase
 HDAC: histone deacetylase complex
 HDR: homology-directed repair
 hPSCs: human pluripotent stem cells
 ICM: inner cell mass
 IDM+/-A: improved differentiation medium +/- vitamin A
 IF: immunofluorescence
 IFL: inner fibre layer
 IN: interneurons
 INM: interkinetic nuclear migration
 IP: immunoprecipitation
 IPCs: intermediate progenitor cells
 IPL: internal plexiform layer
 iPSCs: induced pluripotent stem cells
 ISVZ: inner subventricular zone
 IZ: intermediate zone
 LGE: lateral ganglionic eminence
 LIF: leukemia inhibitory factor
 LM: light microscopy
 lncRNA: long non-coding RNA
 LOF: loss-of-function
 LP: lateral pallium
 MAPK: mitogen-activated protein kinase
 MEA: multielectrode array

mESC: mouse embryonic stem cells
 MGE: medial ganglionic eminence
 miRNA: micro RNA
 MP: medial pallium
 MST: mitotic somal translocation
 MWS: Mowat-Wilson syndrome
 MZ: marginal zone
 NCCs: neural crest cells
 NECs: neuroepithelial cells
 NI: neural induction
 NIM: NuRD interaction motif
 OSVZ: outer subventricular zone
 PAGE: polyacrylamide gel electrophoresis
 PCA: principal component analysis
 PCW: post-conceptional week
 PI3K: phosphoinositide-3 kinase
 PM: plasma membrane
 PNS: peripheral nervous system
 PP: preplate
 PSB: pallial-subpallial border
 PTFE: polytetrafluoroethylene
 QC: quality control
 RMP: resting membrane potential
 RPKM: reads per kilobase per million
 scRNA-seq: single-cell RNA-sequencing
 SDS: sodium-dodecyl phosphate
 SFEB: serum-free culture of embryoid body-like aggregates
 SFSCM: serum-free slice culture medium
 Shh: Sonic hedgehog
 s.d.: standard deviation
 s.e.m.: standard error of the mean
 SIP1: SMAD-interacting protein 1
 SMAD: small mothers against decapentaplegic
 SP: subplate
 SSSCM: serum-supplemented slice culture method
 SVZ: subventricular zone
 TE: thalamic eminence
 TGF β : tumour growth factor beta

TNF α : tumor necrosis factor α
tSNE: t-distributed stochastic neighbour embedding
TTL: transistor-transistor logic
TTX: tetrodotoxin
TUNEL: terminal deoxynucleotidyl transferase dUTP nick end labeling
UL: upper-layer
UMI: unique molecular identifier
VP: ventral pallium
VZ: ventricular zone
WB: western blot
WCE: whole-cell extract
ZEB2: zinc-finger e-box-binding homeobox 2

Abstract

A bioinformatic screen of comparative genomic and transcriptomic datasets identified the transcription factor *ZEB2* as a putative regulator of brain size. In this work we show that in both human brain organoids and mouse embryos *ZEB2* is expressed in telencephalic neuroepithelial cells (NECs) before the switch to radial glia (RGCs). By establishing a human embryonic stem cell (hESC) model of *ZEB2* heterozygous loss-of-function we show that this gene modulates the changes in cell-cell contacts at the transition from NECs to RGCs. Upon partial loss of *ZEB2*, changes in cell adhesion are mirrored by changes in tissue architecture, including thin elongated neuroepithelial buds with densely packed cells. We demonstrate that the secreted growth factor FGF2 is a positive regulator of *ZEB2*, which in turn suppresses *FGF2* expression, thus establishing a link between *ZEB2* and a known regulator of NEC proliferation. Preliminary gain-of-function (GOF) experiments confirm *ZEB2* as a neurogenic driver and pharmacological rescue by dual SMAD inhibition suggests that *ZEB2* may be acting by inhibiting BMP and TGF β at the transition from NECs to RGCs. In an attempt to model also later aspects of the *ZEB2* mutant phenotype we adapt air-liquid interface culture to cerebral organoids. Air-liquid interface cerebral organoids (ALI-COs) develop thick axon tracts with distinct morphologies and hodologies; including long-range projection within and away from the organoid, growth cone turning, decussation and dynamics typical of pioneer and follower axons. Single-cell RNA sequencing on ALI-COs reveals a wide array of cortical cell types and retrograde tracing demonstrates that the tracts established have distinct and accurate molecular identities. ALI-COs develop active neuronal networks and escaping tracts can innervate mouse spinal cord explants and evoke paraspinal muscle contractions. Overall, we establish a novel culture paradigm that allows *in vitro* modeling of axon guidance and network establishment. Lastly, we demonstrate that ALI-COs can be used to study the ultrastructure of navigating axons by cryo-electron tomography.

Chapter 1: Introduction

Opening statement

The neocortex or isocortex is the part of the brain responsible for voluntary motor control, processing of sensory stimuli and higher-order cognitive functions in mammals (Finlay & Darlington 1995). The emergence of this structure is believed to underlie the associative cognitive abilities that led to the evolutionary success of our clade. Its rapid expansion and diversification down the hominin lineage has produced brains capable of the complex abstract reasoning necessary for tasks such as musical composition and poetry (Molnár & Pollen 2014; Krubitzer & Kaas 2005; Montiel et al. 2016).

The six-layered neocortex is the more phylogenetically recent part of the mammalian cortex, which also includes the more ancient and structurally simpler three-layered olfactory (piriform) cortex and the archicortex (Braak 2012). These more primitive structures can give us insight into the evolutionary origin of the neocortex. In fact, a three-layered allocortex reminiscent of the mammalian olfactory cortex is found in the dorsal telencephalon of reptiles and bears homology to layers I, V and VI of the neocortex (Charvet et al. 2009; Molnár & Cheung 2006). In contrast, layers II/III appear to be a more novel structural implementation and, whilst in mice they are not typically distinguished as separate, in primates they are greatly expanded and are regarded as two separate neuronal compartments (Molnár & Cheung 2006; Smart et al. 2002).

This dramatic expansion of layers II/III in primates is an example of how, even within the context of a shared six-layer architecture, brains of different mammalian orders display a high degree of diversity (Giandomenico & Lancaster 2017). Moreover, neuronal scaling rules derived from isotropic fractionation studies have shown that, with the exception of primates where neocortex size and neuron numbers are in a linear relationship, for all other mammals measured to date neocortex size increases exponentially with number of neurons (Herculano-Houzel 2012; Herculano-Houzel et al. 2014). Thus, primates appear to have evolved the ability to build brains with higher neuronal numbers for their size than any other mammalian order, and this likely contributed to their increased cognitive abilities (Herculano-Houzel 2012).

In addition to neuronal scaling, historically, another parameter introduced to describe what may be the biological basis of intelligence is the encephalisation quotient (EQ). The EQ for a given species is calculated as the ratio of its observed brain size to its expected brain size (Jerison 1973). This parameter indicates how much larger or smaller a given species' brain is than what would be expected for its body size. The average EQ for humans is approximately three-fold higher than that of our closest living relative, the chimpanzee and it is estimated that the human neocortex contains roughly 16×10^9 neurons compared to the 6×10^9 of the chimpanzee cortex (Herculano-Houzel 2009; Roth &

Dicke 2005). These figures underscore how, within a relatively short evolutionary time window (~5-6 MYA), the hominin neocortex has undergone dramatic expansion, and spark scientific interest into the molecular determinants of these changes (White et al. 2009).

Whilst most functional studies in vertebrate brain development have been done in chick, mouse, rat and only more recently ferret, most of the work on other amniotes and mammals consists of neuroanatomical studies on post-mortem samples (Long et al. 2016; Florio et al. 2015; Boyd et al. 2015; Wong et al. 2015; Johnson et al. 2018). This has been largely due to obvious ethical issues associated with working with large mammals, the lack of genetic tools, high costs and very limited tissue availability. The result is that at present, despite the wealth of data coming from next generation sequencing studies, our understanding of the molecular mechanisms that shaped the human brain are extremely limited (Pollen et al. 2014; Nowakowski et al. 2017; Fietz et al. 2010). In this context, the recent development of neural organoids has provided the scientific community with a highly tractable *in vitro* system that could open a window on embryonic brain development across mammals (Mora-Bermúdez et al. 2016; Otani et al. 2016). Spurred by the recent advances in organoid technologies the work in this thesis attempts to describe some of the molecular mechanisms at play during early human embryonic brain development. Furthermore, we introduce a novel 3D tissue culture system that captures later stages of cortical development, thus extending the developmental window accessible to us *in vitro*.

The embryonic origin of the human central nervous system (CNS)

Fertilisation, cleavage divisions and implantation in humans

Following fertilisation the single-cell zygote undergoes a series of near-synchronous cleavage divisions that produce seemingly identical blastomeres (Fig. 1a & b). After 3-4 divisions the blastomeres undergo a process termed 'compaction' whereby they start to form tight junctions with one another forming a solid cluster of ~20-30 cells, the embryo at this stage is referred to as morula (Bavister 2012). As development progresses the outer cells of the morula begin to express Na^+ pumps, Na^+/K^+ ATPases and Na^+/H^+ exchangers, leading to osmotic accumulation of fluid inside of the embryo (Eckert & Fleming 2008; Moriwaki et al. 2007). After formation of this fluid-filled cavity (blastocoel or blastocyst cavity) the developing embryo is called blastocyst and comprises of a hollow shell of trophoblast cells containing the inner cell mass (ICM) (Fig. 1c). Cells of the ICM contribute to the three germ layers of the embryo, while trophoblast cells give rise to the foetal membrane system (Fig. 1c).

Through a series of osmotically driven expansion-contraction cycles and enzymatic digestion of the glycoprotein matrix the blastocyst hatches out of the pellucid zone and can interact with the endometrium (Leonavicius et al. 2018) (Fig. 1d). The trophoblast cells in contact with the endometrial epithelial cells form a syncytium (i.e. a single cell comprising several nuclei), known as syncytiotrophoblast, that starts to secrete pro-apoptotic factors and lytic enzymes that erode the basal lamina and expose the underlying stroma for implantation (Fig. 1e). Through this process the blastocyst embeds itself in the endometrium and rapidly becomes surrounded by cells of the proliferating syncytiotrophoblast. At the end of implantation the embryonic bud consists of two juxtaposed hemispheric cavities; the amniotic cavity positioned dorsally and surrounded by epiblast cells (i.e. primitive ectoderm), and the umbilical vesicle positioned ventrally and surrounded by hypoblast cells (i.e. primitive endoderm) (Fig. 1f). These two cell layers lying on one another form the human bilaminar embryonic disk, that through the process of gastrulation will go on to form an embryo comprising three germ layers (Schoenwolf et al. 2014).

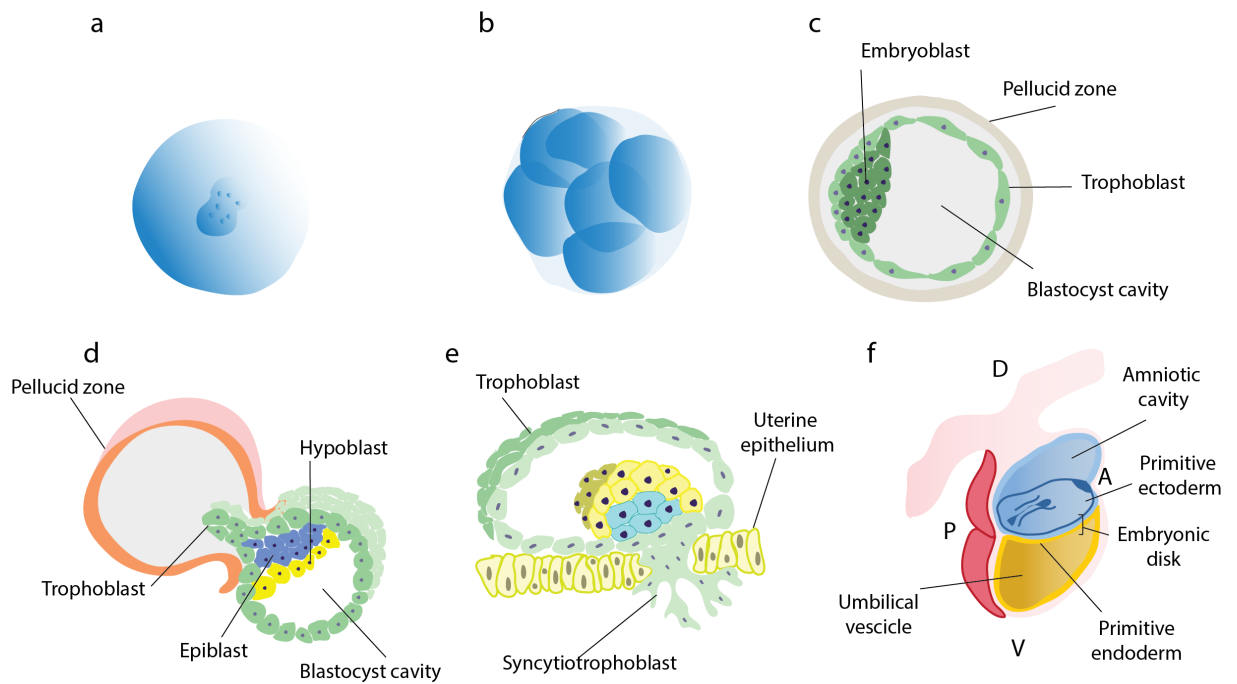


Figure 1 From a fertilized egg to the bilaminar stage embryo.

a, Schematic representation of a zygote 16-20 hrs after insemination. b, Schematic representation of an eight-cell stage embryo, after three rounds of cleavage divisions, approximately 72 hrs after insemination. c, Schematic representation of a blastocyst, after cleavage divisions the embryo undergoes compaction and through accumulation of intercellular fluid the blastocyst cavity becomes established. The blastocyst comprises an embryoblast of ~12 cells that will give rise to the embryonic tissue, the surrounding trophoblast, a single cell layer that contributes the extraembryonic supportive tissue, and the pellucid zone, a glycoprotein layer enveloping the embryo. d, Schematic representation of the embryo emerging from the pellucid zone and the trophoblast cells become able to mediate implantation. e, After hatching out of the pellucid zone the blastocyst starts interacting with the epithelial lining of the endometrium. The syncytiotrophoblast invades the uterine epithelium and secrete pro-apoptotic factors and proteolytic enzymes that erode the basal lamina and expose the underlying stroma for implantation. e, Cross-section of the bilaminar stage embryo after implantation, comprising the embryonic disk, composed of primitive ectoderm overlying the primitive endoderm. Adapted from: <http://www.embryology.ch/anglais/hdisqueembry/triderm01.html>

Formation of the primitive groove, gastrulation and genesis of the notochord

Through proliferation and coordinated movement of epiblast cells the dorsal face of the embryonic disk starts to thicken along the midline. This structure is termed primitive streak and defines the rostro-caudal (anteroposterior) axis of the developing embryo (Fig. 2a). As the primitive streak elongates by addition of epiblast cells at the caudal end of the embryo, an invagination of the epiblast layer forms anteriorly (primitive groove), and progressively spreads in an anterior fashion, forming the primitive pit with the primitive node (Hensen's node in birds) (Fig. 2a & b). The node and the primitive groove act as entry points for migrating epiblast cells in the space between the primitive ectoderm and the primitive endoderm (Fig. 2a & b) (Schoenwolf et al. 2014).

Depending on the time and position of immigration the epiblast cells acquire different fates; the first cells to occupy this space form the definitive endoderm along with the more anterior notochordal process. As the notochordal process grows anteriorly up to the prechordal plate and fuses with the underlying endoderm, the primitive streak recedes back toward the caudal region (Fig. 2b). Part of the fused tissue degenerates, creating an opening in the embryonic disk (i.e. neuroenteric canal), through which the amniotic cavity and the yolk sack communicate for a short time (Fig. 2b). The notochordal process is initially in the form of a flat plate surrounded by endoderm, it then undergoes a process of invagination and delamination that leads to the establishment of an internal rod-like structure running along the antero-posterior (AP) axis, the notochord (Fig. 2b & c) (Ben Pansky 1982; Schoenwolf et al. 2014). Collectively, the series of events leading to the trilaminar stage, when the embryo comprises three germ layers, is commonly referred to as gastrulation and is highly conserved across vertebrates (Solnica-Krezel 2005).

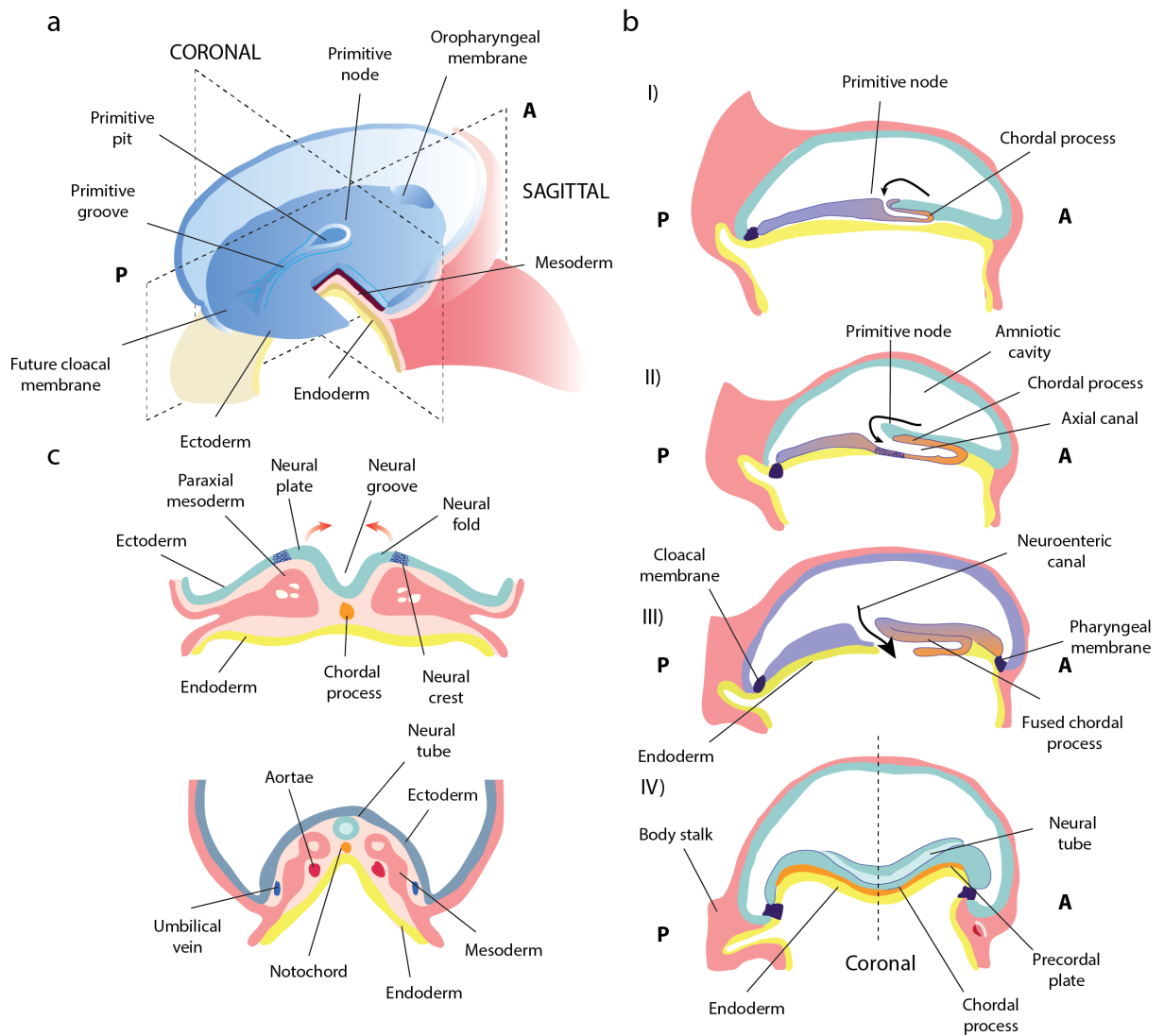


Figure 2 The process of gastrulation.

a, Dorsal magnified schematic of the embryonic disk and slice showing ectoderm, mesoderm and endoderm. The embryo is undergoing gastrulation and epiblast cells of the embryonic disk migrate through the primitive groove to form the mesoderm. The sagittal and coronal planes are annotated. b, Schematic diagrams of embryo sagittal sections showing: I) formation of the chordal process from immigrating epiblast cells through the primitive node, II) genesis of the axial canal through progressive extension of the chordal process, III) establishment of the notochord by separation from the endoderm, leading to the formation of the neuroenteric canal at the posterior end of the notochord. The amniotic cavity and the umbilical cavity are in communication. IV) Sagittal section of an embryo after neural tube closure, the cordal plate has separated from the ectoderm, forming the notochord, which comes to lie in the middle of the mesoderm between the overlying ectoderm and the underlying endoderm. The neural groove has partly fused and the neural tube is progressively closing along the AP axis. The dashed line indicates the coronal plane. c, Schematic coronal sections of the embryo before and after neural tube closure, the top schematic shows the process of neural tube closure, in which the neural plate progressively invaginates forming the neural groove. The neural folds come

progressively closer until touching each other and cells at the boundary between ectoderm and neuroectoderm delaminate, forming the neural crest. Bottom schematic shows the internalised neural tube with overlying ectoderm and underlying notochord and endoderm. The neural tube is surrounded by mesoderm. The schematics shown were adapted from:

<http://www.embryology.ch/anglais/hdisqueembry/triderm01.html>

Neural induction, neural tube closure and formation of brain vesicles

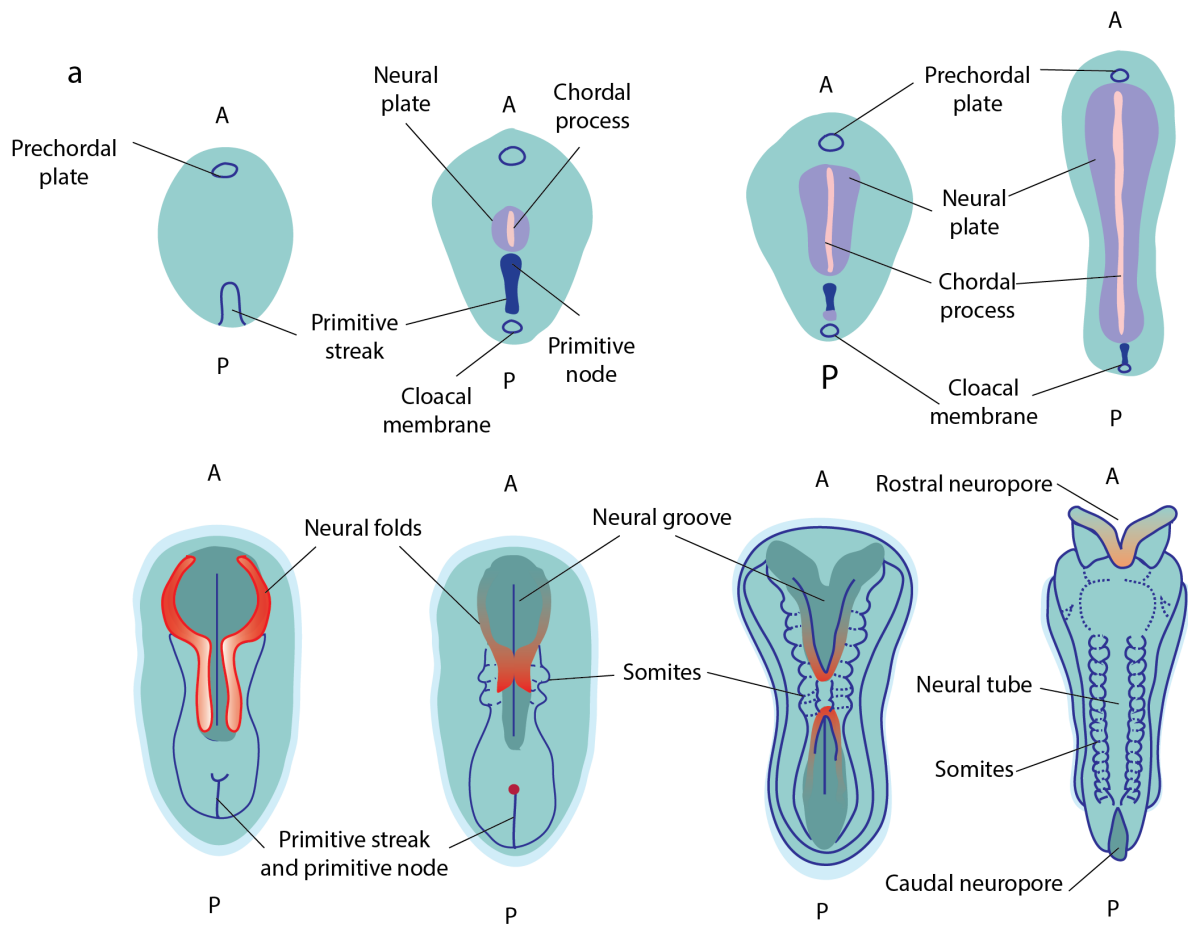
At the same time as the epiblast cells ingress into the interlaminar space, the embryonic ectoderm overlying the notochordal process thickens and forms the neural plate. The neural plate is first induced in the medio-sagittal region of ectoderm rostral to the primitive streak and, as the notochordal process elongates, it widens and extends rostrally (Fig. 2b, c & 3a) (Schoenwolf et al. 2014). Approximately 50% of the ectoderm is instructed to become neuroectoderm, which gives rise to the central nervous system (CNS) of the embryo, the other half of the ectoderm forms the epidermis (Squire et al. 2012). The process of neural induction is driven by instructive cues secreted by the primitive node, the developing notochord and the paraxial mesoderm (Fig. 2c). As development progresses, the cells at the edges of the neural plate relax their cell-cell junctions and start to elevate, forming the neural folds and a central depression of the ectoderm, termed neural groove (Schoenwolf et al. 2014) (Fig. 2c & 3a). Through the process of bidirectional fusion, the neural folds draw progressively closer and eventually adhere to one another to form the neural tube with the overlying surface ectoderm (Fig. 2c & 3a). Neural tube closure begins in the cervical region of the embryo, it then extends towards both ends of the embryo and is completed first at the cranial neuropore (anterior) and shortly after at the caudal neuropore (posterior) (Fig. 3a) (Squire et al. 2012).

Other important cell populations specified in the process of neural induction and neural tube closure are the ectodermal placodes and the neural crest. The ectodermal placodes are thickenings of the cranial ectoderm that generate sensory neurons of the nose and inner ear, nasal pituitary components and the lens of the eye in the adult (Streit 2007). The neural crest is a transient population of highly migratory multipotent cells specified at the neural folds by the interaction of neural and non-neural ectoderm (Sauka-Spengler & Bronner-Fraser 2008). Upon induction, neural crest cells undergo a process of epithelial-mesenchymal transition (EMT), delaminate and migrate across the embryo to generate neurons and glia of the peripheral nervous system (PNS), head mesenchyme, cardiac crest and melanocytes (Fig. 2c) (Kalcheim 2015).

The neural tube comprises of a pseudostratified columnar neuroepithelium surrounding a central cerebrospinal fluid (CSF) -filled cavity. The neural plate is wide rostrally, tapered caudally and upon neural tube closure at the anterior end of the embryo, the three primary cerebral vesicles form (Fig. 3b). These three structures correspond to the prosencephalon (forebrain), mesencephalon (midbrain)

and rhombencephalon (hindbrain), and represent the fundamental building blocks of the adult brain (Fig. 3b) (Squire et al. 2012). During the 5th gestational week in humans and at ~E9.5 in mouse the secondary brain vesicles become established; rostral to caudal, the forebrain becomes subdivided into telencephalon and diencephalon, and the hindbrain into metencephalon and myelencephalon (Fig. 3b). The telencephalon can be further subdivided into dorsal telencephalon or pallium, giving rise to the cortex and hippocampus, and the ventral telencephalon or subpallium, forming the basal ganglia (Fig. 3b) (Squire et al. 2012).

So far, we have described the series of developmental events going from zygote formation to the establishment of the pallium, the early embryonic precursor of the cerebral cortex. Before focusing on the cell biology of neurogenesis and the histogenesis of the cortex, we turn back to neurulation and discuss the molecular signalling pathways that drive neural induction and patterning of the telencephalon.



b

SECONDARY BRAIN VESICLES

TELENCEPHALON

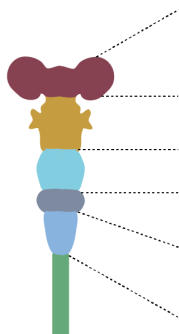
DIENCEPHALON

MESENCEPHALON

METENCEPHALON

MYELNCEPHALON

SPINAL CORD



ADULT STRUCTURES:

Cerebrum: cortex, basal nuclei, hippocampus, white matter

Diencephalon: thalamus, hypothalamus, epithalamus

Brain stem: midbrain

Brain stem: pons, cerebellum

Brain stem: medulla oblongata

CARNEGIE STAGE 16 (~39 DPC)



CARNEGIE STAGE 23 (~56 DPC)

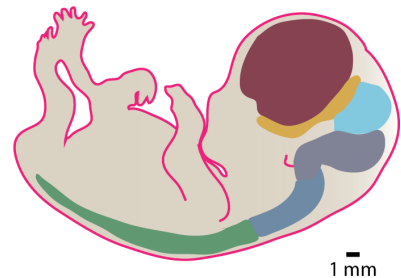


Figure 3 Development of the central nervous system.

a, Dorsal view schematics of the developing embryonic disk represented left to right and top to bottom in order of developmental stage. Initially, the primitive streak elongates anteriorly and the chordal process is induced in close proximity to the primitive node. As gastrulation advances and the embryo elongates, the primitive streak recedes and shifts posteriorly. The chordal process and neural plate expand anteriorly and the primitive streak eventually disappears. The neural plate develops together with the notochord and is first identifiable as a medio-sagittal thickening of the epithelium lying anterior to the primitive node. At the anterior end the neural plate is wider and will give rise to the brain vesicles, at the posterior end is tapered and will form the spinal cord. The neural plate is induced by factors released by the underlying axial mesoderm (AME) and notochord. During the third gestational week the edges of the neural plate rise and the medial neuroectoderm invaginates, forming the neural folds with the central neural groove. The neural folds draw progressively closer to each other and fuse to form the neural tube, which becomes internalised and covered by the ectoderm. Neural tube closure starts in the cervical region and extends both anteriorly and posteriorly. Neural tube closure is completed first at the anterior neuropore and subsequently at the posterior neuropore. In parallel to the development of the neural tube, the epiblast cells that ingressed into the primitive node to form the paraxial mesoderm form a pair of cylinder-shaped epithelial structures lying lateral to the neural groove. Through the process of metamerization these epithelial cylinders become segmented and form the somites, embryonic transition organs that contain precursor cells to the sclerotome (i.e. axial skeleton), myotome (i.e. musculature of neck and trunk) and dermatome (i.e. subcutaneous tissue and skin).

b, Left is a diagram of the secondary brain vesicles with the corresponding adult structures annotated on the right. Top right is a schematic representation of a ~39 day old embryo with overlying diagram of the secondary brain vesicles colour-coded as on the left diagram. Bottom right is a schematic representation of a ~56 day old embryo with overlying diagram of the secondary brain vesicles colour-coded as on the left diagram. The scalebars correspond to 1 mm and give a sense for the notable increase in size of the telencephalon. The schematics reported were adapted and modified from: <http://www.embryology.ch/anglais/iperiodeembry/carnegie07.html>

The molecular drivers of neural induction and telencephalic patterning

The default model of neural induction and axial patterning in the embryo

Important steps in the identification of the molecular players of neural induction were, in the 1920s, the demonstration that in *Xenopus* the dorsal blastopore lip (DBL) acts as an organising centre that specifies the CNS and, in the 1980s, the finding that members of the fibroblast growth factor (FGF) family and transforming growth factor beta (TGF β) superfamily can induce mesodermal identity in animal cap explants (Spemann 1938; Grunz 2013) (Slack et al. 1987; Kimelman & Kirschner 1987). Later, through screens of cDNA libraries, several molecules (i.e. *noggin*, *chordin*, *folliculin*) were identified as the factors secreted by the DBL responsible for its neural inductive properties and, among them, *chordin* was recognised as the homolog of the known *Drosophila* BMP-antagonist *Sog* (Smith & Harland 1992; Lamb et al. 1993; Sasai et al. 1995; Piccolo et al. 1996; Ferguson & Anderson 1992; Wharton et al. 1993). This observation raised the possibility that neural fate induction involved an ancient mechanism of TGF β signalling inhibition, conserved from arthropods all the way to vertebrates. Strong evidence in support of this hypothesis came from the expression of a dominant negative TGF β receptor in *Xenopus*, which was shown to readily convert animal cap explants from epithelial to neural (Hemmati-Brivanlou & Melton 1992). All these lines of evidence formed the basis for the default model of neural induction, which postulates that inhibition of bone morphogenic factor (BMP) signalling, a subtype of the TGF β family, is sufficient to specify neural fate in the ectoderm and that in the absence of any signal the ectodermal cells will spontaneously take up neural fate (Grunz & Tacke 1989; Hemmati-Brivanlou & Melton 1992; Hemmati-Brivanlou et al. 1994; Hemmati-Brivanlou & Melton 1994).

Although a role for BMP signalling inhibition in neural induction has been unambiguously demonstrated, other factors such FGFs and Wnts have been reported to have neural inductive properties and this has led to the formulation of an alternative instructive model of neural induction (Delaune et al. 2005; Linker & Stern 2004; Streit et al. 2000). Some of the key points of contention include the extent to which these other signalling pathways promote neural induction across different species, if they do so in a BMP-independent manner or they converge on downstream effectors of this pathway. These questions have begun to be addressed in mammals with the use of *in vitro* culture of embryonic stem cell (ESC). However, addressing the sufficiency of BMP signalling in mammalian neural induction has been complicated by the fact that culture of both mouse and human ESCs (mESCs and hESCs) requires addition of extrinsic factors such as serum, leukemia inhibitory factor (LIF), FGFs and Wnts. Through a combination of different culture approaches, including limiting dilution, coculture with neuralizing feeders and addition of different cocktails of factors, a requirement for BMP signalling inhibition for efficient neural induction in both mESCs and hESCs was confirmed (Kawasaki et al. 2000; Tropepe et al. 2001). However, due to a number of conflicting reports, to this day, the specific contribution of FGF signalling in neural induction remains ill-defined (Chambers et

al. 2009; Vallier et al. 2004; Greber et al. 2010; Cohen et al. 2010; Smukler et al. 2006; Delaune et al. 2005).

The difficulty in dissecting the precise role and order of signalling events driving neurulation likely stems from the fact that this process *in vivo* is tightly linked to gastrulation and neural tube patterning (Fig. 4a). Therefore, it is not surprising that we are still missing a clear picture of the spatiotemporal series of signalling events at play. The neural plate may appear as a homogenous population of neuroepithelial cells, but already before neural tube closure it starts being subdivided into different domains by differential gene expression along the antero-posterior (AP) and medio-lateral, later DV, axes (Tsuda et al. 2002; Niehrs 2004). A first indication of this came from experiments showing that grafting of the *Xenopus* DBL caused ectopic induction of different CNS regions depending on the age of the donor embryo (Zoltewicz & Gerhart 1997). In the 1950s, Niewkoop's recombination experiments led to the formulation of a model whereby a morphogen gradient induces posterior identity in a dose dependent fashion (Fig. 4b) (Vonica & Gumbiner 2007). Later work characterised the chemical nature of this AP patterning signal; Wnts posteriorize the neural plate through an anterior-low posterior-high gradient established by the expression of secreted Wnt inhibitors (ie. Cerberus, Dickkopf1 and Frzb1) by the notochord (Fig. 4a & b) (Kiecker & Niehrs 2001; Niehrs 2004). At later stages, FGFs and retinoic acid also play a role in AP patterning of the neural tube (Maden 2007; Mason 2007). In a similar fashion, a hierarchy of morphogen gradients was shown to promote patterning along the DV axis. BMPs secreted by the epidermal ectoderm flanking the edges of the neural plate and BMP inhibitors secreted by the axial mesoderm (AME) pattern the neural plate with a lateral-high low-medial gradient of BMP activation (Fig. 4b). It is thought that the main role of BMP signalling is to stimulate secretion of Wnt ligands so that, following neural tube closure, the dorsalizing action of Wnts from the roof plate (RP) antagonises the ventralizing influence of sonic hedgehog (SHH) secreted by the notochord (Chiang et al. 1996; Martí et al. 1995; Le Dréau & Martí 2012; Li et al. 2009; Chesnutt et al. 2004). Thus, a system of quasi-orthogonal BMP and Wnt gradients sets up the basic Cartesian coordinates of the developing embryo and initiates the signalling events that lead to fine-level patterning of the neural tube (Fig. 4b) (Squire et al. 2012).

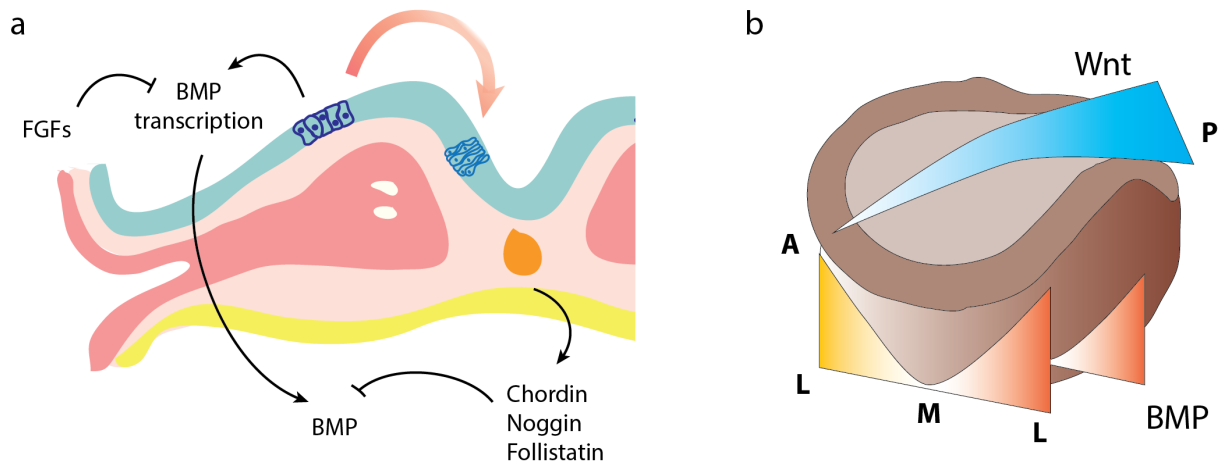


Figure 4 The molecular players of neural induction and embryonic axial plan establishment.

The transformation of ectodermal cells into neural cells is thought to be the default state. However, neural differentiation is antagonised by the tonic release of BMPs by the ectoderm. During gastrulation, BMP- and TGF β -inhibitors such as follistatin, chordin and noggin are secreted by the notochord and inhibit the activation of these signalling cascades in the overlying ectoderm, which is thus induced to become neuroectoderm. This leads to the establishment of the neural plate. Furthermore, FGFs secreted by the anterior neural ridge (ANR) and other sources act by inhibiting BMP transcription. b, Schematic representation of an amphibian embryo at the neurula stage as basic model of the bilaterian axial plan and reported is the double-gradient model of axes formation (Kiecker & Niehrs 2001). The schematic shows orthogonal gradients of Wnts and BMPs high-to-low in the posterior (P)-to-anterior (A) and lateral (L)-to-medial (M) planes, respectively. The schematic shown were adapted from: <http://www.embryology.ch/francais/vcns/tubecrete02.html> and Kiecker & Niehrs 2001.

Telencephalic induction and dorsoventral regionalization

We now focus on the interplay of signalling events that mediate establishment and regionalisation of the telencephalon. The organising centre responsible for specification and patterning of the telencephalon lies at the boundary between the anterior neuroectoderm and the underlying ectoderm, and is commonly referred to as anterior neural ridge (ANR) (Houart et al. 1998; Houart et al. 2002; Shimamura & Rubenstein 1997). In mouse and zebrafish Wnt antagonists (i.e. *Tlc* and *Six3*) secreted by the ANR were shown to be necessary for induction of the telencephalon and drive expression of *Fgf8* (Houart et al. 2002; Lagutin et al. 2003). FGFs (i.e. *Fgf3*, 8, 15, 17 and 18) are additional factors secreted by the ANR important for telencephalic induction (McWhirter et al. 1997; Maruoka et al. 1998). Application of beads soaked in FGF8 to anterior neural plate explants promotes expression of

the telencephalic precursor cell marker *Foxg1*, and *Fgf8* deletion in mice leads to a decrease in telencephalic size and abnormal patterning (Shimamura & Rubenstein 1997; Storm et al. 2006). These results points to an important role of *Fgf8* in telencephalic development, while at the same time suggesting that there may be a certain level of redundancy among FGF family members in this process. In fact, when FGF signalling is abolished in the anterior neural plate by deletion of three FGF receptor genes the entire telencephalon fails to form (Paek et al. 2009). Importantly, *Fgfs* and *Foxg1* appear to form a positive feedback loop and *Foxg1* has been shown to be essential for the establishment of both dorsal and ventral telencephalic domains (Xuan et al. 1995).

The region of the neural plate instructed by the ANR to adopt a telencephalic fate starts to express *Foxg1* along with genes that drive regionalisation of the telencephalon. In fact, even before neural tube closure has occurred the telencephalon becomes subdivided into two molecularly distinct domains, precursors of the pallium and subpallium. Albeit poorly understood, the mechanism responsible for the initial regionalization of the telencephalic neuroepithelium involves a balance between the dorsalizing action of the transcription factor Gli3 in its activator form and the antagonistic, ventralizing activity of Shh secreted by the neural plate midline (Rallu et al. 2002; Tole et al. 2000; Rash & Grove 2007). Overexpression of *Shh* in zebrafish and mouse embryos induces ventral telencephalic markers (i.e. *Dlx2*, *Gsx2*, *Nkx2.1*) in the presumptive dorsal telencephalon and conversely, *Shh* knockout leads to loss of these markers (Kohtz et al. 1998; Barth & Wilson 1995; Chiang et al. 1996). Interestingly, whilst ablation of *Gli3* and *Shh* largely restores early ventral patterning, *Foxg1*^{-/-} mice lack ventral telencephalic progenitors and the phenotype is not rescued by *Gli3* knockout (Rallu et al. 2002; Aoto et al. 2002). This, along with the fact that *Gli3*^{-/-};*Foxg1*^{-/-} mice completely lack telencephalic identity, suggests that these two factors represent the core transcriptional unit responsible for telencephalic induction (Hanashima et al. 2007).

Telencephalic organizing centres and patterning

Immediately after neural tube closure, in a coronal section of the telencephalon, the pallium can be subdivided into four regions; the medial pallium (MP), containing the hem and the hippocampal primordium, the dorsal pallium (DP), which gives rise to the neocortex, the lateral pallium (LP), the precursor of the olfactory cortex, and the ventral pallium (VP), which goes on to form the claustramygdaloid complex (Fig. 5a). Similarly, the subpallium is compartmentalised into medial, lateral and dorsolateral ganglionic eminence (i.e. MGE, LGE and dLGE) (Fig. 5a). The dLGE, also referred to as antihem, and the hem are important signalling centres that organise the telencephalic neuroepithelium (Tole et al. 2000). Along the AP axis, the antihem and the septum are most prominent rostrally and grow progressively smaller towards the posterior end of the telencephalon, conversely the hem and the thalamic eminence (TE) are predominant posteriorly. Both hem and antihem fates are suppressed by expression of *Lhx2*, which marks the presumptive neocortical neuroepithelium (Fig. 5b)

(Bulchand et al. 2001; Monuki et al. 2001; Godbole et al. 2018). Expression of *Bmps* and *Ngn* was reported to be important for specification of hem fate, while *Gsh2* and *Pax6* for antihem (Fig. 5a) (Fernandes et al. 2007; Imayoshi et al. 2008; Carney et al. 2009).

The hem is marked by the expression of several members of the *Wnt* and *Bmp* family, while the antihem expresses members of the epidermal growth factor (EGF) family along with *Wnt* signalling antagonists (Fig. 5a). The hem was shown to be necessary and sufficient for induction of hippocampal fate in the adjacent neuroepithelium and this function appears mediated by secretion of WNTs (Mangale et al. 2008; Godbole et al. 2018; Montiel & Aboitiz 2015). WNTs emanating from the hem, in particular WNT3A, promote proliferation of early dorsal cortex progenitors and together with BMPs contribute to cortical patterning (Caronia-Brown et al. 2014; Munji et al. 2011; Shimogori et al. 2004). The hem region also gives rise to the choroid plexus, a structure comprising capillaries and ependymal cells that produces the CSF in the adult (Montiel & Aboitiz 2015). Although a clear molecular understanding of the function of the antihem is still missing, secretion of Frizzled-related WNT antagonists by this structure is required for specification and maintenance of the ventral pallium (Assimacopoulos et al. 2003; Kim et al. 2001). Furthermore, several studies have implicated the antihem in the regulation of interneuron migration from the MGE and LGE to the cortex and axon guidance (Chapouton et al. 1999; Hirata et al. 2002; Stoykova et al. 1997).

Other important signalling centres for telencephalic patterning include the septum and TE (Abellán et al. 2010; Bielle et al. 2005; Meyer et al. 2002). The septum is found at the anterior end of the telencephalon and is a source of FGFs (Montiel & Aboitiz 2015). *Fgf8*, in particular, is highly expressed in the septum and establishes a concentration gradient along the telencephalon that induces ventral/anterior fates and promotes proliferation (Toyoda et al. 2010; Borello et al. 2008). The TE, found between the telencephalon and the diencephalon, has been recently proposed as an additional organising centre for telencephalic development, after the recognition that it is a source of Cajal-Retzius cells (CRCs) (Cabrera-Socorro et al. 2007; Meyer 2010). These are among the first neurons being produced in the telencephalon, they originate from the hem, antihem, septum and TE and migrate across the outermost layer of the cortex and secrete the glycoprotein Reelin, required for correct cortical lamination.

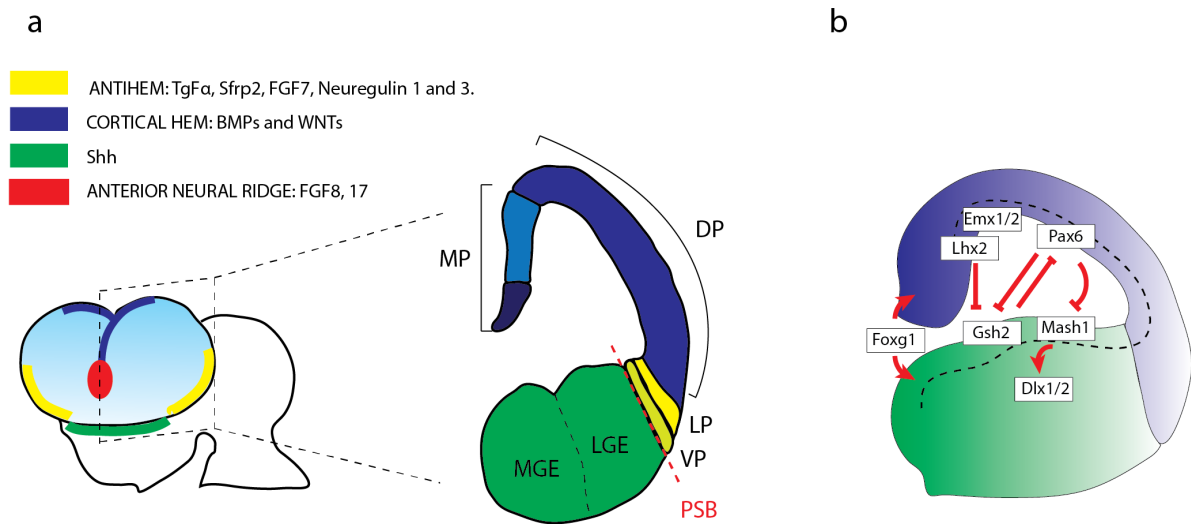


Figure 5 Telencephalic organisers and areal patterning.

a, Schematic representation of the mouse telencephalon (left) and coronal section of a telencephalic hemisphere (right) with annotated domains. Arealization of the cortex occurs through expression of transcription factors according to specific spatial gradients in response to morphogen gradients originating from telencephalic organising centres. FGF8 and FGF17 are secreted from the anterior neural ridge (ANR) (red), Wnts and BMPs are secreted from the cortical hem (blue). The antihem (yellow) is identified based on the expression of secreted signalling molecules including TgF α , Sfrp2, FGF7 and Neuregulin 1 and 3. The expression domain of *Shh* in the ventral telencephalon defines a fourth patterning centre that has no well defined function in telencephalic patterning, although it is important for establishment of dorso-ventral polarisation. The expression of these secreted factors leads to arealization of the telencephalon into: medial pallium (MP), dorsal pallium (DP), lateral pallium (LP), ventral pallium (VP), lateral ganglionic eminence (LGE) and medial ganglionic eminence (MGE). b, Schematic representation of a telencephalic hemisphere coronal section reporting the transcription factor cross-regulation network involved in specifying pallium and subpallium. Expression of *Emx1,2*, *Pax6* and *Lhx2* mark the pallium and are responsible for counteracting the ventralizing effect of *Gsh2* and *Mash1*, which drive expression of the ventral telencephalic markers *Dlx1* and *Dlx2*. Adapted and modified from: O'Leary & Nakagawa 2002; Schuurmans & Guillemot 2002; Tole & Hébert 2013; O'Leary et al. 2013.

Histogenesis of the neocortex

Patterning leads to distinct neuroepithelial domains with diverse neurogenic behaviours

The entire CNS develops from the neural plate, which comprises a simple pseudostratified columnar neuroepithelium. To begin with, this structure is fairly homogenous in terms of cell type composition and morphology. However, as discussed in the previous section, through the establishment of organising centres and morphogen gradients, the embryonic axial plan becomes established and local signalling cascades pattern the neuroepithelium, subdividing it into distinct molecular domains. The transcriptional networks that define these domains are such that even though the fundamental progenitor unit (i.e. the neuroepithelial cell) is common to all regions of the developing CNS, neurogenesis proceeds differently depending on what structure we consider. For example, while in the mouse spinal cord neurogenesis begins around E8 and is largely over by E13, in the telencephalon it starts around E11 and continues until about E17.5 (Kawakami et al. 2009). Interestingly, also the properties of the neurogenic progenitor cells are different in these different domains. In fact, spinal cord progenitors retain epithelial features for the whole duration of the neurogenic period; in contrast, telencephalic progenitors lose epithelial character before starting to make neurons (Götz & Huttner 2005; Aaku-Saraste et al. 1996). Therefore, in this section we will discuss the cell biological processes and progenitor types at play during neurogenesis, with a particular emphasis on the cortex.

Cell biology of neuroepithelial cells (NECs)

The first account of neuroepithelial cells (NECs) in the developing human neural tube dates back to the end of the 19th century (His 1889). In the neural tube NECs are interbound in a single layer of pseudostratified epithelium with apicobasal polarity - the apical cell surface contacts the inner luminal lining and the basal process attaches to the basal lamina. Work in the developing chicken neural tube has shown that NECs are strongly epithelial in character and express markers of adherens (e.g. N-cadherin) and tight junctions (e.g. Occludin and ZO1) (Aaku-Saraste et al. 1996; Hatta et al. 1987; Sakane & Miyamoto 2013). The neuroepithelium is described as pseudostratified because, despite comprising a single cell layer, the nuclei of individual NECs are staggered along the thickness of the neuroepithelium in what appears to be a stratified structure (Sauer 1935). Pseudostratification is a consequence of the behaviour of NECs known as interkinetic nuclear migration (INM), whereby, depending on the cell cycle phase, the cell nucleus will move to a different position of the neuroepithelial wall. At mitosis the cells retract their basal processes and round up at the apical surface, as they enter and progress through G1 their basal processes become re-established and the nuclei translocate to the basal surface of the neuroepithelium where the cells undergo S phase. During G2 the nuclei revert back to the apical surface and the cycle continues (Subramanian et al. 2017). INM

was shown to depend on changes in the actin and microtubule cytoskeleton (Xie et al. 2007; Zhang et al. 2009; Schenk et al. 2009). One hypothesis as to the function of this process is that, the ventricle size being equal, INM and pseudostratification allow more space to accommodate mitotic cells and overall number of progenitors. Another hypothesis is that INM might be a way for the cells to sample their surrounding environment and receive signals that influence their proliferative behaviour (Taverna & Huttner 2010). Recently, timelapse imaging of the human telencephalic neuroepithelium (GW8-10) has shown that NECs predominantly undergo symmetric proliferative divisions that increase the size of the founder progenitor population, thus promoting tangential expansion of the cortex (Fig. 6a & b) (Subramanian et al. 2017).

FGF signalling regulates NECs expansion and the timing of neurogenesis

The FGF family of ligands counts 22 members in mouse and human and many of them play a role in neurodevelopment (Beenken & Mohammadi 2009; Mason 2007). There are four FGF receptors (FGFR1-4) belonging to the tyrosine kinase family. FGF binding to its receptor triggers receptor dimerization, transphosphorylation and activation of two main downstream signalling cascades; the mitogen activated protein kinase (MAPK) pathway and the phosphatidylinositol 3-kinase (PI3K)/AKT pathway. These pathways affect a vast array of cellular processes ranging from cytoskeletal dynamics to proliferation and differentiation (Beenken & Mohammadi 2009; Mason 2007). As previously mentioned, a number of FGF ligands are secreted from multiple sources and organizers along the neural tube, and the extent to which they are redundant or indispensable is difficult to determine. A large body of studies has focused on the function of FGF2 in NECs proliferation. *Fgf2* mRNA is detected as early as E9 in the murine neuroepithelium, and between E14 and E18 both mRNA and protein levels increase dramatically in the progenitors to then tail off postnatally (Nurcombe et al. 1993; Raballo et al. 2000; Vaccarino et al. 1999). *Fgf2* homozygous loss-of-function mutation in mice results in decreased progenitor proliferation and reduced cortical surface, while gain-of-function experiments show the opposite effect (Ortega et al. 1998; Vaccarino et al. 1999; Raballo et al. 2000; Dono et al. 1998). Thus, FGF2 is an important regulator of NECs, promoting proliferation and cortical expansion and delaying neurogenesis. The ability of FGF2 to inhibit neurogenesis seems to occur through induction of the Notch pathway and FGF1 has been reported to mediate similar effects (Faux et al. 2001). Another important NEC regulator is FGF10, which is expressed at the apical surface of the mouse neuroepithelium transiently between E10 and E11.5. In *Fgf10*^{-/-} mice the expression of glial markers, typical of neurogenic progenitors, starts later than in control animals and the onset of neurogenesis is delayed (Sahara & O'Leary 2009). Conversely, gain-of-function experiments by *in utero* electroporation in the cortex of E11.5 mice have shown that FGF10 is sufficient to promote expression of glial markers (Sahara & O'Leary 2009). Therefore, FGF10 seems to regulate the timing of telencephalic neurogenesis.

Apical radial glia cells (aRGCs) and the onset of neurogenesis

Between E10-11 in mouse and GW8-10 in human telencephalic NECs start to turn into a more differentiated neural progenitor type known as aRGCs and neurogenesis begins (Fig. 6a & b). In terms of their molecular profile and morphology NECs and aRGCs are very similar and both express nestin, adherens junctions components and multipotency markers (e.g. SOX2 and PAX6) (Aaku-Saraste et al. 1996; Götz & Huttner 2005). Like NECs, aRGCs display apicobasal polarity but are more elongated and their basal processes stretch significantly as the cortex develops. Also aRGCs undergo INM; however, whilst at mitosis NECs retract their basal processes and round up at the apical surface, aRGCs retain their basal fibres during division (Subramanian et al. 2017; Nakai & Fujita 1994). Retention of the basal fibre is thought to provide a scaffold for the newly born neurons to glide along and occupy more superficial layers of the cortex (Fig. 6a & b) (Rakic 1972; Rakic 1978). The transition from NECs to aRGCs is accompanied by downregulation of tight junctions components and upregulation of astroglial markers including the glutamate transporter GLAST, the intermediate filament protein GFAP and the lipid binding protein BLBP (Campbell & Götz 2002; Kriegstein & Götz 2003; Götz & Huttner 2005). The appearance of cytoplasmic glycogen granules typically found in astrocytes is also a hallmark of aRGCs (Gadisseux & Evrard 1985).

aRGCs extend a long basal process with several endfeet contacting the basal membrane extracellular matrix from which they receive growth factors and extracellular signals that modulate their proliferative behaviour. Blockade of laminin/integrin signalling to perturb the interaction between the basal aRGC fibre and the basal membrane leads to abnormal INM, neuronal migration defects and altered cortical layering (Radakovits et al. 2009; Förster et al. 2002; Haubst et al. 2006). This underscores the importance of the radial glia scaffold for correct cortical histogenesis.

As the mammalian cortex grows in the radial dimension by the addition of layers of more fate-restricted cells, different cellular compartments become established across the cortical wall. Overlying the ventricle is the ventricular zone (VZ), where aRGCs reside, and immediately basal is the subventricular zone (SVZ), populated by more differentiated progenitor types collectively referred to as basal progenitor cells (bPCs) (Fig. 6a & b). Above the SVZ are the intermediate zone (IZ) and the preplate (PP), which contains Cajal-Retzius cells originating from the MGE, LGE, TE and the septum (Fig. 6a & b) (Rakic 1972; Noctor et al. 2004; Marín-Padilla 1992). As previously mentioned, Cajal-Retzius cells secrete the glycoprotein Reelin - guided by this chemotrophic cue, newly born telencephalic neurons migrate and position themselves radially into the PP, forming an organised structure termed cortical plate (CP) (Fig. 6a & b). The CP splits the PP into an inner and outer layer of pioneer neurons, the subplate (SP) and the marginal zone (MZ), respectively (Fig. 6a & b) (Olson 2014). Upon loss of Reelin the PP fails to split and neurons accumulate underneath it (Sheppard & Pearlman 1997; Jossin et al. 2004; Caviness & Sidman 1973). The inside-out organization of the

neocortex arises because, as development progresses, neurons generated in the VZ and SVZ migrate into the CP and occupy progressively more superficial positions (Fig. 6a-c) (Marín-Padilla 1992).

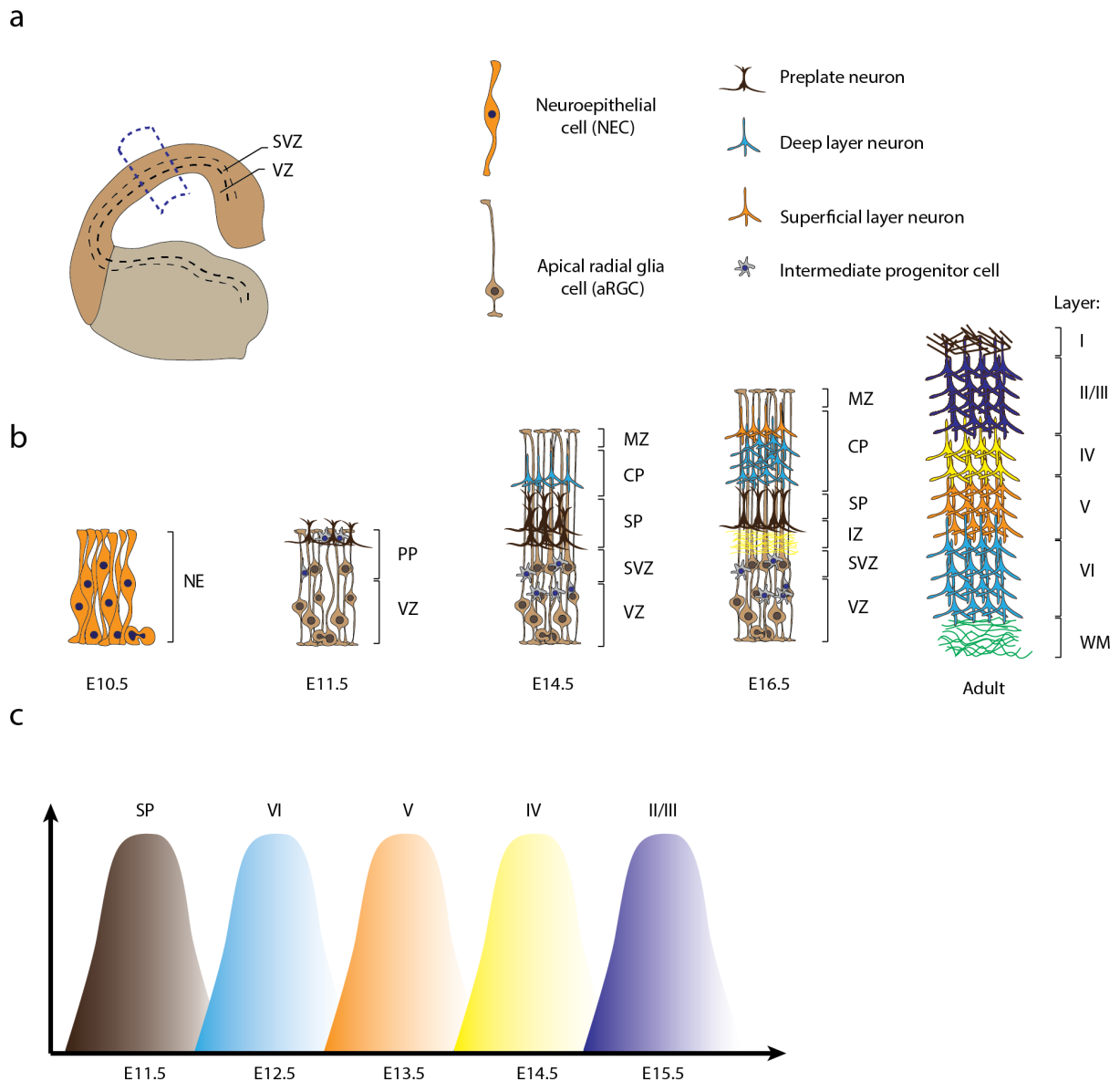


Figure 6 The histogenesis of the cerebral cortex and the inside-out gradient of neurogenesis.

a, Left is a schematic representation of a coronal section of a telencephalic hemisphere, the dashed lines demarcate different histological compartments corresponding to apical progenitors, basal progenitors and neurons. The dashed box highlights the region shown in b as development progresses. Right is a panel with the key cell types that populate the murine cortex throughout development; neuroepithelial cells (NECs), apical radial glia cells (aRGCs), intermediate progenitor cells (IPCs),

preplate neurons, deep layer neurons and superficial layer neurons. b, Schematic representation of the developing mouse cortical wall at different developmental stages. At E10.5, the cells that populate the cortex are NECs, the predominant mode of division is symmetric proliferative and more differentiated cell types such as IPCs and neurons are found in very low numbers. By E11.5 the apical progenitors have switched to an aRGC fate, neurogenesis commences and IPCs and neurons start to accumulate abventricularly. By E14.5 deep layer neurons have invaded and split the preplate into the marginal zone (MZ) and the subplate (SP) and have formed the cortical plate (CP). The accumulation of abventricular progenitors, termed basal progenitor cells (bPCs), leads to the establishment of a proliferative compartment distinct from the VZ, known as subventricular zone (SVZ). The SVZ is separated from the SP by a layer with high density of axonal processes, termed intermediate zone (IZ). At E16.5 there is a switch in production from deep- to superficial-layer neurons. In the adult brain, roughly six layers can be distinguished histologically and markers can be used to identify specific single layers or sets of layers. In the developing brain the separation of neurons into different layers is not well defined. c, Schematic representation of the inside-out-gradient of neurogenesis illustrating how, as development progresses, neurons corresponding to more superficial layers are produced and position themselves accordingly in the developing cortical wall.

Different modes of cell division – direct versus indirect neurogenesis

Similarly to NECs, aRGCs can undergo symmetric proliferative divisions to increase the progenitor numbers, but can also undergo asymmetric divisions that maintain the progenitor pool and produce a more fate-restricted daughter cell, either a neuron or an intermediate progenitor. Alternatively, they can undergo symmetric differentiative divisions in which two neurons are produced at the expense of the progenitor pool (Huttner & Kosodo 2005). Asymmetric cell divisions leading to the production of bPCs with limited self-renewal potential underlie the process of indirect neurogenesis. In contrast, in the process of direct neurogenesis aRGCs undergo division and neurons are produced without a bPC intermediate. Tracer-histology and timelapse imaging studies in mouse and human have shown that symmetric divisions are characteristic of the neuroepithelial stage and are often seen in young aRGCs – E10-12 in mouse and GW8-10 in human (Subramanian et al. 2017; Smart 1972). As neurogenesis progresses, aRGCs shift from a predominantly symmetric to a predominantly asymmetric mode of division (E15-17), and symmetric neurogenic divisions characterise the last stages of neurogenesis (E18) (Matsuzaki & Shitamukai 2015). Despite differences in the size and complexity of the SVZ, the establishment of an abventricular proliferative compartment seems to be shared across mammalian species (Haubensack et al. 2004; Noctor et al. 2004; Miyata et al. 2004; Vasistha et al. 2015). In contrast, reptiles and birds do not form a SVZ and neuronal production largely relies on direct neurogenesis (Cheung et al. 2007; Dugas-Ford & Ragsdale 2015; Cárdenas et al. 2018).

The SVZ – basal radial glia cells (bRGCs) and intermediate progenitor cells (IPCs)

The developing rodent cortex comprises a relatively small SVZ populated predominantly by IPCs (Vasistha et al. 2015). By contrast, in primates and other large-brained mammals the abventricular progenitor pool is greatly expanded, to a point where two distinct proliferative domains can be distinguished; an inner SVZ (ISVZ) and an outer SVZ (OSVZ) separated by an inner fibre layer (IFL) rich in axonal projections (Hansen et al. 2010; Smart et al. 2002; Giandomenico & Lancaster 2017). The OSVZ is characterized by the presence of basal or outer radial glia cells (bRGCs or oRGCs) that similarly to aRGCs express the markers vimentin (VIM), nestin (NES), PAX6 and SOX2, but also express the lineage specific markers HOPX, TNC and ITGB5 (Pollen et al. 2015). As previously mentioned, depending on the phase of neurogenesis, aRGCs will shift from an initial symmetric proliferative mode of division, to asymmetric conservative and lastly to symmetric differentiative divisions (Vasistha et al. 2015; Noctor et al. 2004). In contrast, bRGCs predominantly self-renew and only after a large number of amplification cycles they differentiate to IPCs and neurons (Hansen et al. 2010; Ostrem et al. 2017). Prior to undergoing division, bRGCs undergo mitotic somal translocation (MST), a process in which the soma rapidly ascends towards the cortical plate (Hansen et al. 2010). It has been suggested that, in a manner similar to INM, MST might serve to reduce crowding and allow to accommodate more cells in the OSVZ (Lui et al. 2011).

Morphologically, the distinguishing features of bRGCs are a basal process that extends to the basal lamina, the absence of an apical process and lack of apical polarity markers (i.e. PROM1, ZO1 or PARD3) expression (Hansen et al. 2010). Nevertheless, recent live imaging work in macaque slice culture preparations has showed that OSVZ progenitors can also display a basal process, both basal and apical processes or neither, and they can alternate between morphotypes (Betizeau et al. 2013). Similar reports have also come from analysis of the developing sheep and ferret brains (Pilz et al. 2013). However, because approximately a third of bRGCs in the macaque cortex express the IPC marker TBR2, it is argued that bRGCs with unconventional morphotypes may represent a class of IPCs rather than bRGCs (Ostrem et al. 2017). In this regard, it is unlikely that traditional histological and live imaging approaches will fully address the heterogeneity of morphotypes in the SVZ and OSVZ, and novel single-cell RNA sequencing (scRNA-seq) technologies along with spatial transcriptomics methods have started to provide more comprehensive insight into bPC diversity (Fan et al. 2018; Nowakowski et al. 2017).

In terms of their origin, bRGCs can result either from direct delamination of aRGCs or from asymmetric divisions of aRGCs in which the cleavage plane is parallel to the ventricular surface (LaMonica et al. 2013; Gertz et al. 2014). In contrast, aRGC divisions with cleavage plane perpendicular to the ventricle predominantly produce a self-renewed bRGC and an IPC (LaMonica et al. 2013). This second type of division seems to be predominant in mouse where the BPs are almost

exclusively IPCs, while human aRGCs display equal proportions of vertical and horizontal divisions when the OSVZ is becoming established (Howard et al. 2006; Smart 1973; Ostrem et al. 2017). Thus, changes in cleavage plane preference throughout evolution may have contributed to the establishment of more complex and diverse bPC compartments (Ostrem et al. 2017).

As already mentioned, in the mouse SVZ the most common bPCs are IPCs, unlike bRGCs they do not express the multipotency markers Pax6 and Sox2 and are instead characterised by the expression of *Tbr2* and *Ppp1r17* (Pollen et al. 2015). IPCs arise from asymmetric divisions of aRGCs, they lack adherens junctions, have multipolar morphology and are often found in close contact with blood vessels. It is estimated that 90% of IPC divisions are neurogenic and only 10% are symmetric expanding divisions (Noctor et al. 2004; Haubensak et al. 2004; Miyata et al. 2004). Thus, the transient amplifying potential of IPCs is very limited compared to that of bRGCs. Nevertheless, in mouse most cortical neurons are produced through a process of indirect neurogenesis relying on IPCs (Cárdenas et al. 2018). Although an SVZ as such is not found in reptiles, mitotic TBR2⁺ cells can be found scattered across the reptilian dorsal ventricular ridge and the avian pallium (Martínez-Cerdeño et al. 2012; Martínez-Cerdeño et al. 2016; Nomura et al. 2016). Therefore, from an evolutionary standpoint, TBR2⁺ intermediate progenitors may represent one of the first and most ancient mechanisms to shift from a direct to an indirect mode of neurogenesis (Cárdenas et al. 2018). Through the evolution of a diverse repertoire of progenitor cells with a diverse array of behaviours and mitotic profiles the cortex underwent a dramatic process of complexification that sees one of its highest achievements in the human neocortex (Fig. 7) (Giandomenico & Lancaster 2017).

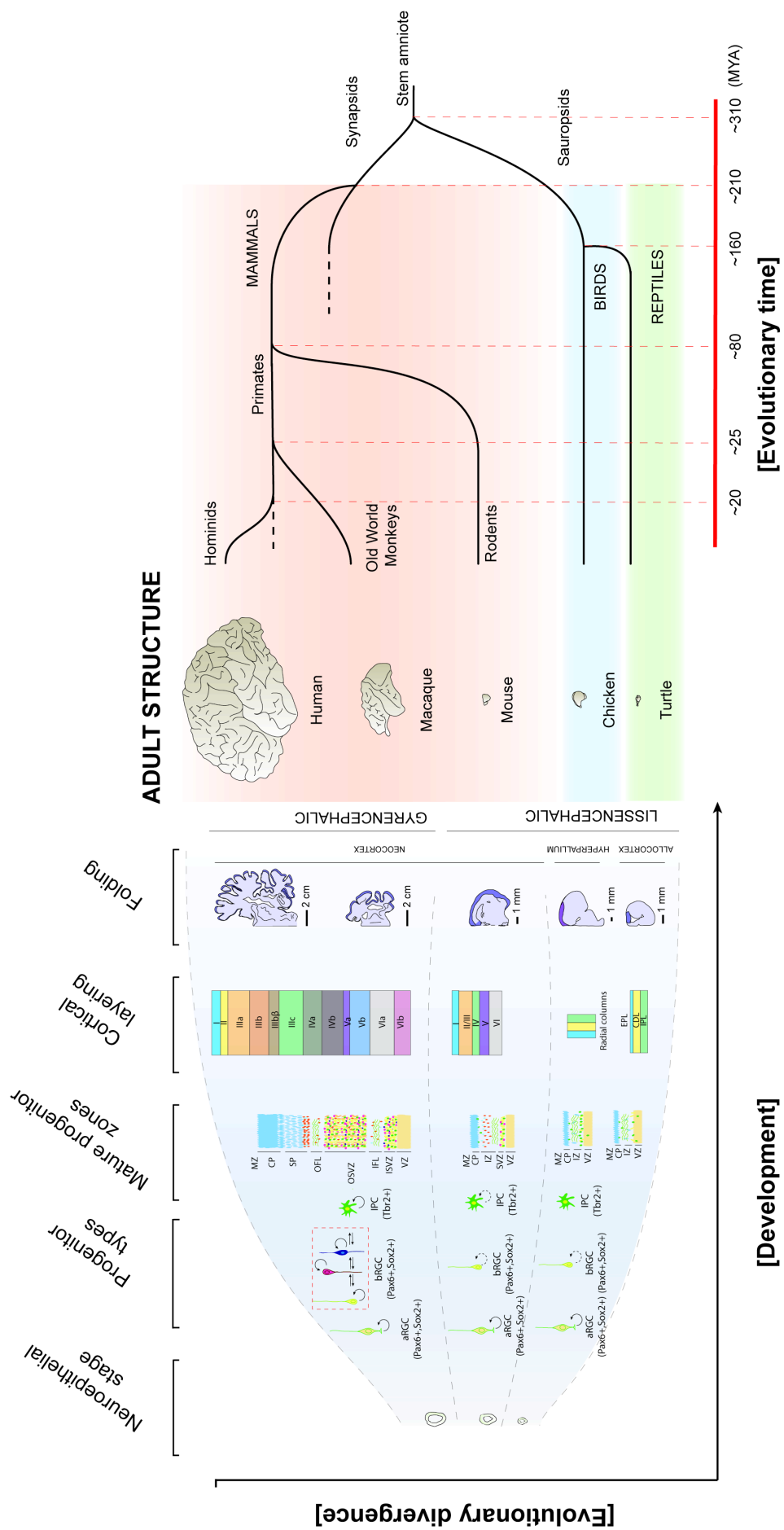


Figure 7 Changes in pallial tissue architecture across evolutionary and developmental timescales across amniotes.

a, Early on, at the neuroepithelial stage, the differences in size of the cortical primordia of reptiles, birds and mammals are comparatively small. However, as development progresses differences in cell-cycle dynamics and lineage plasticity of bPCs produce a dramatic divergence in cortical size, architecture and complexity. Birds and reptiles rely predominantly on direct neurogenesis, they display limited numbers of bPCs, most of which are neurogenic. Lineage-specific developmental differences are also seen across different mammalian species, leading to a diverse repertoire of neocortical configurations. Compared to the murine SVZ, that of primates is dramatically expanded, to include an ISVZ and an OSVZ. Work in Macaque has shown that in terms of cell type composition the SVZ of primates is more complex than that of mouse, displaying a variety of cellular morphotypes (red dashed box) able to interconvert between one another. The reptilian pallium produces a three-layered cortex similar to the mammalian paleocortex and comprising an internal plexiform layer (IPL), a cell dense layer (CDL) and an external plexiform layer (EPL). The avian hyperpallium, does not display layering and is instead organised into columnar-like regions. The mammalian neocortex comprises at least six layers, with primates showing further diversification into sublayers depending on the cortical area considered (e.g. 5-6 additional sublayers in visual cortex area VI are shown as an example). The adult brain structures are reported to scale, highlighting the dramatic increase in brain size over evolutionary time. Rounded arrows next to bPCs in the dashed box indicate self-renewal potential. Solid line—high capacity, dashed line—limited capacity. Reverse arrows indicate the ability to interconvert between morphotypes. The shaded panels delineate the three amniote classes; mammals—red, birds—blue, reptiles—green. The figure was taken from: Giandomenico & Lancaster 2017.

From the radial unit hypothesis to the discontinuous scaffold model

Historically, one theory to describe cortical development has been the radial unit hypothesis, whereby the neurons that populate the cerebral cortex are produced during embryogenesis by aRGCs and migrate along the basal fibre of their mother cell or that of a close neighbour to form a cortical column (Rakic 1988). Symmetric divisions of aRGCs will produce more cortical columns and lead to cortical expansion in the tangential dimension. Within a cortical column the temporal information on the genesis of neurons is encoded in the order of the layers (Rakic 1974). Thus, through development, the two-dimensional positional information encoded in the VZ is converted into a three-dimensional structure where the x and y coordinates correspond to the position of the aRGC progenitor in the telencephalon, while the position along z is determined by the birth date of the cell (Rakic 1988). Evidence in support of this theory has come from several lineage tracing experiments showing that in the cortex of mammals, including macaque and human, neurons form clusters with clonal origin

(Kornack & Rakic 1995; Luskin et al. 1988; Letinic et al. 2002). Furthermore, this theory is consistent with the dramatic increase in surface area and the relatively small increase in cortical thickness seen across primates (Fig. 7) (Rakic 2009). Nevertheless, this theory was recently revisited and expanded to include a more prominent role of the OSVZ compartment in neurogenesis and cortical expansion (Fig. 7) (Nowakowski et al. 2016).

According to the radial unit hypothesis, the aRGC scaffold is responsible for guiding newly born neurons to their final basal position. In humans this seems to be the case until approximately GW16, but from GW18-19 the endfeet of aRGCs appear to no longer contact the basal lamina and their basal processes retract to the ISVZ and OSVZ (Sidman & Rakic 1973; DeAzevedo et al. 2003). Crystals of the lipophilic tracer DiI placed at the apical surface of organotypic slice preparations of human cortex mark aRGC processes spanning the entire cortical wall until GW15.5. The same experiment done at later stages of neurogenesis (GW17-24) reveals that the aRGC basal processes do not stretch further than the OSVZ, and DiI crystals placed at the pia only label the basal fibres of bRGCs (Nowakowski et al. 2016). Therefore, it appears that in humans the cortical radial glial scaffold undergoes reorganisation between GW15 and 17, switching from continuous to discontinuous. Following retraction of the basal process, aRGCs are termed truncated radial glia cells (tRGCs), they acquire a distinct transcriptional profile and their endfeet contact capillaries in the ISVZ and OSVZ. These structural changes appear to be paralleled by changes in the relative neurogenic contribution of the VZ and OSVZ, with bRGCs being the major contributors of supergranular layer neurons (Fig. 7) (Betizeau et al. 2013). According to this model, the switch to a discontinuous radial glia scaffold may have contributed to the expansion of supergranular layer neurons in primates (Nowakowski et al. 2016). Importantly, these results should be interpreted with caution as they have not been independently validated, and the discontinuity of the scaffold may be a technical artefact due to differences in DiI diffusion rate at different developmental time-points. Furthermore, this process may not be unique to primates, and comprehensive characterisation of the truncated radial glia scaffold across different mammalian species is required to evaluate its relevance for cortical expansion and complexification.

Specification of cortical projection neurons

The inside-out gradient of neurogenesis

In the previous section we discussed the different progenitor types that populate the developing pallium, their properties, how they are found in different abundance across mammalian species, and how they can be organised in proliferative compartments of varying complexity. We will now consider how cortical glutamatergic excitatory neurons extend their axons over long distances to intracortical, subcortical and subcerebral targets to establish functional connections.

The cerebral cortex comprises two main types of neurons; excitatory glutamatergic neurons and inhibitory GABAergic interneurons. It is estimated that in the adult mouse neocortex the ratio of pyramidal neurons to interneurons is approximately 5:1 and the correct balance between these two cell types is tightly controlled to ensure the correct establishment of cortical circuits (Sahara et al. 2012). GABAergic inhibitory interneurons represent an extrinsic contribution to the cortex, during development they originate from the MGE and LGE in the ventral pallium and invade the cortex initially by tangential migration along two highly stereotyped paths, the SVZ and the MZ, and then by radial migration into the CP (Tanaka & Nakajima 2012; Anderson et al. 1997; Lavdas et al. 1999; Tanaka et al. 2006; Ang et al. 2003). In contrast, the full complement of cortical pyramidal cells is generated in the VZ and SVZ of the pallium in sequential temporal waves and they migrate radially along the RGC scaffold towards the pia. In their migration, they position themselves basal to earlier-born neurons in a process where layers are added in an inside-out fashion, layers VI and V first, followed by layers IV, III and II. At maturity, the different layers harbour distinct populations of projection neurons with specific morphology, transcriptional profile and projection pattern (i.e. hodology) (Kriegstein & Noctor 2004; Rakic 1972). The adult neocortex is organized into areas corresponding to functional subdivisions with distinct cytoarchitecture, chemoarchitecture, input/output connectivity and transcriptional profile (Molyneaux et al. 2007).

Cortical axons navigation – molecular guidance cues in the CNS

After migrating to and settling in the correct cortical layer, pyramidal cells start to send out axons to establish connections with appropriate targets in a process of circuit formation (Dickson 2002). The growing ends of axons, termed growth cones, consist of a central frame of microtubule bundles with a flat and expanded peripheral region of highly dynamic actin cytoskeleton that drives formation of filopodia and lamellipodia (Huber et al. 2003). Growth cones assume different morphologies, travel at different speeds and display different behaviours in response to their surrounding environment. Growth cones of pioneer axons typically have several active filopodia to sense the surrounding environment, few lamellipodia and display saltatory and exploratory behaviour. In contrast, growth cones of

follower axons are less branched and travel at higher speeds along the pioneers (Bak & Fraser 2003). Growth cones express cell surface receptors that interact with attractive and repulsive cues found on the surface of adjacent cells, in the extracellular matrix (ECM) or as soluble gradients (Kalil et al. 2011). Changes in the complement of receptors expressed at the growth cone and integration between different sets of guidance cues, ECM and cell-surface proteins control cytoskeletal reorganization and axonal navigation (Kalil et al. 2011; Stoeckli 2018).

The four major families of guidance cues include netrins, semaphorins, slits and ephrins (Judas et al. 2003). Netrins are a small family of secreted laminin-related proteins expressed along the ventral midline. In the CNS they establish diffusible gradients that generally attract commissural axons towards the midline (Kennedy et al. 1994; Serafini et al. 1994). The receptors for netrins are DCC and neogenin, and upon ligand binding they trigger attraction and repulsion, respectively (Chisholm & Tessier-Lavigne 1999). The semaphorins are a large family of transmembrane and secreted guidance molecules, they are divided into eight classes and mainly act as chemorepellents, but they can also attract certain classes of axons. Classes 3-7 are the vertebrate semaphorins; class 3 semaphorins are secreted, classes 4-6 are transmembrane proteins and class 7 are GPI-anchored proteins (Chisholm & Tessier-Lavigne 1999; Nakamura et al. 2000). Semaphorins guide axons by binding to receptor complexes composed of neuropilins and plexins (Tamagnone & Comoglio 2000). The most studied member of this family of guidance molecules is Semaphorin 3A, its main receptor is Neuropilin-1 and in complex they mediate sensory and motor axon repulsion, inhibition of cortical collateral branching and pruning of hippocampal axons (Shadrach & Pierchala 2018). Notably, in the telencephalon Neuropilin-1-Semaphorin 3C signalling has been shown to mediate attraction of pre-crossing axons of the corpus callosum (CC) to the midline (Niquille et al. 2009; Piper et al. 2009). Another important family of secreted chemorepellents are the slits, which in mammals include three genes (i.e. *slit1-3*). The Robo family of transmembrane receptors transduce slit signalling (Kidd et al. 1998a; Kidd et al. 1998b). In vertebrates slits are secreted from the floor plate of the spinal cord and from the midline of the forebrain and midbrain. In the spinal cord, post-crossing axons upregulate expression of Robo so that repulsion from slits secreted from the floorplate ensures that midline crossing occurs only once (Zou et al. 2000). Eph-ephrin signalling is also key to the correct wiring of the CNS. Ephrins are surface-associated ligands for the Eph family of receptor tyrosine kinases and vertebrates have two classes of ligands and receptors; EphA and EphB ligands and ephrin-A and ephrin-B receptors (Flanagan & Vanderhaeghen 1998). Differently to the other signalling systems discussed so far, Eph-ephrin signalling is bidirectional and involves activation of signalling pathways in both cells of the interacting pair. Ephs and ephrins have been implicated in several processes including cortical progenitors division, neuronal migration, axon pathfinding and circuit formation (Klein 2001). With regards to axon pathfinding in the cortex, loss-of-function of EphA4 and ephrin-A5 causes incorrect dual targeting of thalamocortical projections to the somatosensory and limbic cortical areas, and mis-expression of EphA7 causes abnormal mapping of corticothalamic projections (Dufour et al. 2003;

Uziel et al. 2002; Torii & Levitt 2005). While early deletion of EphA8 leads to complete agenesis of the CC, expression of a dominant negative form of EphA5 causes defective callosal projection from deep-layer neurons (Park et al. 1997; Hu et al. 2003). Furthermore, ephrin-B1 was shown to interact with Neuropilin-1 to stop the attractive influence of Semaphorin3C on postcrossing callosal axons (Mire et al. 2018). All these findings suggest a role for Eph-Ephrin signalling in afferent, efferent and intracortical axon pathfinding.

Historically, these families of signalling molecules were among the first to be recognised as important factors in axon guidance; however, in recent years new guidance cues have been identified. The morphogen Wnt5A was shown to interact with the receptor tyrosine kinase Ryk expressed by post-crossing callosal axons, acting as a chemorepulsive cue to efficiently drive axons to the contralateral side of the cortex (Keeble et al. 2006). Furthermore, BMPs secreted from the roof plate and Shh from the floor plate together with Netrin-1 were shown to guide commissural spinal cord axons to the ventral midline (Zou & Lyuksyutova 2007). Therefore, it has become increasingly appreciated how morphogens involved in AP and DV patterning can also play an important role in axon guidance.

Cell adhesion molecules in axon pathfinding

Extending axons are covered in a vast array of cell adhesion molecules (CAMs) belonging to the Ca^{2+} -dependent cadherins and the Ca^{2+} -independent immunoglobulin superfamily CAMs (IgSF-CAMs). Several IgSF-CAMs (e.g. NCAM1, NCAM2, L1CAM, ALCAM) are expressed on growing axons and were found to be important for correct axonal navigation and wiring (Pollerberg et al. 2013). As an example, *L1CAM*^{-/-} mice display aberrant thalamocortical and corticospinal projections, failure of callosal axons to decussate and hyperfasciculation (Cohen et al. 1998; Demyanenko et al. 1999). Conversely, in mice lacking NrCAM the anterior commissure shows defasciculation and incorrect targeting (Falk et al. 2005). Homophilic and heterophilic trans-interactions between CAMs on different axons are essential for the process of fasciculation, in which follower axons track their growth cones along pioneers. Fasciculation leads to the establishment of bundles containing axons that project to the same target area. Thus IgSF-CAMs play a dual role, firstly, they act as a sensory molecule, guiding axons to their correct target, secondly, they act as tracks for follower axons and limit their stray (Pollerberg et al. 2013). In addition, experiments in which NCAM1 and ALCAM were provided as the only substrates to axons have shown that IgSF-CAMs are sufficient to promote axonal growth (Sadoul et al. 1983; Thelen et al. 2012). This is likely mediated by interaction with intracellular signalling pathways components such as the MAP kinase Erk, members of the integrin family, FGF receptors and components of the cytoskeleton (Schmid et al. 2000). Therefore, cell adhesion plays an important role at several stages of axon pathfinding; including fasciculation, guidance, target innervation and neurite growth.

Projection neuron types and molecular identity

Neocortical pyramidal cells can be divided into three broad categories based on their projection modality and target area: corticofugal (subcortical and subcerebral), callosal and ipsilateral projection neurons (Fig. 8a & b) (Molyneaux et al. 2007). Corticofugal projection neurons are located almost exclusively in deep layers of the cortex and include subplate neurons, which project to the thalamus during embryonic development and postnatally are either integrated with deep-layer neurons or die (Ozair et al. 2018), corticothalamic neurons located in layer VI and subcerebral projection neurons, located in layer V and projecting to midbrain, hindbrain and spinal cord (Fig. 8b) (McConnell et al. 1989; Molyneaux et al. 2007). In contrast, callosal projection neurons (CPNs) are distributed across layers II/III (~80% in rodents), layer V (~20% in rodents) and are also found in small numbers in layers Va and VI (Fig. 8a) (Greig et al. 2013). The CC is the largest commissure in the brain of placental mammals and it integrates information from the two cerebral hemispheres. Ipsilateral projection neurons are distributed in superficial (II/III) and deep layers (V/VI), are present in larger proportion than contralateral projecting neurons and relay information between different neocortical areas of the same hemisphere (Molyneaux et al. 2007; Molyneaux et al. 2009; Suárez et al. 2018).

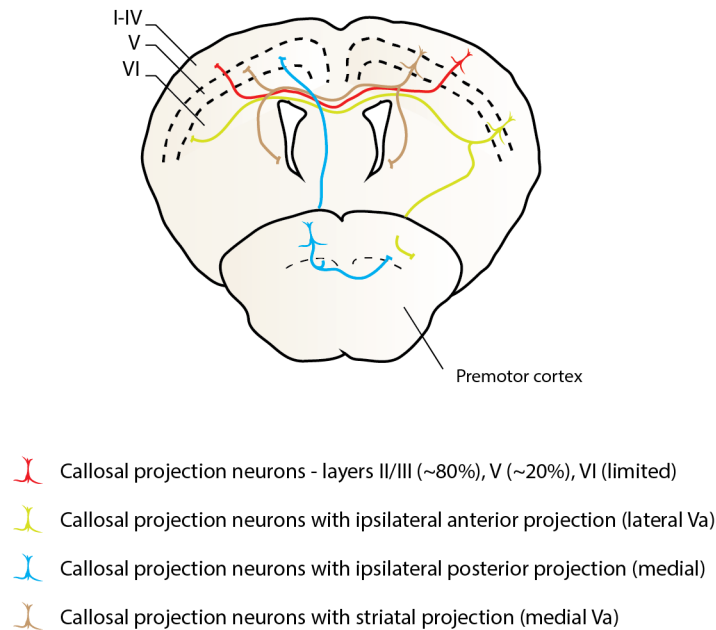
To this day we lack a complete understanding of the cell intrinsic and extrinsic factors that regulate the progressive commitment of VZ and SVZ progenitors to produce distinct neuronal subtypes. Classical transplantation experiments have shown that, as development progresses, progenitor cells become less plastic and, while early progenitors in a more mature niche can switch to producing upper layer neurons, the converse is not possible (McConnell & Kaznowski 1991; Frantz & McConnell 1996). Recently, this dogma was called into question, and cortical progenitors were shown to retain multipotency throughout cortical neurogenesis (Oberst et al. 2018). Nevertheless, several studies have shown that loss of progenitor plasticity is mediated by intrinsic mechanisms, such as cell cycle lengthening, as well as secreted factors, for instance BDNF and NTF3 (Seuntjens et al. 2009; Fukumitsu et al. 2006). During neurogenesis several genes that mark specific neuronal subtypes are turned on in subpopulations of VZ and SVZ progenitors. For example, *Fezf2* is expressed by aRGCs at the time when deep layer neurons are produced and also by postmitotic subcerebral projection neurons. Notably, in *Fezf2*^{-/-} mutant mice subcerebral projection neurons display a projection modality, electrophysiological properties and marker expression consistent with CPN identity (Guo et al. 2013). Furthermore, expression of *Fezf2* in striatal neuron progenitors is sufficient to generate corticofugal neurons (Rouaux & Arlotta 2010). Therefore *Fezf2* and its downstream effector *Ctip2* are examples of genes that, in addition to labelling a specific subset of progenitors, are directly involved in commitment to a specific laminar fate (Chen et al. 2008). As a counterexample, *Cux2* and *Cux1* mark layer II/III postmitotic neurons and are expressed by SVZ progenitors during neurogenesis of upper layer neurons; however, *Cux1*^{-/-};*Cux2*^{-/-} double knockout mice do not display any obvious neuronal migration or lamination defects (Cubelos et al. 2008; Cubelos et al. 2010; Nieto et al. 2004).

This suggests that *Cux* genes may not be directly involved in progenitor specification, but they may regulate maturation of upper layer neurons (Cubelos et al. 2010). Importantly, it is not possible to infer the function of a gene in layer specification based on its expression pattern and mechanistic studies are required.

Molecular determinants of subcerebral projection neurons specification

Subcerebral projection neurons are particularly amenable to studies aimed at understanding neuronal subtype specification because they are specifically located in layer V and their projections can be easily identified. In fact, they all send primary axons through the internal capsule, into the cerebral peduncle and down the pyramidal tract (Greig et al. 2013; Arlotta et al. 2005). Due to their disease relevance, the most studied subset of subcerebral projection neurons are corticospinal motoneurons (CSMNs). They express unique markers, such as *Diap3*, *Igfbp4* and *Crim1*, along with genes that are expressed by all subcerebral projection neurons; *Ctip2*, *Fezf2* and *Pcp4* among others (Arlotta et al. 2005). Important factors in the specification of subcerebral projection neurons include *Fezf2* and *Ctip2*, with their loss leading to defects in neuronal specification, axonal outgrowth, pathfinding and abnormal fasciculation (Chen et al. 2008; Chen et al. 2005). The homeobox transcription factor OTX1 is expressed in putative deep layer neurons VZ progenitors and its expression rapidly declines during upper layer neurogenesis. Suggesting a role for OTX1 in deep layer neuron maturation, it translocates from the cytoplasm into the nucleus upon cell cycle exit and is expressed primarily in subcerebral projection neurons of the visual cortex (Weimann et al. 1999; Frantz et al. 1994). *Sox5* controls sequential and ordered generation of deep layer neurons with distinct identity and morphology (i.e. subplate, corticospinal and corticothalamic). *Sox5*^{-/-} mice show accelerated differentiation of subcerebral projection neurons, defects in subplate neuron connectivity and incorrect differentiation of corticothalamic neurons. Furthermore, supporting retention of a certain degree of progenitor plasticity, re-expression of *Sox5* during genesis of upper layer neurons leads to the reappearance of neurons with corticofugal character (Lai et al. 2008; Kwan et al. 2008). At present *Fezf2*, *Ctip2*, *Sox5* and *Otx1* are the few functionally characterised drivers of subcerebral projection neuron specification.

CALLOSAL PROJECTION NEURONS



CORTICOFUGAL PROJECTION NEURONS

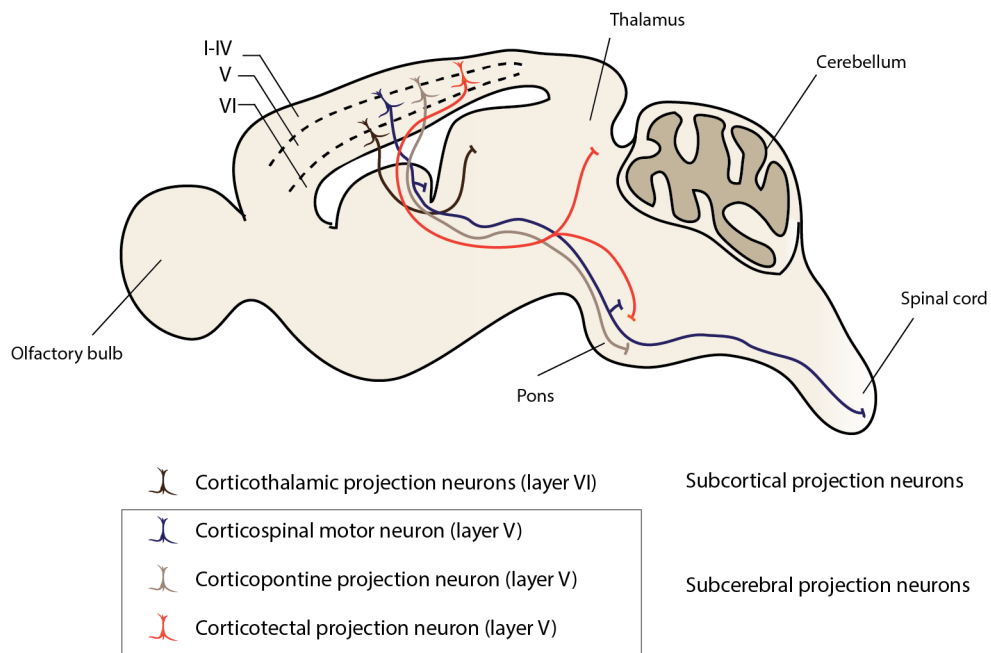


Figure 8 Major classes of projection neurons within the neocortex.

a, Callosal projection neurons are a type of commissural neurons primarily found in layers II/III (~80%), V(~20%) and in small numbers in VI, and project into the corpus callosum (CC). Based on their targets they can be further subdivided into: neurons with a single projection to the contralateral

cortex, neurons with dual projection, to the contralateral and ipsilateral frontal cortex, with dual projection, to the contralateral and ipsilateral caudal cortex, with dual projection, to the contralateral cortex and striatum. Callosal neurons do not project outside the telencephalon. b, The schematic shows the different types of neurons that project away from the cerebral cortex, termed corticofugal. These include corticothalamic projection neurons, primarily located in layer VI and, in fewer numbers, V of the cortex, which project to different thalamic nuclei. Neurons that project outside of the cerebrum, to the brainstem and spinal cord, are termed subcerebral projection neurons. They are located predominantly in layer V and include; corticospinal motor neurons, located primarily in the sensorimotor area of the cortex and sending their main projection to the spinal cord, with secondary collaterals to striatum, pons and medulla. Corticopontine projection neurons have as main projection target the pons, and corticotectal projection neurons are found in the visual area of the cortex and project to the superior colliculus and send collaterals to rostral pons. Reported here are the main classes of subcerebral projection neurons - there are many more that project to different areas of the brainstem but are not reported for simplicity. The figure was adapted from: MacDonald et al. 2013.

Molecular determinants of CPN specification

CPNs neurons connect homotopic regions of the cerebral hemispheres through the CC and surgical or pathological disruption of this pathway is associated with impaired abstract reasoning, intellectual disability and reduced problem solving skills. The broad distribution of CPNs across both superficial and deep layers of the neocortex reflects their heterogeneity in terms of birth date and projection modality (Greig et al. 2013; Fame et al. 2011). In mouse in fact, while CPNs located in layer II/III have predominantly a single axon projecting to the contralateral homotopic region, approximately 40% of CPNs found in layer V have an additional ipsilateral projection to a different cortical area of the same hemisphere (Mitchell & Macklis 2005). Whilst much is known about the molecular determinants of CPN midline crossing, the mechanisms underlying their specification remain elusive. So far the only well documented regulator of CPN specification is the transcription factor *Satb2*. It acts by antagonising the corticofugal projection regulator *Ctip2*, and *Satb2*^{-/-} mutant mice display complete agenesis of the CC, with callosal neurons projecting subcortically rather than to the contralateral hemisphere (Britanova et al. 2008; Alcamo et al. 2008). Recently, adding to our understanding of the molecular-genetic control of CPNs specification, *Cux1* and *Cux2* were shown to regulate spine development, branching and synapse formation in layer II/III CPNs (Cubelos et al. 2008). Furthermore, a combination of *in situ* hybridization, immunohistochemistry and tract-tracing recently identified a subset of genes specific to CPNs of superficial (e.g. *Inhba*, *Cpne4* and *Btg1*) and deep layers (e.g. *Plexin-D1*, *TcrB* and *Dkk3*) (Molyneaux et al. 2009). Therefore, we have started to glean insight into the genetic diversity of this population of pyramidal neurons.

Evolutionary relevance of layer II/III

Layers II/III of the neocortex are often referred to as the supergranular compartment (Betizeau et al. 2013). Supergranular layer neurons are not found in the sauropsid cortex, which comprises only three layers, evolutionarily related to layers I, V and VI of the neocortex (Molnár et al. 2006). All mammals have supergranular layer neurons but in primates this population has undergone a dramatic expansion attributed to the complexification and diversification of the SVZ compartment (Fig. 7). The CC represents the major commissural connection in eutherian mammals and is composed to a large extent by projections from supergranular layer neurons (~80% of CPNs in mice). In contrast, in monotremes and marsupials the major interhemispheric connection is the anterior commissure and the CC is entirely missing (Suárez et al. 2018). This suggests that the evolution of the mammalian brain required the implementation of molecular genetic programs to specify layer II/III neurons, expand their pool size and modify their connectivity (Fig. 7). Thus, understanding the molecular mechanisms driving layer II/III neuron specification and targeting will certainly be of clinical relevance and may also be informative of the evolutionary history of the mammalian brain.

***In vitro* 3D models of cortical development**

An evo-devo approach to neurodevelopmental studies

Understanding the function and the physiology of as complex an organ as the brain requires knowledge of the developmental events leading to its establishment. By framing ontogenetic changes in the context of evolution one can glean a complete picture of the purpose and role of a cell, set of cells or whole organs in a living system (Giandomenico & Lancaster 2017). This is particularly relevant when considering the mammalian brain, since in recent evolutionary time it has undergone rapid and profound diversification. Nonetheless, taking an evo-devo approach involves complementing comparative analyses on phylogenetically related species with functional studies where specific genes or pathways are modulated (Giandomenico & Lancaster 2017). Due to obvious ethical and technical issues, so far, the study of the hominin brain has been limited to comparative neuroanatomical analyses.

Due to a lack of genetic tools, high maintenance costs, long generation time and ethical concerns, only a handful of functional studies were done in ferret and marmoset (Johnson et al. 2018; Florio et al. 2015; Cárdenas et al. 2018; Park et al. 2016). The majority of studies probing gene function in neocortex development have typically relied on mouse, but this approach suffers from limitations (Stahl et al. 2013; Florio et al. 2015). The proliferative compartments of the mouse neocortex are considerably smaller and simpler compared to those of larger mammals. Mouse bPCs are almost exclusively IPCs that preferentially undergo symmetric neurogenic divisions, while mammals with larger cortices and primates in particular display enlarged, diverse and more complex abventricular proliferative zones (Miyata et al. 2004; Haubensak et al. 2004). In addition, in the case where the gene of interest is not found in mouse because it arose later in mammalian evolution, functional gene testing is limited to overexpression, which is less powerful than loss-of-function approaches.

In vitro 2D and 3D neural differentiation

The derivation of human embryonic stem cell lines (hESCs) followed by the discovery of reprogramming factors and induced pluripotent stem cells (iPSCs) opened the possibility of modelling aspects of embryonic brain development *in vitro*. Adherent cultures of neural progenitor cells, termed neural rosettes, were the first step in the development of ever more complex *in vitro* neurodevelopmental models. Neural rosettes were derived by plating iPSC aggregates, termed embryoid bodies (EBs), on coated dishes and differentiated to clusters of NECs (Zhang et al. 2001). Next, derivation of neural rosettes from EBs under serum free conditions with the addition of specific inductive cues led to the establishment of the SFEB method (serum free culture of embryoid bodies) (Watanabe et al. 2005). Nevertheless, 2D culture approaches suffer from a number of limitations;

firstly, the cell-cell and cell-extracellular matrix (ECM) interactions are offset by the artificial interaction between cells and plastic surfaces. Secondly, the mechanical properties of culture vessel plastics are very different to those of the *in vivo* niche, meaning that the apico-basal polarity, migration and proliferative behaviour of cells are altered. Lastly, development crucially relies on the establishment of signalling centres providing a source of morphogens and growth factors, and in 2D methods, this level of regulation is completely absent (Paşca 2018).

Representing a first step towards a fully 3D culture paradigm, in the SFEBq method, an improvement of SFEB, EBs are kept in suspension for a longer period of time before 2D plating, thereby allowing for the generation of larger rosettes with elongated apical lumens that do not completely flatten out (Eiraku et al. 2008; Kelava & Lancaster 2016). A key advancement in the development of 3D culture methods was the discovery that stem cells embedded in a gelatinous mixture of ECM proteins, called Matrigel, allowed for the development of well organised epithelia with apico-basal polarity (Sato et al. 2009). Building on the SFEBq method and using dissolved Matrigel for culture, the first 3D fully in suspension paradigm to generate optic cup structures was developed (Eiraku et al. 2011). Importantly, this study demonstrated that PSCs could differentiate and organise into complex and accurate neural tissue architecture reminiscent of *in vivo* development.

Cerebral organoids – a 3D intrinsic neural differentiation model

The SFEBq and optic cup differentiation protocols rely on directed differentiation, where instructive cues are used to induce neuroectodermal tissue and pattern it to different regional identities. In contrast, cerebral organoids represent an intrinsic differentiation method in which no instructive cues are provided and cells are allowed to spontaneously self-organize to form a variety of brain identities (Lancaster et al. 2013). Whilst the use of growth factors and patterning cues limits the expansion of the neuroepithelium, cerebral organoids generate long continuous neuroepithelial sheets surrounding inner fluid-filled cavities interconnected to form a ventricular system similar to that of the brain. In cerebral organoids a variety of forebrain identities coexist, including ventral, dorsal pallium and choroid plexus (Lancaster & Knoblich 2014; Eiraku et al. 2008). Between these different structures forebrain organising centres secreting growth factors and patterning cues develop. Importantly, the relative positioning of signalling centres and brain regions does not appear to be random but loosely mirrors the *in vivo* pattern. Furthermore, the timed inside-out gradient of neurogenesis followed by production of astrocytes and oligodendrocytes are all features of the organoid model (Renner et al. 2017). Recently, the addition of microscaffolds for EB formation and supplementation of dissolved Matrigel during late culture stages were shown to allow for more reliable generation of forebrain tissue and establishment of the CP (Lancaster et al. 2017).

Cerebral organoids: a tractable system for evo-devo and disease studies

Cerebral organoids achieve a degree of elaboration and complexity superior to 2D approaches. In a cross-section cerebral organoids have macroscopic buds displaying complex tissue architecture with distinct proliferative zones homologous to the VZ and SVZ compartments (Lancaster et al. 2013). Several transcriptomic analyses on cerebral organoids have shown that they produce cell diversity and transcriptional programs close to the early human foetal brain (Camp et al. 2015; Luo et al. 2016; Yoon et al. 2019). A first clue as to the applicability of cerebral organoids as a model for evo-devo studies was the observation that human and mouse cerebral organoids show a different organisation of the abventricular progenitor compartments. Whilst human brain organoids have a sizable bRGC population with some separation into a zone resembling the OSVZ, mouse cerebral organoids have sparse bRGCs, no SVZ compartmentalisation and the majority of bPCs are IPCs (Fig. 9a) (Lancaster et al. 2013). Furthermore, organoid development seems to follow the timing of *in vivo* development; mouse brain organoids, in line with their 20-day gestational period, progress through neurogenesis more rapidly than human organoids (Eiraku et al. 2008).

In recent years several studies were published where iPSC from different species were used for evo-devo studies. Neural rosettes and 3D forebrain organoids derived from human, chimpanzee and macaque iPSCs were used in combination to perform progenitor clonal analyses. This seminal study demonstrated that macaque progenitors stop expanding and switch from deep- to upper-layer neurogenesis earlier than human or chimp progenitors (Fig. 9a) (Otani et al. 2016). In another study, by comparison of human cerebral organoids and mouse embryonic brains it was shown that human bRGCs and IPCs exhibit increased SHH signalling, consistent with increased progenitor proliferation (Wang et al. 2016). Furthermore, a recent publication reported that in human neural organoids aRGC metaphase is ~40-60% longer than in chimpanzee. The same was seen in orangutan aRGCs and, importantly, it appeared to be a feature of this specific cell type, as the iPSCs of origin did not display this behaviour. Interestingly, lengthening of metaphase correlates with symmetric proliferative divisions of aRGCs, and the authors argue that it may have contributed to increasing the neurogenic output of human apical progenitors (Mora-Bermúdez et al. 2016).

Advances in genome editing and reprogramming technologies

Concurrently with the establishment of complex 3D *in vitro* culture systems, important advances were made in the field of somatic cell reprogramming, genome editing and optogenetics (Kogut et al. 2018; Chen et al. 2013; Boyden 2011; Ran et al. 2013). These new technology platforms in combination with the diverse array of organoids that can now be produced (e.g. brain, kidney, liver, gut) hold great potential for disease modelling, the study of development, evolution and functional neuroscience (Qian et al. 2016; Li et al. 2016; Schwank et al. 2013; Quadrato et al. 2017). The high

efficiency of current reprogramming protocols has made it possible to derive iPSCs not only from primary fibroblasts derived from skin biopsies, but also from blood, hair follicle keratinocytes and renal epithelial cells present in urine (Raab et al. 2014). The procedures to derive these cell types are minimally invasive and this has dramatically expanded the cohort of potential donors. Recently, there were reports of iPSCs derived from a diverse array of mammalian species and even birds, fish and insects; suggesting that, perhaps soon, *in vitro* broad species comparison will be possible (Fig. 9b) (Ben-Nun et al. 2011; Rosselló et al. 2013; Wunderlich et al. 2014). Thanks to the development of CRISPR-Cas9 genome editing it is now possible to readily generate knockouts and, albeit with lower efficiency, single-base substitutions, endogenous tagging, silencing and activation can be achieved (Fig. 9b) (Ran et al. 2013; Zheng et al. 2018; Konermann et al. 2015). Importantly, CRISPR-Cas9 allows generation of isogenic lines, thus limiting confounding effects due to different genetic backgrounds. An intriguing avenue to pursue is to use CRISPR-Cas9 to study the effect loss-of-function mutations in human specific genes with a role in brain development (e.g. *ARHGAP11B* and *NOTCH2NLB*) or introducing and correcting disease-related mutations (Fig. 9b) (Florio et al. 2015; Suzuki et al. 2018; Schwank et al. 2013). Furthermore, the new Cas13 system can be used for RNA knockdown and editing, modulation of splicing pattern and RNA localisation studies, thus allowing for fine-detail analysis of the role of miRNAs and lncRNAs in a variety of contexts (Konermann et al. 2018; Cox et al. 2017). With particular relevance to cerebral organoids, the development of halo- and channelrhodopsins together with genetically encoded calcium indicators (GECIs) opens the possibility of manipulating and monitoring neural circuits with light (Fenno et al. 2011). The fortuitous convergence of these recent technological advances enables the scientific community to tackle questions in cancer biology, development, disease biology and neuroscience from completely novel angles (Fig. 9a & b).

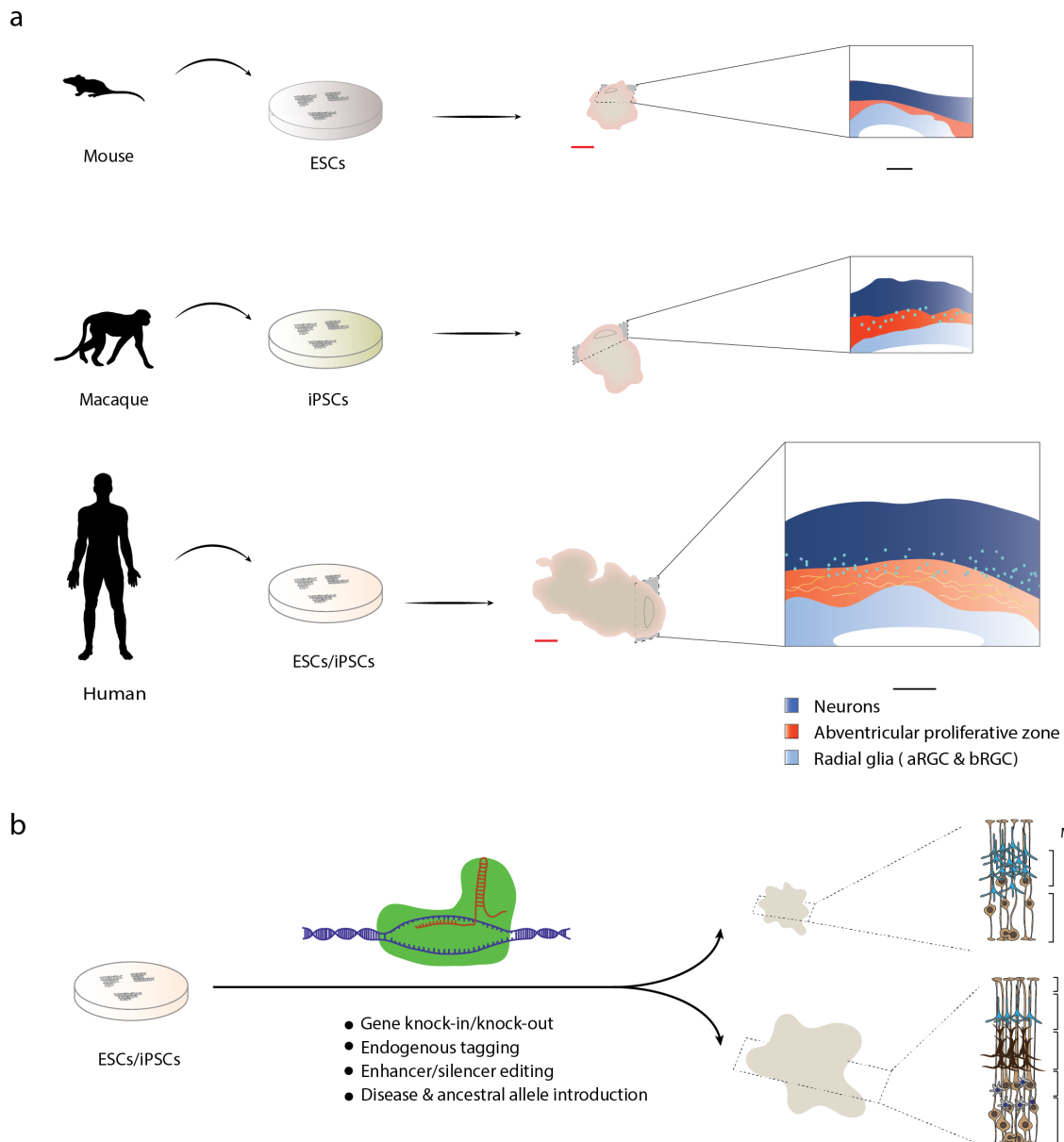


Figure 9 Application of cerebral organoids to evo-devo studies.

a, Cerebral organoids also allow cross-species comparison studies of early brain development on species that would not be accessible by any other means. The figure depicts schematics from two studies that to date have taken this approach. Human iPSC-derived cerebral organoids were shown to harbour a population of abventricular $SOX2^+$ bRGCs separated from the VZ and ISVZ by $TUBB3^+$ neuronal processes. This is somewhat similar to *in vivo* where the OSVZ is separated from the ISVZ by the inner fibre layer (IFL) (Lancaster et al. 2013). By contrast, mouse ESC-derived organoids were generally smaller, showed faster development compared to human organoids and lacked $Sox2^+$ bRGCs (Lancaster et al. 2013). In another example study, the timing of neuronal lamination was studied by a combination of 2D and 3D *in vitro* cultures and revealed that the switch from deep- to superficial-layer neurons in macaque occurs earlier than in humans (Otani et al. 2016). Diagrams of mouse and human organoids are to scale relative to each other (scale bar = 400 μ m). b, CRISPR-Cas9 gene editing in hPSCs can be used to knock-in/out genes to probe their function in brain development.

Endogenous tagging allows for improved biochemical and live cell imaging over traditional overexpression strategies. Editing and replacement of a gene or its regulatory elements to introduce an ancestral variant can give insight into specific changes highly relevant for evolution of certain traits. In the example depicted, control and edited cells produce cerebral organoids of different sizes, revealing a loss of bPCs in the mutants. A combination of state-of-the-art genome editing techniques and organoids opens new avenues for studying gene function in the context of evolution. Panel a of the figure was modified from: Giandomenico & Lancaster 2017.

Present limitations of brain organoids as a model system

Despite their strengths, at present, cerebral organoids have a number of weaknesses that in the future will need to be addressed for careful functional and comparative analyses. Firstly, neither in directed nor in intrinsic differentiation approaches is it possible to control how patterning cues are spatially encoded. Thus, the production of different brain structures and their relative positioning are stochastic and the overall stereotypic architecture of the brain cannot be reproduced (Giandomenico & Lancaster 2017). In this respect, the recent development of assembloids derived by fusing spheroids pre-patterned with different identities represents a first important step towards achieving the stereotypical organisation of structures seen in the brain (Bagley et al. 2017; Birey et al. 2017). Whilst the original organoid protocol allowed for the identification and modelling of relatively strong phenotypes, new ameliorated methods have improved consistency and reproducibility and have the potential to capture more subtle phenotypes (Lancaster et al. 2013; Lancaster et al. 2017; Qian et al. 2016).

Secondly, starting from E10-11 in mouse and 18-20 PCW in humans the telencephalic vascular network starts to develop and it has been shown to be important for maintenance of the stem cell niche and neuronal differentiation (Siegenthaler et al. 2009). Suspension culture of cerebral organoids with agitation vastly improves tissue perfusion by oxygen and nutrients. However, after approximately two months in culture the size of the organoid exceeds the perfusion limit and a necrotic core develops, resulting in the progressive loss of neurons and appearance of reactive astrocytes (Lancaster et al. 2013; Renner et al. 2017). This severely restricts the number of questions that can be asked using this model, and aspects of neuronal maturation such as axon pathfinding and synapse formation have remained elusive. Recent efforts to address this problem include addition of growth factors (e.g. BDNF) and organoid transplantation into the brain of rodents to achieve vascularization (Quadrato et al. 2017; Mansour et al. 2018). Nevertheless, at present we are still missing a practical and scalable approach to expand the developmental time window accessible with organoids.

Lastly, it is important to mention that culture and genome editing of both hESCs and hiPSCs have proven historically challenging. hPSCs are epithelial in character, grow as compact colonies and show

low survival rates upon single cell suspension (Ohnuki & Takahashi 2015). Novel, more robust media formulations with an improved thermostable version of FGF2 together with the development of more specific Rho-kinase inhibitors have greatly simplified these tasks (Daniszewski et al. 2018; Chen & Pruett-Miller 2018). Another important aspect to consider in the context of evo-devo studies is that, whilst reprogramming of human and primate cells can be achieved with high efficiency, reprogramming and maintenance of other species' PSCs often has low efficiency and the cells may not be fully pluripotent (Ben-Nun et al. 2015). Pluripotency is an important aspect to consider when carrying out comparative studies using patient-derived lines or iPSCs from different species. Different PSCs may retain epigenetic marks that make them more prone to generating a certain germ layer over another (Tsankov et al. 2015). Therefore, robust comparative studies with brain organoids require phenotypic characterisation of several clones from multiple individuals.

An *in silico* screen identifies *ZEB2* as a putative regulator of neocortical expansion

A list of brain evolution candidate genes

In an effort to identify genes potentially responsible for human neocortical expansion we performed a metadata analysis of 40 independent publicly available genomic and transcriptomic datasets. The rationale for the analysis was that a good candidate for a role in human brain evolution would exhibit features of human evolutionary selection at the genomic level and would have an expression profile specific to the human brain. A set of 27 independent comparative genomic datasets were used to identify loci with features of human specific evolutionary selection. Cross-comparison of the datasets yielded a list of shared intervals that were then mapped to the reference genome (hg38) to identify genes near or within the intervals. Candidate genes were identified by a Poisson test with occurrence set above or equal to 3 ($p < 0.01$). A second set of 13 independent comparative transcriptomic analyses were used to identify genes with human specific brain expression. One of the 13 datasets was produced through in-house analysis of microarray and RNA-seq data available from the Allen Brain Atlas and the NIH Blueprint Non-Human Primate (NHP) Atlas. First, we identified human genes highly expressed in the pallium by filtering RNA-seq data available from the Brainspan atlas for genes with expression coordinates that correlated with the pallial marker *EMX1*. All genes with significant occurrence ($RPKM \geq 3$) between 8 and 37 PCW in any cortex or hippocampal region were converted to genomic intervals. A similar approach was taken to compile a list of genes with high expression in the macaque pallium. A dataset of genes with expression pattern specific to humans was obtained by excluding genes common to both the human and macaque lists. This dataset was combined with 12 other independent comparative transcriptomic datasets and candidate genes were identified by Poisson's statistics on occurrence equal to or above three as being significantly overrepresented ($p < 0.01$). The overlap of the comparative genomic and transcriptomic lists revealed a total of 139 genes. These were filtered for genes expressed in organoids ($RPKM \geq 3$) at day 20, 40 and 60 of the differentiation protocol, reducing the list of human brain evolution genes to 60 hits with the top candidate being *ZEB2*.

The transcription factor ZEB2

ZEB2 (zinc finger E-box binding homeobox 2), also known as *Zfhx1b* or *SIP1* (Smad interacting protein 1), together with *ZEB1* constitute the *ZEB* family of two-handed zinc-finger/ homeodomain transcription factors. *ZEB2* was originally identified through a yeast 2-hybrid screen as an interactor of the *Xenopus* protein *Xsmad1* (Verschuere et al. 1999). *ZEB* proteins, and in particular *ZEB2*, have a well-established role in cancer biology as master regulators of EMT and tumour metastasis (Stemmler et al. 2019; Pei et al. 2019). *ZEB* proteins have a complex structure comprising a central homeodomain, two widely spaced C2H2 zinc finger clusters and multiple protein interaction domains.

They modulate transcription by binding to tandem E-box-like sequences (5'-CACCT(G) or 5'-CACANNT(G)) in the regulatory regions of target genes through an N- and C-terminal zinc finger cluster (Fig. 10). The N-terminal cluster is composed of four zinc fingers (three CCHH and one CCHC) and the C-terminal cluster of three zinc fingers (all CCHH) (Fig. 10) (Remacle et al. 1999; Verschuere et al. 1999). Their amino acid sequences are highly conserved between *ZEB1* and *ZEB2*, with the N- and C-terminal clusters displaying 95% and 89% sequence identity, respectively (Stemmler et al. 2019). The four PLXL(S/T) (CID) motifs found within *ZEB2* mediate interaction with CtBP (C-terminal binding protein), which binds to histone modifying enzymes, DNA binding proteins, CoREST and chromodomain proteins to form transcriptional repressor complexes (Fig. 10) (Postigo & Dean 1999; van Grunsven et al. 2007). *ZEB2* SUMOylation at residues K391 and K866 regulates its transcriptional activity by disrupting interaction with CtBP (Long et al. 2005). *ZEB2* is also able to interact with the chromatin remodelling histone deacetylase (HDAC) complex NuRD via an N-terminal NuRD interaction motif (NIM) and with the transcriptional activator histone acetyltransferase complexes (HAT) p300/PCAF (Fig. 10) (Verstappen et al. 2008; van Grunsven et al. 2006). Thus, by virtue of its complex structure *ZEB2* can act as both a transcriptional repressor and activator depending on the specific cellular context.

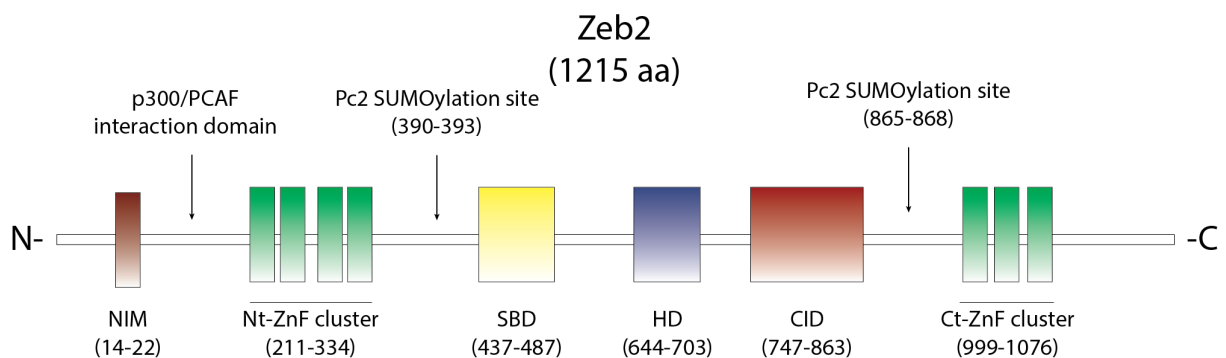


Figure 10 The functional domains of Zeb2.

Schematic representation of the functional domains and post-translational modification (PTM) sites found in the mouse main *Zeb2* isoform (1215 aa). The Nt-ZnF cluster (aa 211-334) and the Ct-ZnF cluster (aa 999-1076) comprise C2H2-type zinc-fingers which bind to tandem E-box sequences. The homeodomain (HD) is centrally located (aa 644-703) and has lost DNA-binding capacity. Corresponding to aa 14-22 is a NuRD complex interaction motif (NIM) and also N-terminal, albeit not mapped, is the p300/PCAF interaction domain. *Zeb2* interacts with p-SMADs via a SMAD-binding domain (SBD) (437-487), downstream of the Nt-ZnF cluster. The CTB interaction domain (CID) is located between aa 747-863 and comprises four PLXL(S/T) motifs. *Zeb2* undergoes SUMOylation at positions: 390-393 and 865-868. The figure was adapted from: Hegarty et al. 2015.

ZEB2 protein levels are controlled by a complex array of transcriptional and post-transcriptional mechanisms. The human *ZEB2* gene is located at 2q22.3 (genomic coordinates chr2:144,364,364-144,524,583 in the assembly GRCh38/hg38), spans approximately 160 kbp and contains several large introns harbouring enhancers, silencers and human accelerated regions (HARs) (Pollard et al. 2006; Lindblad-Toh et al. 2011.; Bar Yaacov et al. 2018; Erwin et al. 2014). HARs are genomic sequences that were conserved across vertebrate evolution but rapidly mutated during human evolution. *ZEB2* transcription is regulated by a number of distal enhancers responsible for tissue and sex specific expression (El-Kasti et al. 2012). In humans *ZEB2* transcription can be initiated from two alternative promoters (i.e. 1a and 1b) located ~2.2 kb apart. TNF α signalling activates the transcription factor AP1, which in turn binds to promoter 1b but regulates transcription from both promoters via long-range chromatin looping (Qiao et al. 2015). The 5'-UTR of *ZEB2* comprises an intron with an internal ribosomal entry site (IRES). Upstream of the *ZEB2* locus is a natural antisense transcript that can bind to the 5'- splice site of intron 1, causing its retention in the mature transcript. IRES retention in the 5'-UTR leads to increased *ZEB2* expression (Beltran et al. 2008). Adding another layer of complexity, *ZEB2* transcripts have a complex 3'-UTR that is targeted by a number of micro RNAs (miRNAs) including the miR200 family (Hegarty et al. 2015).

Regulation of TGF β signalling by ZEB2

In an earlier section we touched upon TGF β and BMP protein family members and their relevance to the process of neural induction. Binding of these proteins to type I and type II homodimeric single-pass transmembrane S/T kinase receptors triggers transphosphorylation and formation of an active tetrameric complex that phosphorylates R-SMAD transcriptional regulators. Active TGF β /activin receptors activate SMAD2 and 3, while BMP receptors activate SMAD1, 5 and 8. Phosphorylated R-SMADs form a complex with the co-SMAD, SMAD4, and translocate to the nucleus where they associate with chromatin modifiers and other cofactors to regulate transcription of target genes (Schmierer & Hill 2007). The SMAD protein family also includes the inhibitory SMADs (I-SMADs) 6 and 7, which bind to R-SMADs and suppress their transcriptional activity. *ZEB2* can interact directly with both TGF β and BMP SMADs via a ~14 aa interaction domain located downstream of the N-terminal zinc finger cluster (Conidi et al. 2013). *ZEB2* binding to the transcriptional activator complex R-SMAD-SMAD4-p300 was shown to trigger transcriptional repression of SMAD target genes (Weng et al. 2012). Furthermore, *ZEB2* can indirectly repress BMP signalling by downregulating *BMP4* expression and inducing expression of the I-SMAD, SMAD7 (Weng et al. 2012). Conversely, TGF β and BMP signalling antagonise *ZEB2* both directly, through SMAD2 binding to its promoter region, and indirectly, by regulating expression of miRNAs that target *ZEB2* (Gregory et al. 2011; Davis et al. 2008; Chng et al. 2010). Nevertheless, regulation of this signalling axis is complex and is strictly dependent on the specific cellular and developmental context.

ZEB2 induces neuroectoderm and neural crest fates

ZEB2 has been shown to play multiple roles during CNS and PNS development and this is not surprising considering it is a regulator of TGF β /BMP signalling. *ZEB2* mRNA is detected in the prospective neuroectoderm of the early *Xenopus*, chicken and mouse gastrula and its expression is retained in the neural tube, retina and neural crest (Yasumi et al. 2016; Miyoshi et al. 2006; Eisaki et al. 2000; van Grunsven et al. 2007). An obstacle to the study of *ZEB2* function in mammals has been that, whilst heterozygous loss-of-function mutant mice do not show any obvious phenotype, *Zeb2*^{-/-} mice die around E9.5 with neural tube closure and NCC migration defects (Maruhashi et al. 2005). Underscoring the specific importance of ZEB2 for early nervous system development, *Zeb1*^{-/-} mice die around birth and do not display obvious nervous system anomalies (Takagi et al. 1998).

XZeb2 loss- and gain-of-function experiments in *Xenopus* suggest necessity and sufficiency of *Zeb2* for neural induction. In *Xenopus* *XZeb2* directly represses *BMP4* transcription and downregulates epidermal genes in a Smad-independent fashion (Nitta et al. 2007; Nitta et al. 2004). The neural inductive properties of *XZeb2* appear to depend on interaction with CtBP and NuRD co-repressor complexes (van Grunsven et al. 2007; Verstappen et al. 2008). Work in mouse has shown that starting from E7.5 *Zeb2* is rapidly upregulated in the prospective neuroectoderm and expression is maintained until E9.5 across the neural tube. While injection of FGF8 into the pro-amniotic cavity leads to increased levels of *Zeb2* expression, Wnt3a injection has the opposite effect. Additionally, ectopic *Zeb2* expression promotes neural stem cell fate even in the absence of FGF signalling (Dang & Tropepe 2010). Thus *Zeb2* induction appears to be downstream of FGF activation and Wnt inhibition and is important for promoting neural stem cell identity in the anterior neural plate. Recently, in an *in vitro* 3D differentiation system of mESCs it was shown that *Zeb2* drives exit from the epiblast state by orchestrating EMT and genome-wide methylation events necessary for downregulation of pluripotency genes and lineage commitment (Stryjewska et al. 2016). In a human 2D neural differentiation model it was shown that *ZEB2* overexpression enhances neuroectoderm induction but its role is to promote maturation of the neuroectoderm. In fact, upon *ZEB2* knockdown the neuroectoderm becomes specified but cannot develop to maturity. In addition, *ZEB2* antagonises mesendoderm induction mediated by the Activin/Nodal pathway (Chng et al. 2010).

Zeb2 has also been implicated in neural crest cell (NCC) specification by limiting BMP signalling at the ectoderm-neuroectoderm boundary. E8.5 *Zeb2*^{-/-} mouse embryos lack this boundary and the vagal neural crest is completely missing (Van De Putte et al. 2003). In addition to being important for neural crest specification, *Zeb2* has been also implicated in the EMT events that drive delamination of NCCs from the ectoderm-neuroectoderm boundary (Rogers et al. 2013). In fact, *Zeb2* has a well-established role as an EMT driver in various types of cancer, particularly in the expression switch from E-cadherin to N-cadherin (Pastushenko & Blanpain 2018). It has been proposed that, similarly to

what occurs in cancer, *Zeb2* may be driving E-cadherin to N-cadherin switch during NCC delamination and migration. Downregulation of E-cadherin in favour of N-cadherin upregulation is also seen during neuroectodermal induction (Rogers et al. 2013).

Zeb2 regulates multiple aspects of cerebral development

In a *Zeb2^{fllox/fllox};Emx1^{IRESCre}* mouse strain, loss of *Zeb2* expression in the dorsal telencephalon leads to agenesis of the hippocampus and CC in neonatal mice. In the pallium *Zeb2* expression at E12.5 and later developmental stages seems to be confined to post-mitotic neurons of the CP (Miquelajauregui et al. 2007). In addition, *Zeb2* is expressed in the developing basal ganglia and thalamus. In the hippocampus *Zeb2* promotes the proliferative and anti-apoptotic effects of Wnt-JNK signalling by repressing expression of the Wnt inhibitor *Sfrp1* (Miquelajauregui et al. 2007). *Zeb2* deletion in young post-mitotic neurons in *Zeb2^{fllox/fllox};Nex-Cre* mice causes early production of upper layer neurons at the expense of deep layer neurons through premature upregulation of *Ntf3* (Seuntjens et al. 2009). *Ntf3* was shown to mediate a non-cell autonomous feedback between neurons and VZ progenitors to regulate the balance of deep and superficial layer neurons (Seuntjens et al. 2009; Parthasarathy et al. 2014). More recently, using a *Zeb2^{KO/fllox};Nex-Cre^{+/-}* line it was shown that loss of *Zeb2* leads to agenesis of the CC and defects in corticospinal tract and anterior commissure formation (Srivatsa et al. 2015). Furthermore, *Zeb2*-deficient neurons fail to form ipsilateral intracortical collaterals and have axonal growth defects. It was shown that these effects were mediated by downregulation of the *Zeb2* transcriptional target *Ninein*, a microtubule associated protein required for axonal growth and branching (Srivatsa et al. 2015). *Zeb2* also regulates several aspects of subpallial development; conditional deletion of *Zeb2* in the mouse subpallium using *Nkx2.1-Cre* leads to a loss of cortical interneurons in favour of an increase in striatal interneurons. In the MGE *Zeb2* binds directly upstream of *Nkx2.1* and represses its expression, inducing cortical interneuron identity (McKinsey et al. 2013). In addition, by regulating the levels of *Unc5b*, which mediates repulsion in response to Netrin, *Zeb2* controls interneuron migration from the MGE to the cortex (van den Berghe et al. 2013).

Zeb2 in glial cell development and myelination

Zeb2 mediates a non-cell autonomous feedback loop from postmitotic neurons to VZ progenitors that regulates the balance between neurogenesis and gliogenesis. *Nex-Cre* driven *Zeb2* deletion in post-mitotic neurons of the mouse cortex causes premature end of neurogenesis and enhanced astrogenesis (Seuntjens et al. 2009). In addition to controlling progenitor lineage commitment *Zeb2* plays an important role in myelination of the CNS and PNS. *Zeb2* is in fact induced by *Olig1* and *Olig2* and promotes oligodendrocyte maturation by blocking TGF β /BMP signalling. While *Zeb2^{fllox/fllox};Olig1^{Cre+/-}* mice do not display any significant difference in the number of oligodendrocyte

progenitors, their maturation is compromised (Weng et al. 2012). Recently, Zeb2 was also shown to control Schwann cell maturation and peripheral nerve myelination. This function of Zeb2 was shown to depend on interaction with the HDAC corepressor complex NuRD to inhibit Notch-Hey2 signalling (Wu et al. 2016; Quintes et al. 2016).

In human Zeb2 mutations cause Mowat-Wilson syndrome

In humans *de novo* heterozygous *ZEB2* mutations in the germline cause Mowat-Wilson syndrome (MWS), a rare condition estimated to occur in only 1 every 50,000-100,000 individuals. MWS is a complex disorder that manifests itself in a number of defects with variable penetrance, including intellectual disability, delayed development, facial dysmorphia and Hirschsprung disease (Mowat et al. 1998). Structural brain abnormalities associated with MWS are dysgenesis and agenesis of CC, hippocampal abnormalities, myelination defects and cortical malformations, in particular microcephaly (Garavelli et al. 2017). The number and diversity of MWS phenotypes reflect the multifarious roles of *ZEB2* during nervous system development and the large array of mutations causing MWS. To date more than 100 different mutations have been identified, the majority of which causes C-terminal truncation of the protein product and heterozygous loss-of-function (Hegarty et al. 2015). Interestingly, *Zeb2*^{+/-} mice do not display any obvious neurodevelopmental phenotype. Because *Zeb2*^{-/-} mice suffer from embryonic lethality, the vast majority of *Zeb2* studies in mouse have relied on conditional tissue-specific ablation of *Zeb2* (Maruhashi et al. 2005). However, one could argue that these models are quite distant from the human system, which shows increased sensitivity to *ZEB2* gene dosage.

Neurogenesis as a gradual process of EMT

Several developmental processes discussed so far rely on EMT; gastrulation, delamination of NCCs from the edges of the neuroectoderm, neuronal migration from the VZ to the correct cortical layer and interneuron migration from the subpallium to the pallium are all examples of EMT. More broadly, the neurogenic process can be seen in its entirety as a gradual and progressive EMT (Aaku-Saraste et al. 1996). An initially tight and compact epithelium marked by expression of E-cadherin and occludin, first transitions to a neuroepithelial state characterised by the expression of N-cadherin and lower levels of tight junction components. Next, neuroepithelial progenitors switch to a radial glia fate, where they retain epithelial character, exemplified by the contacts formed with the apical and basal lamina, but at the same time they start producing mesenchymal cells (i.e. neurons and IPCs). The end result at maturity is a diverse array of cells (i.e. neurons, interneurons, astrocytes and oligodendrocytes) that have completely lost contact with a basal lamina and are fully mesenchymal in character. Historically, EMT has been viewed as a binary process with two cell populations, one

epithelial expressing E-cadherin, and one mesenchymal, expressing vimentin. However, it has now become apparent that EMT is a reversible process, it can occur transiently and to different degrees along a continuum between a fully epithelial and fully mesenchymal endpoint state (Pastushenko & Blanpain 2018; Stemmler et al. 2019).

The EMT transcriptional program is executed by a core set of transcription factors comprising Snail, Slug, TWIST1, ZEB1 and ZEB2. A complex network of enhancer elements, miRNAs and lncRNAs controls their specific spatiotemporal expression patterns. During development they are often expressed in a mutually exclusive fashion (Lamouille et al. 2014; Peinado et al. 2007; Lamouille et al. 2013). For example, at E14.5 *Zeb1* expression is restricted to the VZ and SVZ of the mouse telencephalon, while *Zeb2* is expressed in postmitotic neurons. These transcription factors have non-redundant functions in cancer progression and normal development. Albeit incomplete at the moment, available data suggest that different EMT transcription factors regulate common as well as specific target genes, hence their non-overlapping roles (Stemmler et al. 2019). For instance, while Snail and Slug are dispensable for murine neural crest delamination, TWIST and ZEB2 are essential (Murray & Gridley 2006; Soo et al. 2002; Van De Putte et al. 2003).

Studies on cancer and metastasis have shown that partial EMT is more common than complete execution of the full EMT programme. EMT involves intermediate hybrid states in which cells can retain expression of both epithelial (i.e. Krt5, Krt14, E-cadherin, Grhl1-3, EPCAM) and mesenchymal markers (i.e. *Zeb1,2*, Vimentin, N-cadherin, Twist1,2 and Snai1) (Pastushenko & Blanpain 2018). Interestingly, in pancreatic tumors driven by *KrasG12D/p53cKO*, cells in a hybrid state defined by co-expression of E-cadherin and vimentin were more proliferative than fully mesenchymal cells (Krebs et al. 2017). At the moment our understanding of the mechanisms that stabilize certain hybrid states is limited. EMT transcription factors are known to form complex cross-regulatory networks and mutually inhibitory loops. For instance, the miRNA34/snai1 and the miR200/Zeb loops have been proposed to form metastable switches that can induce EMT hybrid states (Pastushenko & Blanpain 2018; Lamouille et al. 2013). In conclusion, EMT is a very complex phenomenon involving a continuum of cell-states characterised by distinct migratory and proliferative properties. Hybrid EMT states likely have direct relevance for development in general and in particular that of the nervous system. It is thus tantalizing to speculate that by modulating the proliferative and cell-cell contact properties of neural progenitors different tissue architectures may be achieved.

Thesis objectives

The aim of my thesis was to investigate the role of *ZEB2* in human neocortex development using cerebral organoids as a model. Humans display increased sensitivity to *ZEB2* gene dosage compared to mice and heterozygous loss-of-function mutations cause MWS, a complex pathology affecting multiple aspects of nervous system development. So far, the majority studies investigating the role of *Zeb2* in mammalian neural development have relied on mouse strains with tissue specific Cre-mediated deletion. However, such approaches may have missed important physiological and mechanistic aspects of *Zeb2* function and of how the human system is more susceptible. More recently, it was reported that through conditional germ-line ablation of exon 7 in an inbred strain of C57BL/6 some of the symptoms of MWS could be recapitulated (Takagi et al. 2015). Nevertheless, the characterisation of the model was very limited, the phenotypes observed were heavily dependent on the genetic background and therefore we are still missing a model of this disorder. In addition to having clinical importance, understanding how *ZEB2* functions in the human system could yield important insights into the mechanisms that have led to neocortex expansion.

Specific aims of the thesis:

- Establishing *ZEB2*^{+/-} hESCs to test gene dosage sensitivity in human brain development and model Mowat-Wilson syndrome
- Characterising and validating early phenotypes associated with heterozygous *ZEB2* loss-of-function mutation
- Implementing an *in vitro* culture system to capture later phenotypes associated with MWS

Chapter 2: Materials & Methods

Plasmid constructs

All primers used for cloning are listed in the table included in Appendix 1. To generate the construct for stable inducible *ZEB2* expression the coding sequence of the human *ZEB2* transcript variant 1 (NM_014795.3) was purchased as an ultimate ORF clone in the pENTRY221 (Thermo Scientific, #IOH53645). The *ZEB2* ORF was amplified with primers ZEB2_CuO_cloning_F & R, cut with the restriction enzymes *NheI* (NEB, #R3131) and *NotI* (NEB, #R3189) and ligated into the PB-Cuo-MCS-IRES-GFP-EF1 α -CymR-Puro inducible expression vector (System Biosciences, PBQM812A-1) using T4 DNA ligase (NEB, M0202). The reaction was transformed into TOP10 *E. coli* (Thermo Scientific, #C404010) and the colonies that grew on selection plates were sequence validated using primers CuO_seq and CuO_ZEB2_seq_1-7. The construct pCAG-nV5-ZEB2_iso-1 was generated by Gateway recombination between the pENTRY221-ZEB2 and pCAG-nV5-DEST (Lancaster et al. 2013) using the LR Clonase enzyme mix (Thermo Scientific, #11791019). The construct pCAG-nV5-ZEB2_iso-2, encoding isoform 2 of *ZEB2* (NM_001171653.1), was generated linearizing pCAG-nV5-ZEB2_iso-1 by PCR, using Q5 polymerase (NEB, M049L) with primers ZEB2_iso-2_F & R, and religating it using T4 DNA ligase. The plasmid product was verified by sequencing using CAG_F and CuO_ZEB2_seq_1-7. The RNA guides used for CRISPR-Cas9n knockout of *ZEB2* were designed using the online tool at <http://tools.genome-engineering.org> and the sequences are listed in the table in Appendix 1. Cloning of the guides was performed as outlined by Ran et al. 2013; briefly, the sense and antisense strand oligos for ZEB2_sgRNA_1 & 2 were annealed and phosphorylated, and the duplexes were cloned into pSpCas9n(BB) (Addgene, #PX460) by *BbsI* (Thermo Scientific, #FD1014) digestion and ligation with T4 ligase. Colonies were sequence validated using the U6_F primer. For sequence validation of mutant hESC pools, a region of ~100 bp overlapping the edit sites was amplified using primers ZEB2_Cas9n_sequencing_F & R and blunt-end cloned into the pJET1.2 plasmid (Thermo Scientific, #K1232). The ligation reaction was transformed into DH5 α *E. coli* and for each sample 20 colonies were miniprep and sequenced using the pJET1.2 forward sequencing primer. The integrating farnesylated-GFP construct pT2-CAG-fGFP (Addgene, #34879) and the sleeping beauty transposase plasmid pCAGEN-SB100X as modified from pCMV-SB100 (Addgene, #34879) were generated as previously described (Lancaster et al. 2017). The integrating farnesylated FusionRed construct pT2-CAG-fFusionRed was generated by replacing the EGFP in pT2-CAG-fGFP with FusionRed. The EGFP cassette was removed by digestion with *MluI*-HF (NEB, R3198) and *EcoRI*-HF (NEB, #R3101). The FusionRed cassette was PCR amplified from pCi-C-FusionRed-DEST (a gift from Harvey McMahon's laboratory) using primers fFusionRed_F & R and was inserted into the linearized pT2-CAG-farnesyl backbone by Gibson assembly as described in the technical bulletin (NEB, #2611).

Cell culture, transfection and nucleofection

H9 (female) and H1 (male) hESCs (obtained from WiCell and approved for use in this project by the U.K. Stem Cell Bank Steering Committee) were cultured on Matrigel (Corning, #354230) coated plates initially in mTesRTM1 (STEMCELL Technologies, #85850) and then StemFlex (Thermo Scientific, #A3349401). Cells were passaged twice a week as clumps by EDTA treatment. 293T (Clontech, #632617), U87MG (a gift from Harvey McMahon's laboratory) and HeLa cells maintained in DMEM-Glutamax (Gibco, #10566016) supplemented with 1X (v/v) NEAA (Sigma-Aldrich, #M7145-100ML) and 10% FBS (Gibco, #10270106). Cells were typically passaged every 4 days at a 1:8 split ratio by trypsinisation. All lines were grown under standard conditions; 37 °C and 5% CO₂. For establishment of *ZEB2*^{+/-} lines, plasmids pSpCas9n(BB)-*ZEB2*-Guide-A &-B (1 µg/ml) were electroporated into H9 hESC using the Human Stem Cell Nucleofector Kit 1 (Lonza, VPH-5012). Following electroporation, cells were grown in one well of a 24-well plate, reduced to single-cell suspension and seeded into a 96-well plate at a density ranging between 1000 – 20 c/w in mTesRTM1 supplemented with 1 nM ROCK inhibitor (BD Biosciences, 562822). Alternatively cells were seeded at a density of 0.5 c/w in StemFlex supplemented with RevitaCell supplement (ThermoFisher, A2644501). Once the cells reached ~80% confluence the 96-well plate was split to two replica plates, one used for screening by ddPCR and the other used for further expansion. Mutant screening relied on a droplet digital PCR (ddPCR) drop-off assay (Findlay et al. 2016). Screening was performed as described in the '*Droplet digital PCR (ddPCR) and RT-ddPCR*' section of the methods. For establishment of the fFusionRed line pCAGEN-SB100X (0.125 µg/ml) and the transposon donor plasmid pT2-CAG-fFusionRed (0.375 µg/ml) were transfected into H9 hESCs with Lipofectamine Stem (ThermoFisher, STEM00001). After ~10 days from transfection fFusionRed⁺ cells were harvested as a pool by fluorescence activated cell sorting on a MoFlo XDP cell sorter (Beckman Coulter). For establishment of the inducible overexpression lines equimolar amounts of transposon donor plasmids were used; 1 µg of *ZEB2* CuO and 0.6 µg of EV CuO were transfected together with Super PiggyBac transposase vector (System Biosciences, # PB200A-1) in a 1.25:1 ratio (m/m; transposon/transposase). A week after transfection, Puromycin selection (0.6 µg/ml) was applied until single colonies could be seen and picked under a stereo-microscope fitted in a horizontal laminar flow hood. For transgene induction the water-soluble cumate (CuO) solution (System Biosciences, #QM150A-1) was used at 1X and 2X concentration for 6 days.

Karyotyping

Karyotype analyses of the *ZEB2*^{+/-} cell lines were outsourced to Cell Guidance Systems and for each cell culture sample 20 G-banded metaphase spreads were examined. Both samples revealed normal karyotype (46, xx) in all metaphase plates examined.

Organoid culture

For the study on *ZEB2* all organoids were generated according to the enCOR method (Lancaster et al. 2017) – refer to this publication for the media composition details. Briefly, EBs were maintained in EB medium until day 6, they were then switched to neural induction (NI) medium until day 11 when they were embedded in Matrigel (Corning, #354234). Between day 14-17 of the protocol the medium was changed to improved differentiation medium w/o vitamin A (IDM-A) supplemented with 3 μ M GSK3 inhibitor/Wnt activator CHIR99021 (Tocris, cat. #4423). A short 3-day treatment with CHIR99021 was used to promote expansion of the neuroepithelium. On day 17 CHIR99021 was removed and organoids were fed with IDM-A every other day until day 21. On day 21 the Matrigel surrounding the organoids was microdissected away, the medium was changed to improved differentiation medium with vitamin A (IDM+A) and organoids were moved to an orbital shaker. Organoids were cultured in IDM+A with media changes every 3-4 days. On day 40 IDM+A was supplemented with 2% (v/v) dissolved Matrigel (Corning, #354234) to promote the establishment of the cortical plate. For air-liquid interface cerebral organoid (ALI-CO) culture the enCOR protocol or alternatively the STEMdiff Cerebral Organoid Kit (STEMCELL Technologies, #08570) were used. Organoids were grown according to the instructions given in the STEMdiff Cerebral Organoid Kit manual, with the only exception that on day 35 dissolved Matrigel was added to promote establishment of the cortical plate.

Electroporation of cerebral organoids

Between day 40-60 of the protocol, plasmids were delivered to the organoids by injection and electroporation into the ventricles. A P2000 micropipette puller (Sutter Instruments) was used to pull glass microcapillaries (Drummond Scientific, #1-000-0500) with the following settings: heat – 550, filament – 5, velocity – 25, delay – 150, pull – 150. The microcapillaries were opened using dissecting scissors to give a tip taper of ~8-9 mm. For expression of farnesylGFP a total of 5 μ l of a 320 ng/ μ l plasmid solution (80 ng/ μ l pT2-CAG-fGFP and 240 ng/ μ l pCAGEN-SB100) was used for injection and electroporation. The electroporation settings used were as previously described.

Cholera toxin subunit B (CTB) and emGFP labelling

ALI-COs were visualised on an EVOS FL inverted microscope (Thermo Scientific) and <0.2 μ l of 1 mg/ml AlexaFluor 647-conjugate CTB (Thermo Scientific, #C34778) were delivered to the target region of the ALI-CO using a microinjection capillary. To achieve sparse neuronal labelling, ALI-COs were injected with <0.2 μ l of CytoTune emGFP Sendai fluorescent reporter (Thermo Scientific,

A16519). Four days after CTB labelling and 5 days after viral infection ALI-COs were fixed for analysis.

Air-Liquid Interface Cerebral Organoid (ALI-CO) culture

ALI-COs were prepared using a modified version of a published organotypic slice culture protocol (Daza et al. 2007). Mature organoids (~55-60 days old, in some cases up to 90 days) were harvested using a cut P1000 pipette tip, rinsed in HBSS w/o Ca^{2+} and Mg^{2+} (Thermo Scientific, #14175095) and then washed and embedded in 3% low melt (LM) agarose (Sigma-Aldrich, # A9414) at ~40 °C in peel-a-way embedding molds (Sigma-Aldrich, #E6032). The embedded organoids were incubated on ice for 10-15 min until the agarose solidified releasing part of its water content. The blocks were processed on a Leica VT1000S vibrating microtome in cold HBSS w/o Ca^{2+} and Mg^{2+} as 300 μm thick sections. The sections were collected onto Millicell-CM cell culture inserts (Millipore, #PICM0RG50) in 6-well plates and left to equilibrate at 37 °C 5% CO_2 for ~1-2 hrs in serum-supplemented slice culture medium (SSSCM): DMEM, 10% FBS, 0.5% (w/v) glucose, supplemented with penicillin-streptomycin and Fungizone. After incubation in SSSCM the slices were cultured in serum-free slice culture medium (SFSCM): Neurobasal (Gibco, #21103049), 1:50 (v/v) B27+A (Gibco, #17504044), 0.5% (w/v) glucose, 1X (v/v) Glutamax supplemented with Antibiotic-Antimycotic (AA) (Gibco, #15240062). ALI-COs were fed SFSCM daily and maintained at 37 °C and 5% CO_2 . During feedings care was taken dispensing the medium to the side of the cell culture vessel to avoid that the slices be submerged.

ALI-CO live imaging and image analysis

Organoids were imaged only after ~1-2 days at the liquid interface, as during the initial phases of culture the tissue flattens out and easily comes out of focus. Imaging was performed on Zeiss LSM 780 and 710 confocal microscopes with incubation set at 37 °C and 7% CO_2 . Time-lapse movies were acquired as Z-stacks at 10 minute intervals over several hours or days. Temporal projection images were generated in FiJi applying the Temporal-Color Code tool on time-lapse stacks. Axon growth cone tracing was performed using MTrackJ (Meijering et al. 2012) with manual tracking. The data was then plotted as the distance from the start track as a function of time. Linear regression was performed on all tracks and the average best-fit line was calculated for early and late growth stages. The MultiKymograph FiJi plugin was used to generate growth cones kymographs. The Gaussian gradient in the OrientationJ (Rezakhaniha et al. 2012) analysis plugin was used for directionality analysis on GFP^+ tracts – hue was determined by the orientation of the tracts, brightness by the coherency and saturation was kept constant. For quantification of axon bundling in ALI-COs compared to whole organoids, mean grey levels of SMI312 staining were calculated on the entire

tissue area. OrientationJ with Riesz filter settings was used for axon tract morphology measurements on SMI312 stainings. Mean grey values were calculated for both the coherency and energy image outputs on the whole area of tissue. These two values were multiplied to obtain coherency x energy values reflecting the extent of bundling present in a given sample. For quantification of superficial and deep layer neuron abundance in ALI-COs compare to whole organoids, 6 samples for each condition were cryosectioned, stained for CUX2 and CTIP2 and imaged. To control for bias and differences in the distribution of neuronal types across ALI-COs and whole organoids, two images were acquired for each sample, one in the centre and one on the edge of the tissue. The same approach was taken for TUNEL stain image acquisition. Automated NIS Elements Advanced Research macros were optimised for the different stains and were used for cell counts. TUNEL⁺, CUX2⁺ and CTIP2⁺ cells were defined by the co-expression of their respective marker and DAPI. Optimisation of macro parameters was done on an image randomly selected and all images were processed by a batch processing function. Twelve 20-23 day old organoids were fixed, cryosectioned, stained for TBR2 and DAPI and images were acquired on a Zeiss LSM 780 system. Quantification of TBR2⁺ IPCs numbers were performed on 52 (WT) and 68 (ZEB2^{+/-} #2) regions of interest (ROIs) from 12 20-23 day old organoids from two independent batches. Similarly, measurements of ventricle length were performed on 37 (WT) and 23 (ZEB2^{+/-} #2) regions of interest (ROIs) from 6 20-23 day old organoids from two independent batches. Images of ZEB2^{+/-} #2 and control organoids not used for quantifications were acquired on a 3DHISTEC – Panoramic confocal.

Histological and immunohistochemical analysis

Organoids and ALI-COs were fixed in 4% PFA either overnight at 4 °C or at room temperature for 20 min, and washed in PBS (3x10 min). Samples for cryostat processing were incubated in 30% sucrose in 0.2 M PB (21.8 g/l Na₂HPO₄, 6.4 g/l NaH₂PO₄ in dH₂O) overnight, embedded in gelatin (7.5% gelatin, 10% sucrose in 0.2 M PB), plunge frozen in 2-methylbutane (Sigma-Aldrich, #M32631) at ~-40 °C, sectioned and stained as previously described (Lancaster et al. 2013). Because of their thickness (>300 µm) ALI-CO whole-mounts were stained using a modified protocol where all steps were performed in permeabilisation buffer (0.25% Triton-X, 4% normal donkey serum in PBS) at 4 °C. The individual steps were extended as follows; permeabilisation – overnight, primary and secondary antibody incubation – 2 days, wash steps – 3 x 8 hrs. The *In Situ* Cell Death Detection Kit TMR red (Sigma-Aldrich, #12156792910) was used for TdT-mediated dUTP-X nick end labelling (TUNEL) and was performed as outlined in the product's manual. Hematoxylin and Eosin stains were performed as described in the technical bulletin of the H&E stain kit (Atom Scientific, #RRSK26). For SDS antigen retrieval cryostat sections were rehydrated, incubated for 5 minutes in 1% SDS in PBS at room temperature and washed in PBS (3x5 min) before normal staining.

Immunoblotting

Immunoblotting was performed essentially as described previously (Whitmarsh & Davis 2001). Cell and organoid samples were washed twice in ice-cold PBS, pelleted by centrifugation (500g, 3 min) and lysed with modified-RIPA (mRIPA: 1% Triton-X, 0.1% SDS, 150 mM NaCl, 50 mM Tris pH 7.4, 2 mM EDTA, 12 mM sodium deoxycholate) supplemented immediately prior to lysis preparation with protease (Thermo Scientific, #78430) and phosphatase (Sigma-Aldrich, #4906845001) inhibitors. Samples were resolved by SDS-PAGE (4-20% gels) and transferred to Amersham Hybond P 0.45 PVDF blotting membranes (GE Healthcare, #10600023). Membranes were blocked overnight at 4 °C in 5% milk or 5% BSA in TBST. Specific blocking conditions were optimised for each antibody during the initial validation stages. Primary antibodies were incubated overnight at 4 °C. HRP-linked goat anti-rabbit (Dako #P0448, 1:3000) and rabbit anti-mouse (Dako #P0161, 1:3000) secondary antibodies were incubated for ~1 hr at room temperature. The blots were developed using ECL Prime enhanced chemoluminescent detection reagent (GE Healthcare, #RPN2232) and X-ray films (Photon Imaging Systems Ltd, #FM024).

Antibodies

Primary antibodies used for protein detection, with their corresponding dilutions for immunofluorescence (IF), western blotting (WB) and WB blocking conditions were as follows: mouse anti- β -actin (Abcam, 8226, WB 1:2000 in BSA), mouse anti-ZEB2 N-t (Origene, TA802113, IF 1:150, WB 1:2000 in milk), rabbit anti-ZEB2 C-t (Origene, TA319793, IF 1:150), rabbit anti-ZEB2 (Atlas Antibodies, HPA003456, IF 1:200), sheep anti-Tbr2 (R&D Systems, AF6166, IF 1:200), rabbit anti-GSH2 (Millipore, ABN162, IF 1:200), mouse anti-N-cadherin (BD Biosciences, 610920, IF 1:500, WB 1:1000 in milk), mouse anti-E-cadherin (BD Biosciences, 610181, IF 1:500, 1:1000 in milk), rabbit anti-Occludin (Abcam, ab31721, IF 1:200, 1:1000 in milk), rabbit anti-EMX1 (Origene, TA325087, IF 1:200, WB 1:1000 in BSA), mouse anti-FGF2 (G-2) (Santa Cruz, sc-365106, WB 1:1000 in BSA), mouse anti-FGF2 (C-2) (Santa Cruz, sc-74412, WB 1:1000 in BSA), mouse anti-ERK1/2 (C-9) (Santa Cruz, sc-514302, WB 1:1000 in BSA), mouse anti-pERK (E-4) (Santa Cruz, sc-7383, WB 1:1000 in BSA), rabbit anti-BLBP (Abcam, ab32423, IF 1:200), anti-GLAST (Abcam, ab416, IF 1:200), goat anti-DCX (N-19) (Santa Cruz, sc-8067, IF 1:300), mouse anti-ZO1 (BD Biosciences, 610966, IF 1:500), mouse anti-FEZF2/FEZ1 (IBL America, 18997, IF 1:200), chicken anti-MAP2 (Abcam, ab5392, IF 1:500), mouse anti-MAP2 (Chemicon, MAB3418, IF 1:300), rat anti-CTIP2 (Abcam, IF ab18465, IF 1:300), mouse anti-SATB2 (Abcam, ab51502, IF 1:200), rabbit anti-CUX2 (Abcam ab130395, IF 1:200), mouse anti-SMI312 (BioLegend, 837904, IF 1:500), mouse anti-c-Fos (EnCor, MCA-2H2, IF 1:100), mouse anti-Piccolo (PCLO) (Origene, TA326497, IF 1:100), mouse anti-STEM121 (Takara, Y40410, IF 1:500), sheep anti-human-Neuropilin-1 (NRP1) (R&D Systems, AF3870, IF 1:200), rabbit anti-Homer 1 (Synaptic Systems, 160003, IF 1:100), rabbit anti-

Psd95 (Abcam, ab18258, IF 1:500), mouse anti-human-Synaptophysin (EP10) (Thermo Scientific, 14-6525-80, IF 1:200), goat anti-human-Synaptophysin (R&D Systems, AF5555, IF 1:100), chicken anti-GFP (Thermo Scientific, A10262, IF 1:500), mouse anti-Bassoon (Enzo, SAP7F407, IF 1:200), rabbit anti-VGAT (Synaptic Systems, 131013, IF 1:1000), mouse anti-Calretinin (Swant, 63B, IF 1:500), rat anti-Somatostatin (Millipore, MAB354, IF 1:100), mouse anti-GAD67 (Millipore, MAB5406, IF 1:100), mouse anti-Ephrin-B1 (C-6) (Santa Cruz, sc-515264, IF 1:50), mouse anti-WNT5A (A-5) (Santa Cruz, sc-365370, IF 1:50), goat anti-BRN2 (C-20) (Santa Cruz, sc-6029, IF 1:50), mouse anti-TUBB3 (BioLegend, 801202, IF 1:500), rabbit anti-RYK (Abcam, ab5518, IF 1:100), rabbit anti-Netrin 1 [EPR5428] (Abcam, ab126729, IF 1:50), mouse anti-CUX1 [2A10] (Abcam, ab54583, IF 1:100), rabbit anti-GFAP (Abcam, ab7260, IF 1:500), rabbit anti-SOX5 (Abcam, ab94396, IF 1:200). All primary antibodies used had been previously described and validated in the literature and were tested for reactivity on human tissue. No new antibodies were produced for this study. Alexafluor 405, 488, 568 and 647 secondary antibodies were used for detection of primary antibodies.

Whole-cell patch-clamp recordings

ALI-COs were placed in a submerged chamber continuously perfused with room-temperature artificial cerebrospinal fluid (aCSF) (119 mM NaCl, 2.5 mM KCl, 11 mM glucose, 26 mM NaHCO₃, 1.25 mM NaH₂PO₄, 2.5 mM CaCl₂ and 1.3 mM MgCl₂) saturated with 5% CO₂/95% O₂ pH 7.4. Patch-clamp pipettes were pulled from borosilicate glass capillaries (1.5 mm OD x 0.86 mm ID; Harvard Apparatus, Holliston, MA) and typical pipette resistance was between 12-15 MΩ. Pipettes were filled with artificial intracellular solution (145 mM K-gluconate, 5 mM MgCl₂, 0.5 mM EGTA, 2 mM Na₂ATP, 0.2 mM Na₂GTP, 10 mM HEPES) buffered to pH 7.2 with KOH (280-290 mOsm). Recordings were performed in current-clamp configuration using an Axon Multiclamp 700B amplifier (Molecular Devices, San Jose, CA) under a Slicescope (Scientifica, Uckfield, UK) fitted with a 40x objective lens (Olympus, Tokyo, Japan) and a WAT-902H analogue camera (Watec, Newburgh, NY). Resting membrane potential (RMP) was measured in current clamp mode after establishing a seal in whole-cell configuration. Cells with RMP ≤ -50mV were used for analysis (Appendix 2). A frequency-current (FI) curve was determined by applying current steps (800 ms) of increasing amplitude (5 pA steps).

ChIP-seq data visualization and SUMOylation/ubiquitylation analysis

ZEB2 ChIP-seq datasets were accessed via ENCODE with the following accession numbers: ENCSR004GKA, ENCSR322CFO and ENCSR417VWF. The datasets were visualized on the University of California Santa Cruz (UCSC) Genome Browser using the GRCh38/hg38 assembly. ChIP-seq data were displayed by default as fold change values over control with the signal P-value

and optimal IDR thresholded peaks. Interactions between putative regulatory elements were displayed in the GeneHancer Regulatory Elements and Gene Interactions track and the data were visualized using the default settings in the browser. The H3K27Ac mark track was visualized using the default setting in the browser and data for all 7 cell lines available on ENCODE were displayed (GM12878, H1 hESC, HSMM, HUVEC, K562, NHEK and NHLF). For ZEB2 SUMOylation analyses, the protein sequence of the main isoform (O60315-1) and the shorter isoform missing exon IV (O60315-2) were retrieved from UniProt (<https://www.uniprot.org>) and analyzed using the online SUMOplot analysis program (<https://www.abgent.com/sumoplot>). The putative SUMOylation site at K114 was predicted with a confidence score of 0.8. The same sequence analyzed using the prediction software for protein ubiquitylation sites UbPred (<http://www.ubpred.org/>) was predicted to contain a putative ubiquitylation site on K114 with a confidence score of 0.89.

Bioinformatic analysis of scRNA-seq datasets

Third-party gene-expression matrices were downloaded from NCBI GEO. Data corresponding to E9.5 and E10.5 mouse forebrain were obtained from (Dong et al. 2018) [GEO:GSE87038], while for E11.5, E13.5, E15.5, and E17.5 dissected mouse cortices were derived from (Yuzwa et al. 2017) [GEO: GSE107122]. The datasets were analysed using the Seurat R-package. Cells expressing <500 genes and more than %5 mitochondrial genes were filtered out prior to analysis. For each developmental time-point, gene expression for each cell was normalized first by scaling gene expression by total expression, then scaling by e^4 and log-transforming values. Next, variable genes for dimensionality reduction were determined using a dispersion index (log variance over mean) approach (FindVariableGenes function). Gene expression was then scaled while regressing out factors contributing to variation (i.e. High UMI-counts, % of mitochondrial genes). Canonical correlation analysis (CCA) (Butler et al. 2018) was used to identify common cell-types and conserved marker genes across all developmental time points. This also allowed for removal of technical artefacts. First, highly variable genes were selected by intersecting the top 2000 variable genes for time-point and selecting those genes found at two time-points at least. Using those variable genes, CCA was performed (RunMultiCCA function), computing 40 CCAs. The number of CCAs for clustering was chosen based on the shared correlation strength for each CCA (MetageneBicorPlot). Rare non-overlapping filtering (CalcVarExpRatio), CCA subspace alignment (AlignSubspace), followed by t-SNE clustering (resolution '1.2', reduction type 'cca.aligned') were performed using the first 20 CCAs. Marker analysis for each cluster was performed using the function FindAllMarkers and requirements for a gene to be considered were: average log-fold change >0.5, expression in a least 25% of cells of the cluster and significant differential expression between clusters (P-value <0.001). Cluster annotation was curated manually considering the top marker genes for each cluster and performing literature-based research and publications cross-referencing. The markers used to identify each cluster were: dorsal forebrain progenitor glia (Nes, Vim, Sox2, Pax6, Slc1a3, Dbi, Ptprz1), ventral forebrain

progenitors (Dlx1, Dlx2, Sox2, Mki67, Top2a, Gadd45g), intermediate progenitor cells (Eomes, Gadd45g), interneurons (Stmn2, Gap43, Dlx1, Dlx2, Dlx5, Meis2, Gad1, Gad2, Ebf1, Isl1), pyramidal neurons (Stmn2, Gap43, Dcx, Neurod2, Neurod6, Tbr1, Cux1/2, Satb2, Fezf2, Sox5, Pou3f2), microglia (Csflr, C1qa/b/c), blood cells (Car2, Hbb-bh1, Gypa, Blbrb, Hemgn), mesenchymal cells (Col3a1, Col1a2, Ig2, Apod, Anxa2, Ctn, Co1a1), U1 - Unclassified (mt-Cytm, Meg3, Luc7l3, mt-Nd1, Ptprs, Gria2).

Organoid dissociation for single-cell RNA sequencing (scRNA-seq)

Residual LM agarose was removed from two H9 (53+22 days) and two H1 (53+16 days) ALI-COs. The ALI-COs from the same hESC line were pooled and harvested in Hibernate Medium (Thermo Scientific, A1247601) plus B-27 Supplement (Thermo Scientific, 17504044), washed twice in PBS and transferred into gentleMACS C tubes (Miltenyi, 130-093-237) containing 2 ml of Accumax (Sigma, A7089) solution. Dissociation was done on the gentleMACS Octo Dissociator (Miltenyi) using the recommended settings. Any residual cell clumps and debris were removed by passing the cell suspension through a 70 μ m strainer. A small volume of the cell suspension was used for cell counting and the remaining diluted 4-fold in PBS and centrifuged (200g, 5 min). Cells were resuspended in PBS supplemented with 0.04% BSA (Sigma Aldrich, A9418) to give a final concentration of 206 cells/ μ l. The suspension was incubated on ice until processed.

scRNA-seq library preparation and sequencing

Single cell RNA-seq libraries were prepared using the 10X Genomics Chromium Single Cell 3' Library & Gel Bead Kit (10X Genomics, 120237) workflow following the manufacturer's guidelines. The 10X Genomics Chromium Single Cell 3' Chip was loaded with 34 μ l of cell suspension (7000 cells) and with the appropriate amount of Mastermix. Cell capture rate for barcoding ranged between 50-75%, giving ~3500-4400 barcoded cells per sample. According to the protocol, the Chromium Controller was run to produce single cell gel beads in emulsion. Reverse transcription and amplification were performed on a C1000 Touch Thermal Cycler (Bio-Rad) – the cDNA was subject to 12 cycles of amplification. Prior to sequencing, the quality of the libraries was assessed using the 2100 Bioanalyzer Instrument (Agilent) and their concentration measure by qPCR. Samples were pooled together and sequenced on an Illumina HiSeq 4000 platform.

scRNA-seq data analysis

CellRanger, Seurat and Monocle software packages were used to build the scRNA-seq data analysis pipeline. CellRanger 2.1.1 was used to align the reads to the GRCh38 reference genome. This gave a gene expression matrix of 13,333 cells with a median of 2,320 genes and 29,086 mean reads per cell post-normalisation. Quality of both intronic and exonic reads was assessed by FastQC and showed 87.2% fraction reads in cells. Only reads that mapped uniquely to the transcriptome were used for unique molecular identifier (UMI) counting in CellRanger. Read depth was normalized in 'Aggr' function between the libraries of the samples. UMI (transcript) counts for each cell were normalized to the total counts, multiplied by 10,000 and transformed into log-space. Cells expressing between 200 and 5,000 genes with a maximum of 15% mitochondrial genes and genes expressed in a minimum of three cells were kept during filtering. Further processing with the Seurat 2.3.0 R package yielded a final object of 13,280 cells for the combined libraries, which was then scaled and normalised. Unbiased clustering was obtained by principal component analysis (PCA) of highly variable genes defined by setting the standard deviation as dispersion function in the 'FindVariableGenes' option (bin = 20). The maximum number of dimensions for cluster separation was determined using PCElbowPlot and clustering was driven by the recommended solution (i.e. 0.16). Clusters were visualized in 2D and 3D space based on t-distributed stochastic neighbour embedding (tSNE) separation in R. Clustering robustness was determined by comparing the top differentially expressed genes for each cluster with cut-off at 25% expression frequency within a population. Six well-defined clusters were identified. The cell identity of the clusters was assigned by gene enrichment analysis using cell type, layer, region, DV position and lobe specific gene sets from databases (Allen Brain Atlas at <http://human.brain-map.org>) and published work (Lancaster et al. 2013; Renner et al. 2017; Quadrato et al. 2017; Zhong et al. 2018; Watanabe et al. 2005; Pollen et al. 2015; Preissl et al. 2018; Lake et al. 2016). Based on the relative proportion of cells expressing the particular reference genes the final cluster identities were assigned. The Gene Ontology Consortium online software (<http://www.geneontology.org>) was used for GO term analysis. Gene enrichment was defined by Fisher's exact test with false discovery rate (FDR) multiple test correction and the top 3 biological process annotations for the enriched genes were presented on the basis of the highest fold-enrichment among the most significant terms ($p < 0.001$). In order to compare the developmental profile of ALI-COs and fetal brain, the R-package Monocle was used to derive a gene expression pseudotime trajectory based on the scRNA-seq data. The raw gene expression matrices of 12 and 13 PCW human fetal brains were processed through the same QC test and filtering in Seurat, this dataset was then used as input in Monocle. Expression levels along the established pseudotime trajectories were visualized as heatmaps comparing ALI-COs and human fetal brains. In order to compare the representation of distinct developmental cell states in ALI-COs (69-75 days) with those from other studies, Pearson correlation was applied to expression profiles of layer-specific genes. Raw count matrices were uploaded onto Seurat and the same filtering parameters were applied across all datasets. Cells with

less than 400 expressed genes were excluded from the analysis, the upper threshold on number of expressed genes was determined as for the ALI-COs. The Jupyter notebook and Python Seaborn were used for analysis and data visualization.

Multielectrode array (MEA) recordings

Between ~12-24 hrs prior to recording, ALI-COs were moved to BrainPhys (STEMCELL Technologies, #0590) supplemented with Neurocult SM1 neuronal supplement (STEMCELL Technologies, #05793). Extracellular recordings of spontaneous activity in ALI-COs (n=10) were acquired on an MEA system (MEA1600, Multi Channel Systems). Immediately prior to recording, ALI-COs were transferred to a 3D grid MEA(60-3DMEA200/12iR-Ti-gr, 60 electrodes, 12 μ m diameter, 200 μ m spacing, with an internal reference electrode). Enough media was removed to allow the tissue to settle on the array – ~100-200 μ l of medium were left in the chamber to bathe the tissue – and the temperature was maintained at 37 °C throughout the recordings (TC01 controller and TCX-Control software, Multi Channel Systems). Application of 1-2 μ M tetrodotoxin (TTX) was sufficient to block activity in ALI-COs (n=3). Sampling was performed at 25 kHz on the 64-channel data acquisition board (MC Card) and MC Rack software (Multi Channel Systems). Electrodes with noise fluctuations greater than 50 μ V were grounded prior to recording. The data was exported as a binary file in Matlab (MathWorks), the raw signal was bandpass filtered (third-order Butterworth, 600-8000 Hz) and a threshold of 6 times the standard deviation above background noise was applied to detect extracellular spike waveforms in each channel with a 2 ms refractory period imposed after each spike. The spike time tiling coefficient was used to compare correlated spontaneous activity between electrodes with a synchronicity window (Δt) of 40 ms. In order to do this, the publicly available script in C (https://github.com/CCutts/Detecting_pairwise_correlations_in_spike_trains) was translated into Matlab. Custom code used for MEA analysis is publicly available at: <https://github.com/Timothysit/organoids>.

Mouse embryos harvesting and mouse spinal cord-ALI-CO co-culture

C57BL/6 pregnant female mice were euthanized and the uterine horns were harvested by a trained animal technician of the MRC-LMB animal facility within the MRC Centre, covered by the ‘Certificate of Designation’ and in accordance with Schedule 1 – Humane Methods of Euthanasia of Animals for tissue removal and as controlled under the ‘Animal (Scientific Procedures) Act 1986’. All the following steps were carried out in ice-cold PBS w/o Ca^{2+} and Mg^{2+} . Embryos were separated by cutting the uterine horns between implantation sites. Individual embryos were exposed by removing the muscle layer, the decidua and any remaining extra-embryonic tissue using precision tweezers (IDEAL-TEK, 5SA). For histological analyses embryos at different developmental stages (E10.5 –

E16.5) were fixed in PFA overnight at 4 °C and prepared as described in the '*Histological and immunohistochemical analysis*' section of the methods. Embryos at E12.5 were used for establishment of mouse spinal cord-ALI-CO co-cultures. In order to isolate the spinal cords with dorsal root ganglia (DRGs) and overlying paraspinal muscles, 0.15 mm Ø dissecting pins (Fine Science Tools, 2600215) were inserted in the head and pelvic-regions to stabilise the embryos. First, the embryo was positioned face-down with straddled limbs and the skin overlying the spinal cord was peeled off. Next, the limbs were removed by cutting the embryo along its length in a posterior-to-anterior fashion, at a distance of approximately 1 mm from the midline, on either side of the spinal cord, using 3 mm cutting edge spring scissors (CohanVannas, 15000-01). The embryo was then placed sideways and the internal organs were excised. Lastly, the embryo was placed with its ventral side up and any remaining undesired tissue was removed, including the head and tail.

The muscle-spinal cord explants were incubated in ice-cold PBS prior to embedding. For embedding, one organoid (age: 45-60 days) and two mouse spinal cord-muscles were washed once in ice-cold HBSS w/o Ca^{2+} and Mg^{2+} , they were then washed and embedded in 3% LM agarose at ~40°C. Immediately after embedding, before agarose polymerization, the organoid was positioned centrally at the bottom of the mold on a layer of solidified agarose. The mouse spinal cord explants were then placed flat on either side of the organoid with the roof plates pointing inwards and leaving a ~1-3 mm gap between the organoid and mouse tissues. For vibratome sectioning the block was oriented so as to cut the spinal cords along their axial plane. Sectioning was performed as outlined in the methods section '*Air-Liquid Interface Cerebral Organoid (ALI-CO) culture*'. Mouse co-culture slices were maintained in SFSC medium supplemented with 1x AA with daily media changes. After ~2-3 weeks human tracts could be seen innervating mouse spinal cords.

ALI-CO stimulation and axotomy

Spontaneous contractions of mouse spinal muscles in organoid-mouse innervated co-cultures were typically seen after ~20-30 days at the ALI. Contractions were imaged and recorded on a Nikon TE2000 equipped with an Andor Neo sCMOs camera using the NIS Elements software for image acquisition. Data was acquired as either an .avi or .nd2 file depending on downstream analysis and a custom macro in ImageJ (NIH) was used to calculate the tissue displacement upon muscle contraction as a function of time. Contractions evoked by extracellular stimulation of the organoid axonal tract were elicited using stainless steel electrodes (A-M Systems, 57100) connected to a constant isolated stimulator (0.2-30 mA, 120-180 µs manually- or TTL-triggered pulses, model DS3, Digitimer). When operating the stimulator in TTL-triggered mode, TTL pulses at set frequency (5 ms duration) were generated using an Arduino running on its internal clock.

For latency analysis, the stimulator TTL trigger (which triggered the stimulator) and the camera 'expose-out' TTL (indicating the exposure time of each frame) were recorded using an oscilloscope with sampling rate of 200 kHz (Picoscope, 2406B). This allowed for precise estimation ($\pm 5\mu\text{s}$) of the delay between the first frame of the movie and the previous TTL pulse. It was therefore possible to compute the time delay between each frame and the previous stimulation based on the hardware timestamps of each frame and the frequency of the TTL pulses.

For axotomy, the filters were retrieved from the imaging vessels, placed on a plastic support, visualized on an inverted tissue culture microscope at 10x magnification and a microknife (FST, 10316-14) was used to perform the incision. In order to detect the muscle contractions from acquired image sequences, the average of the difference between two consecutive frames for the region of interest (ROI) was computed. The resulting temporal signal was then decomposed into the sum of a baseline, stimulation and residual motion. The baseline was estimated as a 1D rolling ball and the stimulation peaks were detected as outliers ($12 \times \text{SD}$) from the mean. Processing was implemented as an ImageJ macro that was applied to a selected ROI. The camera fire TTL signal was used to synchronize the acquired images and the electrical stimulation signal, latencies were computed using a Matlab script as the delay between each recorded stimulation TTL pulse and the time when the nearest residual motion went above $2 \times \text{s.d.}$. The code used for latency analysis and instructions on how to use it are available at: <https://github.com/jboulanger/stimulation-motion>.

PCR analysis

For *ZEB2* splice variant detection, primers binding upstream and downstream of exon 4 were designed and the sequences are reported in the primer table in Appendix 1. For splice variant discrimination and any other application aimed at amplicon size comparison GoTaq Green Master Mix (Promega, #9PIM712) was used according to the manufacturer's guidelines. For molecular cloning or any other application requiring sequence fidelity Q5 High Fidelity 2X Master Mix (NEB, # M0492S) was used. PCR analysis of pluripotency markers was done using the Human Pluripotent Stem Cell Assessment Primer Pair Panel (R&D Systems, SC012) and amplification was done using GoTaq Green. Novex TBE 10% gels (Thermo Scientific, # EC6275BOX) were used for DNA-PAGE analysis of *ZEB2*^{+/-} mutant gDNA. The primers used were ZEB2_DNA_PAGE_F & R, GoTaq green was used for amplification and 1X SYBR Gold Nuclei Acid Stain was used for detection (Thermo Scientific, S11494). Samples were prepared as outlined in the PAGE gels technical sheet.

Droplet digital PCR (ddPCR) and RT-ddPCR

In order to detect CRISPR-mutants and perform enrichment by sib-selection a TaqMan-based ddPCR drop-off assay was designed (Findlay et al. 2016). An amplicon of 198 bp overlapping the

edited genomic region (GRCh38/hg38 chr2:144,517,275-144,517,351) was produced using primers ZEB2_Cas9n_screening_F & R. The assay was designed so as to have a 5'-HEX-labelled 3'-BHQ1 probe binding to the edited site (i.e. ZEB2_drop-off_probe) and a 5'-FAM-labelled 3'-BHQ1 probe binding to both edited and WT amplicons (i.e. ZEB2_reference_probe). The specific sequence of primers and probes used in the assay are listed in the table included at the end of the methods section. The assay was performed using the ddPCR Supermix for Probes (BioRad, 1863024) as described in the product's technical bulletin. Briefly, reaction mixes (20 µl/reaction) were prepared as follows: 100 nM primers, 200 nM probes, 10 U MseI (NEB, R0525S), 1x ddPCR supermix for probes and 50-300 ng of genomic DNA (gDNA). The reactions were loaded into DG8 cartridges (Bio-Rad, #1864008) with droplet generation oil for probes (Bio-Rad, 1863005), the cartridge was then fitted with the DG8 gaskets (Bio-Rad, 1863009) and run on the QX200 droplet generator (Bio-Rad, 10031907). The droplet-oil emulsion was transferred to a ddPCR 96-well plate that was sealed with the PX1 PCR Plate Sealer (Bio-Rad) and the PCR reaction was run on a C1000 touch thermal cycler following the PCR protocol detailed in the technical bulletin. After thermal cycling, data were acquired on the QX200 Droplet Reader (Bio-Rad) using the QuantaSoft Software (Bio-Rad). RT-ddPCR was used in order to quantify target gene expression levels. Briefly, RNA was isolated from organoid tissue or cells using the RNeasy mini kit (Qiagen, 74104). Samples were treated with DNaseI to remove any contaminating gDNA (Qiagen, 79254). Complementary DNA (cDNA) was synthesized from 240 ng-1 µg total RNA using the SuperScript™ III first-strand synthesis supermix (Thermo Scientific, 18080400) following the product's manual. Primers used for RT-ddPCR are detailed in the table in Appendix 1. With the exception of the *ZEB2* and *EIF2B2*, which were manually designed to bind across different species (i.e. mouse, gorilla and human), all other primer sequences were downloaded from PrimerBank (<https://pga.mgh.harvard.edu/primerbank/>). Amplicons were validated and thermocycling conditions were optimized for individual targets. After reverse transcription, cDNA concentration was not measured - for samples synthesized starting from 240 ng of RNA 0.33 µl of cDNA were used per reaction, while samples synthesized starting from 1 µg of RNA were first diluted 1:5 and 0.33 µl were used per reaction. Detection relied on EvaGreen chemistry (Bio-Rad, 1864034) and because the loading control (i.e. *EIF2B2*) was run separately and not as an internal control, all reactions were run in triplicates. As negative control, for each condition tested and each target analysed a reaction with the RNA as template was run. Reaction mixes (20 µl/reaction) were prepared as follows: 0.33 µl sample, 100 nM primers, 1x QX200 ddPCR EvaGreen supermix (Bio-Rad, 1864034). The ddPCR reactions were set up as described for the TaqMan probe-based assay above, with the only difference being that the QX200 Droplet Generation Oil for EvaGreen (Bio-Rad, 1864005) was used for emulsion. For analysis, the concentration values for the different targets were normalized to the loading control *EIF2B2* and mean and standard deviation (s.d.) values for the three technical replicates were calculated and reported as target mRNA normalized fold change.

Luciferase reporter assay

The reporter constructs used for the luciferase reporter assay for TGF β (SBE4-Luc, #16495) and BMP (pGL3-BRE Luciferase, #45126) signalling cascades were purchased from Addgene. The Renilla luciferase control vector pRL-TK (Promega, #E2241) was used as internal control. Recombinant human TGF β -1 (R&D Systems, # 240B002) and recombinant human BMP4 (R&D Systems, #314BP010) were reconstituted to 20 μ g/ml and 50 μ g/ml, respectively, in PBS supplemented with 4mM HCl and 0.1% BSA. For the reporter assay, 293T cells were seeded into 12-well plates and the next day they were transfected. The reactions comprised the *Renilla* luciferase control vector pRL-TK (10 ng), pCAG-nV5-ZEB2-isoform1 (1 μ g) or alternatively pCAG-nV5 (i.e. EV) (1 μ g), and the TGF β reporter construct (200 ng) or the BMP reporter construct (200 ng). Polyethylenimine (PEI) was used for transfection in a 1:2 (DNA:PEI) (μ g/ μ l) concentration, 2.42 μ l of PEI/reaction and the reaction mix was made in 100 μ l Opti-MEM reduced serum medium (Thermo Scientific, # 31985062). On day four, the medium was changed and the cells were induced with either TGF β -1 (1 ng/ml), BMP4 (40 ng/ml) or mock (PBS, HCl 4 mM, 0.1% BSA). On day 5 the cells were lysed with modified-RIPA (mRIPA: 1% Triton-X, 0.1% SDS, 150 mM NaCl, 50 mM Tris pH 7.4, 2 mM EDTA, 12 mM sodium deoxycholate) supplemented with protease (Thermo Scientific, #78430) and phosphatase (Sigma-Aldrich, #4906845001) inhibitors. The Dual-Luciferase Reporter Assay System (Promega, E1910) kit was used for detection of firefly and *Renilla* luciferase in the same sample and chemiluminescence was measured on a standard luminometer. For analysis, each treated transfection condition was normalized by its corresponding mock treated control to obtain a relative fold luminescence change.

Cryo-CLEM on ALI-CO tracts

Organoids were electroporated and sectioned for ALI-CO culture as previously described. During vibratome sectioning due care taken to remove all Matrigel surrounding the organoids and tissue slices were manipulated with scalpel blades (Swann-Morton, SM0501) and collected on cell culture insets. Carbon- (Quantifoil R2/2 Cu 200 mesh) and gold-coated grids (UltrAuFoil R2/2 Au 200 mesh) were incubated at room temperature overnight with 0.01% polyornithine (Sigma-Aldrich, #P4957-50ML), the next day they were washed in PBS, coated with 10 μ g/ml laminin (Sigma-Aldrich, #L2020) and 0.001% fibronectin (Sigma-Aldrich, # F0895) and incubated at 37 °C for four hours. ALI-COs were visualised on an EVOS FL inverted microscope (Thermo Scientific) and grids were placed adjacent to GFP⁺ foci. The ALI-CO media was changed daily and care was taken not to disturb the grids. After approximately 2-3 weeks GFP⁺ tracts could be seen spreading across the surface of the grids as far as their centre. Biopsy punches were used to retrieve the grids with overlying axons, and they were immediately plunge frozen in liquid ethane using a foot operated plunger. Grids were screened for GFP⁺ axons on a cryo-fluorescence microscope (Leica EM Cryo CLEM, Leica Microsystems),

equipped with an Orca Flash 4.0 V2 sCMOS camera (Hamamatsu Photonics) and a HCX PL APO 50X cryo-objective with NA = 0.9, a Sola Light Engine (Lumencor) and a L5 filter, excitation 480/40, dichroic 505, emission 527/30 for detection of GFP, in a humidity-controlled room (humidity below 25%). The stage was kept at -195 °C for cryo-FM imaging. Tile scan overviews around the center of the grid were acquired both in the GFP and brightfield channel using the Leica LAS X software. Subsequently, focal stacks with 1µm step size were taken around areas of interest on the grid. The imaging settings were kept at: 17% - intensity and 500 ms - exposure, 30 % - intensity and 50 ms - exposure for the GFP and brightfield channel, respectively.

ECT data acquisition at pre-identified GFP⁺ axons were collected on a Titan Krios (FEI) operated at 300 kV using a Quantum energy filter (20 eV slit width) and a K2 direct electron detector (Gatan) using SerialEM (Mastronarde 2005). Low magnification montages were taken around the center of the grid with 170 nm pixel size. Grid squares with GFP⁺ tracts were identified and overview montages of these squares were acquired at a pixel size 5.1 nm. From these overview maps individual GFP⁺ tracts were targeted for ECT. Tilt series were acquired in counting mode at 3.7 Å pixel size between ±60° starting from 0° with 1° increment using SerialEM following a grouped dose-symmetric acquisition with a group size of four (Bharat et al. 2018; Hagen et al. 2017), and at 5 µm defocus. A dose of approximately 0.9 e⁻/Å² was applied per image of the tilt-series and images were acquired as frames. Frame alignment and tomogram reconstructions were performed using IMOD (Kremer et al. 1996). For better visualisation in figures the tomograms were reconstructed at a pixel size of 7.4 Å by simultaneous iterative reconstruction technique (SIRT) with 10 iterations. Cryo-FM and EM overlays were generated using landmark features in both images with the eC-CLEM correlation plugin for Icy (Paul-Gilloteaux et al. 2017).

Chapter 3: The zinc-finger transcription factor *ZEB2* regulates cell-cell contacts and architecture in the developing neuroepithelium

Introduction

The neuroepithelium represents the CNS primordium and along the AP axis it generates a variety of structures of different sizes, diverse architectures and functions. Nevertheless, despite this ability to generate considerable structural and functional diversity, at the cellular level the neuroepithelium appears highly homogenous. Histological examination of NECs of the trunk neural tube and of those of the pallium does not reveal any obvious morphological difference. As development progresses and NECs transition to aRGCs, through regional differences in cell cycle dynamics, cell adhesion and proliferation the neural tube starts to diversify. An example of this structural divergence is the OSVZ, a proliferative compartment unique to the developing cerebral cortex that is thought to have allowed for increased cortical neurogenesis.

Nevertheless, already at the neuroepithelial stage regional differences in progenitor proliferation lead to divergent growth of the secondary brain vesicles. In fact, if we consider the proliferation dynamics of human pallial and midbrain/hindbrain NECs, we observe that although initially the cortical neuroepithelium is of smaller size compared to the midbrain/hindbrain neuroepithelium, over time it grows considerably larger (Altman et al. 1995). Intriguingly, comparison of the human and rat neocortical neuroepithelium reveals evolutionary differences in the pattern of regional NECs expansion. Whilst in humans NECs proliferate for approximately 8-9 weeks, rat neocortical NECs expand for only ~6 days before switching to neurogenic divisions (Altman & Bayer 2007; Altman et al. 1995). These early differences in NECs expansion in human and rat produce protomaps with profoundly different neurogenic output potential (Fernández et al. 2016; Nowakowski et al. 2016; Geschwind & Rakic 2013).

Thus, the neuroepithelial stage is undoubtedly an interesting developmental window for examination of evo-devo changes that led to differences in neocortex size. Looking at the literature, it is surprising how little is currently known on this subject compared to later aspects of neocortical development. This has been largely due to the fact that in the mouse the neuroepithelial stage lasts only a couple of days, from the moment of anterior neuropore closure (~E8.5) to the onset of neurogenesis (~E11). At this stage the embryo is not easily accessible, the boundary between pallium and subpallium is ill-defined both anatomically and molecularly, and, in addition, we are missing a – Cre driver gene to efficiently manipulate gene levels so early and over such a short time window. In this regard, cerebral organoids represent a precious tool to examine early neurodevelopmental stages. In this chapter we will discuss how cerebral organoids were used to investigate the role of *ZEB2* in the establishment of human neuroepithelial architecture.

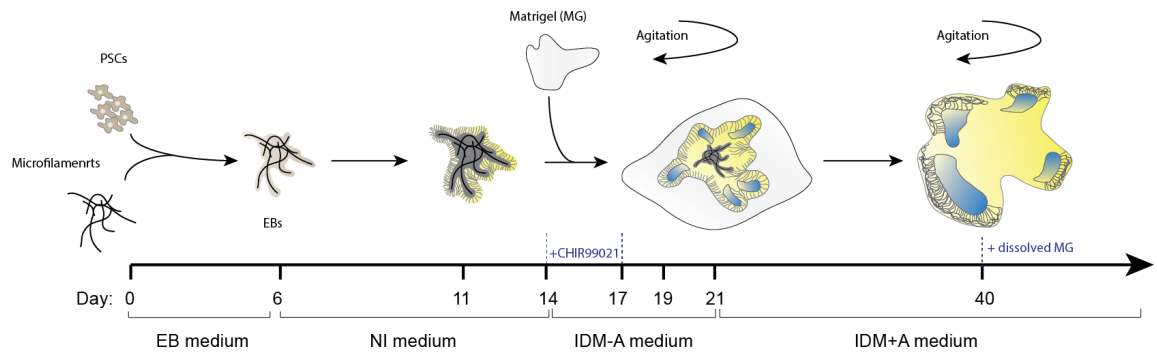
ZEB2 is highly expressed in early neural progenitor cells

After identification of *ZEB2* as a putative regulator of human neocortex size through an *in silico* screen detailed in the Introduction section, we decided to characterise the expression dynamics of this gene throughout the developmental time-line of the cerebral organoid protocol (Lancaster et al. 2017). The protocol used relies on the intrinsic ability of PSCs to differentiate to neural ectoderm without the need for inductive cues that could potentially lead to skipping of important developmental intermediates. Fig. 11a reports a schematic diagram of the protocol with the key steps highlighted, a detailed description of the protocol can be found in the Materials & Methods section.

We first examined *ZEB2* expression at key transition steps of the protocol by immunofluorescence. Our analyses showed that *ZEB2* started to be expressed on day 14 of the protocol in early neuroepithelial progenitors, when only few DCX^+ neurons could be seen (Fig. 11b). *ZEB2* expression in NECs was maintained until day 21, when neurogenesis started, as shown by the increased numbers of DCX^+ cells accumulating on the basal surface of the organoid buds (Fig. 11b). By day 25, several layers of DCX^+ cells could be seen overlying the intermediate zone and the ventricular zone. At this time point, the progenitor cells of the VZ showed reduced levels of *ZEB2*, with a salt-and-pepper pattern of expression (Fig. 11b). By day 31, *ZEB2* expression in the VZ was completely lost and some DCX^+ neurons could be seen expressing *ZEB2* (Fig. 11b). Analysis of day 60 organoids revealed strong *ZEB2* expression in neurons of the cortical plate and the IZ with some overlap with the deep-layer neuron marker CTIP2 (Fig. 11b).

Our immunofluorescence data showing *ZEB2* expression in neurons was in agreement with previous reports of *ZEB2* expression in postmitotic neurons of the cortical plate in the mouse cortex at E16.5 (Seuntjens et al. 2009). Detection of *ZEB2* protein in early neural progenitor cells was not entirely unexpected as previous RNA *in situ* hybridization experiments had shown expression in the telencephalon of E9.5 and E10.5 mouse embryos (Miyoshi et al. 2006). However, our data showed that, whilst being initially expressed in early neural progenitor cells, *ZEB2* was rapidly downregulated in progenitors and upregulated in neurons at the onset of neurogenesis. Having identified *ZEB2* through a bioinformatic screen for genes with a putative role in brain size determination, we reasoned that its expression in early neural progenitors might indicate an important function of this gene in the establishment of a cortical protomap and decided to pursue this further.

a



b

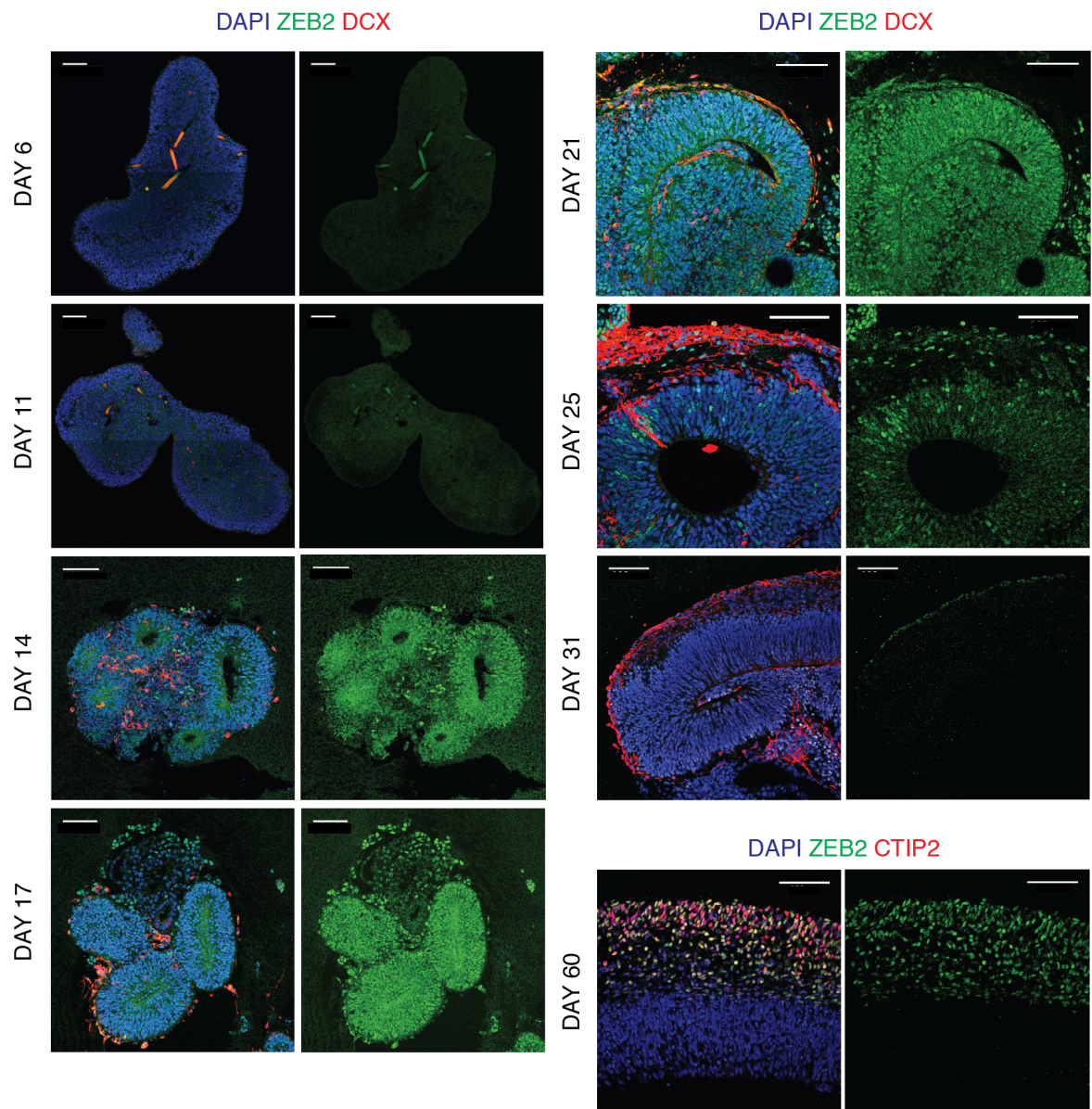


Figure 11 *ZEB2* is expressed early in NECs and late in postmitotic neurons.

a, Schematic representation of the enCOR protocol, pluripotent stem cells (PSCs) are reduced to a single cell suspension and seeded into low-adhesion U-bottom microwells along with fibrous microscavolds. The embryoid bodies (EBs) are cultured for the initial 6 days in EB medium and are then moved to neural induction (NI) medium until day 11, when they are embedded in Matrigel. On day 14, EBs are moved to improved differentiation medium without vitamin A (IDM-A) supplemented with the Wnt agonist CHIR99021 which is removed three days later. EBs are fed every other day with IDM-A until day 21, when they are switched to improved differentiation medium with vitamin A (IDM+A) and moved to an orbital shaker to promote oxygen and nutrient exchange. From day 40 on, addition of dissolved matrigel to the growth medium promotes establishment of the cortical plate. b, Immunofluorescence staining of H9 hESC-derived cerebral organoid cryosections at day 6, 11, 14, 17, 21, 25, 31 of the protocol for *ZEB2* (TA802113), DAPI and the immature migrating neuron marker doublecortin (DCX). Day 60 organoids were stained for *ZEB2* (TA802113), DAPI and the deep-layer neuronal marker (CTIP2). Images are representative of two independent experiments. Scale bars, 100 μ m (b).

Next, we performed western blots to estimate the relative *ZEB2* protein levels at the time points examined by immunofluorescence. Along with *ZEB2* we also probed for the dorsal telencephalic marker *EMX1* to control for any differences in organoid tissue identity within the batch. By western blot *ZEB2* was not detectable in hESCs, it was highest at day 6 and 11 of the protocol, then steadily declined between day 14 and 21 and was undetectable between day 25 and 30 (Fig. 12a). *ZEB2* was detectable at very low levels at day 40 but not at day 50, while at day 60 and 70 *ZEB2* expression was restored (Fig. 12a). The western blot results showing that, beginning at day 14, *ZEB2* was gradually downregulated and then upregulated at later stages was in agreement with immunofluorescence data. However, while *ZEB2* was not detectable by immunofluorescence at day 6 and 11, western blot showed that at these two time points its expression was highest (Fig. 11b & Fig. 12a). The same antibody was used for both immunofluorescence and western blot and its application for western blot was validated by knockdown. In order to verify the western blot results we performed RT-ddPCR and quantified *ZEB2* transcript levels from stem cells up to day 21 organoids. By RT-ddPCR *ZEB2* was undetectable in hESCs, its expression peaked at 6 and then steadily declined over the remaining time points (Fig. 12b), thus supporting the western blot results.

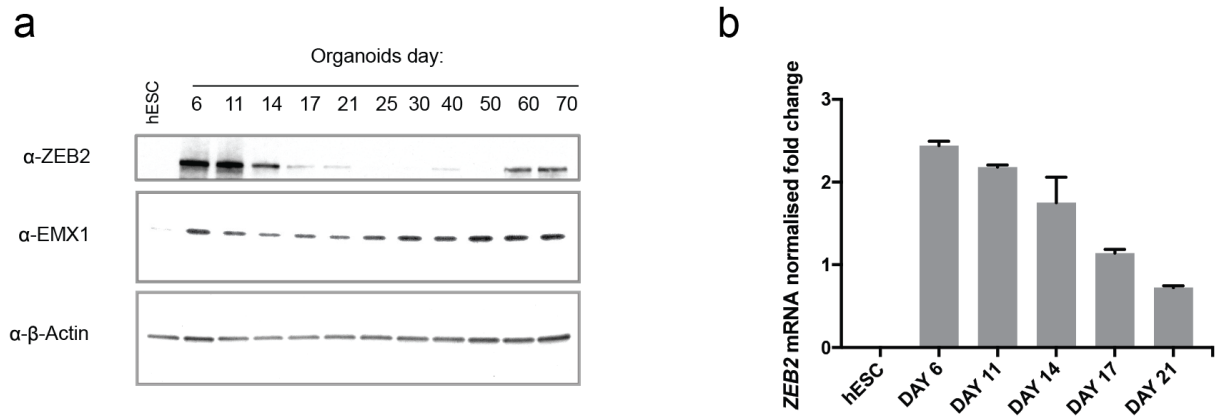


Figure 12 Western blot and RT-ddPCR analyses reveal high *ZEB2* expression in day 6 and 11 EBs.

a, Immunoblot analysis of protein extracts from H9 hESC-derived cerebral organoids at stages: hESCs, day 6, 11, 14, 17, 21, 25, 30, 40, 50, 60 and 70 of the protocol. Shown are blots for ZEB2 (TA802113), the dorsal telencephalic marker EMX1 and the loading control β -Actin. The blots show that ZEB2 protein levels peak at day 6 and 11 and gradually decrease, between day 25 and 30 ZEB2 is undetectable and starting from day 40 on becomes upregulated. b, RT-ddPCR analysis of ZEB2 transcript levels in H9 hESCs and day 6, 11, 14, 17 and 21 EBs reveal that *ZEB2* mRNA levels peak at day 6 and progressively decrease throughout the time course. Shown are mean \pm s.e.m. values of normalised *ZEB2* mRNA fold change relative to the internal control amplicon *EIF2B2* on three technical repeats of the experiment. Experiments shown in a and b were performed on organoids from two independent batches, each experiment performed had two technical repeats and the findings presented in the figure were consistent with data from multiple independent experiments on different batches of organoids.

At day 6 of the protocol ZEB2 protein is present but not detectable by immunofluorescence

After confirming by RT-ddPCR that *ZEB2* was expressed at day 6 and 11, despite not being detectable by immunofluorescence, we hypothesised that at these early stages the protein might be localised to the cytoplasm. We reasoned that because in early EBs cells are very tightly packed what might appear as antibody background could in fact be real cytoplasmic signal. We thus performed nuclear-cytoplasmic fractionation of day 6 and day 21 organoids to test whether differences in intracellular protein localisation could be seen. The experiment revealed that at both stages ZEB2 localised to the nucleus and corroborated earlier observations that at day 6 ZEB2 protein levels were higher than at day 21 (Fig. 13a). All biochemical experiments up to this point appeared to contradict histological data showing an absence of ZEB2 before the step of Matrigel embedding. The antibody was shown to be suitable for both western blot and immunofluorescence analysis, and therefore we sought to reconcile these apparently conflicting results.

Whilst for SDS-PAGE the sample is fully denatured and linearized, for immunofluorescence analyses the tissue is fixed and proteins retain conformations and interactions that resemble more closely the normal cellular state. Because in samples from day 14 to 25 ZEB2 was detectable in neural progenitors by immunofluorescence, we ruled out possible fixation artefacts as a possible explanation for these conflicting results. We thus hypothesised that the observed differences in ZEB2 detectability may be caused by differences in antigen presentation and we tested this by performing immunofluorescence on cryosections treated with 1% SDS to denature and linearize the proteins on the slide. While normal immunofluorescence staining without SDS treatment did not show signal, incubation in 1% SDS revealed strong nuclear immunostaining in an adjacent section (Fig. 13b). This result suggested that between day 6 and 11 of the protocol the protein might be in complex with other factors or in a different conformational state that would mask the epitope.

Next we examined the antigen against which the antibody was raised and found that it corresponded to amino acids 1-350 of ZEB2 (Fig. 13c). To validate our findings up to this point we repeated staining on day 6 organoids with a rabbit polyclonal antibody raised against the last 50 amino acids of ZEB2. Immunofluorescence analysis using this antibody revealed strong nuclear staining and confirmed biochemical and immunofluorescence data on SDS treated samples (Fig. 13c). Interestingly, while the last 50 amino acids of the protein do not map to any known functional domain of the protein, amino acids 1-350 of ZEB2 overlap the NuRD complex interaction motif (NIM), the N-terminal Zn²⁺-finger cluster and the p300/PCAF interaction domain (Hegarty et al. 2015) (Fig. 13c). Thus developmental stage-specific interaction with any of these partners could explain these findings.

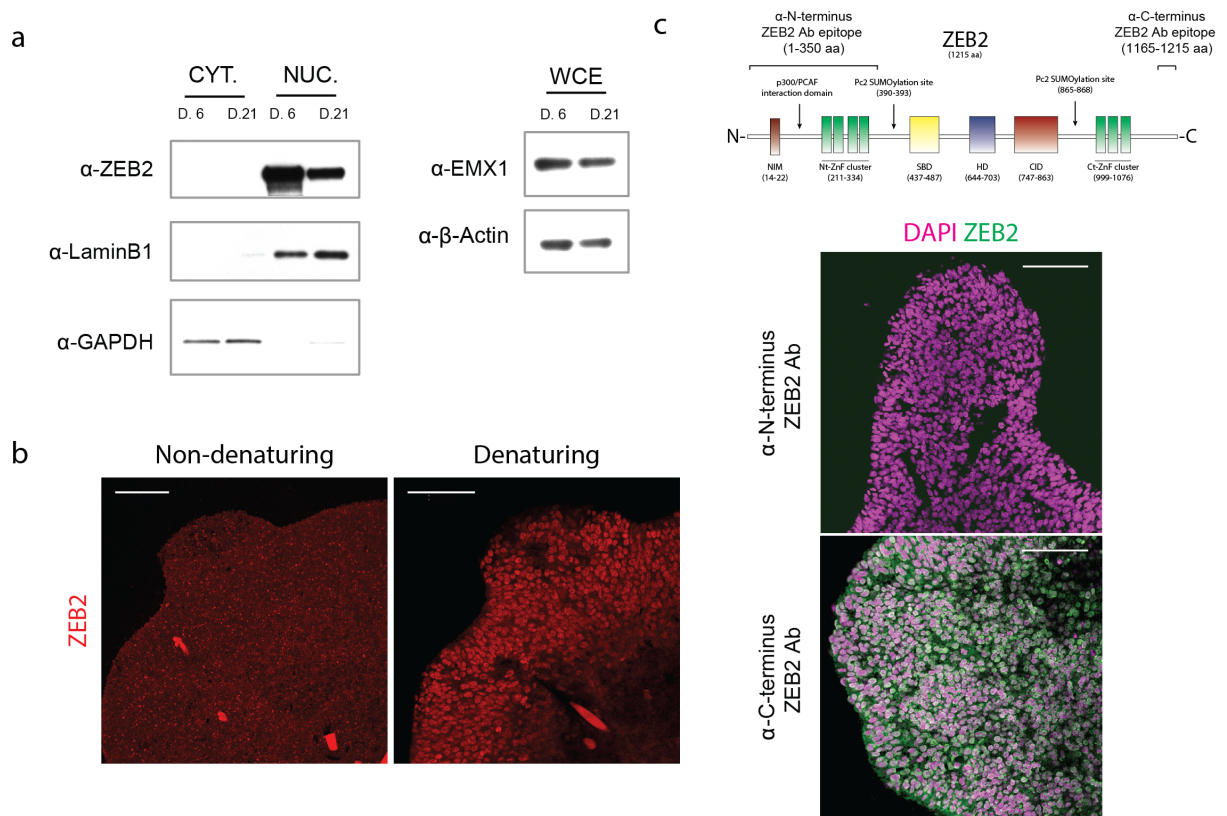


Figure 13 ZEB2 protein is expressed in day 6 organoids but is not detected by an antibody against its N-terminus in immunofluorescence.

a, On the left are western blots of nuclear and cytoplasmic extracts from day 6 and day 21 H9 hESC-derived EBs against ZEB2 (TA802113), the nuclear envelope protein LaminB1 and the cytoplasmic marker GAPDH. On the right are western blots of whole-cell extracts (WCE) used as input for fractionation, probing for the dorsal telencephalic marker EMX1 and β -Actin as loading control. The blot shows that both at 6 and day 21 ZEB2 localises to the nucleus and confirms the previous observation that at day 6 ZEB2 protein levels are higher than at day 21. b, Immunofluorescence images of adjacent cryosections of day 6 H9 hESC-derived organoids with and without incubation in 1% SDS prior to primary antibody staining. Treatment with 1% SDS (denaturing) reveals intense ZEB2 nuclear staining, which is completely absent in the untreated (non-denaturing) sample. c, Top is a schematic representation of the ZEB2 protein primary sequence annotated with known functional domains, interaction domains, post-translational modification (PTM) sites and the sequences recognised by the two antibodies used for analyses are reported above. Below are immunofluorescence images of day 6 H9 hESC-derived organoid cryosections stained for DAPI and ZEB2 using antibodies against the N- (TA802113) and a C-terminus (TA319793). While staining using the N-terminal antibody fails to detect ZEB2, staining using the C-terminal antibody reveals intense nuclear staining. Scale bar, 100 μ m (b, c).

Exon IV of ZEB2 contains a putative SUMOylation/ubiquitylation site that controls protein stability

Since this change in ZEB2 detectability could be caused by a different conformational state or cellular interaction relevant for the function of this gene in neurodevelopment we decided to investigate this further. We reasoned that the best way to test whether this behaviour was caused by ZEB2 binding to specific cellular interactors would be to take an unbiased approach such as BioID or immunoprecipitation followed by mass spectrometry. However, a number of technical limitations made these approaches difficult to pursue. In fact, this behaviour of ZEB2 was specific to a well-defined developmental window, and it was not possible to move to a simpler 2D culture system, as it may not recapitulate this particular process. A BioID experiment, albeit very sensitive compared to traditional mass spectrometry approaches, relies on the fusion of biotin ligase to the protein of interest, which can be done by overexpression of the fusion construct or by taking an endogenous tagging approach. Endogenous tagging would be the best strategy as transgene overexpression is likely to generate false positive. Nevertheless, we decided against this as CRISPR-mediated homology directed repair (HDR) has very low efficiency in stem cells. On the other hand, a more traditional antibody pull-down approach suffered from the limitation that there are no reported ChIP-grade ZEB2 antibodies available and antibodies against the N-terminus of the protein would likely be unsuitable for the experiment. We thus started optimisation of immunoprecipitation (IP) conditions using the antibody recognising the C-terminal portion of ZEB2 (data not shown).

In parallel, we examined the annotated *ZEB2* splice variants and found that alternative transcript II of the gene differs from the main isoform only for the absence of a 72 bp exon. This caught our attention as the difference in size between the two protein isoforms would not be detectable by SDS PAGE, but could still affect its conformational state and interaction ability, leading potentially to the observed changes in detectability. We therefore designed, validated and optimised primers to detect changes in the relative abundance of isoform I and II, these would bind upstream and downstream of exon IV, generating two bands corresponding to the two alternative transcripts that could be resolved on a gel (Fig. 14a). While collecting samples for a time-course of splice variants usage from hESC to day 21 of the protocol, we cloned ZEB2 isoform II with an N-terminal V5 tag to start preliminary biochemical characterisation. First, we expressed the two isoforms in HeLa cells and performed a cycloheximide (CHX) chase experiment to assess their stability. Interestingly, isoform I displayed longer half-life than isoform II (Fig. 14b). In addition, expression of ZEB2 isoform I produced two bands, one of the expected molecular weight (MW) along with a ~10 kDa heavier form (Fig. 14b and c). This additional band was not observed upon expression of isoform II (Fig. 14b and c).

These data suggested that exon IV of the gene contained a motif responsible for covalent modification of isoform I. We analysed the amino acid sequences of the two isoforms through a

variety of online analysis tools, looking for a post-translational modification (PTM) consistent with a ~10 kDa MW higher size shift. Within exon IV, corresponding to amino acids 113-116 we identified a putative SUMOylation/ubiquitylation recognition motif predicted with very high probability (Fig. 14d). Around the same time, collection of RNA samples for the time-course was completed and a time-course of splice variants usage was performed by PCR. This, however, did not show any changes in the relative abundance of the two transcripts and transcript I appeared predominant across all time points. After this we stopped characterisation of isoform II as it could not explain the change in detectability observed.

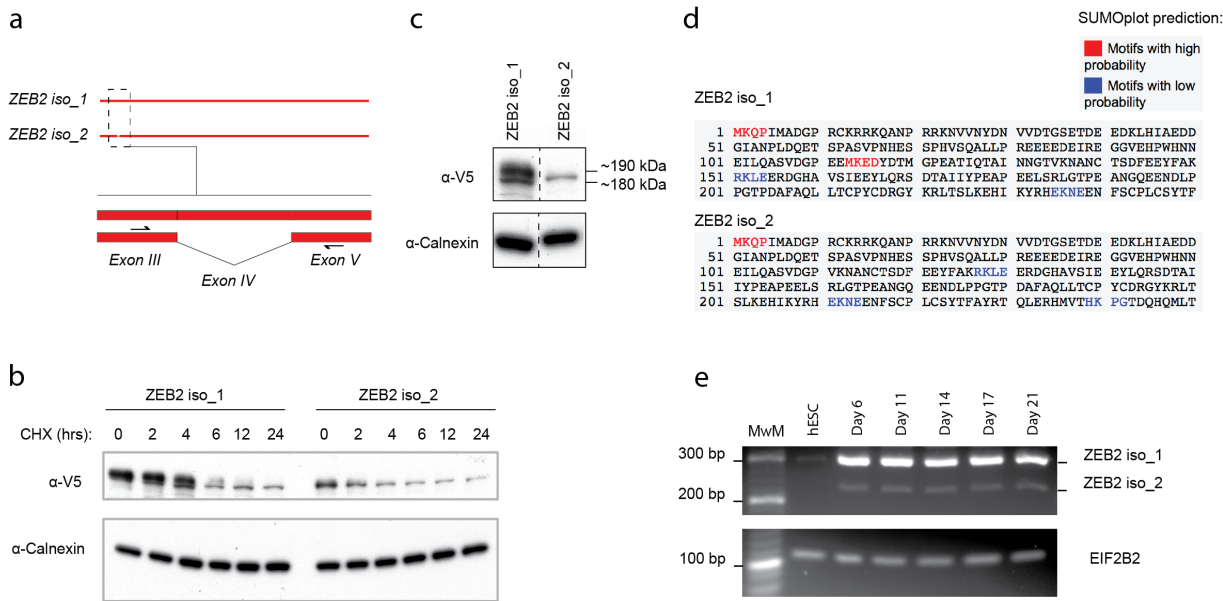


Figure 14 Transcript variant II of *ZEB2* contains a putative SUMOylation/ubiquitylation site that leads to longer protein half-life.

a, Schematic representation of *ZEB2* transcript variant I and II, dashed box and inset show exon IV and the upstream and downstream exons with primers designed to detect the two isoforms by PCR, producing a 72 bp shift on an agarose gel. b, Cycloheximide (CHX) chase experiment in HeLa cells expressing the two different *ZEB2* isoforms bearing an N-terminal V5 tag. Immunoblotting for V5 and the ER resident protein Calnexin as loading control reveals that the longer *ZEB2* isoform has increased stability compared to the shorter isoform missing exon IV. c, Enlarged single images of lanes 3 and 10 of the blot shown in b reveal the presence of two bands, with ~10 kDa size difference, in the sample expressing isoform 1. This second higher molecular weight band is not observed in the sample expressing transcript variant II of *ZEB2*. d, Sequence analysis using the online resource SUMOplot identifies a putative SUMOylation site corresponding to amino acids 113-116 encoded by exon IV of *ZEB2* and prediction was deemed to have high probability. The ubiquitylation motif prediction software identified at the same site a putative ubiquitylation site. The shorter *ZEB2* protein isoform does not contain this putative SUMOylation/ubiquitylation site as exon IV, containing this

sequence, is spliced out of the transcript. The legend reports the colour-coded SUMOplot prediction confidence. UbPred results are not shown. e, PCR analysis of *ZEB2* transcript usage in H9 hESC and day 6, 11, 14, 17 and 21 H9 hESC-derived EBs showing that there is no evident switch in isoform usage across any of the time-points. In H9 hESCs, which express *ZEB2* at very low levels, only the major isoform is detectable by PCR. Data shown in b and c are representative of two independent experiments, while data shown in e are representative of one experiment.

ZEB2 is expressed transiently in dorsal telencephalic progenitors and is repressed after the switch from NECs to aRGCs

Interested in the dynamic expression profile of *ZEB2* we proceeded to examine the specific identity of the tissue it was expressed in. In fact, engineered cerebral organoids (enCORs) generate forebrain tissue and we wanted to verify that *ZEB2* was expressed in dorsal telencephalic progenitors (Lancaster et al. 2017). While early *EMX1*⁺ dorsal telencephalic progenitors express *ZEB2*, expression is lost at later stages (Fig. 15a). This is in contrast to *GSH2*⁺ ventral telencephalic progenitors, which retain *ZEB2* expression even at later stages of the protocol (Fig. 15b). We had previously observed that *ZEB2* downregulation in organoids was accompanied by a sizable increase in neurons, suggesting it may coincide with the switch to neurogenesis (Fig. 11b). The shift from symmetric expansive to asymmetric differentiative divisions corresponds to the transition from NECs to aRGCs and its defining feature is upregulation of glial genes. We thus stained day 31 organoids for the glial markers *GLAST* and *BLBP* and observed that, whilst regions retaining *ZEB2* expression were negative for these glial marker genes, regions of the tissue positive for these markers did not express *ZEB2* (Fig. 15c and d). The mutually exclusive staining pattern of *ZEB2* and glial genes suggests that *ZEB2* expression is suppressed in dorsal telencephalic progenitors after they have transitioned to a radial glia neurogenic state; however, in agreement with previous reports the same was not observed for ventral telencephalic progenitors (Miquelajauregui et al. 2007).

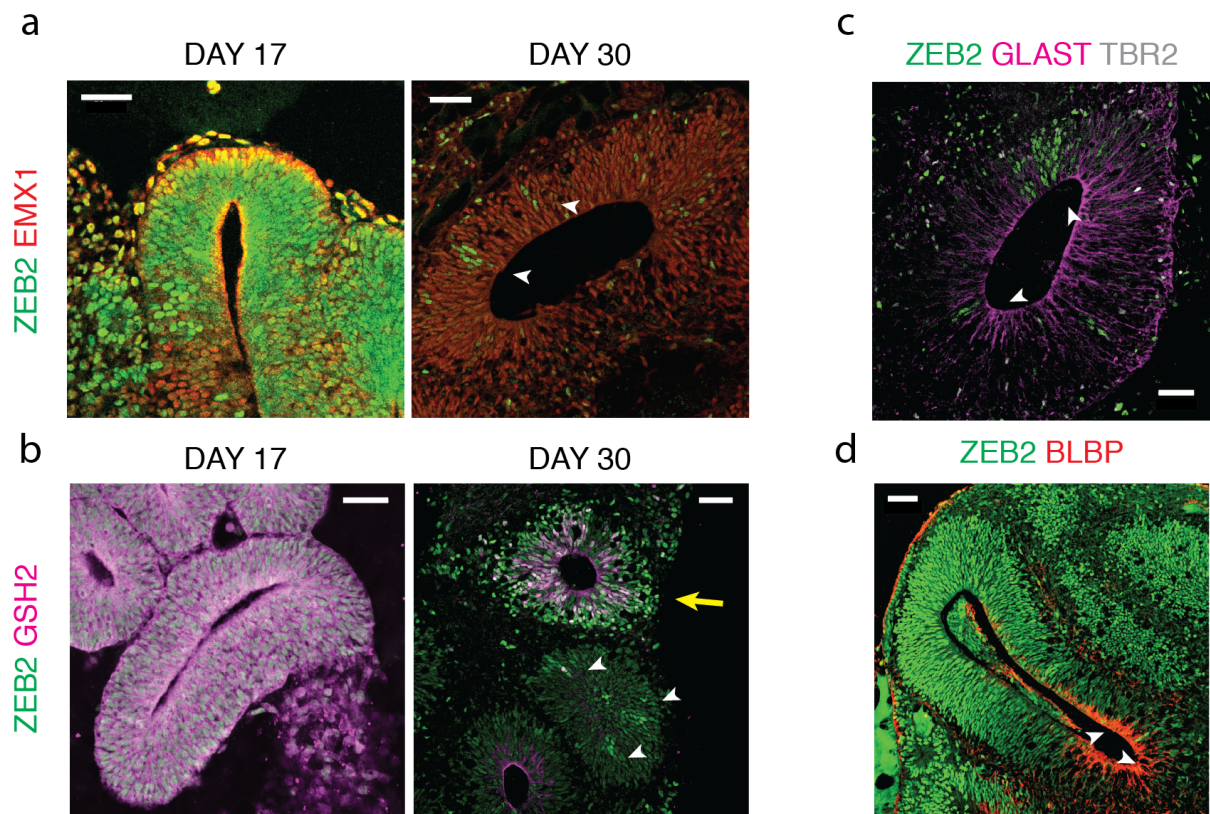


Figure 15 ZEB2 is expressed transiently in the neuroepithelium prior to the NEC to aRGC switch.

a, Immunofluorescence images of cryosections of H9 hESC-derived organoids at day 17 (left) and 30 (right) of the protocol for ZEB2 (TA802113) and the dorsal telencephalic marker EMX1, revealing even ZEB2 protein expression across the neuroepithelium at day 17 and only sparse clusters of ZEB2⁺ cells at day 30 (white arrowhead). b, Immunofluorescence images of cryosections of H9 hESC-derived organoids at day 17 (left) and 30 (right) of the protocol for ZEB2 (TA802113) and the ventral telencephalic marker GSH2, revealing even ZEB2 protein expression across the neuroepithelium at day 17 and sustained ZEB2 protein expression in day 30 ventricles with ventral identity (GSH2⁺, yellow arrow). By contrast, GSH2⁻ ventricles display only sparse clusters of high ZEB2 expression (white arrowheads). c, Immunofluorescence image of day 30 H9 hESC-derived organoids stained for ZEB2 (TA802113), the glial marker GLAST and the intermediate progenitor and dorsal telencephalic marker TBR2, revealing that neural progenitor cells expressing GLAST appear negative for ZEB2, whereas clusters of ZEB2⁺ cells coincide with regions where GLAST is not expressed (white arrowhead). The data suggest that with the switch from NEC to aRGC, upregulation of GLAST is accompanied by downregulation of ZEB2. d, Immunofluorescence image of day 30 H9 hESC-derived organoids stained for ZEB2 (TA802113) and the glial marker BLBP reveals that neural progenitor cells expressing BLBP appear negative for ZEB2 (white arrowheads), whereas cells retaining ZEB2 expression do not yet express BLBP. The data suggest that with the switch from NECs to aRGCs, upregulation of BLBP is accompanied by downregulation of ZEB2. Data shown in a and b are representative of three independent experiments and data shown in c and d are representative of 2 independent experiments. Scale bars, 50 μ m (a-d).

ZEB2 has a similar expression pattern in the developing mouse dorsal telencephalon

Having observed a switch in *ZEB2* expression from progenitors to neurons in human cerebral organoids, we next asked whether this change in expression was physiologically relevant and not an *in vitro* artefact of the protocol. By *in situ* hybridization *Zeb2* mRNA expression had been previously reported in the dorsal telencephalon of mice at E9.5-E10.5 but the observed switch in expression from progenitors to neurons had not been reported (Miyoshi et al. 2006). We thus analysed publicly available scRNA-seq datasets of microdissected mouse telencephalon at E9.5 and E10.5 (Dong et al. 2018) along with datasets of mouse cortices specifically at E11.5, E13.5, E15.5 and E17.5 (Yuzwa et al. 2017). The datasets were analysed as detailed in the Materials & Methods, and following unbiased clustering 9 clusters were identified corresponding to: radial glia cells, interneuron precursor cells, intermediate progenitor cells, interneurons, pyramidal neurons, microglia, blood and mesenchymal cells and an unidentified cluster (U) to which identity could not be assigned (Fig. 16a).

We then visualised the contribution from each sample to the different cell clusters. Although different total numbers of cells were sequenced at the different time-points, a temporal developmental trajectory could be seen going from progenitors, more prevalent at early stages, to neurons, predominant at later stages (Fig. 16b). In fact, despite the low total number of cells, the majority of cells at E9.5 and E10.5 populated the progenitor cluster and similarly at E11.5 (Fig. 16b). At later stages such as E15.5 and E17.5 the majority of cells mapped to the neuron and interneuron clusters, and only few progenitors could be seen (Fig. 16b). Supporting these observations, a feature plot of the distribution of *Vimentin* and *NeuroD2* expressing cells clearly revealed two distinct clusters overlapping the radial glia progenitor cluster and the pyramidal neuron cluster, respectively (Fig. 16c). The clear separation between these two populations of cells confirmed that cluster separation was robust and that *Zeb2* expression could be analysed at the different time-points (Fig. 16c).

We next produced violin plots for expression of the progenitor markers *Nestin* and *Sox2*, the neuronal marker *NeuroD2* and *Zeb2* (Fig. 16d). These revealed a sharp drop in *Zeb2* expression at E11.5 (Fig. 16d), which was particularly striking, considering that the majority of cells at E11.5 were radial glia progenitors (Fig. 16b). Expression of *NeuroD2* confirmed that E11.5 corresponds to the onset of neurogenesis, and as more neurons are being produced the expression of radial glia markers *Nestin* and *Sox2* declines. By contrast, following a sharp drop between E10.5 and E11.5, *Zeb2* expression resumes (Fig. 16d). Therefore, analysis of publicly available scRNA-seq datasets confirmed our findings in cerebral organoids of a drop in *Zeb2* expression after NEC-aRGC transition, when neurons start to be made, with later expression in neurons. To verify that *Zeb2* protein showed similar dynamics, we performed immunofluorescence analysis of mouse dorsal telencephalon from E10.5 to E16.5. In agreement with data from human cerebral organoids and scRNA-seq, at E10.5 *Zeb2* was detected in dorsal telencephalic progenitors (Fig. 16e). By contrast, from E12.5 to E16.5

Zeb2 was absent from progenitors in the VZ and was instead found in neurons of the cortical plate (Fig. 16e).

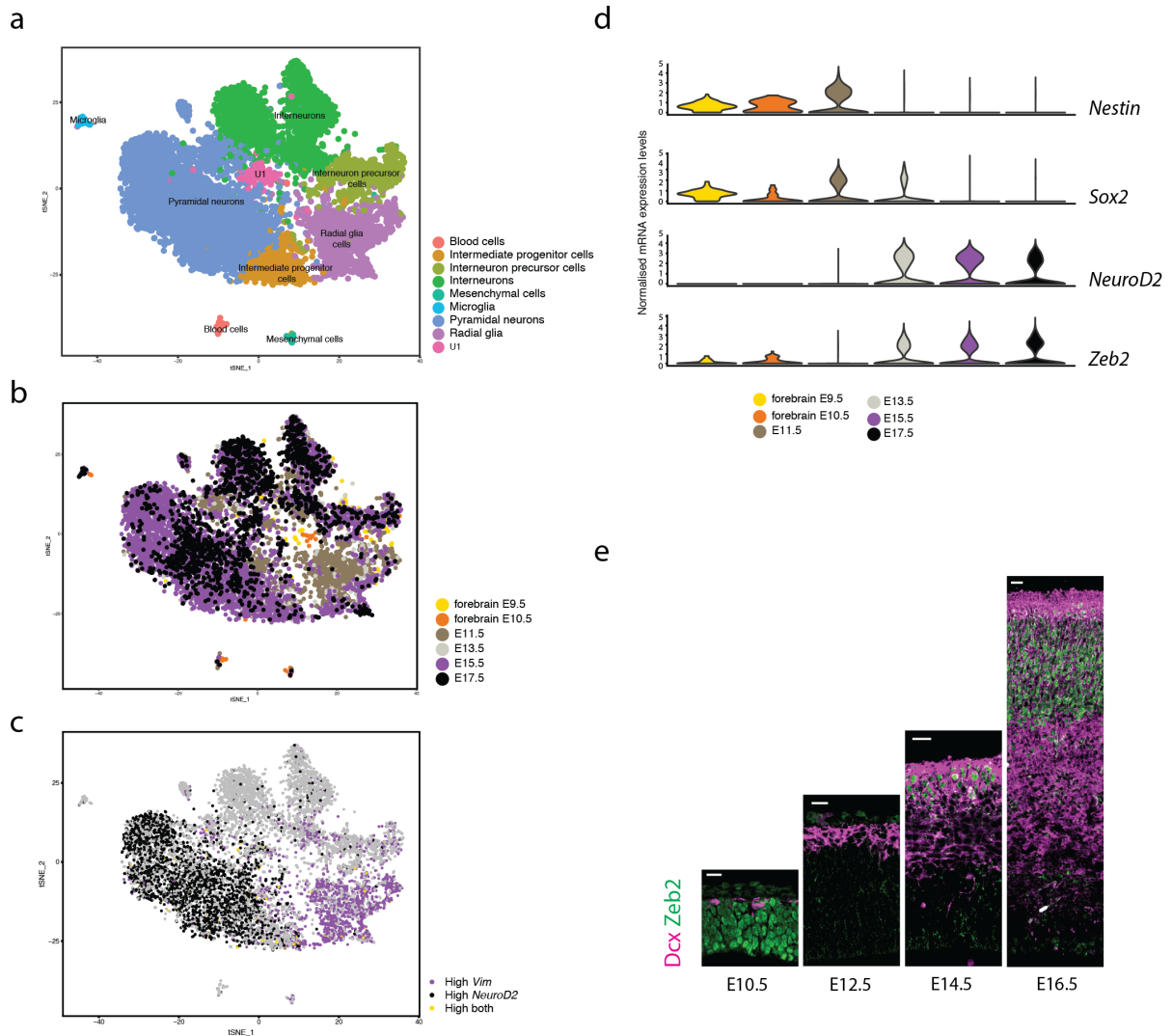


Figure 16 scRNA-seq and immunofluorescence analyses confirm a switch in *Zeb2* expression from NECs to postmitotic neurons in the mouse dorsal telencephalon.

a, t-SNE plot of integrated cell clusters identified in mouse telencephalon and cortex samples by the Seurat computational pipeline at E9.5, E10.5, E11.5, E13.5, E15.5 and E17.5. Shown here are the cell clusters identified, corresponding to: radial glia cells, interneuron precursor cells, intermediate progenitor cells, pyramidal neurons, interneurons, microglia, blood cells, mesenchymal cells and a cluster U of unidentified identity. b, t-SNE feature plot of cell distribution across cell clusters colour-coded by developmental time-point as: E9.5 telencephalon, E10.5 telencephalon, E11.5, E13.5, E15.5 and E17.5 cortices, revealing a developmental trajectory from progenitors to neurons from earlier to later samples. c, t-SNE feature plot of overlaid *Vimentin* and *NeuroD2* mRNA expression colour-coded according to normalised expression value per cell, grey (no expression) purple (high *Vim*), black (high *NeuroD2*), and yellow (high both).

black (high *NeuroD2*), or gold (high *Vim* and *NeuroD2* coexpression). d, Violin plots showing the expression probability distributions for *Nestin* (NPC), *Sox2* (NPC), *NeuroD2* (Pyramidal neurons) and *Zeb2* normalised mRNA expression across developmental time points colour-coded as in b. e, Immunofluorescence analysis of C57BL/6 mouse E10.5, 12.5, 14.5 and 16.5 dorsal telencephalon cryosections stained for Zeb2 C-t (TA319793, green) and the immature migrating neuron marker doublecortin (Dcx, magenta) reveals that after the NEC-aRGC switch, which in mouse occurs between E10.5-11.5, *ZEB2* is no longer expressed in progenitor cells but in postmitotic neurons of the cortical plate primarily, and to a lesser extent in neurons of the subplate. Scale bars, 20 μ m (c). Max Kellner analyzed the scRNA-seq data on embryonic mouse brain and produced figures a-d.

Generation of *ZEB2* mutant hESCs for interrogation of *ZEB2* function and modelling Mowat-Wilson syndrome in cerebral organoids

Having characterised the expression dynamics of *ZEB2* in organoids and having confirmed that they resembled those of the developing mouse cortex we set out to study *ZEB2* function in human cerebral organoids. Interestingly, whilst *Zeb2*^{+/-} mice do not show any obvious phenotypic abnormality, heterozygous loss-of-function mutation in humans causes a number of neurodevelopmental defects, including agenesis of the corpus callosum, intellectual disability, interneuron migration defects and microcephaly. Due to the hard-to-transfect nature of neural progenitor cells, the complex 3D organisation of organoids and the extended duration of the protocol, transient RNAi methodologies are not suited for the study of gene function in this model. Therefore, we decided to establish stable H9 hESC-knockout lines by CRISPR-Cas9 genome editing.

In order to reduce the risk of off-target effects we took a double-nickase strategy, where Cas9 D10A was targeted to the first coding exon of *ZEB2* (i.e. exon II) by two guide RNAs (gRNAs) (Fig. 17a). Quantification of genome editing events relied on a TaqMan probe-based drop-off assay, in which the edited genomic region was PCR amplified to give a ~200 bp amplicon. The assay comprised two probes; one HEX-labelled drop-off probe designed to bind to the site targeted by Cas9 and a FAM-reference probe designed to bind indiscriminately to all amplicons, thus acting as a counter (Fig. 17a). In an unedited negative control sample, both the drop-off probe and the reference probe would bind to all amplicons and the ddPCR 2D-plot displayed only two populations of droplets, empty droplets and double positives (Fig. 17b). By contrast, in a positive control sample, a third FAM-only positive population in the top-left quadrant of the plot could be seen (Fig. 17b). Through iterative rounds of pooled-selection, termed sib-selection (Miyaoka et al. 2014), and single-cell cloning we were able to isolate multiple samples showing single positive ddPCR droplets (Fig. 17b). We then performed PCR analysis to detect shifts in the size of the amplicons and sequencing by CloneJET cloning (Fig. 17c and d). Although we could not obtain *ZEB2*^{-/-} cells, we were successful in retrieving two *ZEB2*^{+/-} lines harbouring a 13 bp and a 23 bp deletion, respectively. Interestingly, only very few samples showed biallelic *ZEB2* mutations and all of them invariably harboured an out-of-frame deletion and an in-frame deletion, resulting in the loss of only a few amino acids (Fig. 17e). This might suggest a requirement for *ZEB2* function for hESC viability, and in fact, albeit very low *ZEB2* protein was detectable in hESC samples.

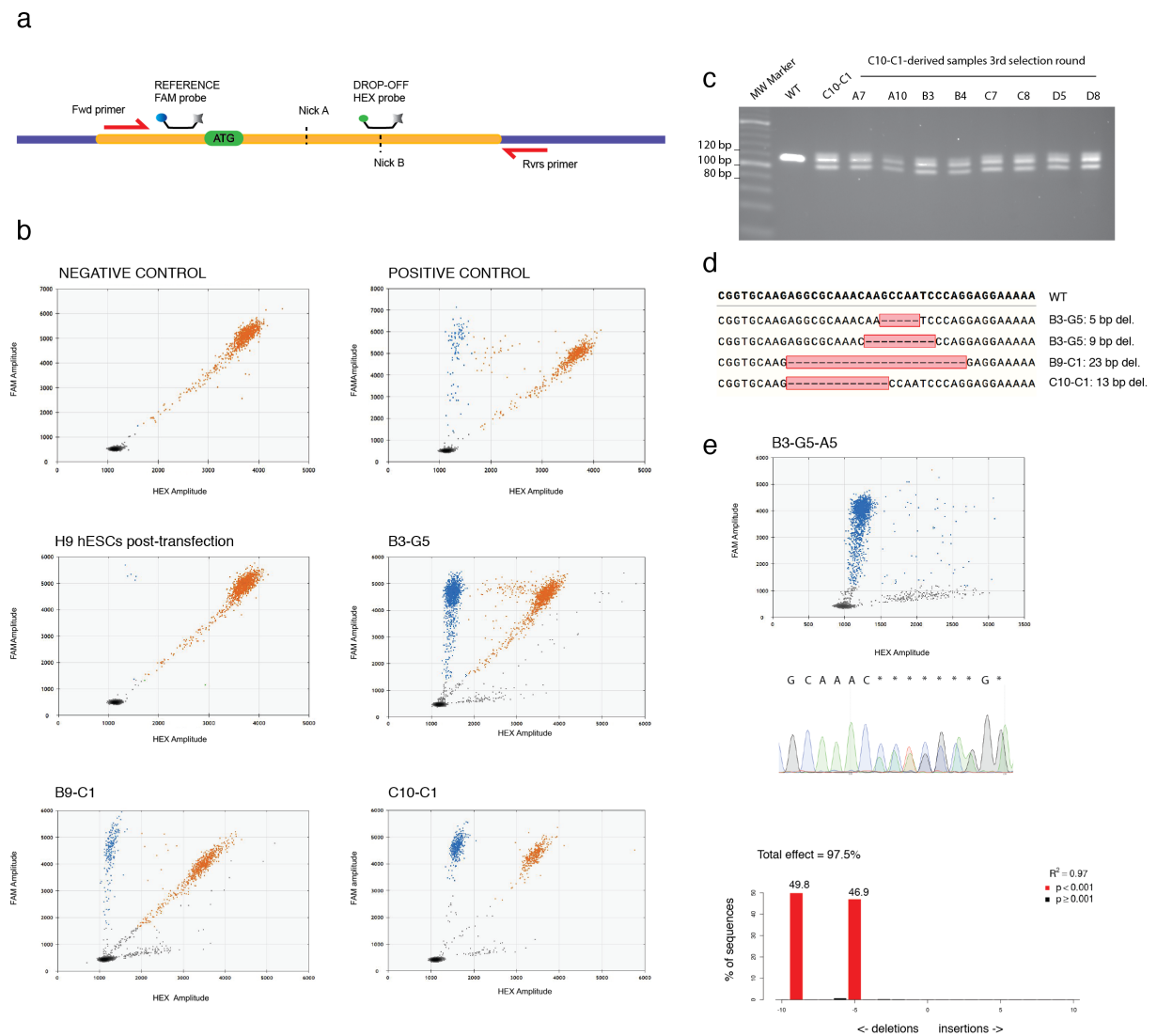


Figure 17 CRISPR-Cas9n targeting of *ZEB2* generates two heterozygous loss-of-function mutants and compound heterozygotes with one in-frame deletion.

a, Schematic representation of the CRISPR-Cas9n editing strategy, where the first coding exon of the *ZEB2* gene was targeted by two nickases (dashed lines) and screening was done by assaying the drop-off frequency of a HEX-labelled probe, binding to one of the nick sites, relative to a FAM-labelled reference probe binding away from the disrupted region. b, Example ddPCR 2D scatter-plots of a negative control sample (WT 293T cells), showing only a FAM-HEX double positive (red) and an empty droplet cluster (black) (top-left plot) and a positive control sample (293T cells expressing WT Cas9 and *ZEB2* guides), showing a FAM-only cluster (blue) in the upper-left quadrant of the 2D plot corresponding to edited alleles (top-right plot). Middle left is a 2D plot of H9 hESC cells 48h after electroporation with Cas9n and *ZEB2* guides, the frequency of genome editing events was estimated to be approximately 1%. Following two rounds of sib selection at 1000 and 20 c/w density three pools were recovered; B3-G5 (middle-right), B9-C1 (bottom-left) and C10-C1 (bottom-right) with mutant

frequencies of ~51%, ~21% and ~50%, respectively. c, Example analyses showing how a region of 113 bp spanning the genome-edited region was amplified from the C10-C1 pool and 8 different subpools obtained from a third round of sib selection, and resolved on a high-percentage agarose gel. All samples show the WT allele and a 13 bp deletion, indicating the presence of a heterozygous loss-of-function line. d, A region of 198 bp spanning the genome edited sites was amplified from gDNA extracted from the three wells, the PCR product was then cloned into the pJET1.2 vector and for each sample, DNA extracted from 20 colonies was sent for sequencing. Sequencing confirmed the presence of alleles harboring 5, 9, 13 and 23 bp deletions. e, Following a third round of selection several pools derived from B3-G5 showed 100% mutant frequency on a ddPCR 2D plot but mixed chromatogram traces. Sequence trace deconvolution by TIDE confirmed that the isolated lines were compound heterozygotes carrying a 9 and 5 bp deletion allele ($p < 0.001$).

***ZEB2*^{+/-} mutants display a ~50% reduction in *ZEB2* protein, retain pluripotency, are karyotypically normal but show a structural phenotype upon differentiation**

We isolated two *ZEB2*^{+/-} mutant cell lines carrying a 13 bp and a 23 bp deletion as indicated by sequencing. DNA-PAGE analysis of a small amplicon overlapping the edit sites in WT H9 hESCs and the two mutants showed a shift consistent with a 13 bp deletion in *ZEB2*^{+/-} #1 and 23 bp *ZEB2*^{+/-} #2, thus confirming sequencing results (Fig. 18a). We then performed RT-PCR for key pluripotency markers on the edited lines and while a decrease in *ZEB2* RNA levels was evident in the mutants, expression of *SOX2*, *NANOG*, *OCT3/4* and *DPPA5* was unaffected (Fig. 18b). Western blot analysis confirmed a ~50% decrease in *ZEB2* protein in the two mutant hESC lines compared to WT (Fig. 18c). Cytological analysis of *ZEB2*^{+/-} mutant karyotypes did not reveal any gross genetic abnormality (Fig. 18d). These data suggested that the *ZEB2* mutant lines were healthy and suitable for the study of *ZEB2* function in neural organoids. We thus generated organoids from WT and mutant hESCs and already at day 17, it was possible to see differences in the translucence of the neuroepithelial buds by brightfield microscopy. While WT buds had fuzzy edges caused by abventricular accumulation of neurons, mutant buds appeared more translucent and smoother (Fig. 18e). Hematoxylin and eosin (H&E) stain of WT and mutant tissue revealed that, while WT buds were thick with clear cell pseudostratification, mutant buds had the tendency to be thinner with densely packed nuclei, giving the tissue an overall darker appearance (Fig. 18e).

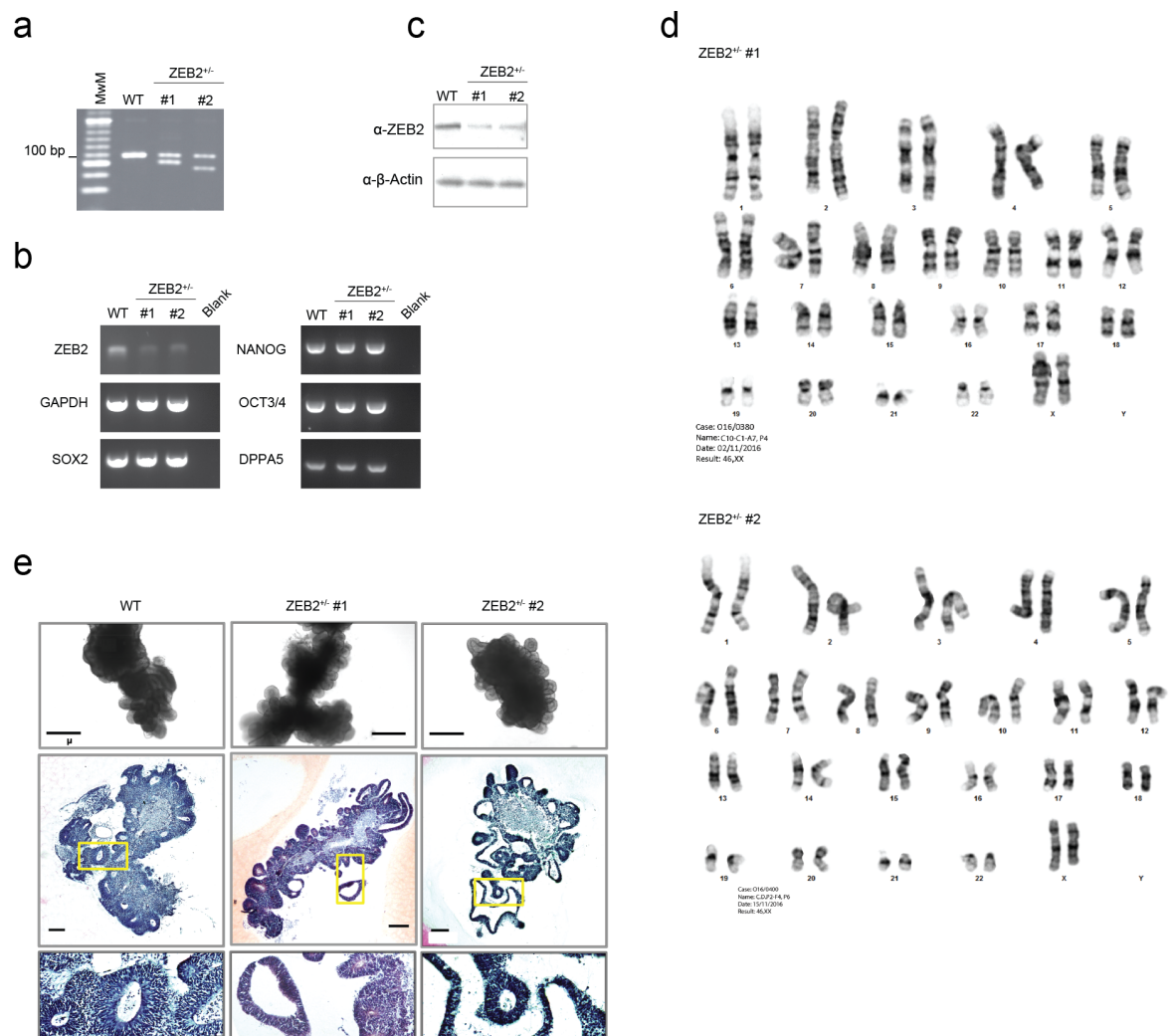


Figure 18 *ZEB2*^{+/-} H9 hESCs show an approximately 50% reduction in *ZEB2* mRNA and protein, retain pluripotency and normal karyotype but present a structural phenotype upon cerebral organoid differentiation.

a, DNA-PAGE analysis of a 123 bp amplicon overlapping the nick sites from WT H9 hESCs and the mutant cell lines *ZEB2*^{+/-} #1 & #2, carrying a 13 and 23 bp deletion, respectively, as shown by sequencing analysis following pJET1.2 cloning. By DNA-PAGE the two mutants show a band consistent with the WT allele and lower molecular weight bands corresponding to a 13 and 23 bp deletion. b, RT-PCR analysis for expression of *ZEB2*, the key pluripotency markers *SOX2*, *NANOG*, *OCT3/4* and *DPPA5* and the loading control *GAPDH*, revealing that upon a ~50% reduction in *ZEB2* mRNA levels the mutant stem cells retain expression of pluripotency markers at comparable levels to WT H9 hESCs. c, Western blot for expression of *ZEB2* and the loading control β -Actin reveals a ~50% reduction in *ZEB2* protein levels in *ZEB2*^{+/-} #1 & #2 cells compared WT H9 hESCs control. d, Representative images of karyotype analysis on 20 G-banded metaphase spreads from the *ZEB2*^{+/-} #1 (top) & #2 (bottom) culture samples used to generate the stock, revealing normal karyotypes in *ZEB2* heterozygous loss-of-function cells. e, Top-panel shows brightfield images of day 17 organoids

derived from WT H9 hESCs and mutant lines $ZEB2^{+/-}$ #1 & #2. Whilst WT organoids appear dark with fuzzy edges, as a consequence of the production of neurons, IPCs and other cells with mesenchymal character, $ZEB2^{+/-}$ organoids present more elongated and translucent buds. Middle-panel are overview H&E images of day 22 WT H9-derived organoids and day 23 $ZEB2^{+/-}$ #1 & #2 organoids showing that mutants have increased abundance of elongated buds with tightly packed nuclei, as indicated by the intense hematoxylin staining. Yellow boxes are regions shown at higher magnification in the bottom panel illustrating how the typical pseudostratified architecture of the WT is different in the mutants, which present thinner and more elongated buds. The higher magnification inset for $ZEB2^{+/-}$ #1 is rotated by 90° relative to the overview image. Scale bars, 500 μ m (e top panel), 200 μ m (e middle panel). Data shown in e for $ZEB2^{+/-}$ #1 are representative of one experiment while data for WT and $ZEB2^{+/-}$ #2 are representative of three independent experiments.

***ZEB2* heterozygous loss-of-function mutation leads to increased cell adhesion in the neuroepithelium**

Since *ZEB2* is a well-established regulator of cell-cell contacts and EMT in various cellular models, we decided to test if the observed differences in neuroepithelial architecture of *ZEB2*^{+/-} mutant organoids were accompanied by changes in the cell adhesion properties of the tissue. Having observed that the two mutants produced comparable phenotypes, in depth analyses were done on *ZEB2*^{+/-} #2. Western blot at day 21 showed that mutant organoids display increased levels of E-cadherin and Occludin and reduced levels of N-cadherin compared to WT (Fig. 19a). Blotting for EMX1 confirmed that the observed changes in cell adhesion properties involved cortical tissue and were not the result of differentiation along a different lineage (Fig. 19a). In support of this, immunofluorescence stain of day 21 WT and mutant organoids showed that while in WT buds N-cadherin was predominant and E-cadherin was virtually undetectable, in mutant buds N- and E-cadherin could be seen coexpressed (Fig. 19b). Similarly, mutant buds displayed higher levels of Occludin that spread further along the cell-cell junctions (Fig. 19c). Preliminary RT-ddPCR expression analysis of key cell adhesion and neural genes revealed that during normal organoid development a sharp surge in *ZEB2* mRNA levels at day 6 correlates with increased expression of neural genes such as *N-cadherin* and *HES1* (Fig. 19d). By contrast, *E-cadherin* mRNA levels showed the opposite trend and progressively declined from the hESC stage to day 21 organoids (Fig. 19d). Interestingly, *Occludin* levels did not decrease as steeply as *E-cadherin*, and after the surge in *ZEB2* levels, *Occludin* transcripts were steadily downregulated (Fig. 19d).

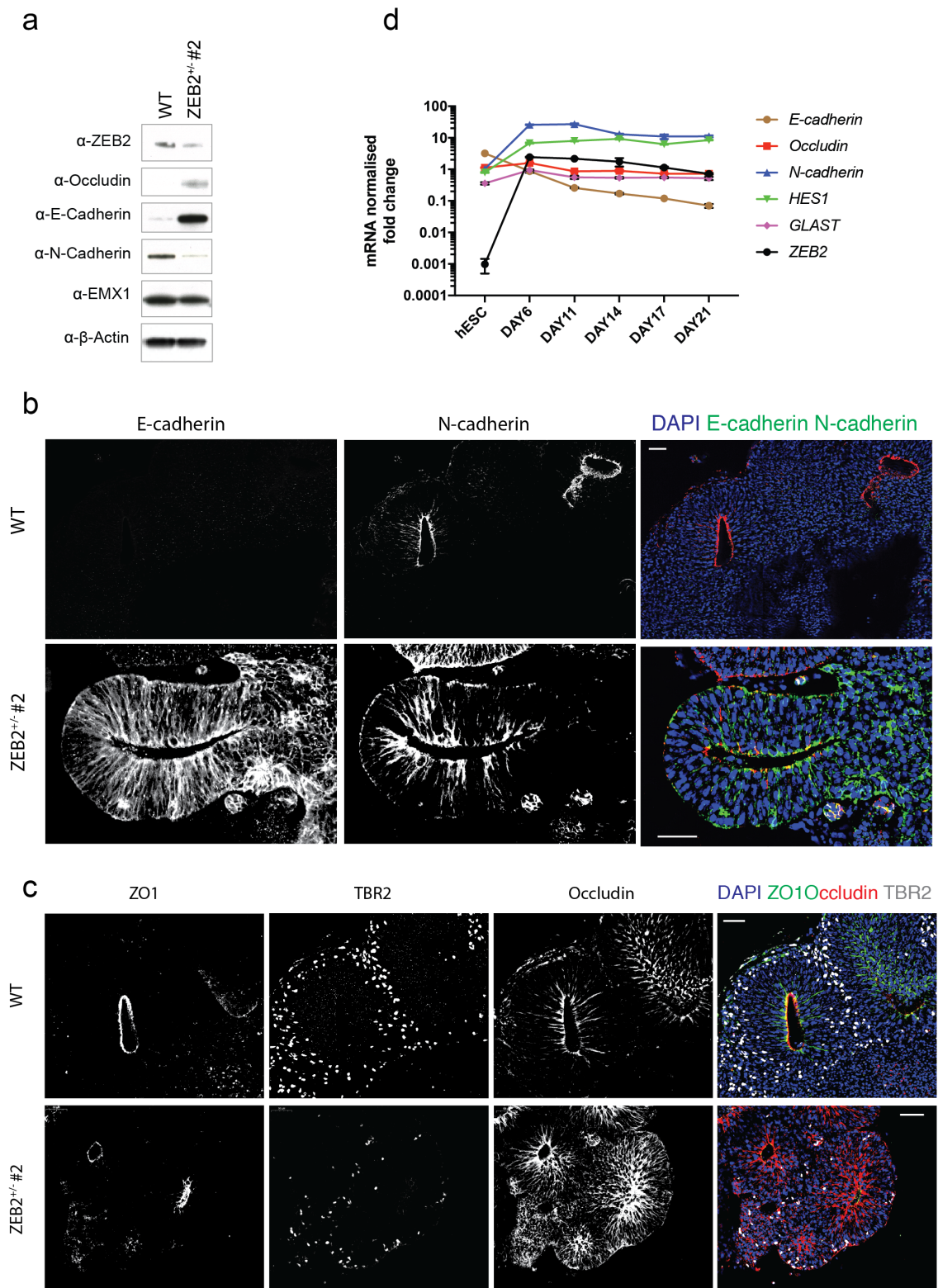


Figure 19 *ZEB2* heterozygous loss-of-function mutation leads to changes in the cell adhesion properties of the neuroepithelium.

a, Western blot analysis of H9 WT and *ZEB2*^{+/-} #2 hESC-derived organoids at day 21 for ZEB2, the tight-junction protein Occludin, the adherens junction components E- and N-cadherin, the dorsal telencephalic marker EMX1 and the loading control β -Actin. The blots show a sizeable increase in E-

cadherin and Occludin and a decrease in N-cadherin whilst EMX1 levels, and thus dorsal telencephalic identity appears to be largely unaffected. b, Representative immunofluorescence image of H9 WT and ZEB2^{+/-} #2 hESC-derived organoids at day 21 stained for neural cadherin (N-cadherin) and epithelial cadherin (E-cadherin) showing that ZEB2^{+/-} #2 mutant neuroepithelial buds co-express E-cadherin and N-cadherin and thus display increased epithelial character compared to WT buds. c, Representative immunofluorescence image of H9 WT and ZEB2^{+/-} #2 hESC-derived organoids at day 21 stained for the IPC marker TBR2 and the tight-junction components Occludin and ZO1 showing that in ZEB2^{+/-} #2 mutant neuroepithelial buds Occludin extends further along the edges of the neural progenitors compared to WT and fewer TBR2⁺ IPCs are observed than in the control. d, RT-ddPCR expression analyses of key cell adhesion (*E-cadherin*, *Occludin*, *N-cadherin*), neural (*HES1*) and glial (*GLAST*) genes in WT hESCs and day 6, 11, 14, 17 and 21 EBs in relation to *ZEB2* mRNA levels. Analyses reveal that mirroring the initial surge in *ZEB2* expression *N-cadherin* and *HES1* mRNA levels rise, while *Occludin* and *E-cadherin* mRNA levels steadily decline. *GLAST* transcript levels do not show any notable change. Shown are mean \pm s.e.m. values of normalised mRNA fold change for each gene relative to the internal control amplicon *EIF2B2* on three technical repeats of the experiment. Data shown in a, b and c are representative of three independent experiments, the experiment shown in d was performed once. Scale bars, 50 μ m (b and c).

***ZEB2*^{+/-} organoids display elongated *EMX1*⁺/*TBR2*⁺ neuroepithelial buds and reduced numbers of *TBR2*⁺ intermediate progenitors**

Next, we quantified the degree of ventricular expansion seen in *ZEB2*^{+/-} organoids. To ensure that quantifications were performed on neuroepithelial buds with pallial identity, images for analysis were acquired on *EMX1*⁺ buds containing some *TBR2*⁺ cells. This was important as we noticed that, although the vast majority of the *ZEB2*^{+/-} mutant tissue was positive for *EMX1*, many buds did not resemble cortical tissue histologically, but more medial identities such as hem and choroid plexus primordium (data not shown). Quantifications revealed a slight but significant increase in ventricle length in *ZEB2*^{+/-} organoids compared to WT (Fig. 20a & b). We then decided to test whether this increase in lateral expansion was accompanied by a decrease in neurogenesis. Because mammalian neurogenesis is by and large indirect and *TBR2*⁺ intermediate progenitors are the first cell type produced after the switch from NECs to aRGs (Cárdenas et al. 2018), we quantified the numbers of *TBR2*⁺ IPCs in WT and mutant organoids (Fig. 20a & c). Our data showed a significant decrease in the number of *TBR2*⁺ IPCs in *ZEB2*^{+/-} organoids compared to WT (Fig. 20a & c).

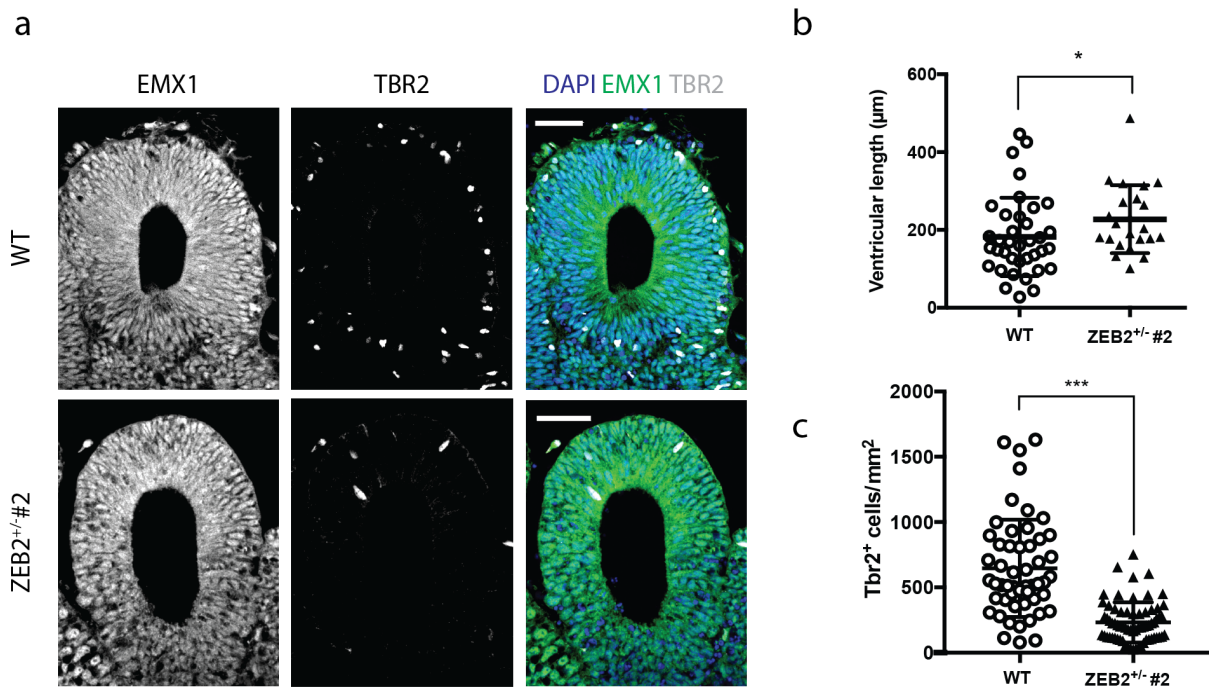


Figure 20 *ZEB2*^{+/-} organoids display elongated buds and reduced numbers of *TBR2*⁺ IPCs.

a, Representative immunofluorescence images of day 20 WT and *ZEB2*^{+/-} organoids stained for the dorsal telencephalic marker *EMX1* (green) and the IPC marker *TBR2* (grey). Left are single channel images for *EMX1* and *TBR2*, right are composite images of DAPI (blue), *EMX1* (green) and *TBR2* (grey). The images reveal a decrease in *TBR2*⁺ IPCs with a concomitant increase in ventricle length in *ZEB2*^{+/-} organoids compared to WT. b, Quantifications of ventricle lengths on WT (n=37) and *ZEB2*^{+/-}

#2 (n=23) neuroepithelial buds positive for both EMX1 and TBR2. The organoids used for analyses were from two independent batches. *P=0.0217, Mann-Whitney test. Reported are mean \pm s.d. values. c, Quantifications of TBR2⁺ IPC numbers in WT (n=52) and ZEB2^{+/-} #2 (n=68) neuroepithelial buds. The organoids used for analyses were from two independent batches. ***P<0.0001, Mann-Whitney test. Reported are mean \pm s.d. values. Scale bars, 50 μ m (a).

Evidence suggests that FGF2 and ZEB2 may form a negative feedback loop

Having observed an increase in ventricle length in *ZEB2*^{+/-} organoids we performed a literature search for ZEB2 transcriptional targets with a potential role in progenitor proliferation. Previous work had shown that ZEB2 regulates transcription of FGF9 in postmitotic neurons and mediates a non cell-autonomous feedback loop from neurons to progenitors, which controls the balance between superficial- and deep-layer neurons (Seuntjens et al. 2009). We therefore reasoned that the FGF family of secreted growth factors would be an obvious set of potential targets to start to analyse, and we proceeded to examine three ZEB2 ChIP-seq datasets available on ENCODE. Two of the datasets were technical repeats of ChIP for endogenous ZEB2 in the immortalised myelogenous leukemia cell line K562, and the third dataset was ChIP for GFP in HEK293 cells where the endogenous *ZEB2* locus was GFP-tagged by site-specific recombination.

Analysis revealed the presence of distinct and highly enriched ChIP-seq peaks in the near vicinity of the FGF2 locus (Fig. 21a). Many of the peaks overlapped or were in the immediate vicinity of H3K27Ac marks, often found near transcriptional regulatory elements (Fig. 21a). Although the two different cell lines showed ChIP peaks at different sites around the FGF2 locus, the GeneHancer Regulatory Elements and Gene Interaction track revealed that all putative regulatory elements had interactions converging on the FGF2 promoter (Fig. 21a). FGF2 is a well-established regulator of neural progenitor proliferation (Vaccarino et al. 1999; Raballo et al. 2000) and so we decided to test whether *ZEB2*^{+/-} organoids displayed altered levels of FGF2 compared to WT. Immunoblot for FGF2 revealed that mutant organoids have higher FGF2 levels compared to control (Fig. 21b).

Recently it was reported that FGF2 regulates transcription of EMT genes in human *ex vivo* corneal endothelium, and *ZEB2* was among its targets (Lee et al. 2018). This raised the possibility that FGF2 and ZEB2 might establish a negative feedback loop where FGF2 positively regulates ZEB2, which in turn suppresses FGF2 expression. We thus tested whether treatment with FGF2 was sufficient to induce ZEB2. The experiment was performed in the glioblastoma line U87MG as it models neural progenitor cells with higher fidelity than other immortalised cell lines. Cells were treated with increasing concentrations of FGF2, which led to a concentration-dependent increase in ERK phosphorylation, demonstrating that the FGF cascade was activated (Fig. 21c). Concomitantly, an FGF2 concentration dependent increase in ZEB2 levels was observed (Fig 21c). To test whether this was accompanied by a decrease in endogenous *FGF2* transcription we performed RT-ddPCR on samples treated in the same way. However, treatment failed to show any noticeable effect on *FGF2* transcript levels (Fig. 21c). A possible explanation for this is that the cells were not treated for long enough to detect a transcriptional effect on *FGF2*.

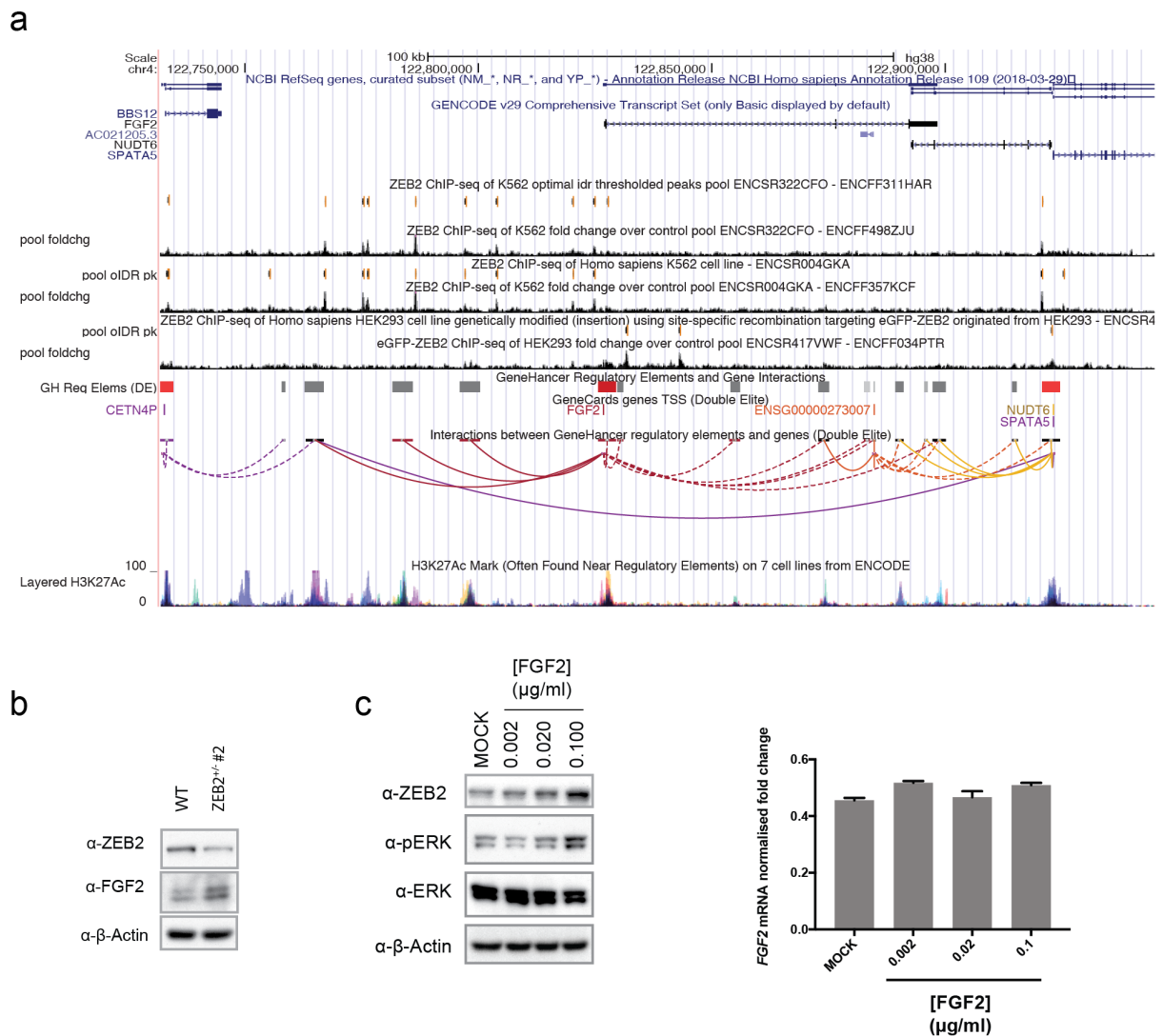


Figure 21 FGF2 and ZEB2 show reciprocal regulation.

a, University of California, Santa Cruz (UCSC) Genome Browser tracks showing the *FGF2* (NM_001361665) locus (Chr 4: 122,826,708-122,898,236 in GRCh38) and neighbouring genes according to RefSeq gene predictions from NCBI. The GENCODE v29 Comprehensive Transcript Set track reports the transcript variants with corresponding PDB entries. Displayed are two ZEB2 ChIP-seq experiments in K562 cells and one GFP-ZEB2 ChIP-seq experiment in HEK293 cells, the tracks show fold change over control. The ENCODE accession codes of the ChIP-seq datasets are listed in the methods. The GeneHancer Regulatory Elements and Gene Interactions track displays human regulatory elements (enhancers and promoters) and their target genes inferred from integrating regulatory elements from multiple genome-wide databases. Red indicates promoters, grey enhancers and increasing colour brightness indicates higher element confidence score. The Layered H3K27Ac track reports the levels of enrichment of the H3K27Ac histone mark across the genome of seven cell lines available on ENCODE as determined by a ChIP-seq assay. ZEB2 ChIP-seq data reveal a number of putative DNA binding sites overlapping active regions of chromatin in the vicinity of the *FGF2* locus, suggesting that ZEB2 might transcriptionally target *FGF2*. b, Western blot of H9 WT and

ZEB2 #2 hESC-derived day 21 organoids reveal that partial loss of ZEB2 leads to an increase in FGF2 protein levels. c, On the left is a western blot of U87MG glioblastoma cells treated for four days with different concentrations of FGF2, probing against the MAP-kinase ERK and its phosphorylated active form p-ERK, ZEB2 and β -Actin. The western blot shows that upon activation of the FGF signalling cascade, indicated by increased levels of p-ERK, ZEB2 protein levels increase in an FGF2 concentration-dependent fashion. On the right, RT-ddPCR analysis of *FGF2* mRNA levels in U87MG cells treated in the same way fail to show a noticeable change in *FGF2* transcripts. Shown are mean \pm s.e.m. values of normalised *FGF2* mRNA fold change relative to the internal control amplicon *EIF2B2* on three technical repeats of the experiment. Data shown in a is a preliminary finding from analysis of one experiment, the western blot results shown in c are consistent with two independent experiments on two different cell lines, while RT-ddPCR was performed only once.

Preliminary gain-of-function experiments support a neurogenic role of ZEB2

Our loss-of-function data up to this point suggested that ZEB2 is involved in neuroectodermal induction and in driving the changes in progenitor cell adhesion that occur before the switch from expanding NECs to neurogenic aRGCs. To validate these findings we decided to perform the converse experiment and overexpress *ZEB2* specifically in NECs. Technically this experiment presented a number of challenges. Whilst at late stages of the protocols constructs can be delivered to organoids by injection and electroporation into ventricles, at the EB stage this is not possible due to the small size of ventricles and the fragility of the neuroepithelial buds. An additional challenge was posed by the MG embedding step at day 11 of the protocol, which formed a virtually impenetrable shell around the organoid. We thus decided to establish an inducible *ZEB2* overexpression line that would allow for transgene induction by simple addition of a compound to the culture media. We decided to use a Cumate (CuO)-inducible PiggyBac transposon system as the construct was readily available and all steps to generate the line could be performed in a standard CL1 tissue culture lab. The *ZEB2* open reading frame (ORF) was cloned downstream of a CuO responsive element, which in its basal state is kept inactive by the expression of a repressor driven by the EIF1 α promoter (Fig. 22a). CuO binding to the repressor element triggers a conformational change that makes it inactive, driving expression of the transgene (Fig. 22a). An additional advantage of an inducible overexpression system is that it allows us to test the effect of changes in *ZEB2* expression timing and levels on the switch from NECs to aRGCs.

Following transfection of H9 hESCs with the *ZEB2* CuO inducible and empty vector (EV) constructs we applied Puromycin selection and recovered single clonal lines by colony picking. Colonies were screened for construct integration by duplex PCR on gDNA for the Puromycin cassette (i.e. Puro) and the *RPP30* gene (Fig. 22b). *RPP30* is a gene commonly used for copy number variation analyses (Mazaika & Homsy 2014) and was used as an internal control to examine the relative abundance of integration events across the different clones. The *Puromycin* and *RPP30* cassettes were specific, as shown by PCR on H9 WT cells and on the plasmid (Fig. 22b). All colonies that survived selection harboured the transposon but, whilst colonies *ZEB2* CuO #1 and EV CuO #1 showed high levels of integration, all other colonies had lower integration levels (Fig. 22b). This was particularly favourable as having several colonies with different numbers of integration events would give us more control over the *ZEB2* induction potential and would offer alternatives in case the construct became silenced in one particular line.

The next step we took was to test the *ZEB2* induction potential in one of the lines. Beginning from day 11 of the protocol organoids were induced with two concentrations of Cumate and a week later samples were collected for western blot and histological analysis. Western blot showed that addition of increasing concentrations of Cumate led to higher *ZEB2* induction (Fig. 22c). This increase in

ZEB2 levels was paralleled by a decrease in E-cadherin and a robust increase in N-cadherin (Fig. 22c). Immunofluorescence stainings revealed that with increasing levels of ZEB2, the size of the neuroepithelial buds shrunk and large clusters of TUBB3⁺ neurons accumulated at the periphery of the tissue, away from the main mass of the organoid (Fig. 22d). These changes in neuroepithelial architecture were accompanied by changes in Occludin distribution. In untreated (UT) organoids Occludin was seen distributed along sides of the neural progenitor cell bodies, spanning almost the entire width of the developing neuroepithelium (Fig. 22d). By contrast, increased ZEB2 levels led to a loss of Occludin staining from the apical lumens of the buds (Fig. 22d).

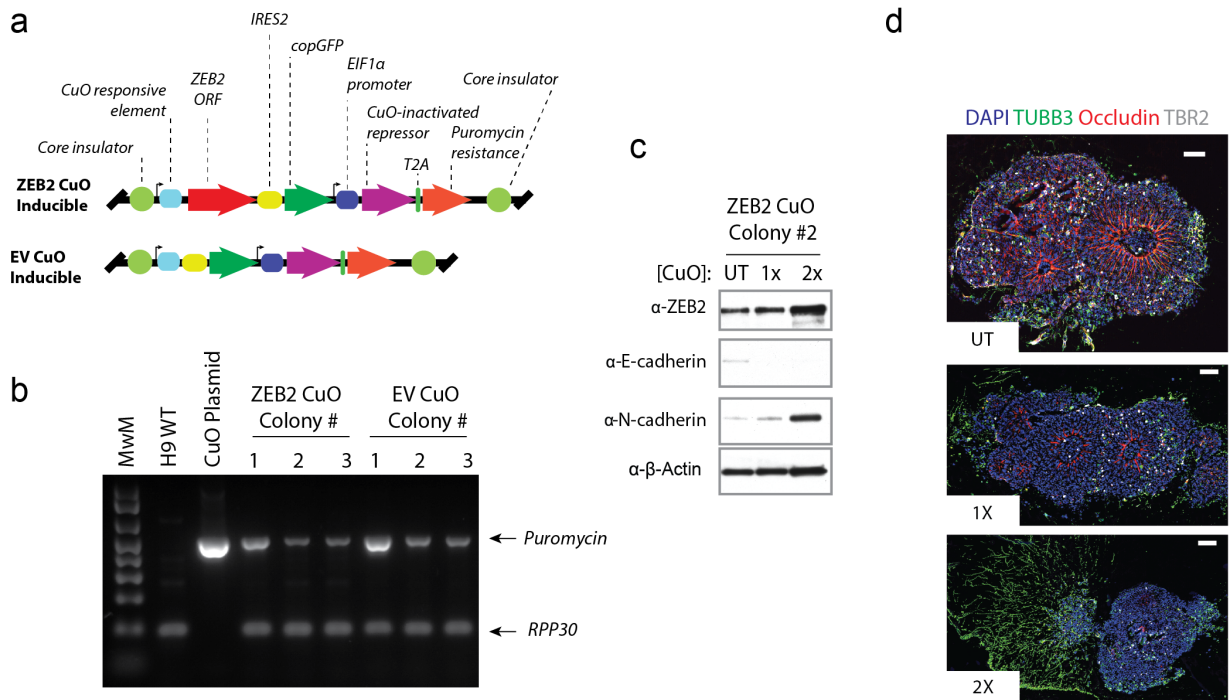


Figure 22 Inducible overexpression of *ZEB2* in early stage organoids appears to drive premature neurogenesis and shrinkage of neuroepithelial buds.

a, Cumate (CuO) inducible cassette maps of the ZEB2 CuO and EV CuO inducible constructs containing core insulator sequences on either side, to reduce the degree of silencing by spread of nearby heterochromatin, the EIF1α promoter driving constitutive expression of the CuO-inactivated repressor and linked to the Puromycin resistance gene by a T2A sequence. The *ZEB2* ORF is under the control of a CuO-responsive element that becomes active upon CuO binding to the repressor element, and is followed by an IRES-copGFP cassette. The EV construct differs from the ZEB2 CuO construct only for the absence of the transgene ORF. b, Duplex PCR screening of Puromycin-resistant hESC colonies transfected with ZEB CuO and EV plasmids showing single bands in the H9 WT gDNA and CuO plasmid controls and two bands, corresponding to the genome-integrated puromycin resistance cassette and the *RPP30* gene in the colonies recovered after selection. Screening reveals

ZEB2 CuO and EV CuO clones carrying different levels of transgene integration events. c, Western blot of a 6-day *ZEB2* transgene test induction in ZEB2 CuO colony #2-derived organoids at day 17. Probing for ZEB2, N- and E-cadherin and β -Actin in untreated (UT), 1X and 2X CuO induced organoids confirms inducibility of the transgene, as shown by the increase in ZEB2 protein levels upon treatment with increasing concentration of CuO. Increased transgene expression leads to a decrease in E-cadherin and an increase in N-cadherin. d, Immunofluorescence analyses of 6-day UT, 1X and 2X CuO-induced ZEB2 CuO colony #2 derived organoids at day 17, from the same experiment as shown in c, revealing that transgene overexpression leads to progressively smaller neuroepithelial buds, with decreasing Occludin staining across the depth of the neuroepithelium and increased TBR2⁺ intermediate progenitor and TUBB3⁺ neuron numbers. The samples were stained with four colours despite the presence of GFP because expression from the IRES2 is so weak that GFP is not detectable unless an antibody is used to augment the signal. Data shown in c and d are preliminary results from an initial test experiment of transgene inducibility. Scale bar, 100 μ m (d).

Dual SMAD inhibition partially rescues the *ZEB2*^{+/-} phenotype

ZEB2 was originally identified in a yeast two-hybrid screen as an interactor of the SMADs. Later work showed that *ZEB2* inhibits TGFβ and BMP signalling both by interacting directly with activated SMADs and through their transcriptional repression (Hegarty et al. 2015). We thus reasoned that *ZEB2* might be involved in TGFβ and BMP signalling inhibition in the developing neuroectoderm. First we performed reporter assays for these two signalling cascades to verify the antagonistic effect of the major *ZEB2* isoform on these pathways. The reporter assay was established in 293T cells and optimisation experiments were performed to determine the optimal concentrations of reporter constructs and growth factors to achieve maximal pathway induction (data not shown). *ZEB2* overexpression in 293T cells produced a significant reduction in BMP reporter activity (Fig. 23a). By contrast, *ZEB2* expression did not have any significant effect on TGFβ reporter activity (Fig. 23a).

After verifying that *ZEB2* negatively regulated BMP signalling we decided to test whether suppression of TGFβ and BMP signalling by dual SMAD inhibition would be sufficient to rescue some of the features of the *ZEB2* heterozygous loss-of-function phenotype. We reasoned in fact that partial loss of *ZEB2* function would lead to hyperactivation of TGFβ and BMP signalling, and thus inhibition of the SMADs might restore physiological levels of signalling. Although the luciferase reporter assay had failed to show an effect of *ZEB2* on the TGFβ branch of the pathway, as a preliminary experiment starting from day 11 we treated organoids for 10 days with both the TGFβ inhibitor SB-431542 and the BMP inhibitor Noggin.

As previously mentioned, by brightfield *ZEB2*^{+/-} neuroepithelial buds appeared thin, elongated and highly translucent. By contrast, WT neuroepithelial buds were typically thicker and less translucent (Fig. 23b). By brightfield, treated WT organoids appeared darker than control and with a fuzzy outline, suggesting an accumulation of neurons at the periphery of the neuroepithelium (Fig. 23b). Strikingly, dual SMAD inhibition on *ZEB2*^{+/-} organoids produced more rounded and thicker neuroepithelial buds that closely resembled WT structures (Fig. 23b). H&E staining revealed that dual SMAD inhibition on WT organoids accelerated their development, leading to the establishment of a VZ with overlying neurons and IPCs (Fig. 23b). In contrast, control WT organoids were still at the neuroepithelial stage and the tissue comprised of a single layer of pseudostratified neuroepithelium. *ZEB2*^{+/-} organoids displayed elongated neuroepithelial buds with tightly packed nuclei, as illustrated by the prominent eosin stain (Fig. 23b). However, dual SMAD inhibition appeared to restore correct neuroepithelial architecture, normal pseudostratification and cell packing (Fig. 23b).

We then tested if these structural changes were accompanied by changes in the levels of key adhesion molecules E-cadherin and N-cadherin. Western blot showed that while untreated *ZEB2*^{+/-} organoids displayed increased E-cadherin and reduced N-cadherin levels compared to WT, dual

SMAD inhibition was sufficient to restore WT levels of E-cadherin in the mutant background (Fig. 23c). The effect on E-cadherin was particularly striking; however, albeit subtle, dual SMAD treatment might have also produced an increase in N-cadherin in *ZEB2*^{+/-} organoids (Fig. 23c). Preliminary immunofluorescence analyses supported a partial rescue of the *ZEB2*^{+/-} phenotype. While dual SMAD inhibition on WT organoids had a strongly neurogenic effect with production of large numbers of TUBB3⁺ neurons, treatment of *ZEB2*^{+/-} organoids produced smaller neuroepithelial buds with high numbers of TBR2⁺ IPCs (Fig. 23c). These results seem to suggest that during the phase of neuroepithelial expansion, which in human cerebral organoids ranges between day 11 and day 21 of the protocol, one of the roles of ZEB2 is to antagonise TGFβ and BMP signalling to drive neurogenesis.

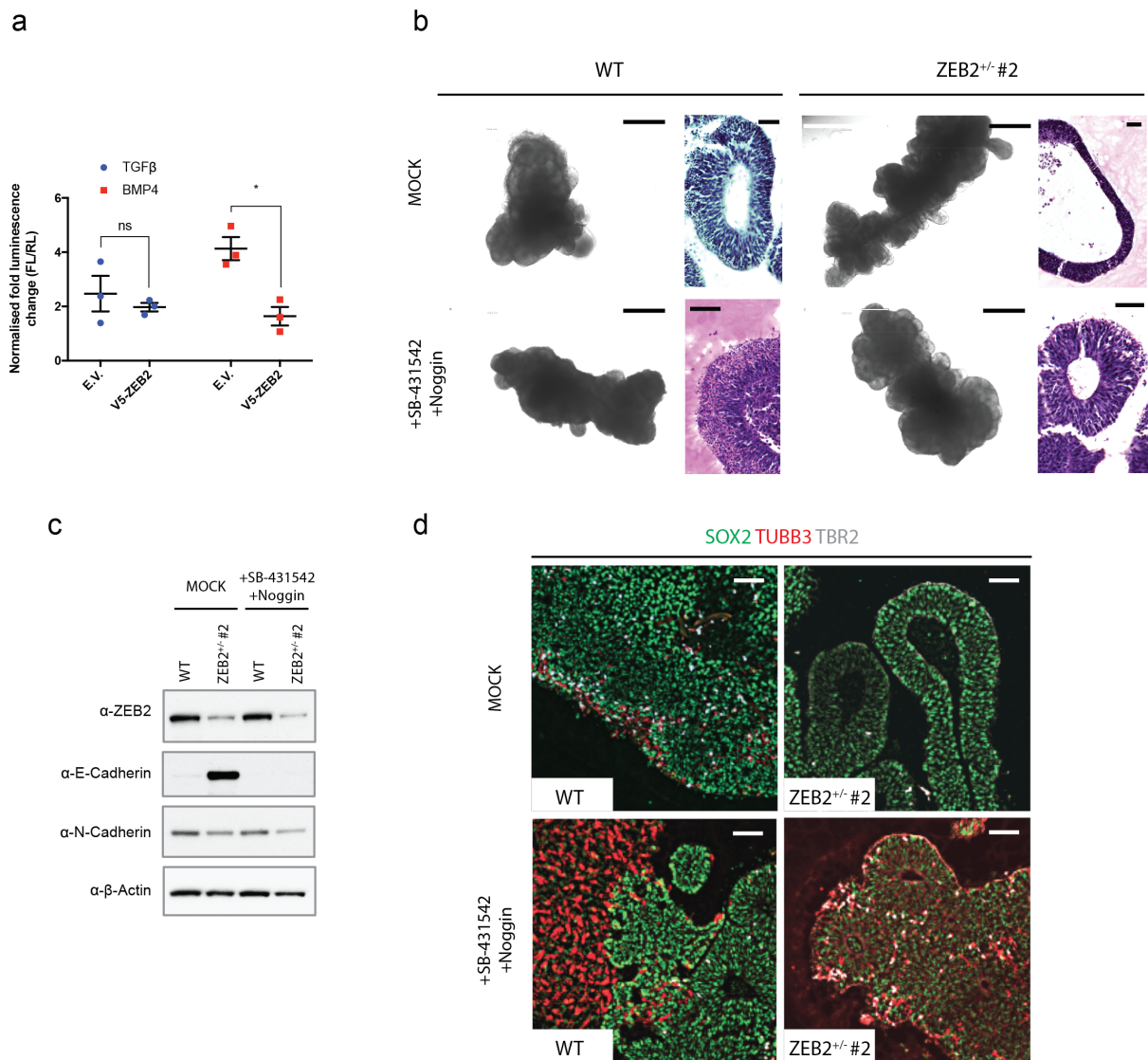


Figure 23 Dual SMAD inhibition appears to restore normal neuroepithelial architecture and neurogenesis in *ZEB2*^{+/-} organoids.

a, Luciferase reporter assay experiment in 293T cells transfected with a *Renilla* control plasmid, a firefly luciferase reporter plasmid for the TGF β or the BMP pathway and either a V5 empty vector construct (EV) or a construct expressing V5 N-terminally tagged ZEB2. The scatter plots report normalised fold change of firefly luminescence relative to *Renilla* luminescence (FL/RL), individual data points are independent experiments and reported are mean \pm s.e.m., *p=0.0114, unpaired t-test with Welch's correction. The experiments reveal that *ZEB2* expression leads to a significant decrease in BMP pathway activation, whilst the same is not seen in the case of the TGF β cascade. b, Brightfield images of day 21 WT and *ZEB2*^{+/-} organoids following 10-day treatment with the BMP pathway inhibitor Noggin and the TGF β pathway inhibitor SB-431542 or mock – juxtaposed are H&E histological stainings on cryosections of neuroepithelial buds from corresponding samples. Dual SMAD inhibitor treatment on WT organoids appears to have a strongly neurogenic effect, whilst on *ZEB2*^{+/-} organoids it appears to restore normal neuroepithelial morphology. c, Immunoblot on day 21 WT and *ZEB2*^{+/-} organoids treated with Noggin and SB-431542 for 10 days – staining for the adherens junction components E- and N-cadherin, ZEB2 and the loading control β -Actin. The western blots reveal that treatment restores WT E-cadherin levels in organoids. d, Immunofluorescence stainings for the pluripotency marker SOX2, the neuronal marker TUBB3 and the intermediate progenitor marker TBR2 on day 21 WT and *ZEB2*^{+/-} organoids following 10-day treatment with Noggin and SB-431542 confirms a strongly neurogenic effect of dual-SMAD inhibition on H9 WT hESC-derived organoids and reveals that treatment partially re-established normal neuroepithelial architecture and neurogenesis in the *ZEB2*^{+/-} background. Data presented in b-d are preliminary results, experiments were performed twice but only one repeat was fully analysed; however, upon preliminary analysis the two experiments gave consistent results. Scale bar, 500 μ m (b brightfield), 50 μ m (b H&E, d). Elizabeth Apsley performed the luciferase reporter experiments presented in a under my supervision.

Chapter 4: Air-Liquid Interface Cerebral Organoids (ALI-COs) display diverse nerve tracts with functional output

Introduction

Cerebral organoids have been shown to capture numerous of aspects of early cerebral cortex development, including histological organization, diverse progenitor types and timed production of neurons with distinct layer identity. More recently, by fusing organoids prepatterned with dorsal and ventral identities, it has been possible to recapitulate interneuron migration from the subpallium (i.e. MGE and LGE) to the pallium and, strikingly, organoids harbouring rod-like photosensitive cells were shown to respond to light and establish networks that can support self-organised activity patterns (Birey et al. 2017; Bagley et al. 2017; Quadrato et al. 2017). Nevertheless, due to shortage of nutrients and oxygen supply, later neuronal maturation is severely compromised, leaving the possibility that work done so far may have underestimated the level of complexity that can be achieved *in vitro*. In an attempt to address the inherent limitations of organoid cultures, transplantation of cerebral organoids into the brain of a rodent host was shown to promote the establishment of a vascular network able to support neuronal maturation and integration of the organoid within the host's neural network (Mansour et al. 2018).

This suggests that by implementing culture conditions able to efficiently sustain all cell types within an organoid it is in principle possible to expand the array of neurodevelopmental processes accessible *in vitro*. This is particularly appealing as transplantation is tedious, requires specialist skills, drastically limits scalability and introduces additional confounding variables to the analyses. Therefore, a modification of the current protocol to improve nutrient supply without reducing throughput would be ideal for more extensive *in vitro* studies. In the context of our work, the establishment of more mature cultures would allow characterisation of *ZEB2* function in axon guidance and CC establishment. We thus set out to establish a novel system to culture late-stage organoids and model aspects of axon pathfinding, bundling and network establishment.

Culture of cerebral organoids at the air-liquid interface (ALI) leads to improved tissue morphology

In an effort to improve neuronal survival and maturation several different media compositions were tested as an alternative to IDM+A (Lancaster et al. 2017) (data not shown); however, alternative media formulations were not sufficient in limiting the expansion of the necrotic core characteristic of mature organoids (i.e. after 80 days in culture). We thus reasoned to improve nutrient and oxygen perfusion by reducing the thickness of the tissue. Organoids between day 45-60 of the protocol were sectioned on a vibratome and grown as slices on interface-culture inserts. In this culture paradigm, the tissue slice rests on an inert and anti-adhesive polytetrafluoroethylene (PTFE) mesh with high transmembrane oxygen diffusion properties, and the bathing medium is delivered from below through capillary action (Fig. 24a).

After optimisation of sectioning settings and media composition we found that ALI conditions allowed for long-term culture of organoid tissue and, overall, air-liquid interface cerebral organoids (ALI-COs) appeared healthier than similarly staged organoids. Whilst whole organoids from ~70-80 days on displayed an expanded central region lacking neuronal processes, the entire surface of ALI-COs stained positive for MAP2⁺ dendrites and SMI312⁺ axons (Fig. 24b). Moreover, correct tissue morphology was retained and ALI-COs typically displayed several lobules with radially aligned neuronal cell bodies in the cortical plate. While in ALI-COs axon- and dendrite-rich regions delimited individual DAPI⁺ lobules (Fig. 24b, white arrows), in whole organoids neuronal processes appeared disorganised and lacking any pattern.

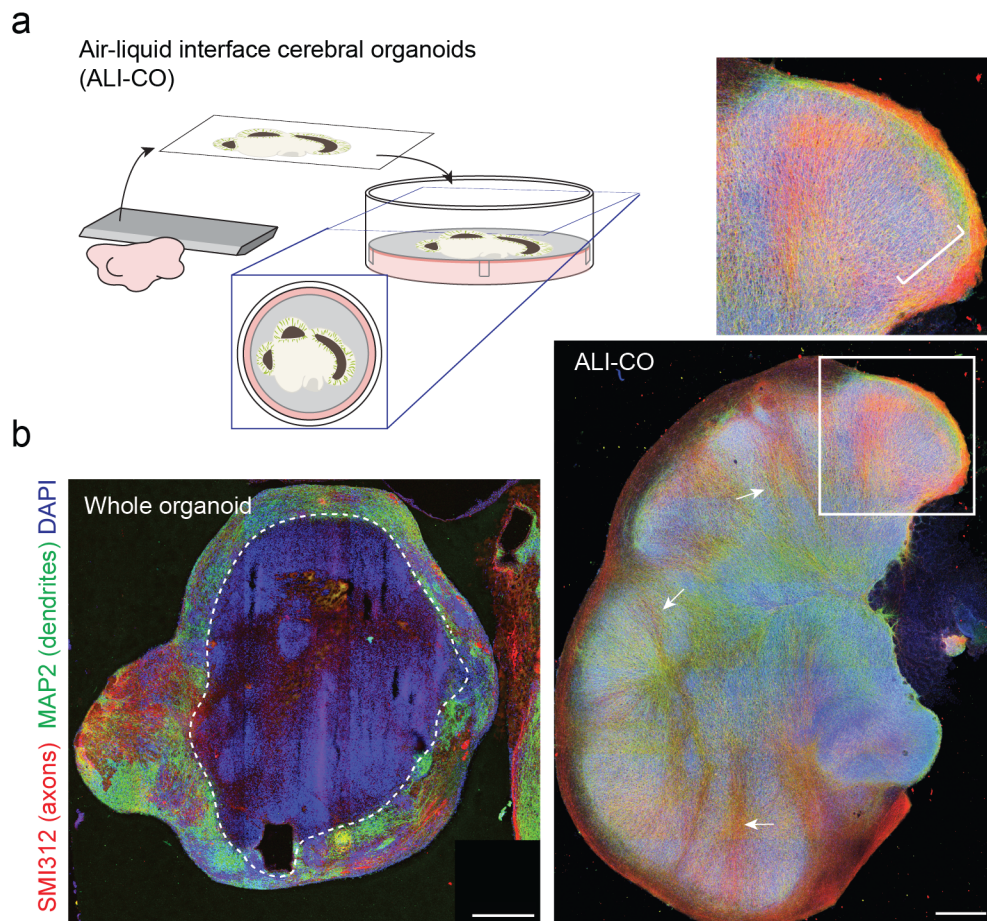


Figure 24 Air-liquid interface culture cerebral organoids (ALI-COs) display improved morphology.

a, Schematic of the air-liquid interface (ALI) culture set-up as detailed in the methods section. b, Immunofluorescence staining for the axon-specific marker SMI312 (red) and the dendritic microtubule marker MAP2 (green), shown are representative images of a 90 day cerebral organoid section and an 82 day old ALI-CO (vibratome sectioned at day 61 and cultured at the ALI for 21 days). Dashed line in the whole organoid image marks the border between healthy tissue and necrotic core. Inset shows a higher magnification image of an ALI-CO lobule with neurons radially aligned in the cortical plate (bracket) and arrows point to SMI312⁺ axon bundles projecting within the organoid slice. Scale bars, 500 μ m (b). Madeline A. Lancaster acquired images in b.

ALI-COs display improved neuronal survival compared to whole organoids

We next tested whether ALI culture improved survival over conventional suspension culture of whole organoids. To this end, we performed TUNEL stain on cryostat sections of whole organoids and ALI-COs and quantified the number of TUNEL⁺/DAPI⁺ cells. TUNEL was selected over cleaved Caspase-3 staining as it more accurately captured the levels of total cell death in the tissue. In fact, cleaved Caspase-3 immunostaining only marks the early stages of apoptosis and does not detect hypoxia-induced necrosis, accidental cell death, late stages of apoptosis or other types of regulated cell death that do not rely on the caspase cascade. Analyses were done on similarly staged organoids and ALI-COs (i.e. 98-105 days) from three and two independent batches, respectively. Slices were selected randomly and in order to eliminate bias quantifications were performed on both internal and external regions of tissue. Overall, whole organoids displayed approximately two-fold higher numbers of TUNEL⁺ cells compared to ALI-COs (n=6, **p=0.0022) (Fig. 25a & b).

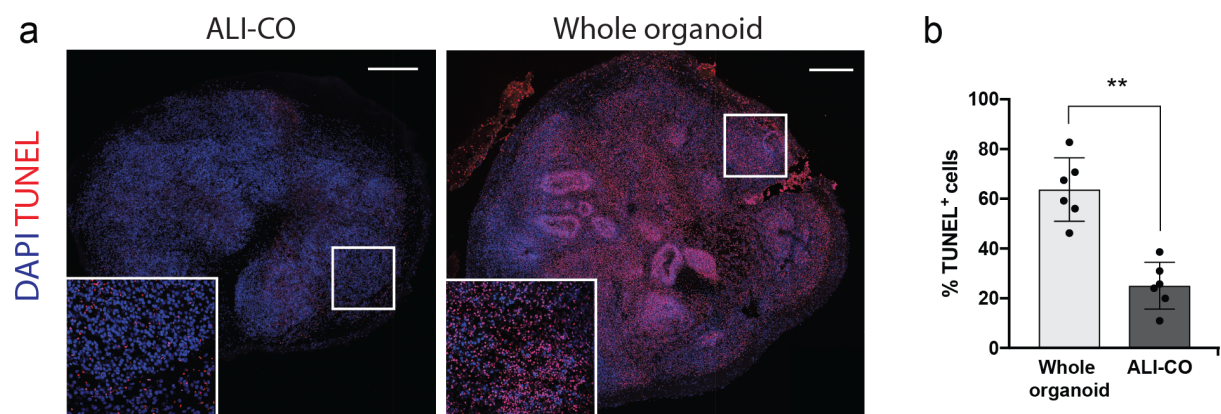


Figure 25 ALI-COs display reduced numbers of TUNEL⁺ cells compared to whole organoids.

a, Representative TUNEL stain (red) of whole organoid and ALI-CO cryosections used for quantifications shown in b revealing more abundant cell death in whole organoids compared to ALI-COs. Inset is a higher magnification image of the boxed regions and shows single TUNEL⁺ cell nuclei.

b, Quantification of TUNEL⁺/DAPI⁺ cells in six whole organoids from three independent batches and six ALI-COs from two independent batches aged 98-105 days total in culture. Culture at the ALI results in a significant decrease in cell death compared to standard whole organoid culture .

**P=0.0022, two-tailed Mann-Whitney test, n=6, shown are mean ± s.d.. Scale bars, 500 μ m (a).

ALI-COs display higher numbers of both deep- and superficial-layer neurons

TUNEL stain results showed that ALI culture improved neuronal survival; however, this effect could be specific to only a certain population of neurons and might not reflect overall survival across different neuronal cell types. Thus, we decided to compare the number of deep- and upper-layer neurons in whole organoids versus ALI-COs. Analyses were performed at the same timepoints as for TUNEL quantifications (i.e. 98-105) days. CTIP2 was used as a marker of deep-layer neurons while CUX2 as a marker of superficial layer neurons. Our results showed that ALI-COs display significantly higher numbers of both deep- (n=6, *p=0.0411) and superficial-layer neurons (n=6, **p=0.0022) compared to organoids (Fig. 26a & b).

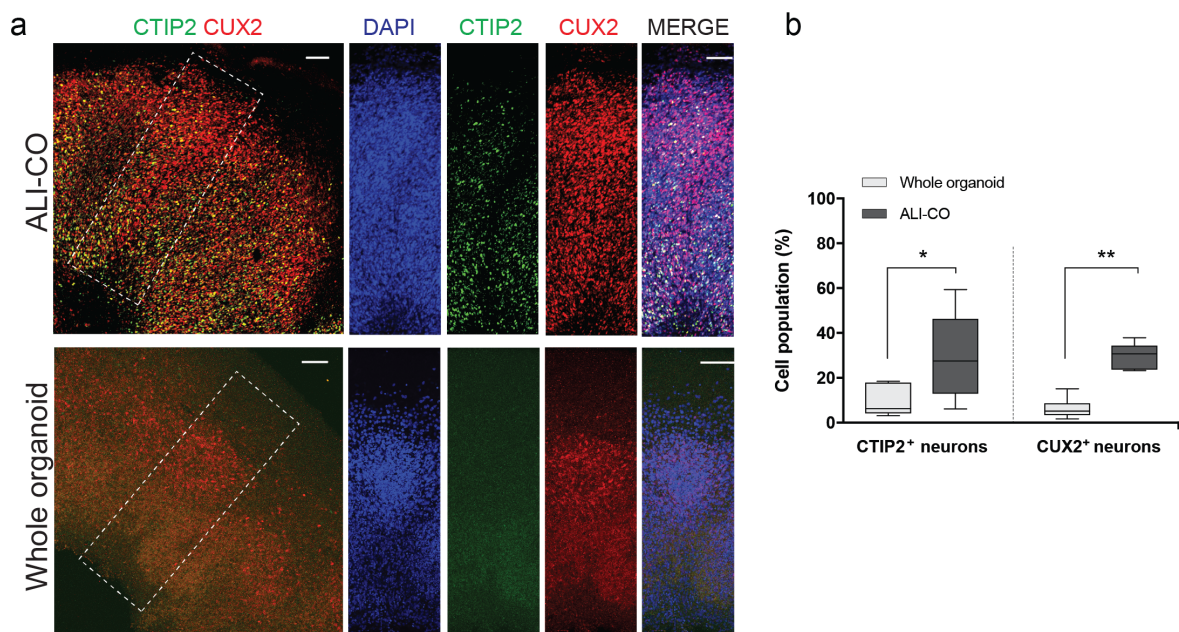


Figure 26 Culture at the ALI promotes survival of deep- and superficial-layer neurons.

a, Representative immunofluorescence staining for deep-layer (CTIP2⁺, green) and superficial-layer (CUX2⁺, red) neurons reveals increased numbers of both neuronal types in ALI-COs compared to whole organoids. The effect on survival is particularly marked in the case of deep-layer neurons, with ALI-COs showing abundant CTIP2⁺ nuclei, whereas the CTIP2 signal in whole organoids is largely unspecific background stain. Age of the whole organoid is 116 days and age of the ALI-CO is 120 days total, of which 36 days under ALI conditions. b, ALI-COs display significantly higher numbers of both CTIP2⁺ and CUX2⁺ cells compared with whole organoids. Statistical analysis was performed on a total of six whole organoids from three independent batches and six ALI-COs from two independent batches with ages ranging between 98-105 total days in culture. *P=0.0411, **P=0.0022, two-tailed Mann-Whitney test, n=6, whiskers are minimum and maximum values, centre line is the median and limits are upper and lower quartiles. Scale bars, 100 μ m (a).

ALI-COs develop highly directional and coherent tracts

Newborn neurons migrate from the VZ and SVZ to settle in the cortical plate, where they start to send out axons and establish connections. The observation that ALI-COs display distinct lobules delimited by bundles of neuronal processes (Fig 1.b) prompted us to examine the degree of axon bundling under these new culture conditions and in standard whole organoids. ALI-COs and whole organoids were stained for the pan-axonal marker SMI312, which labels all major types of neurofilaments (i.e. NF-L, NF-M and NF-H). Quantifications of overall SMI312 pixel intensity showed that ALI-COs have significantly higher numbers of axonal processes compared to whole organoids (n=6, **p=0.0022) (Fig. 27a & b). However, we were also interested in assessing and comparing the level of organisation, directionality and bundling of axons under these two different culture conditions. We thus performed orientation analyses using the OrientationJ plugin to produce a coherency value, indicative of the alignment of SMI312⁺ processes, and an energy value, which reflects how anisotropic and thus directional staining is. The product of these two parameters was used to compare the degree of alignment as a proxy for axonal bundling. Orientation analyses showed that axons in ALI-COs have significantly higher directionality and organisation compared with whole organoids (n=6, **p=0.0022) (Fig. 27c & d).

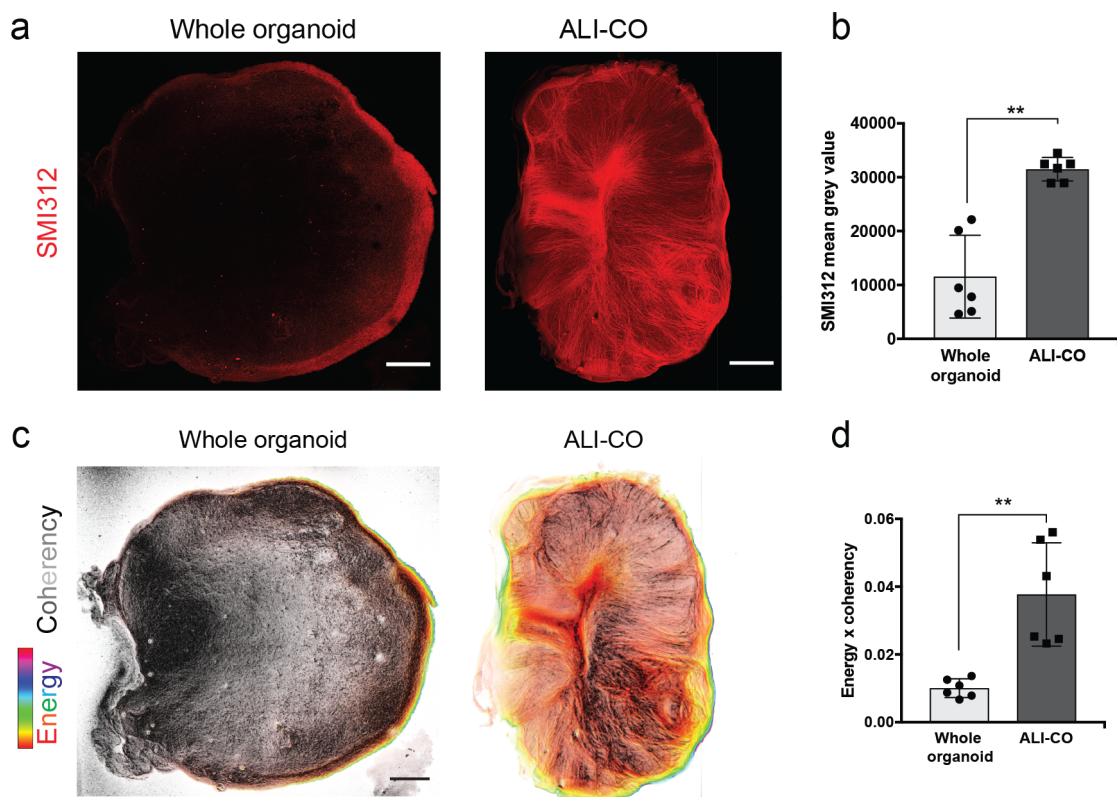


Figure 27 ALI-COs develop directional and coherent axon bundles.

a, Representative images of SMI312 (red) staining of a whole organoids compared with an ALI-CO used for OrientationJ quantifications shown in b. b, Quantifications of overall SMI312 levels reveals significantly higher axonal staining in ALI-COs compared to age-matched organoids. ^{**}P=0.0022, two-tailed Mann-Whitney test, n=6 whole organoids from two independent batches (ages: 90-105 days) and n=6 ALI-COs from two independent batches (ages: 85-92 days), reported are mean \pm s.d. c, OrientationJ analysis (as detailed in the methods section) indicates that ALI-CO axons are significantly more aligned and directional than axons in whole organoids. SMI312 pixel brightness corresponds to the coherency of the aligned structures and hue corresponds to energy, where a higher energy value corresponds to higher anisotropy and increased orientation. Images are representative of six whole organoids and six ALI-COs from two independent batches each with ages ranging between 85-92 days. d, The OrientationJ energy and coherence output were multiplied to obtain a composite value that reflected the extent of bundling and directionality in ALI-COs and whole organoids, with ALI-COs displaying a significantly higher degree of directional bundling compared to whole organoids. Reported are mean \pm s.d., ^{**}P=0.0022, Mann-Whitney test, n=6. Scale bars, 500 μ m (a and c). Madeline A. Lancaster analysed the data presented in a-d.

Culture at the ALI promotes long-term neuronal survival and astrogenesis

At this point we asked the question of how long organoid slices could be kept at the ALI and retain improved morphology, neuronal survival and astrogenesis. We thus compared the health state of axons (SMI312⁺), dendrites (MAP2⁺), whole neurons (TUBB3⁺) and astrocytes (GFAP⁺) at 24, 30 weeks and one year in culture. At 24 weeks, ALI-COs showed a thick TUBB3⁺ neuropil populated by GFAP⁺ astrocytes displaying healthy morphology with numerous fine processes (Fig. 28a). By contrast, in 24 week old whole organoids sparse TUBB3⁺ staining was confined to the outermost layers of the tissue and accumulation of reactive astrocytes was observed. Similarly, while staining of 24-week old ALI-COs for SMI312 and MAP2 revealed large axon bundles and elongated dendrites, typical of maturing neurons, in 24-week old organoids bundling was seen to a very limited degree and dendrites appeared sparse and less developed (Fig. 28a). At week 30 the difference between whole organoids and ALI-COs was even more marked, with organoids displaying virtually no axons and very few dendrites, and ALI-COs showing abundant axonal stain and numerous dendrites (Fig. 28b). In 30-week old whole organoids TUBB3 staining was restricted to a very thin and superficial layer of the organoid and only astrocytes could be seen in the expanded necrotic core (Fig. 28c). In contrast, ALI-COs retained a dense TUBB3⁺ neuropil along with astrocytes displaying healthy morphology (Fig. 28c). Culture of whole organoids was not continued past week 30 and only ALI-COs were examined at one year. Even after one year in culture ALI-COs displayed abundant healthy astrocytes and neurons with well-developed axons and dendrites (Fig. 28d).

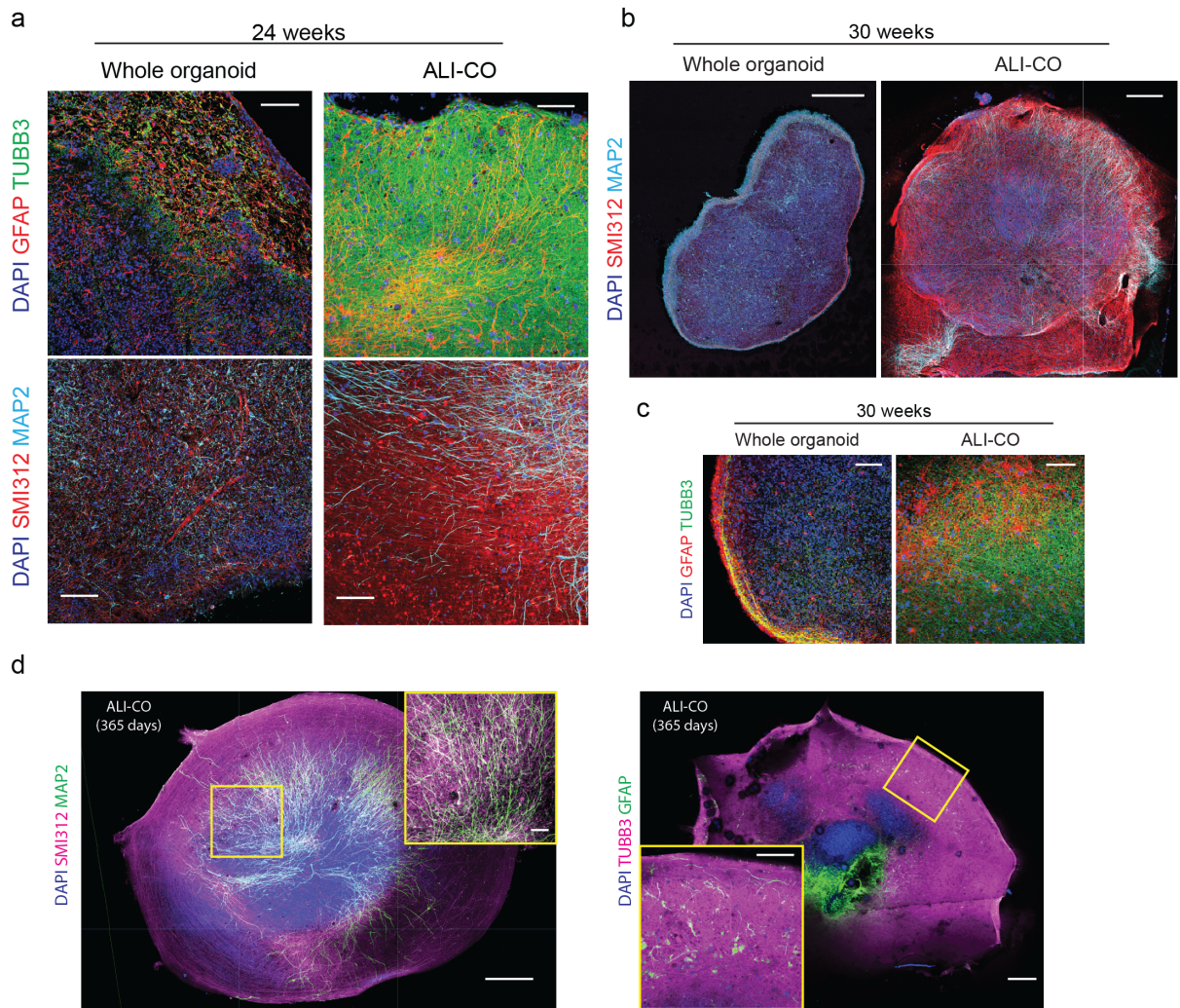


Figure 28 ALI culture allows for extended survival and maturation of neural tissue *in vitro*.

a, Representative high magnification images of 169 day-old ALI-COs (69+100 days at the ALI) show a dense TUBB3⁺ (green) neuropil with GFAP⁺ (red) astrocytes displaying smooth elongated processes; by contrast age matched whole organoids display disrupted tissue with few TUBB3⁺ neurons and high densities of GFAP⁺ astrocytes with reactive morphology. SMI312 (axons, red) and MAP2 (dendrites, cyan) staining reveals large axon bundles and high densities of dendrites in ALI-COs, while organoids show sparse bundling and limited dendritic stain b, ALI-COs at 210 days (68+142 days at the ALI) stained for axons (SMI312⁺, red) and dendrites (MAP2⁺, cyan) show continued neuronal survival and improved health compared with age-matched organoids. c, Higher-magnification images of 210 day ALI-COs (68+142 days at the ALI) and age-matched organoids stained for astrocytes (GFAP⁺, red) and neurons (TUBB3⁺, green) show increased neurons and healthier astrocytes in ALI-COs compared to whole organoids. d, Immunofluorescence stains of one-year old ALI-COs (90+275 days at the ALI) stained for the axonal marker SMI312 (magenta), the dendritic marker MAP2 (green), the pan-neuronal marker TUBB3 (magenta) and the astrocytic marker GFAP (green) reveal abundant healthy neurons and astrocytes. Three ALI-COs from one organoid were stained with similar results. Scale bars, 500 μ m (b and d), 100 μ m (a and c).

ALI-CO neurons acquire complex morphology and display mature synapses

Having observed that these improved culture conditions better sustained long-term tissue survival and maturation we decided to examine neuronal morphology in more detail. We thus performed sparse labelling with GFP either by injection and electroporation of a transposon donor plasmid encoding farnesylated-GFP (fGFP) or by injection of Sendai virus carrying emerald-GFP (emGFP). Via this approach we were able to observe, as previously reported, aligned neurons in the cortical plate (Fig. 29a & c). By performing the experiment on ALI-COs of increasing age we were able to observe progressively more mature morphologies. In 80-day old ALI-COs (43+37 day at the ALI) we could see typical pyramidal morphology with primary and basal dendrites (Fig. 29b). At this stage extensive synaptic staining was already present throughout the tissue (Fig. 29b). Neurons of older ALI-COs (92+51 days at ALI) started displaying complex dendritic architecture with numerous spines developing on the primary dendrite (Fig. 29c). After one year in culture we observed a high degree of maturity with very complex dendritic branches and spines (Fig. 29d). Furthermore, staining for the pre-synaptic markers SYT1, SYP and Bassoon and the post-synaptic markers PSD95 and Homer1 demonstrated the presence of mature synapses with juxtaposed pre and post-synaptic termini (Fig. 29e).

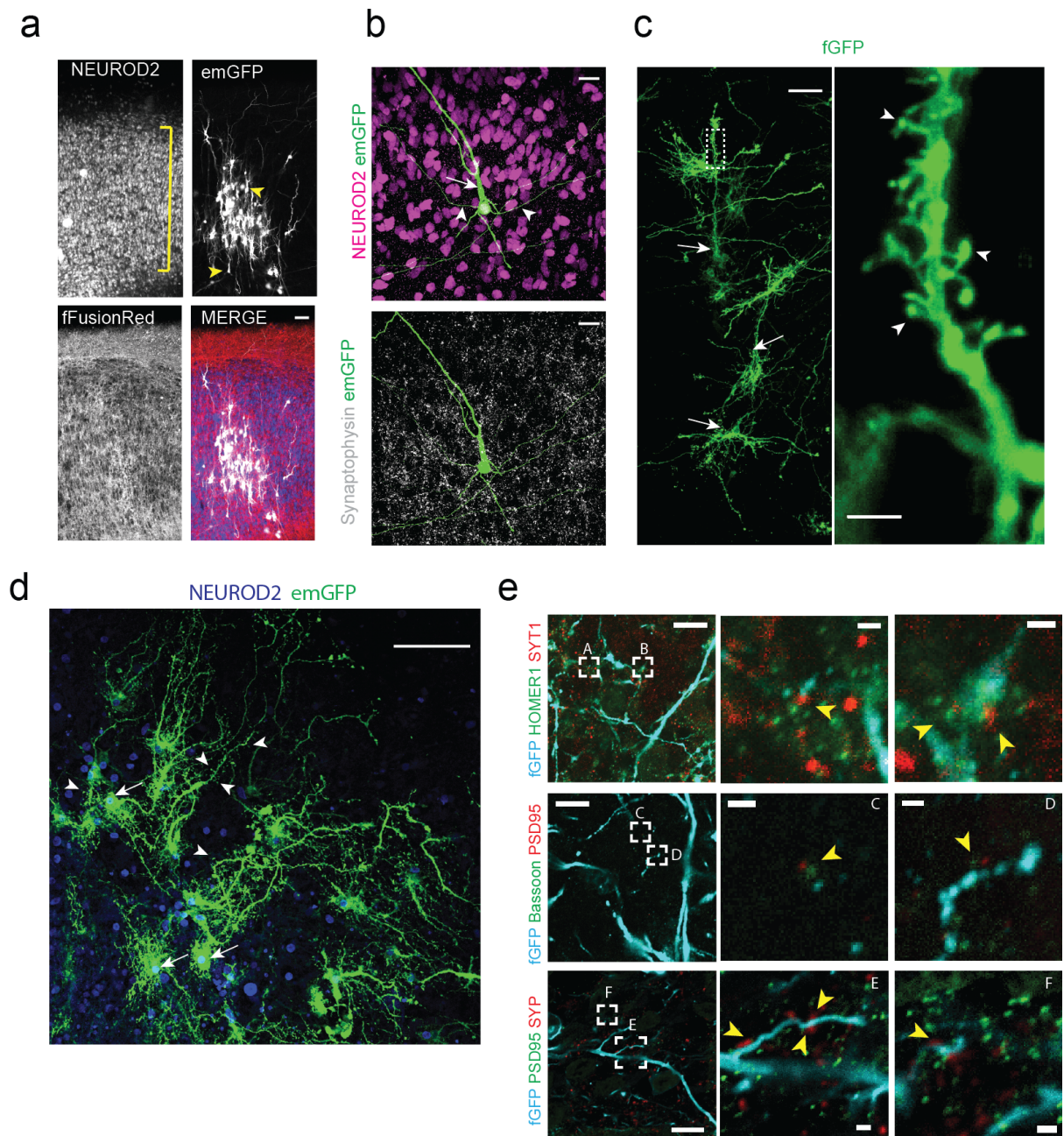


Figure 29 Neurons in ALI-COs display complex dendritic architectures and mature synapses.

a, Sparse labelling of an ALI-CO (53+37 days at the ALI) by Sendai emGFP (white) reveals radially aligned neurons (NEUROD2⁺, magenta) of the cortical plate (bracket) with complex neuronal architectures and pyramidal morphologies (arrowheads). The organoid was derived from a H9 line constitutively expressing mFusionRed to capture overall tissue morphology. b, High magnification maximum-intensity projection image of a single emGFP (green) labelled pyramidal neuron (NEUROD2⁺, magenta) displaying a primary dendrite (arrow) and basal dendrites (arrowheads). Immunofluorescence staining for synaptophysin (white) reveals the presence of synapses throughout the tissue. c, ALI-CO (92+51 days at the ALI) electroporation with a membrane-targeted farnesylated GFP (fGFP, green) shows radially aligned pyramidal neurons with complex dendritic architecture

(arrows). The primary dendrites have evident spines (arrowheads, inset). The high magnification image shown is a maximum-intensity projection. d, After one year in culture, sparse labelling of an ALI-CO (90+275 days at the ALI) by Sendai emGFP (green) reveals individual neurons (arrows) with highly complex dendritic architectures and dense dendritic spines (arrowheads). e, Cryosections of ALI-COs derived from organoids electroporated with fGFP display mature synapses with juxtaposed pre- (SYT1, Bassoon, SYP) and post- (Homer1, PSD95) synaptic termini (arrowheads). ALI-CO age: 55 + 40 days at the ALI (95 total) and 89 + 23 at the ALI (112 total). Sparse labelling with emGFP and fGFP (a-e) was performed on three ALI-COs from distinct batches with similar results. Scale bars, 50 μm (a and c), 20 μm (b), 5 μm (c inset), 100 μm (d), 10 μm (e) and 1 μm (e inset).

Interneurons are present within ALI-COs

Interneurons are essential for the correct establishment of cortical networks. As previously mentioned, interneurons arise predominantly in the MGE and LGE, migrate tangentially into the cortex and modulate circuit activity through release of the neurotransmitter GABA. Engineered cerebral organoids (enCORGs) were shown to produce predominantly forebrain tissue, including dorsal and ventral telencephalon (Lancaster et al. 2017). Therefore, we decided to examine if ALI-COs harboured interneurons originating from tissue regions with ventral identity. Immunostaining revealed GABA⁺/VGAT⁺ interneurons and numerous VGAT punctae in ALI-COs, suggesting the presence of GABAergic synapses (Fig. 30a). Additionally, staining for somatostatin and GAD67 revealed the presence of other interneuron subtypes (Fig. 30b). In samples electroporated with fGFP we were able to observe punctae co-positive for the GABA transporter VGAT and the pre-synaptic structural protein PCLO decorating the dendritic spines of neurons with pyramidal morphology, suggesting GABAergic input on pyramidal cells in ALI-COs (Fig. 30c).

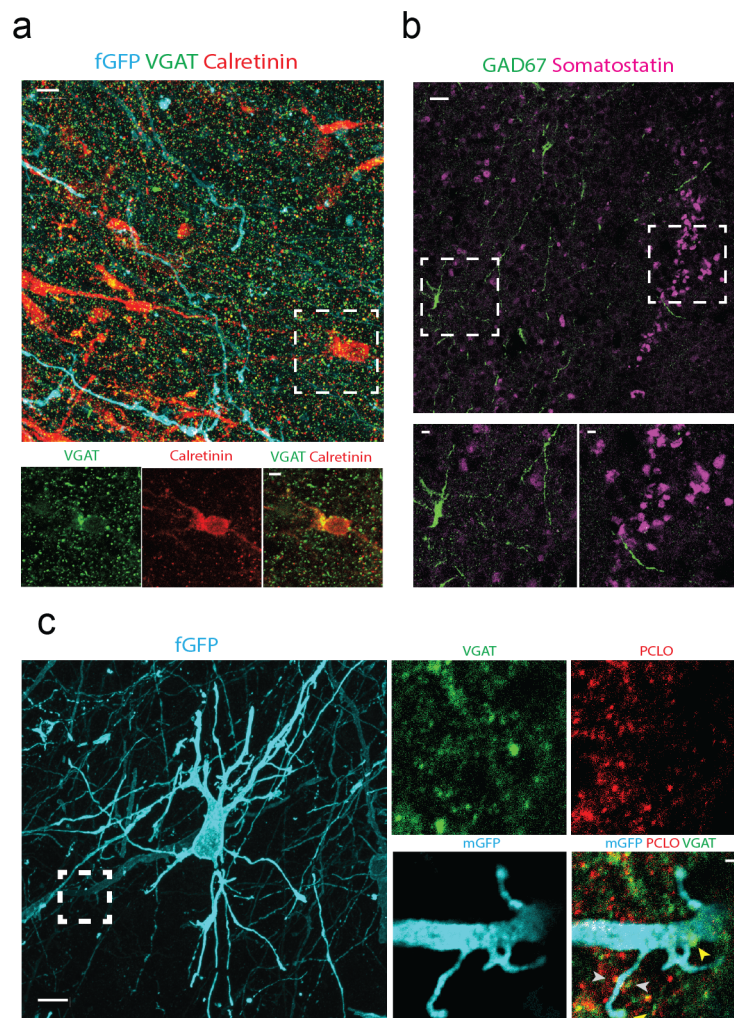


Figure 30 Interneurons and GABAergic synapses are found within ALI-COs.

a, Immunofluorescence staining of an fGFP electroporated ALI-CO (57+49 days at the ALI) cryosection for the interneuron markers VGAT (green) and Calretinin (red) reveal numerous interneurons and VGAT⁺ punctae throughout the tissue, suggesting GABAergic synapses. Maximum-intensity projection image shown. Inset image shows an individual cell body with cytoplasmic VGAT⁺ staining. b, Immunofluorescence staining of an ALI-CO (57+49 days at the ALI) cryosection demonstrates the presence of additional Somatostatin⁺ (magenta) and GAD67⁺ (green) interneuron subtypes. Insets are higher magnification images of these two interneuron populations. c, Immunofluorescence staining of an fGFP electroporated ALI-CO (55+50 days at the ALI) cryosection showing a fGFP⁺ (cyan) pyramidal neuron with dendritic spines decorated by double positive punctae (yellow arrowhead) of VGAT (green) and PCLO (red), a pre-synaptic structural protein (inset, arrowheads), suggesting the presence of GABAergic synapses onto the pyramidal neuron. White arrowheads point to VGAT⁺ punctae. Overview image in c is a maximum-intensity projection. Sparse labelling with fGFP was performed on three ALI-COs from three organoids with similar results. Scalebars, 20 μm (a and b), 10 μm (c), 5 μm (a and b insets) and 1 μm (c inset).

ALI-COs are electrophysiologically active

The presence of mature synapses with juxtaposed pre- and post-synaptic termini suggested that ALI-COs might display electrophysiological activity. We thus performed multielectrode array (MEA) recordings of unstimulated cerebral organoid slices and were able to observe spontaneous activity (Fig. 31a). Low density electrode arrays can be in fact used to detect individual extracellular action potentials (EAPs) as well as changes in extracellular field potential (Bridges et al. 2018). Over the course of a representative two-minute recording from a single MEA electrode we observed numerous negative deflections corresponding to EAPs and overlay of the single spikes demonstrated the trace profile typical of EAPs (Gold et al. 2007) (Fig. 31b). Immunofluorescence staining for the marker of neuronal activity c-Fos revealed numerous positive nuclei in ALI-COs (Fig. 31c) and treatment with the Na^+ -channel blocker TTX was sufficient to eliminate all spontaneous activity (Fig. 31d, e & f). Furthermore, whole-cell patch-clamp recordings demonstrated that, upon positive current injection, ALI-CO neurons are able to respond with trains of action potential with frequency dependent on current intensity (Fig. 31g, h and appendix).

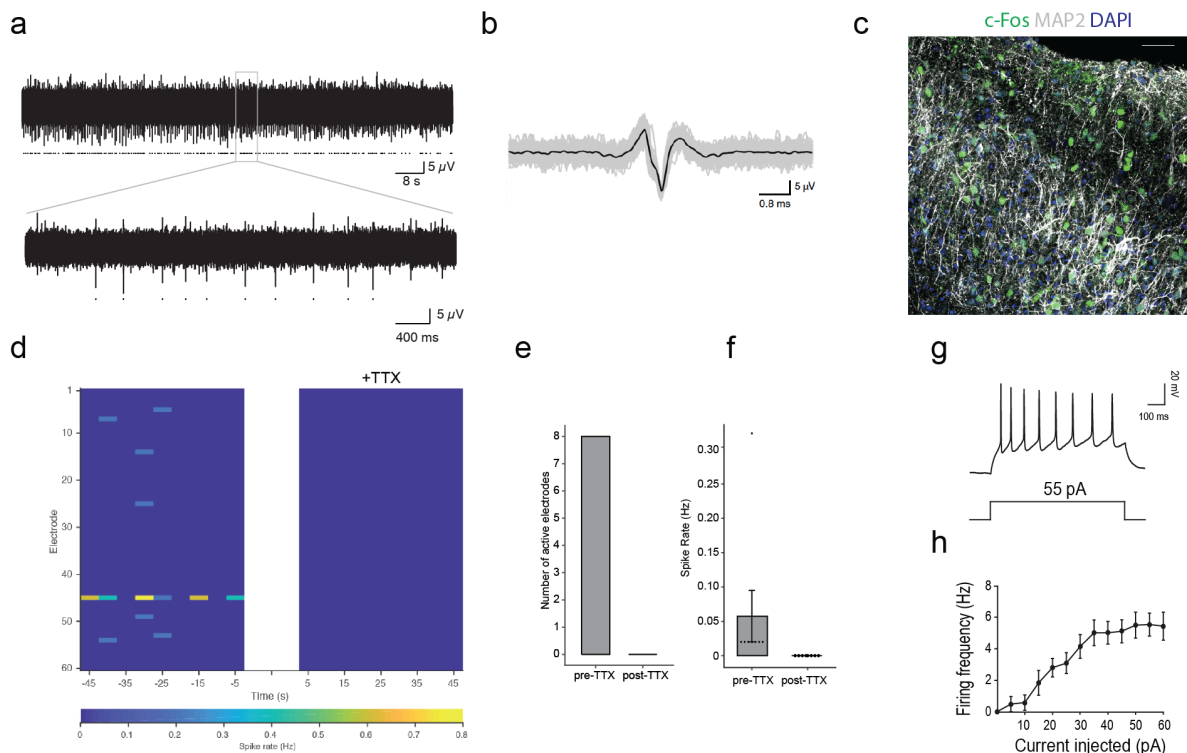


Figure 31 ALI-COs display electrophysiological activity.

a, Two minutes of spontaneous activity recorded from a single electrode of an MEA from an ALI-CO after 54 days at the ALI (117 days total), detected action potentials are marked by dots underneath the peaks. Inset is a 5 second window from the recording expanded from the grey box. b, Overlay of all

spikes detected in a (gray, marked with dots) with the average waveform in black. c, Immunofluorescence image of a 114 day ALICO (54+60 at the ALI) stained for MAP2 (dendrites, grey), DAPI (blue) and the transcription factor c-Fos (green), which marks the nuclei of active neurons. Shown is a representative image of independent three experiments. d, Rasterplot of spike frequency (averaged in 5-ms time bins for each electrode) in an ALI-CO 75 seconds before (left) and after (right) TTX application, demonstrating loss of activity upon Na^+ -channel blockade. e, Quantification of number of active electrodes before and after TTX application in one of three ALI-CO recordings where TTX was applied. f, Quantification of average spike frequency (error bars are s.e.m) in the eight active electrodes of e before and after TTX application. g. Representative whole-cell patch-clamp recordings of action potentials evoked by injection of 55 pA current. h, Frequency-current (F-I) curve showing increasing action potential firing rates upon injection of higher intensity currents. Error bars are s.e.m., n=13 out of 20 cells from seven ALI-COs from three independent organoid batches. Appendix 2 reports the full dataset. Scale bar, 50 μm (c). Data shown in a, b, c, d, e and f are representative of three independent experiments. Data presented in a, b, d-f were acquired by Susanna Mierau and me and analysed by Timothy Sit. Data presented in g and h were acquired and analyzed by Laura Masullo under the supervision of Marco Tripodi.

Early-stage ALI-COs display highly dynamic growth cones

As previously pointed out, in contrast to whole organoids, which display disorganised axons, ALI-COs develop thick directional axon tracts (Fig. 27a-d). In order to characterise how axons bundle and form tracts we performed live imaging on ALI-COs. This culture preparation, in fact, lends itself well to live imaging analyses over extended time periods. To achieve stable GFP expression in neurons, between day 45 and 60 of the protocol, cerebral organoids were injected and electroporated with the pCAG-fGFP transposon donor plasmid and the Sleeping Beauty transposase plasmid pCAGEN-SB100 (Lancaster et al. 2017) (Fig. 32a). Approximately one- to two-weeks after electroporation, organoids were prepped for air-liquid interface culture, and GFP-positive buds retained the original morphology after sectioning (Fig. 32b). Live imaging on early stage ALI-COs showed large fGFP⁺ foci that included both dividing progenitors and neurons. Tracking of individual growthcones over time revealed highly dynamic behaviours of isolated axons, displaying saltatory extensions and retractions (Fig. 32c).

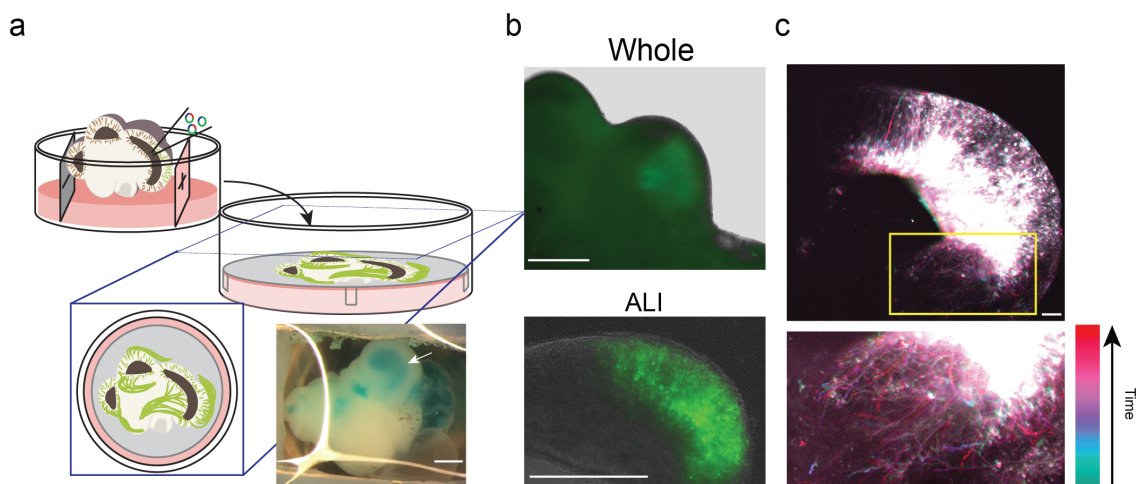


Figure 32 Organoid electroporation and live imaging reveal axon guidance dynamics in ALI-COs.

a, Schematic of electroporation and preparation of ALI-COs for live imaging. Inset shows an organoid after plasmid injection with the blue dye (FastGreen) marking the injected ventricle (arrow). b, Widefield image of a fGFP-electroporated ventricle before (top) and after (bottom) sectioning and ALI-CO establishment. c, Temporal projection image of an early-stage fGFP⁺ ALI-CO (64+2 days at the ALI) pseudocoloured by time shows highly disorganised, saltatory axon dynamics with multiple cycles of growthcone extension and retraction. b and c are representative images out of 5 similarly staged and live imaged ALI-COs. Scale bars, 1 mm (a inset), 500 μ m (b) and 100 μ m (c). Madeline A. Lancaster analysed the data presented in b and c.

More mature axons form robust and directional tracts

While growth cones of individual early axons typically underwent cycles of extension and retraction (Fig. 32c & 33a), at later stages growth cones within axon bundles moved in a more directional and linear fashion with greater velocity (Fig. 33b & c). In ALI-COs axons formed thick and robust bundles that became reinforced over time, stayed coherent and did not splay or randomly fill the entire tissue (Fig. 33c & d). Within bundles, growth cones of follower axons projected at fast pace along pioneers but as a whole, the bundle front progressed at a much slower rate (Fig. 33f). GFP⁺ tracts showed diverse projection modalities; while some tracts were seen to project locally, some extended over long distances within the organoid and even out of the main mass of cell bodies (Fig. 33g & h). Some tracts crossed each other and yet maintained distinct trajectories, in a similar fashion to *in vivo* decussation of tracts across the midline, and some tracts displayed turning behaviour (Fig. 33i).

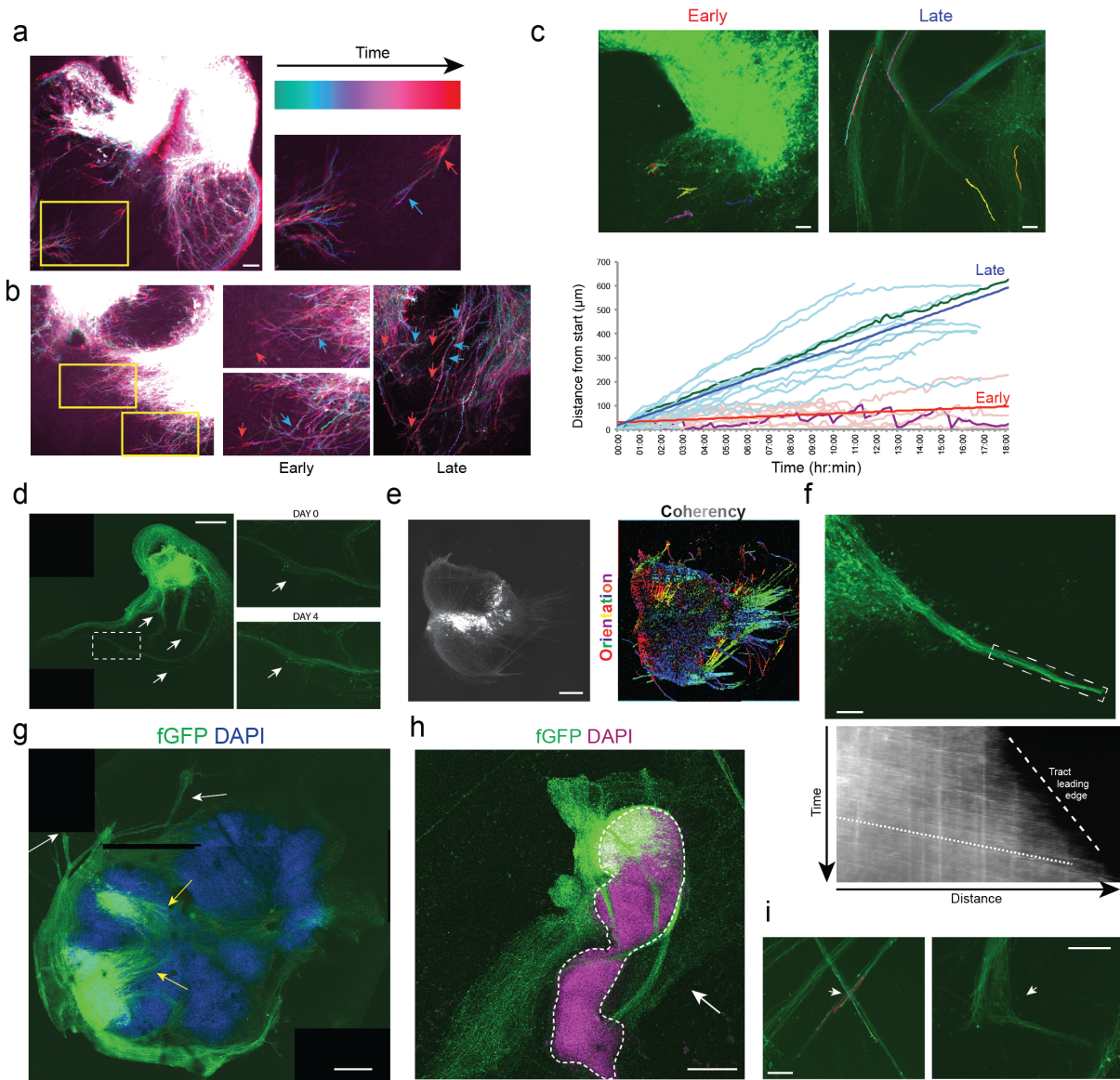


Figure 33 Neurons of ALI-COs exhibit dynamic axon guidance behaviours and form robust bundles.

a, Temporal projection image of an early-stage fGFP⁺ ALI-CO (64+5 days at the ALI) pseudocoloured by time shows highly dynamic axon outgrowth with growth-cone retraction indicated by blue arrow (early position) and red arrow (late position). The image is representative of five similarly staged and imaged ALI-COs. b, Temporal projection image of a more mature ALI-CO (64+9 days at the ALI) shows more directed progression of axon growth-cones with progressive extensions indicated by the blue (early position) to red (late position) arrows. The image is representative of three similarly staged and imaged ALI-CO samples. c, Tracing of individual growth cones over time shows convoluted trajectories with little directionality in early ALI-COs (2-5 days at the ALI, top left), while in more mature ALI-COs (14-24 days at the ALI, top right) growth cones advance with high directionality along linear trajectories. Below is a plot of the growth cone positions over an 18-hour live imaging time-course relative to their starting position. In mature cultures growth cones (14-24 days at the ALI, purple lines) display higher velocities (illustrated by the steepness of the average linear regression lines for the dataset) than growth cones in early cultures (2-5 days at the ALI, green lines), which instead exhibit dynamic retractions (illustrated by the highlighted example trace in green compared to purple). Tracing was done on 12 late growthcones and 9 early growth cones from four organoids of two independent batches. d, Axon tracts of a representative 18 day ALI culture (70+18 days at the ALI) shows several dense and long bundles (arrows) with directional projection pattern. Insets show that over the course of four days the bundles maintain their overall appearance but become reinforced by incoming follower axons. The image shown is representative of seven similarly staged and imaged ALI-COs. e, Source image of an fGFP⁺ ALI-CO (left) and pseudocoloured ALI-CO (left) according to the orientation (hue) and coherency (brightness) of axon tracts. The data shown are representative of five such analyses. f, Still image (top) and kymograph (bottom) of an extending tract (dashed box). From the kymograph it can be seen that individual axons progress at higher velocities (shallow slope, dotted trend line) than the front of the tract as a whole (steep slope, dashed line). The data shown are representative of three independent experiments. g, Example image of an fGFP-electroporated ALI-CO (70+20 days at the ALI) showing both internal (yellow arrows) and escaping (white arrows) tract hodologies. h, Example image of fGFP⁺ axon tracts projecting out of the main ALI-CO (64+24 days at the ALI) mass of cell somas (DAPI⁺). White arrow points to a tract with escaping behaviour. i, Example images of fGFP⁺ axon tracts crossing each other (left, 83+17 day ALICO), a behaviour resembling decussation, and turning (right, 70+14 day ALI-CO). Scale bars, 100 μ m (a-d, g and i), 500 μ m (f and h). Madeline A. Lancaster analysed the data presented in a-i.

Organising centres secreting guidance cues are found within ALI-COs

The complex trajectories and guidance behaviours observed by live imaging pointed to the possibility that signalling centres might become established within these cultures. However, tract labelling by fGFP could only capture a small subset of axons present within ALI-COs. To visualise the full diversity of axon tracts, mature ALI-COs were stained for the pan-neurofilament marker SMI312, which specifically labels axons. We were thus able to observe dense tracts originating within discrete lobules and merging to form thick tracts (Fig. 34a) resembling *in vivo* intracortical axon bundles. For characterisation and analysis we chose to focus on the CC as its molecular markers and guidance effectors have been extensively characterised in the literature. To test for the presence of callosal tracts in ALI-COs we stained for the membrane bound Semaphorin co-receptor NRP1. Within ALI-COs we found a subset of SMI312⁺/NRP1⁺ tracts that often appeared thicker and more fibrous than SMI312⁺/NRP1⁻ tracts and had curved appearance, suggesting turning behaviour (Fig. 34b & c).

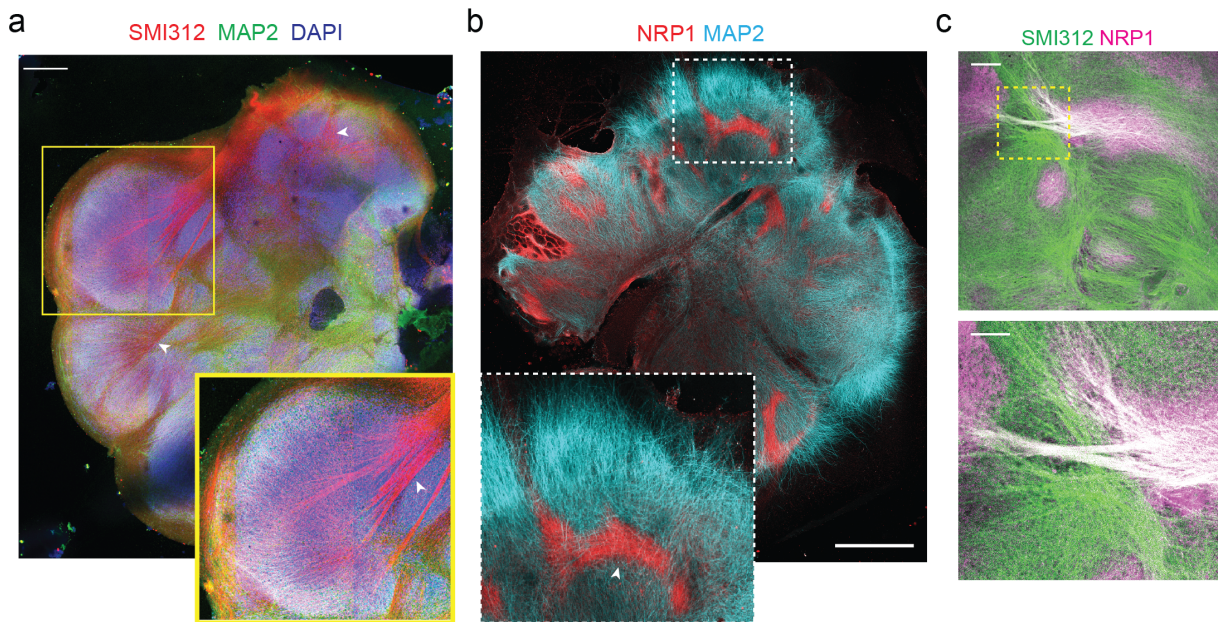


Figure 34 ALI-COs develop robust internal tracts with callosal identity.

a, Pan-axonal (SMI312, red) and dendritic (MAP2, green) stain on an 85 day old ALI-CO (49+36 days at the ALI) shows thick tracts (arrowheads) projecting across the organoid between DAPI⁺ (blue) lobules and coalescing into large bundles (inset image, arrowhead). The image is representative of seven ALI-COs stained with similar results. b, Immunofluorescence staining of a 120 day ALI-CO (71+49 days at the ALI) for the dendritic marker MAP2 (cyan) and the membrane receptor NRP1 (red) which marks callosal tracts *in vivo*. The image is representative of four ALI-COs with similar results and shows several NRP1⁺/MAP2⁻ thick axon bundles that appear to be turning (inset,

arrowhead). c, Immunofluorescence stain for SMI312 (axons, green) and NRP1 (magenta) reveals that only a subset of axons in a 147 day old ALI-CO (92+55 days at the ALI) display callosal identity. The image is representative of four ALI-COs stained with similar results. Scale bars, 500 μ m (a), 1 mm (b), 200 μ m (c). Madeline A. Lancaster acquired images in a and b.

We next stained for secreted molecules and receptors known to guide callosal axons across the midline. Staining for the chemoattractant Netrin-1 revealed large foci in the central regions of ALI-COs with numerous SMI312⁺ axon tracts projecting inwardly towards the Netrin-1 source (Fig. 35a). Work in mouse has shown that gradients of Wnt5a secreted from the glial wedge at the site of decussation are responsible to drive callosal axons across the midline by Wnt5a-mediated repulsion via the Ryk receptors (Keeble et al. 2006). We thus stained ALI-COs for WNT5A and NRP1 and observed WNT5A foci in the near vicinity of tracts with callosal identity (Fig. 35b). Furthermore, staining for NRP1 and RYK revealed callosal axons expressing this tyrosine kinase-related receptor (Fig. 35c). Another important factor controlling *in vivo* navigation of post-crossing callosal axons is Ephrin-B1 (Mire et al. 2018) and we were able to observe internal axon tracts specifically positive for Ephrin-B1 (Fig. 35d)

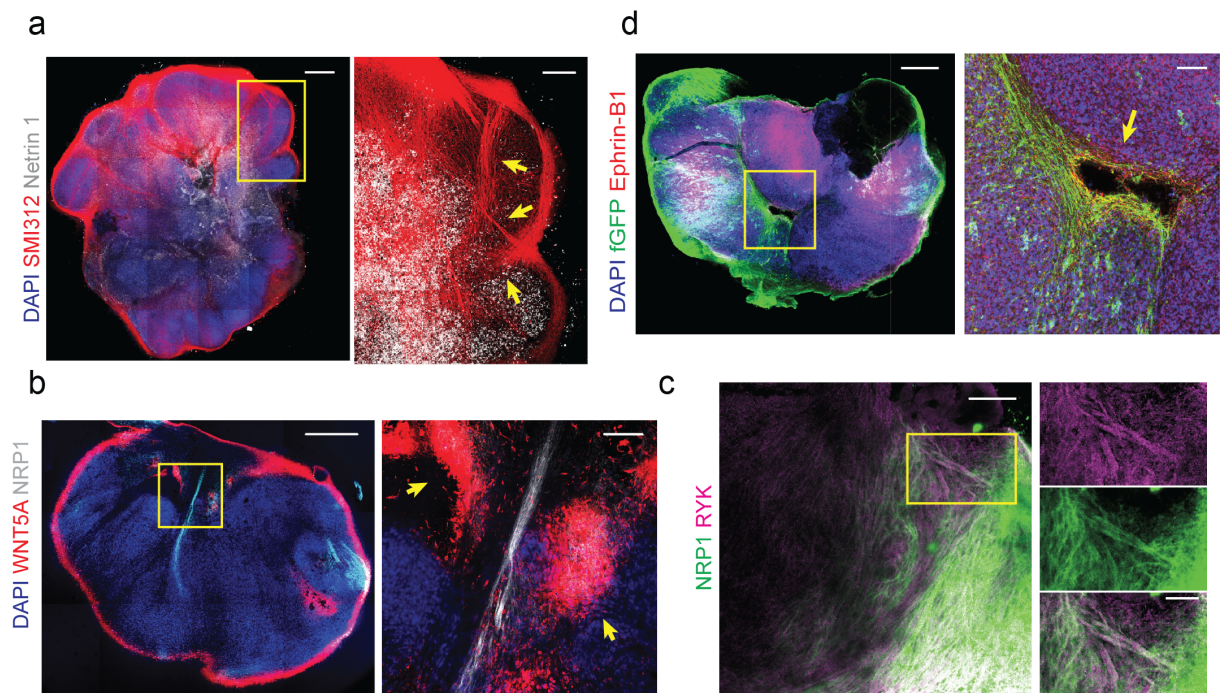


Figure 35 ALI-COs display foci of secreted guidance cues and axon tracts display specific cell-surface receptors.

a, Immunofluorescence staining for SMI312 (axons, red) and the secreted chemoattractant Netrin1 (white) in a 81 day old ALI-CO (49+32 days at the ALI). Inset image (right) shows a large internal Netrin1⁺ region with axon tracts (yellow arrows) projecting towards it. Image is representative of three ALI-COs showing comparable results. b, Immunofluorescence stain for NRP1 (CC, white) and the

secreted chemorepellent of callosal axons WNT5A (red) in a 117 day old ALI-CO (63+54 days at the ALI) reveals discrete WNT5A⁺ regions. Inset image (right) shows a higher magnification of WNT5A⁺ foci surrounding a NRP1⁺ tracts with callosal identity. The image is representative of two ALI-COs stained. c, Immunofluorescence staining for the callosal marker NRP1 and the tyrosine kinase receptor RYK in a 84 day old ALI-CO (65+19 days at the ALI) revealing callosal axons expressing this receptor. Inset is higher magnification image of the NRP1⁺/RYK⁺ tracts. d, Immunofluorescence staining of a fGFP⁺ 84 day old ALI-CO (65+19 days at the ALI) for the cell surface receptor Ephrin-B1 reveals a subset of internally projecting tracts that express this guidance molecule (inset, yellow arrow). The image shown is representative of two independent experiments. Scale bars, 500 μ m (a-c), 100 μ m (b inset, c and d inset), 200 μ m (a inset), 50 μ m (c inset).

scRNA-seq reveals a large array of cortical neuron types in ALI-COs

Our data suggested that the different projection behaviours and tract identities seen might correspond to specific neuronal identities. To test this possibility and examine the full repertoire of neuronal types present within ALI-COs we performed scRNA-seq. Six slices taken from three ALI-CO preparations of H1 and H9 hESC-derived organoids were analysed through the 10X single-cell genomics platform. Unbiased clustering by principal component analysis (PCA) of highly variable genes identified 6 cell populations (C1-C6) (Fig. 36a) that were visualised by dimensionality reduction using t-distributed stochastic neighbour embedding (tSNE) (Fig. 36b). Gene Ontology (GO-) term analysis (false discovery rate (FDR)>0.1% with highest fold-enrichment) of the 50 most differentially expressed genes suggested that developmental cell states may be defining the 6 cell populations identified (Fig. 36c).

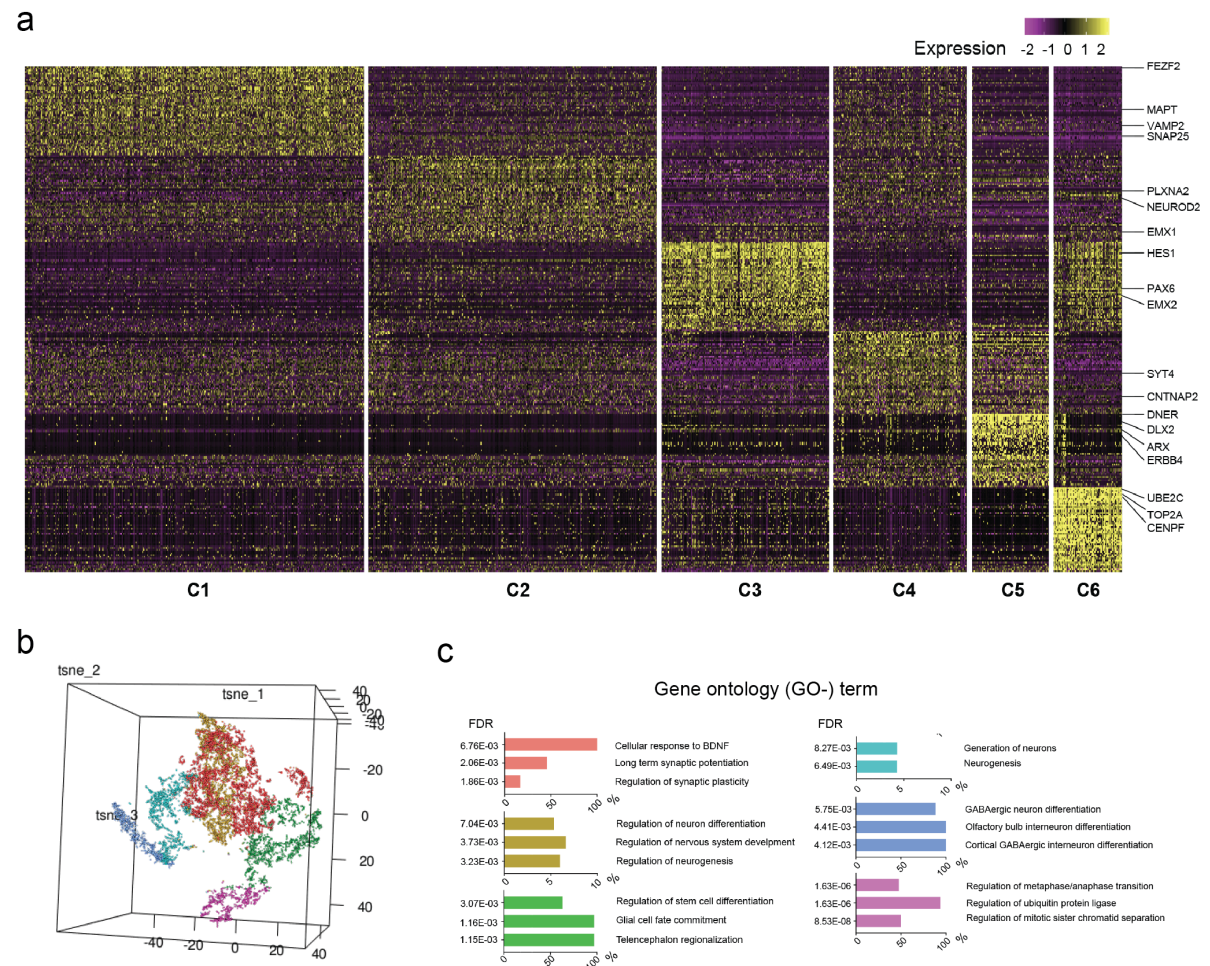


Figure 36 scRNA-seq of ALI-COs reveals a wide array of cortical cell types.

a, Heat map displaying the expression levels of the top 50 differentially expressed genes in clusters C1-6 of the scRNA-seq experiment with key marker genes for each cluster indicated on the right. The colour bar reflects the expression levels, purple being lowest and yellow highest. b, Unbiased tSNE clustering of scRNA-seq data derived from 13,280 cells from six ALI-COs – two sections from each

of three organoids, two H1 and one H9 – identifies six main cellular clusters visualised in 3D space. c, Histograms of the top three gene ontology (GO) biological-process annotations defined on the basis of the highest-fold enrichment of most significant terms (Fisher's exact test with FDR multiple test correction above 0.1% by <http://geneontology.org> $P < 0.001$, $n = 50$ top differentially expressed genes per cluster). The data presented were acquired and analysed by George Gibbons, Lea M.D. Wenger and András Lakatos on ALI-COs generated by me.

Pseudotime and correlation analyses of 75 day ALI-COs and published fetal brain datasets supported clustering according to cell state. The expression trajectories of key marker genes of the VZ, SVZ and neuronal layers over pseudotime demonstrated that ALI-COs show temporal transcriptional programs comparable to those of age-matched fetal brain samples (Fig. 37a). Furthermore, whilst expression of these key marker genes showed strong correlation in ALI-COs, other datasets showed weaker correlation (Fig. 37b, c & d). Therefore, while in ALI-COs expression of layer specific genes is very consistent and separates neuronal cell-types according to cell- and layer-identity, the same was not seen in other publicly available dataset (Quadrato *et al.* 2017; Camp *et al.* 2015).

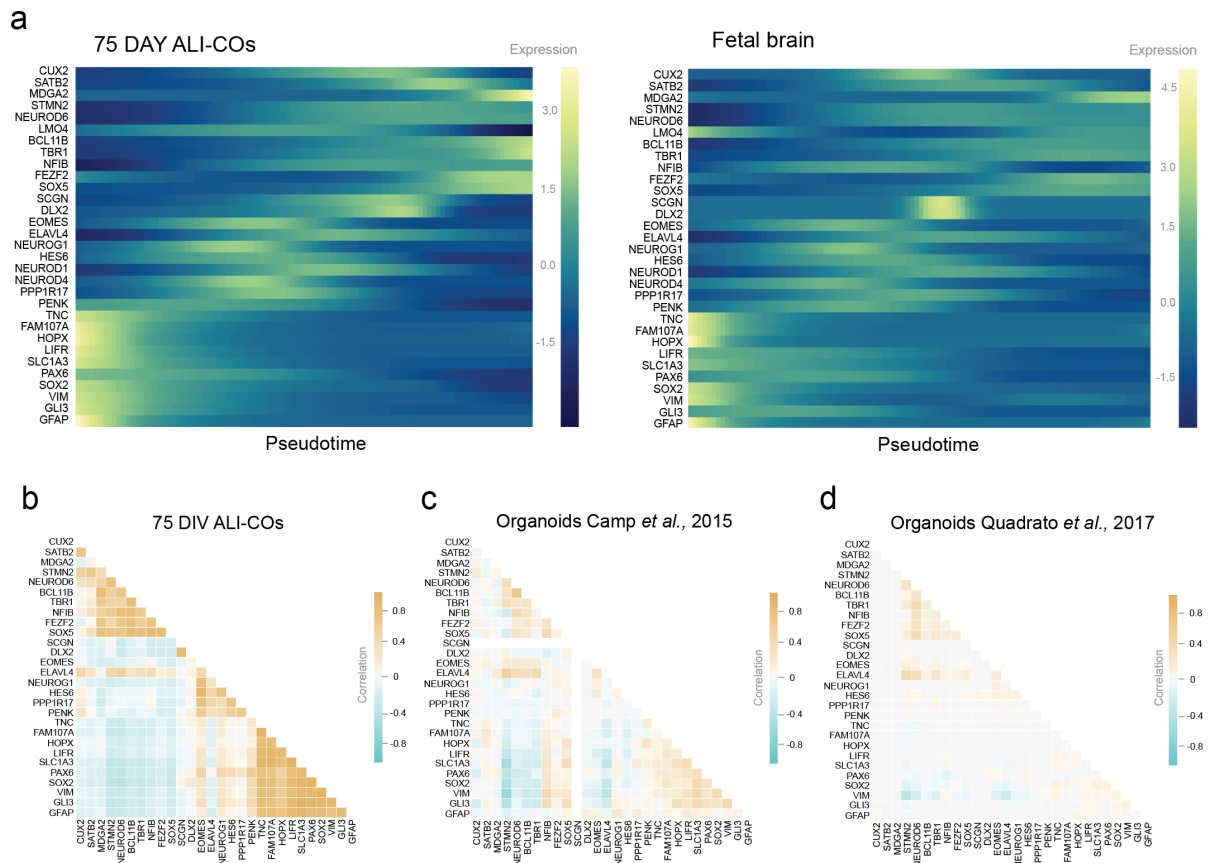


Figure 37 Pseudotime and correlation analyses reveal similar gene-expression profiles in ALI-COs and human fetal brain.

a, Heatmaps showing normalised layer-specific gene expression ordered by pseudotime in 75 day old ALI-COs (left) and 12-13 week old human fetal brain cells (right). Colour bars reflect gene expression levels. b, Pearson correlation matrices of gene expression for developmental layer-specific markers in ALI-COs side by side with analyses on human cerebral organoids from Camp et al. (2015) (c) and Quadrato et al. (2017) (d). Colour bars represent correlation values with blue indicating negative correlation and yellow indicating positive correlation. The study by Camp et al. (2015) comprised 508 cells from 9 organoids and the study by Quadrato et al. (2017) comprised 66,889 cells from 19 organoids.). The data presented were acquired and analysed by analyzed by George Gibbons, Lea M.D. Wenger and András Lakatos on ALI-COs generated by me.

Next we compared the average expression of genes belonging to three categories; cell type-, cell state- and region-specific genes, and found that the identities of the clusters identified by PCA were better defined by cell types and cell states rather than regional identity (Fig. 38a & b). This was in line with previous findings that enCOR organoids, used to establish the ALI cultures used for scRNA-seq, predominantly generate forebrain identity over other brain regions (Lancaster et al. 2017). Based on cell-type and cell-state markers we annotated six cluster identities: corticofugal projection neurons (C1 - CTIP2⁺, FEZF2⁺), intracortical and predominantly callosal superficial-layer neurons and post-mitotic intermediate progenitors (C2 – SATB2⁺, EOMES⁺), aRGCs and oRGCs (C3 – GFAP⁺, FAM107⁺), a cluster of more mature neurons including both deep- and superficial-layer identities (C4 – FOXP2⁺, CUX2⁺), interneurons (C5 – DLX2⁺) and actively dividing cells expressing both intermediate progenitor and RGC markers (C6 – CENPE⁺, EOMES⁺, GLAST⁺) (Fig. 38a & b). The fact that in C2 we observed expression of both SATB2 and EOMES suggested that at the time scRNA-seq was performed (i.e. 69-75 days total) upper layer neurons were still being actively produced and is consistent with the inside-out gradient of neurogenesis (Fig. 38b).

We then examined if the cell identities assigned to the different clusters were associated with transcriptional programs that defined their cellular function. A large number of these genes were among those identified as differentially expressed. Genes involved in axon guidance and tract formation (e.g. L1CAM and NRN1) were enriched in the neuronal clusters C1, C2 and present to a lesser extent in C4 (Fig. 38c & d). This was likely due to the advanced maturity of C4, marked by high expression of genes involved in later developmental processes such as synapse formation (e.g. VGLUT, CNTNAP2, SYT4) (Fig. 38c & d). High expression of DLX2, DLX4, ERBB4 and VGAT in C5 (Fig. 38c & d) indicated the presence of a very distinct interneuron population and supported earlier histological staining data (Fig. 30a,b & c). Only few RGC progenitors in C3 expressed markers of astroglial maturity (e.g. AQP4, GJA1) and oligodendrocyte lineage (e.g. OLIG1, PDGFRA) and the C6 progenitor cluster displayed high expression of cell cycle genes (e.g. CENPF, TOP2A) (Fig. 38c &

d). Overall, these analyses revealed a clear correspondence between cell types and the transcriptional program underlying their function.

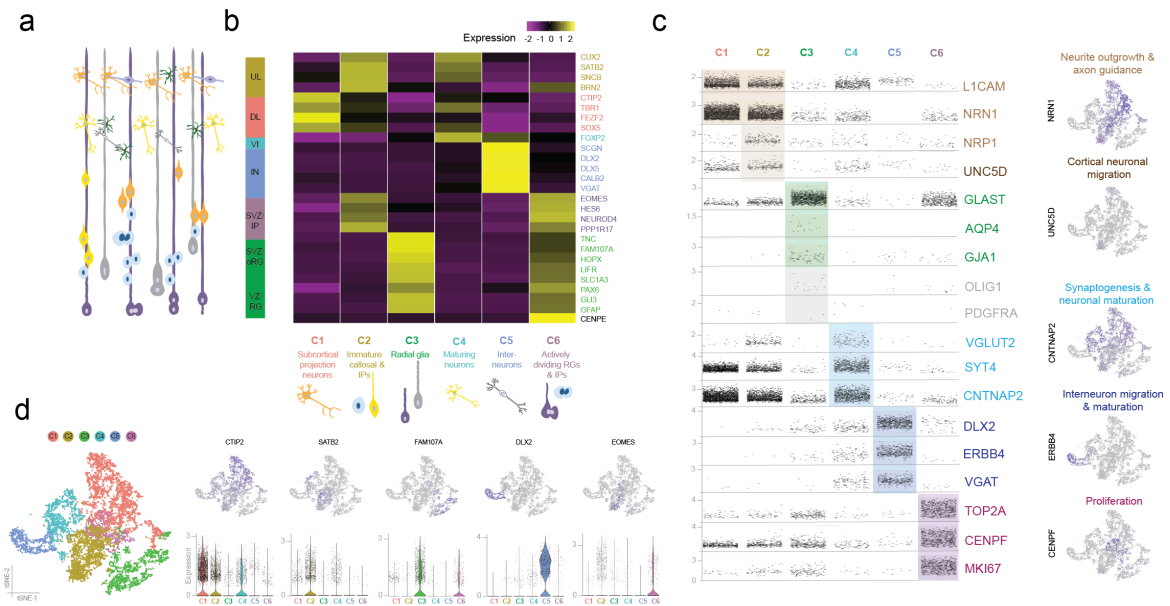


Figure 38 scRNA-seq clustering is driven by cell type identity and developmental cell state.

a, Schematic of the cell types that populate the developing human fetal neocortex : ventricular zone (VZ) containing aRGCs and , subventricular zone containing bRGCs and IPCs, deep (DL) and upper cortical layers (UL) of neurons, interneurons (IN) and layer VI neurons. b, Heat map showing scaled mean expression levels of layer- and cell type-specific genes within the six clusters identified by PCA. Cell layers, cell types (bottom) and marker genes (right) are colour-coded according to cluster identity (C1-6, bottom). Colour bar reflects the gene expression levels, purple being low expression and yellow being high expression. c, On the left are scatterplots of normalised gene expression levels per cell within each cluster for genes relevant for progenitor, glial and neuronal function. On the right are two-dimensional tSNE feature plots showing example genes confined to a particular cluster or multiple cell populations. Colour coding represents functional gene association. d, On the left is a 2D tSNE plot of colour-coded clusters and on the top right are 2D tSNE feature plots showing the distribution of cells expressing the DL marker CTIP2, the UL marker SATB2, the bRGC marker FAM107, the ventral telencephalic marker DLX2 and the IPC marker EOMES (i.e. TBR2) across the six main clusters identified by PCA (C1-6). At the bottom right are scatter plots showing normalized expression values per cell within each cluster for the 5 selected genes, violin plots are shown where the proportion of cells expressing a given gene is the highest. Tails of the plot were trimmed to represent expression levels maxima and minima. The central hinge represents the median value for each cluster. The distribution in each cluster is based on the filtered and merged datasets derived from the six organoid slice samples (n = 4191 cells for C1, 3565 cells for C2, 2068 cells for C3, 1658 cells for C4, 1658 cells for C5, 1658 cells for C6).

for C4, 952 cells for C5, 846 cells for C6).). The data presented were acquired and analysed by analyzed by George Gibbons, Lea M.D. Wenger and András Lakatos on ALI-COs generated by me.

ALI-COs present distinct populations of deep- and superficial-layer neurons with specific projection patterns

To validate the scRNA-seq analyses findings that ALI-COs harbour distinct populations of deep- and superficial-layer neurons we performed immunostainings for well-characterised neuronal layer markers on samples from different batches. Although early in development the cortical wall does not display well-defined layers with sharp borders, broad clustering of superficial- and deep-layer neurons can already be observed. Staining for the callosal neuron marker SATB2 and the corticofugal projection neuron marker CTIP2 revealed SATB2⁺ neurons distributed more superficially than CTIP2⁺ neurons, found predominantly in more central regions of the tissue (Fig. 39a). Similarly, FEZF2⁺ and SOX5⁺ corticofugal projection neurons were found in more central regions of the tissue, while CUX1⁺ upper layer neurons sat in more external regions of ALI-COs (Fig. 39b & c). BRN2, which in the adult brain is expressed in layer I-III and Vb neurons showed a much broader distribution across the ALI-CO (Fig. 39b).

Broadly, in ALI-COs we observed two axon tract types, inwardly projecting (Fig. 39d) and escaping (Fig. 39e), reminiscent of *in vivo* intracortical and corticofugal projections, respectively. To test whether in ALI-COs, like *in vivo*, deep- and superficial-layer neurons project as coherent tracts with distinct hodology, we performed retrograde labelling with cholera-toxin subunit B (CTB) on internal and escaping tracts marked by fGFP expression. Samples were stained for the callosal identity marker CUX2 and the corticofugal projection neuron marker CTIP2, and the following three neuronal populations were quantified: CTB⁺/CUX2⁺, CTB⁺/CTIP2⁺, CTB⁺/CUX2⁺/CTIP2⁺ (Fig. 39f & g). While $91.1 \pm 11.0\%$ (mean \pm s.d.) of neurons projecting into internal tracts were positive for CUX2, only $35.7 \pm 19.9\%$ of escaping tracts stained CUX2⁺ (Fig. 39h). By contrast, $65.4 \pm 24.3\%$ of escaping tract projection neurons were CTIP2⁺ with $20.6 \pm 6.4\%$ being positive for only this marker, compared with $1.1 \pm 1.5\%$ of internally projecting neurons (Fig. 39h). These data suggest that tract hodology and morphology largely match correct molecular identity.

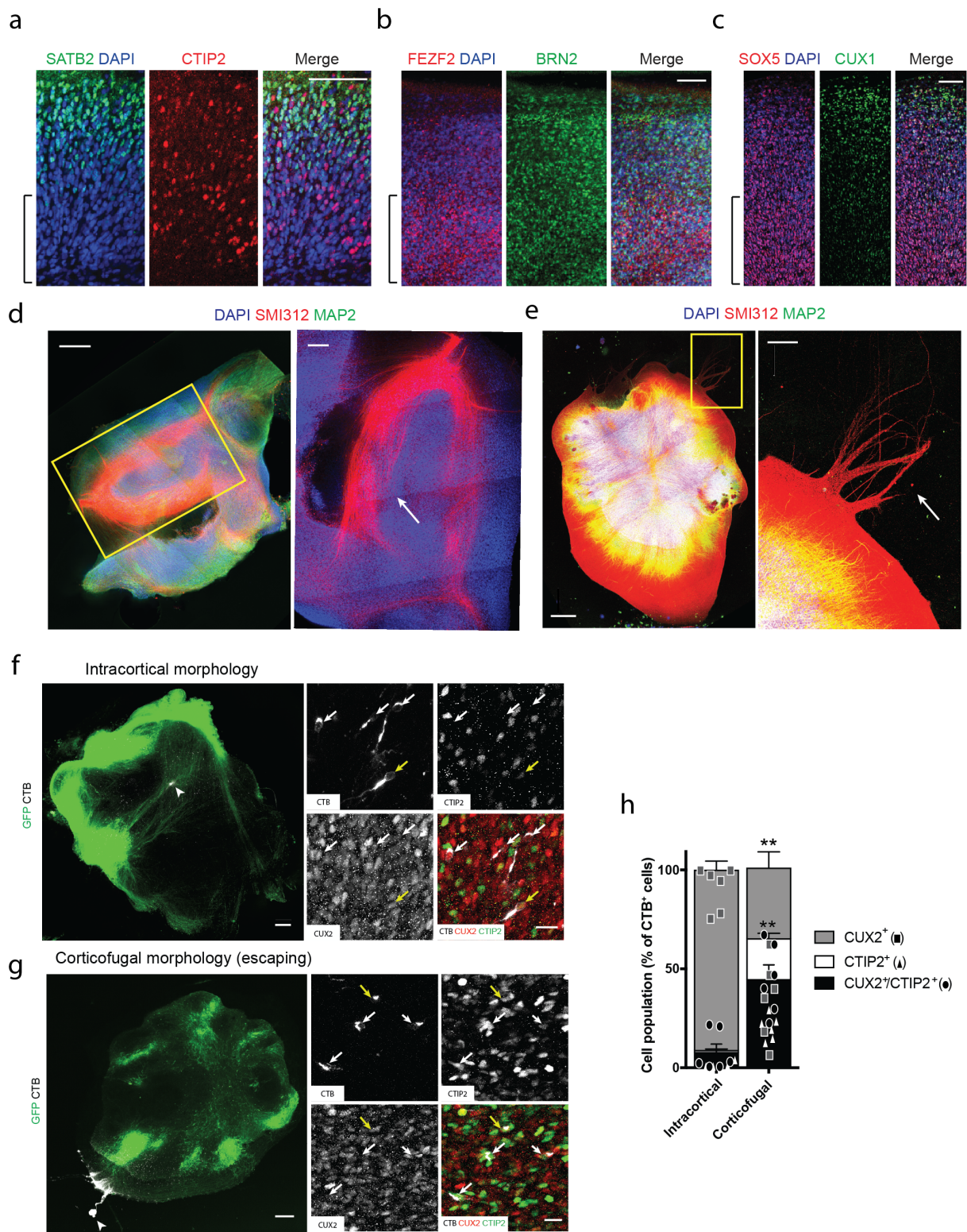


Figure 39 Deep- and superficial layer neurons in ALI-COs show immature layering and project into bundles with discrete non-random identities.

a, Immunofluorescence staining for the superficial-layer neuronal marker SATB2 (green) and the deep-layer neuronal marker CTIP2 (red) in a 90 day old ALI-CO (70+20 days at the ALI) reveals SATB2⁺ neurons distributed more superficially than CTIP2⁺ neurons. b, Immunofluorescence staining

for the superficial-layer neuronal marker BRN2 (green) and the deep-layer neuronal marker FEZF2 (red) in a 90 day old ALI-CO (70+20 days at the ALI) shows broad distribution of BRN2⁺ neurons and FEZF2⁺ stain more confined to internal regions of the cortical plate. c, Immunofluorescence staining for the superficial-layer neuronal marker CUX1 (green) and the deep-layer neuronal marker SOX5 (red) in an 84 day old ALI-CO (64+20 days at the ALI) shows segregation of CUX1⁺ cells in the external layers of the ALI-CO and SOX5⁺ neurons more internally. Images a-c are representative regions from a single stained ALI-CO each. d, Immunofluorescence staining for the axonal marker SMI312 (red) in a 107 day old ALI-CO (59+48 days at the ALI) shows a large SMI312⁺ axon tract projecting internally into the main DAPI⁺ mass of cell bodies. Inset is a rotated high magnification image of the tract (white arrow). e, Immunofluorescence staining for the axonal marker SMI312 (red) and the dendritic marker MAP2 (green) in a 89 day old ALI-CO (55+34 days at the ALI) reveals escaping tracts projecting away from the main mass of ALI-CO cell bodies in a manner reminiscent of corticofugal projections. Images in d and e are representative images of three independent samples each. f, On the left is a representative image of an ALI-CO with internally projecting fGFP⁺ tracts (green) injected with the retrograde tracer CTB (white), on the right are three individual channel images (i.e. CTB, CUX2 and CTIP2) and merge with CTIP2- green, CUX2-red and CTB-white. g, On the left is a representative image of an ALI-CO with escaping fGFP⁺ tracts (green) injected with the retrograde tracer CTB (white), on the right are three individual channel images (i.e. CTB, CUX2 and CTIP2) and merge with CTIP2- green, CUX2-red and CTB-white. Yellow arrows indicate CTIP2⁺/CUX2⁺ double-positive cells and white arrow indicate CUX2⁺ cells in f and CTIP2⁺ cells in g. Images shown in f and g are representative of six CTB injected ALI-COs each. h, Quantifications of CTB⁺ cells indicate that tracts with internal projection morphology (f) traced back primarily to CUX2⁺ callosal identity cells while escaping corticofugal morphology tracts traced back primarily to CTIP2⁺ corticofugal projection neurons as well as CTIP2⁺/CUX2⁺ double-positive cells. For each condition (i.e. escaping and internal tracts) six ALI-COs derived from four organoids were labelled and all CTB⁺ cells across the entire depth of antibody penetration in whole ALI-COs were counted for CUX2⁺, CTIP2⁺ and CTIP2⁺/CUX2⁺ nuclei. **P=0.0022, Mann-Whitney test, n=6, reported are mean ± s.e.m. values. ALI-COs were fixed 4 days after CTB injection and cultured for a total of 33 days at the ALI (97 days total age). Scale bars, 100 µm (a-c), 500 µm (d and e), 200 µm (d and e insets), 300 µm (f and g) and 20 µm (f and g insets). Madeline A. Lancaster acquired images in a and b, and the quantifications shown in c were done by Magdalena Sutcliffe.

ALI-COs establish neural networks with functional output

Having characterised the cellular composition and projection modalities of organoids grown at the ALI, we sought to test the functionality of both internal and escaping tracts. In order to infer and describe features of functional connectivity we employed three-dimensional (3D) MEA chips to perform extracellular recordings on ALI-COs and analyse correlated spontaneous activity (Fig. 40a). We observed network bursts during which neurons near multiple electrodes across the array fired synchronously, as seen in mature neural networks (Fig. 40b-d). Comparison of correlated activity revealed densely connected local networks where individual nodes would make connections with many others (Fig. 40e). Both long- and short-range connections between nodes showed highly correlated activity and although the strongest connections were found over short distances, activity was most highly correlated at distances greater than the 200 μm inter-electrode distance (Fig. 40e & f). This suggests that ALI-COs show specific network patterns that are not simply nearest-neighbour connections. Correlation analyses of ALI-COs point to specific connectivity patterns becoming established in these cultures.

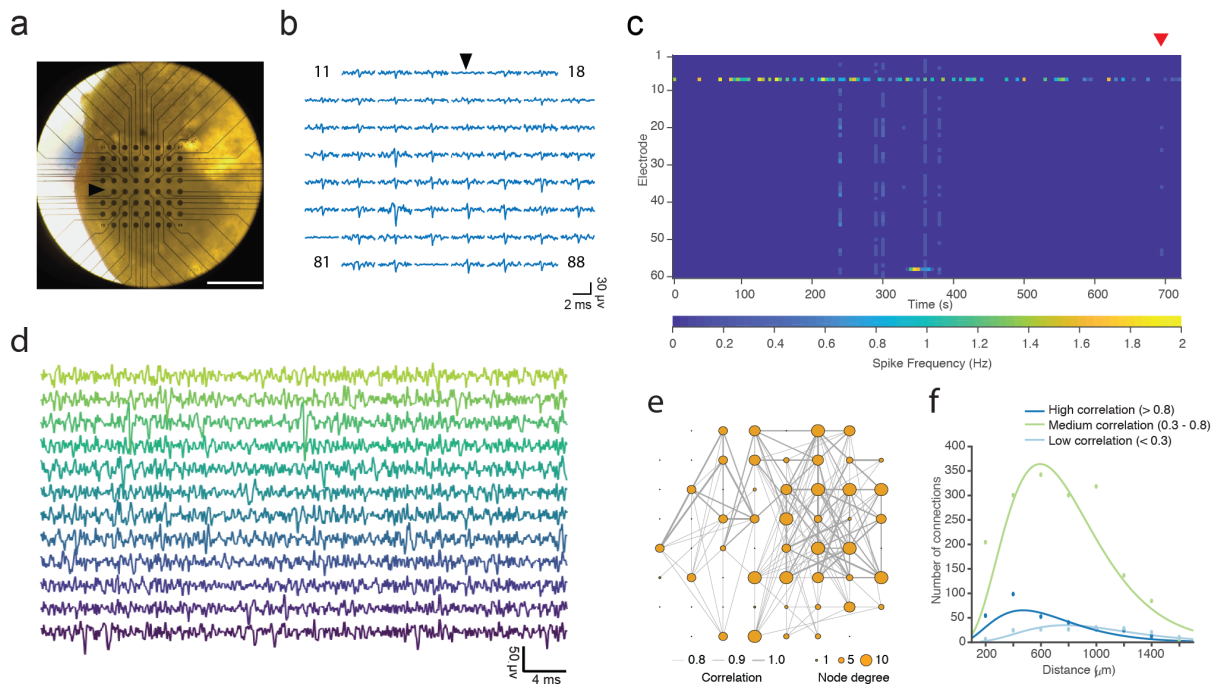


Figure 40 ALI-COs display specific spatial patterns of connectivity.

a, Representative image of a 130 day old ALI-CO (91+39 days at the ALI) upon transfer to a 3D MEA. b, Traces of spontaneous activity (3.2 ms duration) in the 59 electrodes at the time of a network burst. Black arrowheads in a and b indicate the reference electrode. c, Rasterplot of spike frequency (5 ms timebins shown for each electrode) during a twelve minute recording with the red arrow pointing to a network burst shown in d. High resolution 50 ms traces from 12 electrodes at the time of a network

burst showing some of the ms time differences (i.e. jitters) in the initiation of the action potential at different electrodes. e, Network plot displaying functional connectivity patterns between specific electrodes of the ALI-CO shown in a. Line thickness represents the strength of correlation between two nodes of the network and node size denotes the number of connections made by each node. The spike-time tiling coefficient was used to determine correlated activity as described in the Materials & Methods section. f, Distance distribution between functionally connected nodes in e colour-coded according to correlation strength classes; high-blue, medium-green, low-light blue. The plot shows highest correlated activity at 400 μm , 600 μm for medium correlated activity and 800 μm for low correlated activity. Scale bar, 1 mm (a). The data shown were acquired by Susanna Mierau and me and analysed by Timothy Sit.

In order to examine the functionality of escaping tracts we established a chimeric co-culture system of ALI-COs and mouse spinal cord explants. Prior to vibratome sectioning mouse spinal cords with dorsal root ganglia and overlying paraspinal muscles were dissected from E12.5 mouse embryos and embedded with organoids in LM agarose (Fig. 41a). Coronal sections of mouse spinal cord explants were thus cultured adjacent to ALI-COs (Fig. 41a). After approximately 2-3 weeks in culture dense axon tracts positive for the human specific marker STEM121 could be seen projecting from the ALI-CO (STEM121⁺/MAP2⁺) to the mouse spinal cord explants (STEM121⁻/MAP2⁺) (Fig. 41b). High magnification imaging of the mouse spinal cords in co-culture revealed the presence of mature synapses, comprising human-specific pre-synaptic synaptophysin and post-synaptic Psd95, juxtaposed between human processes (STEM121⁺) and mouse spinal cord neurons (STEM121⁻/MAP2⁺).

Live imaging of the mouse paraspinal muscle tissue revealed high amplitude concerted contractions with irregular frequency (Fig. 41d). These high amplitude contractions were coordinated and of higher amplitude than those of non-innervated spinal cord explants (Fig. 41e). In order to test whether contractions of innervated spinal cords depended upon connection with the ALI-CO we performed lesion of the ALI-CO axonal tract. Following axotomy, high amplitude contractions were replaced by low-amplitude uncoordinated single-muscle fibre fibrillations (Fig. 41d). To verify that loss of high amplitude contractions was not caused by simple perturbation of the mouse spinal cord explant we performed an incision in the agarose near the spinal cord of an un-innervated explant (Fig. 41e). Disturbance of the mouse spinal cord did not have any apparent effect on the ability of the explant muscles to contract, thus suggesting that concerted high amplitude contractions depended on the connection to the ALI-CO (Fig. 41e).

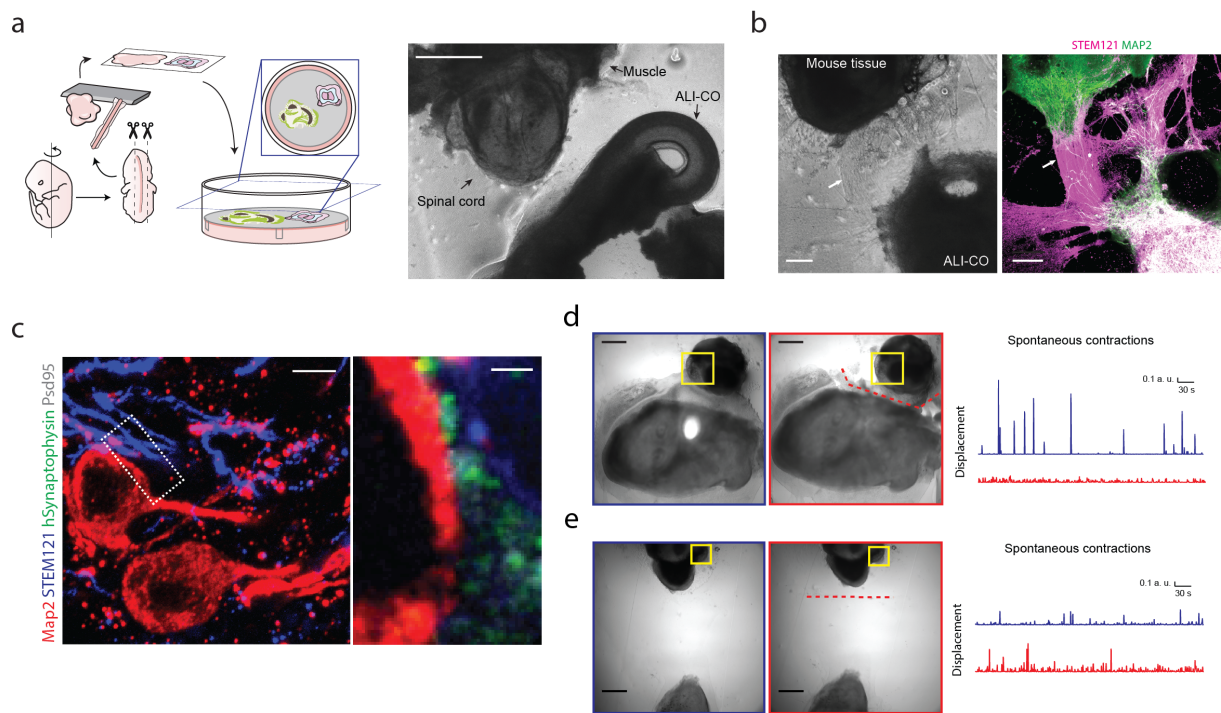


Figure 41 ALI-COs establish functional connections with mouse spinal cord explants.

a, Schematic depicting the ALI-CO-mouse spinal cord explant co-culture procedure, mouse spinal cords with intact paraspinal muscles were dissected from E12.5 mouse embryos, co-embedded in LM agarose adjacent to ALI-COs, vibratome sectioned and cultured at the ALI as detailed in the methods section. Image shows a co-culture 24 hrs after establishment with arrows pointing to the mouse spinal cord explant, intact muscles and the ALI-CO. b, Immunofluorescence image of a 123 day old co-culture (55+68 days at the ALI) for the human specific cytoplasmic marker STEM121 (magenta) and the dendritic marker MAP2 (green) shows a MAP2⁺/STEM121⁺ ALI-CO projecting via a STEM121⁺/MAP2⁻ axon tract (white arrow) into the mouse spinal cord explant (MAP2⁺/STEM121⁻). c, On the left is a maximum-projection immunofluorescence staining of a cryosection of mouse spinal cord explant connected to an 84 day old ALI-CO (52+32 days at the ALI) showing MAP2⁺/STEM121⁻ mouse spinal cord neurons in close contact to STEM121⁺ human axons. The higher magnification inset on the right shows the point of contact between a mouse spinal neuron soma and a human axon with foci of human-specific Synaptophysin and Psd95, suggesting the presence of mature synapses between ALI-CO neurons and mouse spinal cord neurons. d, Widefield image showing a human ALI-CO (bottom) connected to a mouse spinal cord explant (top right) after 36 days at the ALI (100 day old ALI-CO). Left image is before (blue box) axotomy, right image is after (red box) axotomy, and the site of incision is indicated by the red dashed line. On the right are corresponding traces, before (blue) and after (red) axotomy. Following axotomy high amplitude contractions are lost and replaced by low amplitude fibrillations of individual muscle fibres. e, Widefield image showing an ALI-CO (bottom) mouse spinal cord explant (top) coculture after 40 days at the ALI (104 day old ALI-CO) where no connection was yet established. Left image is before (blue box) axotomy, right image is after (red box)

incision of the agarose surrounding the mouse spinal cord explant (red dashed line). On the right are corresponding traces, before (blue) and after (red) axotomy. Disturbance of the mouse spinal cord does not cause a decrease in the size or frequency of contractions. Scale bars, 500 μm (a, d and e), 200 μm (b), 5 μm (g), 1 μm (g inset).

To further test whether ALI-CO corticofugal tracts could control mouse paraspinal tissue we performed extracellular stimulation of the ALI-CO tracts. Stimulation with single current steps of increasing intensity was sufficient to elicit contractions of increasing amplitude (Fig. 42a – c). Contractions were intensity dependent but above a certain voltage we observed saturation, and the muscles could not generate higher amplitude contractions (Fig. 42c). Stimulations given at a time interval of 30s and 15s were seen to reliably give on-demand contractions (Fig. 42d) and repeated stimulation over a 30s time interval by a TTL-pulse generator could reliably drive trains of muscle contractions up to a frequency of 1 Hz (Fig. 42e). Application of the same stimulation protocols following severing of the connection between ALI-CO and spinal cord did not result in any contraction response, suggesting that the effect seen was dependent on the axonal connection and not caused by spread of the electrical current (Fig. 42a, d & e). In support of this, sample immunostaining after axotomy revealed robust STEM121⁺ human tracts innervating the mouse spinal cord (Fig. 42f).

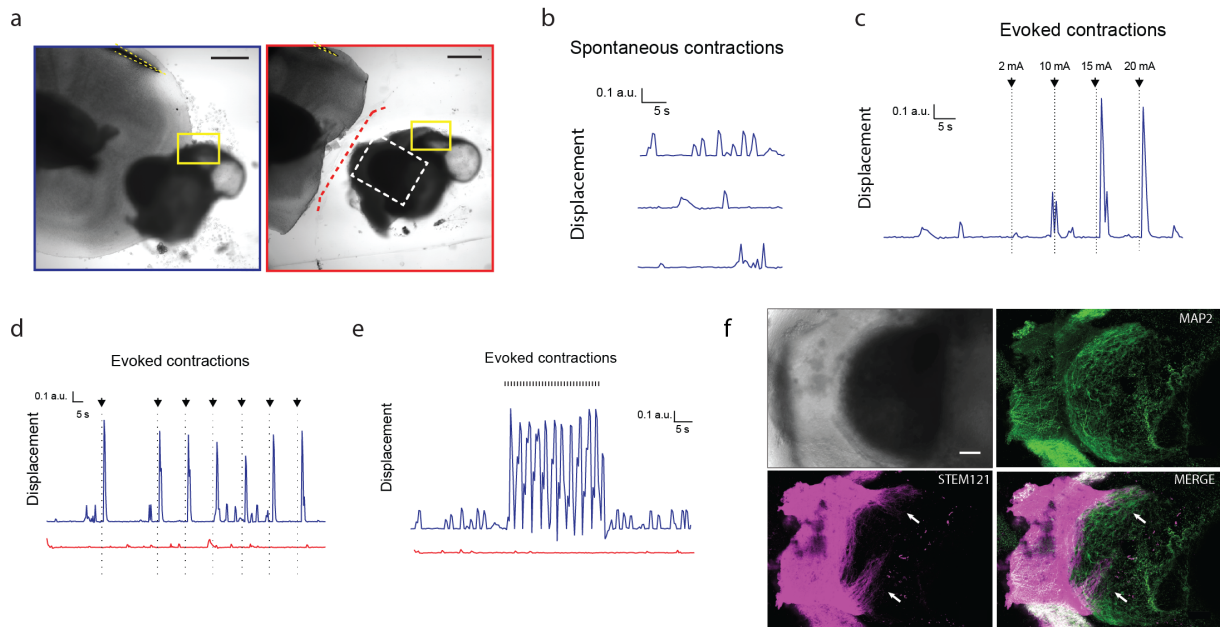


Figure 42 Stimulation of the tract connecting the ALI-CO to the mouse spinal cord explant elicits contractions that are abolished by axotomy.

a, Widefield images of the ALI-CO-mouse spinal cord explant co-culture (52+32 days at the ALI) used for recordings b-e and immunofluorescence analysis in f. Blue boxed image was taken before axotomy and red boxed image after axotomy, boxed yellow is the region of interest used for motion analyses, red dashed line indicates the site of axotomy, white dashed box is the region shown in f and dashed yellow is the outline of the stimulation electrode b, 30 second traces of spontaneous contraction of the mouse paraspinal muscle measured as displacement. c, Application of single steps of increasing current (2, 10, 15 and 20 mA, 120 μ s long, black arrows) at 30, 40, 50 and 60 s of the recording triggers contractions (i.e. displacement) of increasing amplitude (blue trace). d, Application of single current steps (15 mA, 120 μ s long, black arrows) at 30, 60, 75, 90, 105 and 120 s of the recording reliably evokes muscle contractions (blue trace). e, Evoked muscle contractions (i.e. displacement) in response to 30 s of 1 Hz TTL stimulation with 15 mA current pulses (period of stimulation marked by black hash marks, 120 μ s pulses) (blue trace). Axotomy of the tract between the mouse spinal cord tissue and the ALI-CO leads to a complete loss of evoked contractions upon administration of the same stimulation paradigms (red traces) in d and e. Note in d some small residual spontaneous contractions after axotomy. f, Maximum intensity projection immunofluorescence staining for the human specific cytoplasmic marker STEM121 (magenta) and the dendrite marker MAP2 (green) reveals human axon tracts innervating the mouse spinal cord and shows that, whilst the human tissue was severed in the axotomy, the mouse spinal cord was preserved intact. The data shown are representative of six independent experiments of which two included axotomy. Scale bars, 500 μ m (a) and 100 μ m (f). Microelectrode stimulation was performed by me and Susanna Mierau, and analyses were done by me using an ImageJ macro written by Jerome Boulanger.

To further validate that muscle contraction was dependent on the connection established between ALI-CO neurons and mouse spinal cord neurons we repeated the same stimulation paradigms on a different ALI-CO-mouse spinal cord co-culture (Fig. 43a). We then repositioned the stimulation electrode at a comparable distance from the mouse spinal cord as previously but, rather than in a tract, placement was in an internal region of the organoid, that lacked any obvious direct connection with the mouse spinal cord (Fig. 43b). While application of 1Hz frequency current steps with increasing amplitude over 10s time windows elicited contraction responses of increasing amplitudes when the electrode was placed in the tract, this was not observed following electrode displacement or axotomy (Fig. 43b & c). Post-axotomy immunofluorescence analyses confirmed the presence of thick human axon tracts innervating the mouse spinal cord (Fig. 43d). Lastly, the median latency of response from stimulation to beginning of muscle contraction was measured to be approximately 37 ms (with a measurement uncertainty of 17 ms, the time interval between two consecutive frames) (n=35). The latency measurement supports the fact that muscle contraction was mediated by synaptic transmission.

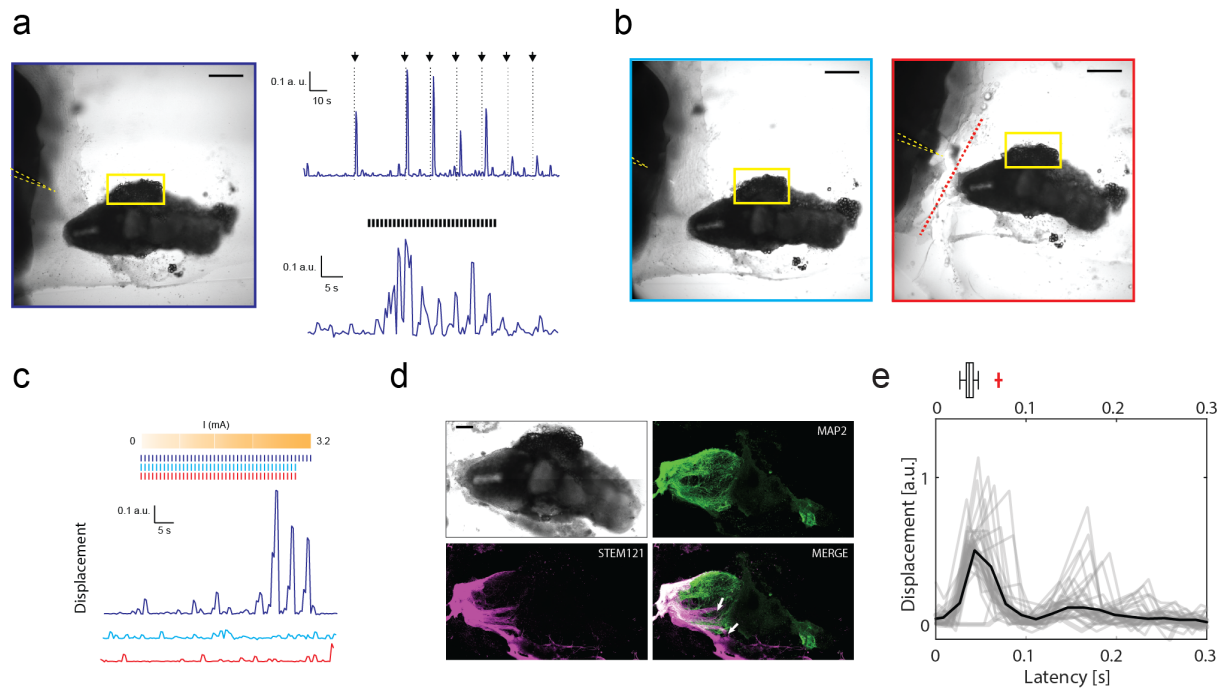


Figure 43 Displacement of the stimulation electrode and axotomy abolish evoked contractions and contractions display latency.

a, Widefield image of the ALI-CO-mouse spinal cord explant co-culture (48+31 days at the ALI) used for recordings a and c. The top trace (blue) shows muscle contractions (i.e. displacement) evoked by single current stimulation (black arrows, 3.2 mA, 120 μ s) at 30, 60, 75, 90, 105 and 120 s. The bottom trace (blue) shows trains of contractions in response to 30 s of 1 Hz TTL pulses (period of stimulation indicated by black hash marks, 3.2 mA, 120 μ s). b, Widefield image of the ALI-CO shown in a after stimulation electrode displacement (left, light-blue box) and axotomy right (right, red box). In a,b and c blue indicates pre-axotomy, red indicates post-axotomy, and light-blue indicates electrode displacement, yellow box marks the ROI used for displacement quantifications, dashed yellow outline marks the positioning of the stimulation electrode and red dashed line marks the incision site. c, Precise electrode placement determines the ability to evoke muscle contractions by stimulation and upon electrode displacement (shown in b left) the response to stimulation is lost (middle, light-blue trace). Placement of the stimulation electrode on the axon tract connecting the ALI-CO to the mouse spinal cord explant leads to evoked responses upon stimulation (top blue trace), while axotomy of the tract leads to a complete loss of high-amplitude evoked contractions leaving only spontaneous low-amplitude fibrillations (bottom, red trace). The stimulation protocol applied to all three sample configurations in c was 1 Hz TTL-triggered pulses (120 μ s, increasing current intensity every 10 seconds for 0.2, 0.8, 1.6 and 3.2 mA) with the final 1Hz TTL-stimulation window lasting 14 s for the control trace (top, blue trace). The data shown are representative of six independent experiments of which two included axotomy. d, Maximum intensity projection immunofluorescence staining for the human specific cytoplasmic marker STEM121 (magenta) and the dendrite marker MAP2 (green)

reveals human axon tracts innervating the mouse spinal cord and shows that, whilst the human tissue was severed in the axotomy, the mouse spinal cord was preserved intact. e, Overlay of evoked muscle contraction waveforms elicited by repeated current pulses (15 mA, 160 μ s, 0.6 Hz) and waveform average (black), showing the first peak at \sim 37 ms after stimulation. Reported above is a box and whiskers plot capturing the spread of the individual contraction events (n=35), center line is the median, limits are quartiles, whiskers are minimum and maximum. Red cross is an outlier, with another outlier recorded at 1 s (not shown), recording was done at 104 days (42 days at the ALI). Scale bars, 500 μ m (a and b) and 200 μ m (d). Microelectrode stimulation was performed by me and Susanna Mierau, and analyses were done by me using an ImageJ macro written by Jerome Boulanger. The latency shown in e was computed by Jerome Boulanger with help from Emmanuel Derivery

Electron cryotomography (ECT) of ALI-CO escaping tracts uncovers elements of ultrastructural organisation of developing axons

Not only do ALI-CO culture conditions extend the range of developmental processes that can be studied *in vitro*, but they can also help to expand the array of techniques applicable to the study of such processes. A particularly intriguing avenue of research is the study of the axon ultrastructure during development. Historically, electron microscopy (EM) has revealed a wealth of information on the intracellular organisation of neurons. However, because in an electron microscope specimens are exposed to vacuum, traditionally samples for transmitted electron microscopy (TEM) were fixed, dehydrated, embedded in plastic and sectioned (Oikonomou et al. 2016). These procedures cause sample denaturation and introduce artefacts in the analyses.

These limitations were overcome by the development of cryofixation techniques in which specimens are cooled so rapidly that the water molecules, rather than forming ice crystals, produce a thin layer of vitreous ice, which preserves intact native cellular structures (Oikonomou et al. 2016). Plunge freezing is one of the main techniques used for cryofixation and involves plunging the sample into liquid ethane by means of a guillotine. One of the major hurdles in achieving vitrification is sample thickness, which should be less than 500 nm for high-resolution ECT studies. For this reason, while prokaryotes and viruses are particularly amenable to ECT, mammalian cells are challenging samples and work on tissues is virtually out of reach (Mahamid et al. 2016; Ader et al. 2019). Therefore, ECT studies on neuronal *in situ* cellular architecture are typically performed on dissociated primary neuronal cultures and rely on focused ion beam (FIB) milling to achieve the required thickness (Bäuerlein et al. 2017).

Albeit powerful, this approach suffers from limitations, FIB milling is technically involved and reduces throughput, already very low in these studies and it might not be strictly necessary when analyses focus on neuronal processes. If the research question is aimed particularly at axons, using dissociated cultures does not allow easy distinction between axons and dendrites on ECT grids. Moreover, we previously discussed how neurons *in vitro* do not form bundles, rather they send out processes in a random fashion. This precludes the study of ultrastructural aspects of axon pathfinding and fascicle formation. With this in mind, we reasoned that ALI-CO cultures and in particular their escaping bundles could be leveraged to glean cellular insight into axonal architecture by ECT.

In order to test the feasibility of such an approach we prepared samples for a cryo-correlative light and electron microscopy (cryo-CLEM) experiment. By this technique, specific or dynamic information from fluorescent microscopy (FM) can be integrated with high-resolution structural information from EM to study the effect of genetic perturbation of the system (Ader et al. 2019). ALI-COs were electroporated with fGFP and prepared following the standard protocol, with the only

difference that care was taken to remove any LM agarose surrounding the tissue before collection on PTFE inserts (Fig. 44a & b). After a week in culture, carbon and gold EM grids coated with laminin and fibronectin were placed adjacent to the organoid slices (Fig. 44a & c). After 2-3 additional weeks at the ALI axons could be seen extending to the centre of the EM grids in regions suitable for acquisition (Fig. 44d). Grids were retrieved from ALI inserts by stamping with biopsy punches and immediately plunge frozen into liquid ethane by means of a foot-operated guillotine. Grids were screened by cryo FM and single GFP⁺ axons could be seen within bundles over the grid (Fig. 44e). Suitable axon target regions for ECT were chosen for tomogram acquisition (Fig. 44f). Reconstructed tomograms revealed the crowded molecular environment of the axon with an intricate meshwork of microtubule bundles and closely intermingled sheets of endoplasmic reticulum (ER) (Fig. 44g, false coloured golden). The experiment demonstrates the feasibility of cryo-CLEM on ALI-CO-derived axons to acquire high-resolution structural information.

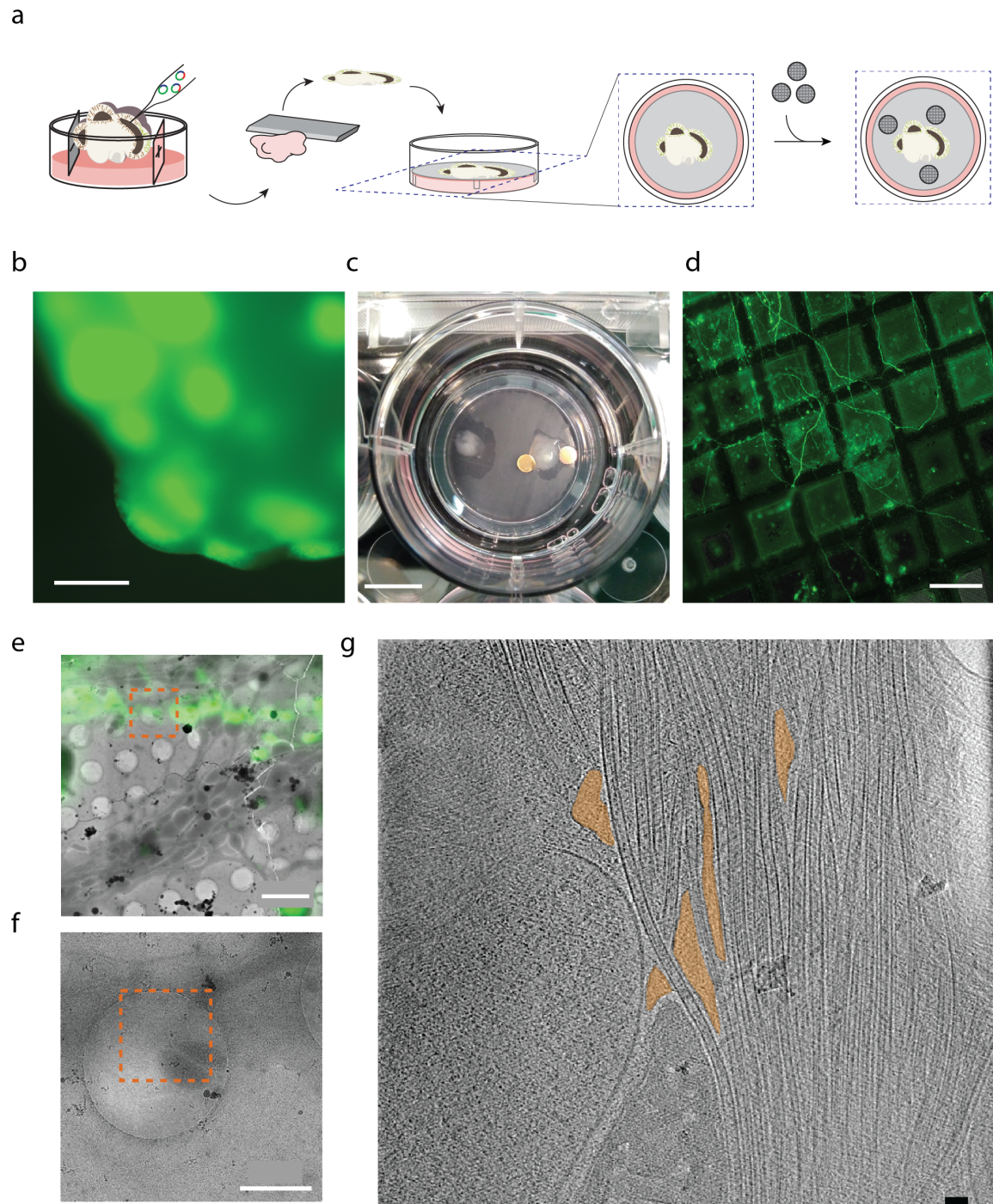


Figure 44 Workflow for cryo-CLEM on ALI-CO-derived axons.

a, Schematic of the steps for cryo-CLEM on ALI-CO-derived axons, where organoids were electroporated, sectioned and cultured at the ALI for a week before placement of EM grids. Detailed procedure is described in Materials and Methods. b, Widefield fluorescence image of a fGFP⁺ organoid prior to ALI-CO preparation. c, Overview image of a PTFE cell culture insert with ALI-COs and adjacent EM grids immediately after placement. d, Cryofluorescence tiled overview image of ALI-CO axons grown on EM grids after approximately 3 weeks at the ALI. The image shows how

GFP⁺ axons have extended away from the main mass of the organoid and grown on the grids reaching regions suitable for tomogram acquisition. e, High-magnification image overlay of brightfield and fluorescence of escaping ALI-CO bundles on grids with single GFP⁺ axons. Red dashed boxes indicate the regions where the EM micrograph shown in f was acquired. f, Cryo-EM overview image of the area outlined by the red dashed square in g. The tilt-series was acquired at the site indicated by the red dashed boxes. g, Example virtual slice through an electron cryo-tomogram acquired on the GFP⁺ ALI-CO shown in e and f. False-coloured golden structures are ER sheets intermingling with microtubules and closely juxtaposed to the plasma membrane. The virtual slice shown is rotated by -90° relative to e and f. Scale bars, 500 μ m (b), 1 cm (c), 100 μ m (d) 5 μ m (e), 2 μ m (f) and 100 nm (g). The data presented in d-g were acquired and analyzed by Patrick Hoffmann from samples I prepared.

Chapter 5: Discussion

ZEB2 is dynamically expressed in the developing neuroepithelium

We have shown that ZEB2 protein is detectable in human cerebral organoid progenitors from day 6 to approximately day 21. Immunofluorescence has revealed that *ZEB2* and glial markers exhibit a mutually exclusive expression pattern in progenitor cells, suggesting that *ZEB2* is no longer needed in progenitors after the transition to aRGCs. From this point on, *ZEB2* expression shifts from neural progenitors to postmitotic neurons. Bioinformatic analyses on published datasets as well as immunofluorescence data from E10.5 to E16.5 mouse cortices have confirmed this switch in expression from progenitors to neurons. Furthermore, our expression data are in agreement with previous reports (Miyoshi et al. 2006; Seuntjens et al. 2009), suggesting that organoids are a valid model to study the function of *ZEB2* at such early developmental stages. This was an essential validation step as organoid studies to date have only focused on later neurodevelopmental aspects, such as production of deep and superficial layer neurons.

ZEB2 has a well-established role in EMT induction in a variety of cellular models and we found intriguing its expression in the early neuroepithelium. *ZEB2* has been shown to limit the mesendoderm-inducing effects of Activin-Nodal signalling and promote neuroectodermal induction in hESCs (Chng et al. 2010). In mouse, *Zeb2* is critical for exit from the epiblast state and links the pluripotency and methylation networks with differentiation (Stryjewska et al. 2016). Although we are missing quantitative expression data for *ZEB2*, in the mouse neuroectoderm its expression sharply drops between E10.5 and E11.5. By contrast, in human organoid NECs, after the initial neuroectodermal induction phase, between day 6 and 11, *ZEB2* protein and mRNA levels appear to steadily decline over the course of 10 days. These different expression trajectories in mouse versus human may have an effect on the behaviour of NECs, influencing their initial expansion.

Interestingly, the sudden change in detectability of *ZEB2* protein before and after day 11 may indicate different functions of this factor at these two stages. Our data seem to suggest that before day 11 the N-terminus of *ZEB2*, which overlaps several known functional domains of the protein, is either engaged in cofactor interactions or in a different conformational state than after day 11. We examined the possibility that this change could be due to differences in splice isoform usage but we were not able to observe any stage-specific isoform switch. Splice variant PCR analyses revealed that transcript I and II of *ZEB2* maintain the same stoichiometric ratio throughout the time points assayed. This leaves the possibility that the difference in detectability may be due to binding to a different interaction partner, which might underpin a different *ZEB2* function. It is in fact known that depending on its interaction partners *ZEB2* can act either as a transcriptional repressor or activator and

work in *Xenopus* has shown that the N-terminal zinc-finger cluster is strictly required for neural induction (Nitta et al. 2007).

Studying the interactome of ZEB2 in organoids is extremely challenging. First of all, this type of analysis requires very large amounts of starting material, which are difficult to obtain due the minute size of early EBs and several labour intensive steps in the protocol. Secondly, we are currently missing a ZEB2 antibody suitable for pull-down experiments (Stryjewska et al. 2016) and the majority of commercially available ZEB2 antibodies are raised against the N-terminus of the protein, which according to our analysis should be inaccessible before day 14 of organoid protocol. Introducing a C-terminally tagged exogenous version of ZEB2 is a possible strategy but our work suggests that overexpression of this gene leads to a premature switch to neurogenesis, thus constitutive expression in stem cells may have adverse effects. CRISPR-Cas9 mediated tagging of the endogenous locus by HDR would be in principle the best approach but suffers from low success rate and long editing time. A more feasible strategy might be to introduce in the *ZEB2*^{+/-} background an exogenous copy of *ZEB2* carrying a C-terminal epitope tag. In fact, possible detrimental effects of the introduction of the transgene may be offset by the absence of a functional copy of the gene, leading potentially to a functional rescue of the phenotype. In addition, the C-terminal epitope would provide us with a direct handle on the protein, and the high specificity and affinity of available antibodies against these tags might reduce the amount of starting material required for analysis.

ZEB2 regulates the cell adhesion properties and architecture of the neuroepithelium

To study *ZEB2* function in cerebral organoids we established heterozygous loss-of-function hESCs. We demonstrated that after genome editing the cells maintain normal karyotype and are not affected in their pluripotency. However, upon differentiation they display a remarkable phenotype, characterised by thin and elongated buds. In depth characterisation of one of the mutants revealed that these structural changes are accompanied by an overall increase in cell-cell adhesion within the tissue (Fig. 45). As mentioned in the introduction, under many aspects, neurogenesis resembles a progressive and extended EMT process where the epithelial cells of the neuroectoderm eventually produce fully mesenchymal type cells such as neurons and astrocytes (Aaku-Saraste et al. 1996). Notably, many genes upregulated during the initial ectoderm-neuroectoderm transition, including *N-cadherin* and *Vimentin*, are typically associated with increased cell-motility and are widely regarded as markers of EMT (Pastushenko & Blanpain 2018; Stemmler et al. 2019). *ZEB2* was previously shown to be involved in cell fate decisions between neuroectodermal and mesendodermal fates, exit from the epiblast state in mouse and *ZEB2* mRNA is expressed in the prospective neuroectoderm of the *Xenopus*, chicken and mouse gastrula (Chng et al. 2010; Stryjewska et al. 2016; Miyoshi et al. 2006; Eisaki et al. 2000; Yasumi et al. 2016). Altogether, these data suggest a proneurogenic role of *ZEB2*.

Interestingly, our data show that loss of one functional copy of *ZEB2* does not lead to a large decrease in EMX1 protein levels, suggesting that differentiation down the neural lineage is not impaired. Nevertheless, we observed a sharp decrease in TBR2⁺ cells and a significant increase in ventricle length. For the latter analysis, a conservative approach was taken and EMX1⁺ buds that did not display any TBR2⁺ cells were excluded. This was done because, although the majority of the *ZEB2*^{+/-} organoid tissue stained positive for EMX1, many elongated buds histologically did not resemble cortical tissue, but more medial identities such as hem and the choroid plexus primordium. This is intriguing as it may indicate that through regulation of *ZEB2* levels different architectonic and neurogenic outcomes can be achieved. *ZEB2* is known to antagonise BMP signalling and BMP4 was identified as the key trigger for choroid plexus induction *in vitro* (Eiraku et al. 2008; M. Watanabe et al. 2012). Therefore, upregulation of BMP signalling following partial loss of *ZEB2* may contribute to induction of more medial hem and choroid plexus identities.

On cortical tissue, decreased *ZEB2* levels appear to delay neurogenesis and promote lateral expansion. Conversely, preliminary gain-of-function experiments show that increased *ZEB2* levels reduce cell adhesion, promote neurogenesis and lead to a reduction in ventricle length. Initial experiments in which *ZEB2*^{+/-} organoids were treated with BMP and TGFβ inhibitors showed a partial rescue of the phenotype, with a noticeable increase in TBR2⁺ cells and restoration of thicker, less elongated neuroepithelial buds. Given that overexpression and rescue data are based on a limited number of experiments, findings from such analyses should be treated with a note of caution. However, the fact that results from a variety of approaches support each other and are in good agreement with previous reports substantiates our observations.

Although we did not examine how partial loss of *ZEB2* affects long-term neurogenic output, our work can explain some of the features associated with Mowat-Wilson syndrome. The neuroepithelial buds of *ZEB2*^{+/-} organoids display abnormally high levels of epithelial-character proteins E-cadherin and Occludin. Despite an overall increase in ventricle length the aberrant delay of mutant NECs in switching to neurogenesis might ultimately lead to a reduction in neurogenic output and microcephaly. Other aspects of this pathology, such as seizures, likely linked to interneuron specification and migration, agenesis of the CC and neural crest defects would require examination at later stages of the protocol and for this ALI-COs represent a valuable tool. Importantly, our data on the effects of partial loss of *ZEB2* function in NECs concur with findings by Rogers et al. (2013) on the role of *Zeb2* in E- to N-cadherin switch during chicken cranial neural crest EMT. The authors showed that Morpholino-mediated knockdown of *Zeb2* in the chicken neural tube leads to an accumulation of E-cadherin and loss of N-cadherin, with resulting failure of NCCs to delaminate (Rogers et al. 2013). Notably, their *Zeb2* knockdown was near complete and the E- and N-cadherin phenotype observed was comparable to our data from *ZEB2*^{+/-} human brain organoids. This, along with the fact that *Zeb2*^{+/-} mice do not display evident neural defects (Maruhashi et al. 2005), might indicate that during human evolution

lower levels of *Zeb2* expression may have been selected for in the developing neural tube. This, in turn, might have promoted a longer phase of NEC proliferation with lateral expansion, leading to an overall increase in cortex size.

Furthermore, our data show that the secreted growth factor FGF2 is a positive regulator of *ZEB2* in a glioblastoma model, and preliminary results from human brain organoids indicate that *ZEB2* in turn suppresses *FGF2* expression (Fig. 45). We thus establish a link between *ZEB2* and a known regulator of neuroepithelial proliferation (Raballo et al. 2000; Vaccarino et al. 1999). Whilst FGF2 was already known to induce expression of several EMT transcription factors, including *ZEB2* (Lee et al. 2018), to the best of our knowledge, *ZEB2*-mediated repression of FGF2 has not been previously reported. Although this finding should be interpreted with caution and more work is necessary to prove its validity across cellular models and establish the precise hierarchy of cellular events, it provides a link between *ZEB2* and a known regulator of NEC proliferation. Furthermore, it explains how an increase in *ZEB2* levels, in addition to changing the cell adhesion properties of NECs, could potentially alter their proliferative behaviour. Therefore, our work provides evidence for *ZEB2* being an important player in neuroepithelial architecture and we go as far as speculating that an evolutionary reduction in *Zeb2* levels in the developing cortical neuroepithelium might have shaped the neocortical primordium across different mammalian species (Fig. 45).

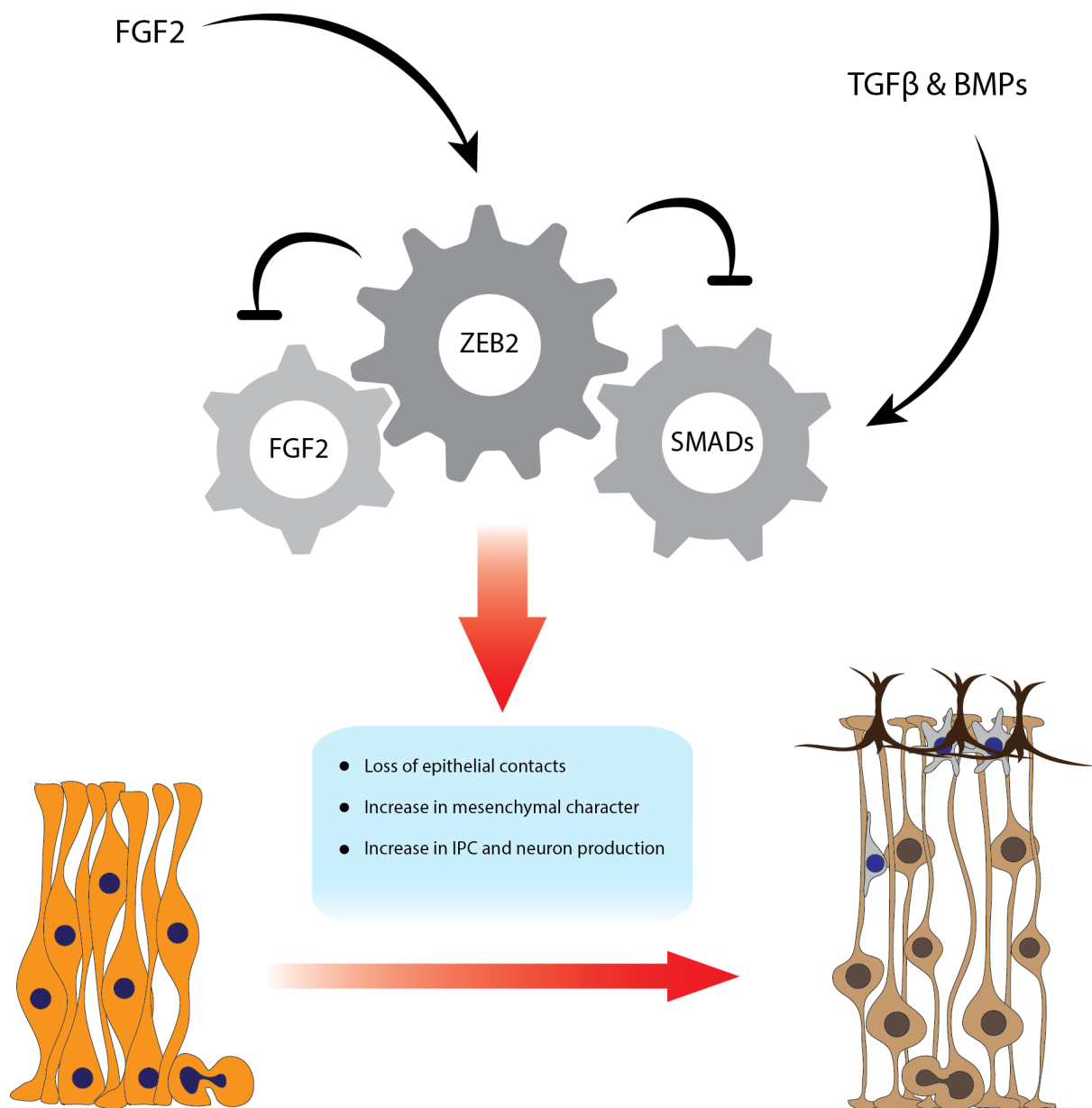


Figure 45 ZEB2 is a central regulator of neuroepithelial architecture.

Schematic model of ZEB2 function. Our experiments have shown that partial loss of ZEB2 leads to increased epithelial contacts and reduced mesenchymal character, reflected by delayed or impaired neurogenesis. Conversely, increased ZEB2 levels lead to a loss of epithelial contacts, an increase in mesenchymal character and higher numbers of neurons and intermediate progenitor cells. Dual SMAD inhibition on *ZEB2*^{+/-} organoids appears to partially rescue the mutant phenotype, with a net reduction in E-cadherin back to WT levels and restoration of IPC and neuron production. Furthermore, our data suggest that whilst FGF2 is a positive regulator of ZEB2, in the developing neuroepithelium ZEB2 acts by reducing FGF2 levels. Thus, we put forward a model where ZEB2 is a central regulator of cell-cell contacts and proliferation in the developing neuroepithelium. By virtue of this key role in NECs we hypothesize that evolutionary changes affecting *ZEB2* expression in the cortical primordium likely had an impact of cortex size determination.

ZEB2: future directions and experimental considerations

Our work on *ZEB2* in human cerebral organoids has opened up several interesting research avenues. We suspect that the apparent masking of the N-terminus prior to day 14 of the protocol likely concerns the early role of *ZEB2* in neural induction, while differences in absolute expression levels after neuroectodermal fate establishment might be driving interspecies differences in NEC expansion. We are currently characterising in more detail the *ZEB2* gain-of-function phenotype; so far we have shown good inducibility of the transgene but potential leakiness remains to be tested. Once the exact experimental conditions for inducible overexpression have been determined, we will carefully quantify the changes in TBR2⁺ IPCs numbers, mitotic figures and ventricle length.

With regard to the rescue experiment by dual-SMAD inhibition, the experiment will be repeated to include treatment with either inhibitor in isolation. This will allow us to determine which cascade *ZEB2* is specifically modulating in the developing neuroepithelium. Importantly, we have validated antibodies against SMAD1,5,8, SMAD2,3 and their phosphorylated forms and this will allow us to biochemically dissect the rescue phenotype. In parallel to biochemical analyses we will quantify the degree of phenotypic rescue through quantification of TBR2⁺ IPC numbers, mitotic figures and ventricle length. We also aim to analyse in more detail the apparent increase in FGF2 levels in *ZEB2*^{+/-} cells. FGF2 treatment on WT organoids should give us insight into what may be the effects of higher FGF2 levels in the *ZEB2*^{+/-} background and ChIP-qPCR experiments will be performed to validate the ChIP-seq data presented. Furthermore, our next experiments will focus on quantifying proliferation in WT and *ZEB2*^{+/-} organoids as well as prolonging FGF2 treatment on immortalised cells to hopefully capture a reduction in endogenous FGF2 transcription.

In order to frame our findings in the context of evo-devo gene expression changes across different mammalian species, over the last few months we have optimised conditions to grow cerebral organoids from mouse, chimpanzee and gorilla, and we have designed cross-species specific PCR primers to perform RT-qPCR profiling of *ZEB2* and its key transcriptional targets. We thus hope to test our model, whereby a decrease in *ZEB2* levels in primates, or more specifically in hominins, may have led to a prolonged NEC proliferation phase and expansion of the starting progenitor pool. One important technical aspect to consider is that in order to draw meaningful conclusions from cross-species comparisons in organoids, modifications of the protocol to match the developmental requirements of different species should be kept to a minimum. Previous work by Otani *et al.* (2016) has shown that *in vitro* differentiation faithfully captures *in vivo* heterochrony, it follows that the timing of the organoid differentiation protocol has to be adapted to each species specifically using morphological and histological benchmarks for optimisation. If unavoidable, addition of patterning cues or growth factors should be kept to a minimum, and ultimately any observations made through

comparative analyses should be used to generate genetically testable predictions. Therefore, should we see the expected differences in *ZEB2* expression across the different species examined, it will be of the essence to test either by gain- or loss-of-function experiments whether alterations of *ZEB2* levels yield results consistent with our model.

ALI-COs: a novel culture system able to model axon pathfinding and tract formation

In an attempt to model later phenotypic aspects of the *ZEB2* heterozygous loss-of-function phenotype, in particular agenesis of the CC, we developed a protocol for air-liquid interface cerebral organoid (ALI-CO) culture. We have shown that by culturing cerebral organoids on cell culture insets at the air-liquid interface it is possible to improve and maintain tissue survival and maturation over extended periods of time (one year was the maximum tested). Importantly, we show that in addition to reducing cell death and improving survival of both deep- and superficial-layer neurons, radial alignment of neurons in the cortical plate is retained. Vibratome sectioning for ALI culture is performed after establishment of the CP in organoids, so as to preserve correct tissue morphology. In this respect, the protocol is very similar to slice culture preparation of foetal cortices at mid-neurogenesis. We presume that it is because neurons radially align within the CP that ALI-COs display remarkable axon projection and bundling behaviours.

Live-image analysis of fGFP-labelled axons revealed striking dynamics, including the early exploratory and saltatory progression of pioneer axons as well as the highly directional and high-velocity movement of follower axons within bundles (Fig. 46). The projection and bundling patterns that ensue indicate a high degree of intrinsic organisation and lead to the establishment of robust tracts. This is remarkable since *in vitro* 2D neural cultures typically display indiscriminate fasciculation between clusters of neighbouring neurons and in organoids random projections are usually seen. Previously, some level of bundling has been achieved *in vitro* either by encasing organoids in agarose cylinders (Cullen et al. 2018), by placing them in micro-chambers (Kawada et al. 2017), and more recently cortico-thalamic assembloids were shown to develop reciprocal projections with a considerable level of bundling (Xiang et al. 2019). Pan-axonal labelling by SMI312 revealed that within ALI-COs axons generate numerous distinct and thick tracts that appear to project between lobules rich in cell bodies. These tracts express different cell-surface receptor molecules, as revealed by the NRP1, RYK and EphrinB1 stains, which mark a distinct subset of callosal bundles within ALI-COs (Mire et al. 2018; Piper et al. 2009). Furthermore, staining for the secreted guidance molecules WNT5A and Netrin-1 showed the presence of discrete organising centres reminiscent of the glial wedge in ALI-COs (Keeble et al. 2006).

It is important to note that these results indicate a remarkable degree of spontaneous organisation of signalling centres and sorting of axons into bundles with coherent identity. Underscoring this, CTB retrograde tracing experiments demonstrated that bundles with internal and escaping hodology, resembling intracortical and corticofugal projections, respectively, map back to neuronal populations with significantly different proportions of upper- and deep-layer neurons. Whilst retrograde tracing on internal tracts revealed an overwhelming majority of CTB⁺/CUX2⁺ cells, escaping tracts had a significantly higher abundance of CTIP2⁺ neurons but also showed considerable numbers of CTIP2⁺/CUX2⁺ cells. It must be noted that in addition to upper-layer neurons, during neurogenesis CUX2 also labels a subset of bRGCs that generate multiple subtypes of cortical projection neurons located across layers II-VI (Eckler et al. 2015; Guo et al. 2013). It is thus plausible that CTIP2⁺/CUX2⁺ cells may represent a population of basal radial glia committed to a deep-layer neuronal fate. Because it is technically challenging to go above four-colour multiplexing, the palette of antigens available for cell type classification by standard fluorescence microscopy is limited. Therefore, our analysis can capture large differences in relative neuronal abundance but it does not have the power to identify small and diverse cell populations in different developmental cell states.

In an effort to overcome this limitation, we employed scRNA-seq to probe the full spectrum of cell types generated in ALI-COs (Fig. 46). These analyses identified five clusters with well-defined molecular signatures corresponding to deep-layer neurons (C1), aRGCs and oRGCs (C3), mature deep- and superficial-layer neurons (C4), interneurons (C5) and actively dividing cells (C6). Interestingly, C3 identified a population of neurons co-expressing the IPC marker TBR2 (i.e. EOMES) and the superficial-layer neuronal marker SATB2 and likely represent non-mitotic IPCs that are differentiating to neurons. Thus, scRNA-seq allows for a more comprehensive analysis of cell identity and cell states. A powerful approach would be to combine retrograde tracing experiments on fGFP⁺-tracts and scRNA-seq. Instead of relying on CTB as retrograde tracer, this approach could employ viruses encoding different fluorescent proteins with distinct oligonucleotide barcodes preceding the poly-A (Rosenberg et al. 2018). Following tract labelling with the virus, it would be possible to visualise the different clusters of neurons expressing GFP and a specific virally-encoded fluorescent protein. Next, scRNA-seq would allow for precise and extensive transcriptional profiling of the neurons giving rise to the specific projection behaviour observed (Fig. 46).

ALI-CO neurons mature and establish functional networks

By means of GFP single-cell viral labelling we have shown that neurons in ALI-COs achieve a remarkable degree of maturity. Neurons display complex dendritic arborifications with numerous spines and abundant mature synapses with juxtaposed pre- and post-synaptic termini. Immunofluorescence and scRNA-seq analyses have revealed the presence of several different interneuron types in ALI-COs, suggesting that functional connectivity may become established in this

system. Previous work has in fact shown that neurons in organoids are active and give rise to networks that can support self-organised activity patterns (Lancaster et al. 2013; Birey et al. 2017; Quadrato et al. 2017). By whole-cell patch-clamp and MEA recordings we have shown that neurons in ALI-COs display spontaneous firing and are able to respond with trains of action potentials upon stimulation (Fig. 46). Furthermore, analysis of correlated activity across the MEA showed that the highest correlated activity was seen at distances greater than the 200 μm inter-electrode distance, underscoring a degree of spatial specificity in the connections made.

Establishment of chimeric co-cultures of mouse spinal cord and organoid slices further demonstrated the ability of ALI-COs to establish functional connections. Whilst lesion of the tracts connecting the ALI-CO to the mouse spinal cord explants produced a loss of spontaneous contractions, stimulation of the ALI-CO tracts evoked muscle contractions. Displacement of the stimulation electrode or lesion of the tract led to a loss of evoked contractions in response to stimulation. Immunofluorescence analysis of the innervated spinal cords revealed human axons projecting onto mouse spinal motor neurons with mature synapses formed, and latency measurements are consistent with a circuit comprising multiple synapses. We thus establish a minimal *in vitro* motor circuit comprising an ALI-CO and a mouse spinal cord explant. This experiment was based on previous co-culture experiments (Pini 1993; Peterson & Crain 1981; Streit et al. 1991) where *in vitro* reconstitution of a minimal circuit allowed access to the cellular and molecular mechanisms underlying target innervation and circuit formation.

Recently, taking a comparable approach, fusion of cortical and thalamic organoids allowed modelling of thalamocortical and corticothalamic connections (Xiang et al. 2019). Importantly, the authors showed that fusion of thalamic and cortical organoids leads to reciprocal synaptic transmission, which is necessary for maturation of thalamic neurons (Xiang et al. 2019). *In vitro* assembly of a minimal circuit represents a powerful approach to dissect and study the function of individual component parts at the cellular and molecular level. In particular, by using organoids to generate the circuit building blocks we can readily introduce mutations in the stem cells of origin to probe the specific function of a given gene in axon guidance, target innervation and synapse formation. In this regard, one obvious advantage of ALI-COs over standard suspension culture of organoids is that it allows ready access to the culture for confocal live imaging over extended periods of time. We thus hope that this model will prove helpful in furthering our understanding of the cues that guide axons during development and of the minimal circuits that become established intrinsically within cerebral organoids (Fig. 46).

Cryo-CLEM on ALI-CO escaping axons

With a preliminary cryo-CLEM experiment on ALI-CO escaping tracts we have demonstrated that it is possible to acquire high-resolution tomograms of axons without the need for FIB milling (Mahamid et al. 2016; Bäuerlein et al. 2017). The experiment was done on fGFP electroporated axons that projected away from the organoid onto the adjacent grids. Samples were screened in a cryo-fluorescence microscope and tomograms of both GFP⁺ and GFP⁻ axons were acquired (Ader et al. 2019). We thus demonstrate that it is possible to acquire ultrastructural information on axons labelled with a membrane-targeted fluorescent protein. Therefore, in principle, by this method it should be possible to introduce fluorescently labelled transgenes and study their effect on axonal ultrastructure (Fig. 46).

One important aspect to consider is that excessive tissue growth on the grid will slow down the freezing process, leading to formation of ice crystals (Oikonomou et al. 2016). Because ultra-rapid cooling is essential for formation of vitreous ice and preservation of intact cellular structures the amount of biomaterial on the grid should be kept to a minimum. This may pose problems if the gene studied has a strong growth phenotype. In fact, during the time needed for modified axons to reach the central region of the grid, WT axons will likely overgrow the entire grid, making vitrification impossible. However, simply from this preliminary proof of concept experiment we were able to observe a striking pattern of ER packing within the axonal varicosities. ER sheets were seen closely intermingled with the microtubule frame of the axon, making contacts with the axonal plasma membrane.

Because growing axons are dependent on lipids synthesized at the ER for growth, the observed pattern of ER organisation is particularly interesting. This has drawn our attention to the extended synaptotagmin (E-SYT) family of proteins, which includes proteins E-SYT1, 2 and 3, involved in ER-plasma membrane tethering and lipid exchange (Sclip et al. 2016; Tremblay & Moss 2016). These proteins show a high degree of evolutionary conservation in eukaryotes, which suggests an important cellular function. However, interestingly, yeast and mammalian cells lacking all three members of this protein family are viable (Sclip et al. 2016; Kikuma et al. 2017). Even more surprisingly, *E-Syt* triple-knockout mice develop normally and do not display obvious developmental phenotypes, are viable and fertile. More recently, it was shown that overexpression of the only E-syt ortholog in *Drosophila* motor axons enhances synaptic growth (Kikuma et al. 2017). We thus plan to investigate by Cryo-CLEM the effect of *E-SYTs* overexpression on the cellular organisation of developing cortical axons in ALI-COs.

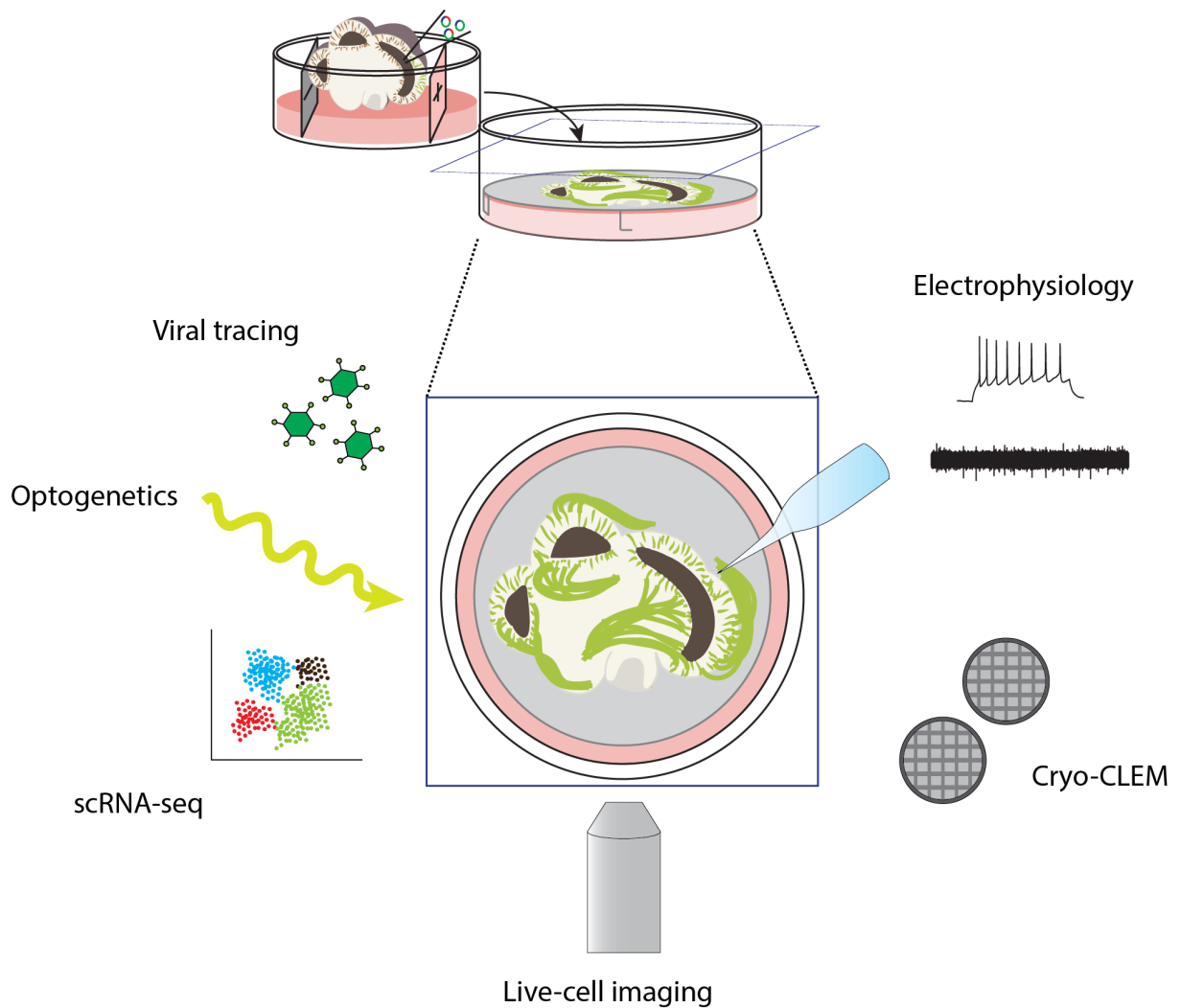


Figure 46 Future applications of ALI-COs.

ALI-COs display improved maturation and long-term survival, thus allowing the study of later neurodevelopmental events. A combination of ALI-COs and novel techniques has the potential to improve our understanding of processes such as axon pathfinding, target selection, synapse formation and network establishment. By live cell imaging we have started characterising the dynamics of growth cones and scRNA-seq analysis has revealed a complex and diverse array of cortical types in these cultures. By combining electrophysiological recordings, viral tracing and optogenetics we can begin to understand what is the intrinsic potential of neurons to spontaneously organise into networks and the degree of complexity of these. Furthermore, ALI-COs open the possibility to specifically study the ultrastructural organisation of axons by cryo-CLEM. This gives us the possibility to visualise with an unprecedented level of detail, not only the intracellular organisation of axons, but also how axons interact with one another to form bundles. Overall, this new culture paradigm will be valuable in complementing and integrating findings from whole organoids and *in vivo* studies.

ALI-COs: future directions and experimental considerations

We have shown that ALI culture conditions improve survival of late-stage neural organoids, thereby extending the range of developmental processes that can be modelled with this system *in vitro*. This culture preparation is easily accessible by microscopy and allows the study of axon pathfinding and bundling by live imaging. The presence of endogenous chemotactic cues together with the turning behaviour seen by live imaging point to similarities between *in vitro* and *in vivo* development. Therefore, future work will focus on later aspects of the ZEB2^{+/-} phenotype as well as modulation of axon trajectories through the administration of exogenous cues by electroporation. CTB tracing experiments have shown that, similarly to normal development, superficial-layer neurons have the tendency to project within the boundaries of cortical tissue, while deep-layer neurons preferentially project outside the organoid tissue as escaping bundles. As previously mentioned, further tracing experiments with a more comprehensive readout, such as scRNA-seq, are needed to identify the specific neuronal identities present within the different tracts.

Focusing on the activity patterns observed in organoids, we believe our work has only touched upon this new area of research (Fig. 46). Further experiments are already underway, and optimisation of recording conditions along with the use of a newer MEA system that allows stimulation at specific sites of the array have already given promising results. One of the main limitations we are facing at the moment is that commercially available 3D MEAs can only cover a restricted portion of the entire ALI-CO slice, so that at the moment long-range connections across the entire sample surface cannot be studied. To overcome these technical limitations and dissect the activity patterns in ALI-COs we are currently establishing channelrhodopsin and genetically-encoded calcium reporter constructs. In the long term, we hope to employ the chimeric co-culture system presented to study whether the motor circuits established can be entrained.

Lastly, we have already cloned GFP-tagged ORFs for all three *E-SYTs* in a sleeping beauty transposon donor construct that allows stable integration of the transgene. Our goal is to study the effects of overexpression of these ER-PM tethers on the structure of axons and on the *in situ* cellular architecture. This work will serve as proof of concept of how ALI-COs can be used to study the cellular architecture of axons specifically. ALI-COs are a developmental model and we believe that the relevance of this work lies in the fact that it can give new insight into aspects of cellular ultrastructure in the context of development.

Conclusions

In summary, we have uncovered a role for *ZEB2* in modulating cell-cell contacts in the developing human neuroepithelium. *ZEB2* heterozygous loss-of-function leads to tighter cell-cell contacts that hinder the transition of NECs to neurogenic aRGCs, with a net decrease in TBR2⁺ IPCs and a significant increase in ventricle length. Conversely, preliminary gain-of-function experiments lead to higher N-cadherin and reduced E-cadherin levels, with a concomitant increase in TUBB3⁺ neurons and a decrease in ventricle size. Dual SMAD inhibition appears to partially rescue the *ZEB2*^{+/-} phenotype, suggesting that in the neuroepithelium *ZEB2* may act by antagonising the BMP and TGFβ signalling cascades. Furthermore, we have shown that FGF2 is a positive regulator of *ZEB2*, which in turn downregulates FGF2. These findings are consistent with previous reports in other model systems and point to a potential role for differences in *Zeb2* expression as a means to regulate the size of the cortical primordium.

Furthermore, in an attempt to model later aspects of the *ZEB2*^{+/-} phenotype, we have developed a slice-culture protocol that promotes long-term neuronal survival and axon outgrowth in organoids. The thick axon tracts that develop display a variety of projection modalities including long-range projections within and away from the organoid, growth-cone turning and decussation. Analysis by scRNA-seq revealed a wide array of cortical cell types and CTB retrograde tracing demonstrated that there is appropriate correspondence between neuronal identity and hodology. ALI-COs display functional neural networks and escaping tracts can innervate mouse spinal cord explants and modulate contraction of mouse paraspinal muscles. Overall, this culture system reveals a remarkable degree of self-organization of corticofugal and callosal tracts with functional output. Lastly, by combining ALI-COs and cryo-CLEM we have shown that this system provides new opportunities to study relevant aspects of CNS development across a variety of scales.

Bibliography

- Aaku-Saraste, E., Hellwig, A. & Huttner, W.B., 1996. Loss of occludin and functional tight junctions, but not ZO-1, during neural tube closure--remodeling of the neuroepithelium prior to neurogenesis. *Developmental biology*, 180(2), pp.664–679.
- Abellán, A. et al., 2010. Differential expression of LIM-homeodomain factors in Cajal-Retzius cells of primates, rodents, and birds. *Cerebral cortex*, 20(8), pp.1788–1798.
- Ader, N.R. et al., 2019. Molecular and topological reorganizations in mitochondrial architecture interplay during Bax-mediated steps of apoptosis. *Elife*, 8, p.303.
- Alcamo, E.A. et al., 2008. Satb2 regulates callosal projection neuron identity in the developing cerebral cortex. *Neuron*, 57(3), pp.364–377.
- Altman, J. & Bayer, S.A., 2007. *The human brain during the early first trimester*, CRC press.
- Altman, J. et al., 1995. *Atlas of prenatal rat brain development*, CRC Press.
- Anderson, S.A. et al., 1997. Interneuron migration from basal forebrain to neocortex: dependence on Dlx genes. *Science*, 278(5337), pp.474–476.
- Ang, E.S.B.C. et al., 2003. Four-dimensional migratory coordinates of GABAergic interneurons in the developing mouse cortex. *The Journal of neuroscience : the official journal of the Society for Neuroscience*, 23(13), pp.5805–5815.
- Aoto, K. et al., 2002. Mouse GLI3 regulates Fgf8 expression and apoptosis in the developing neural tube, face, and limb bud. *Developmental biology*, 251(2), pp.320–332.
- Arlotta, P. et al., 2005. Neuronal subtype-specific genes that control corticospinal motor neuron development in vivo. *Neuron*, 45(2), pp.207–221.
- Assimacopoulos, S., Grove, E.A. & Ragsdale, C.W., 2003. Identification of a Pax6-dependent epidermal growth factor family signaling source at the lateral edge of the embryonic cerebral cortex. *The Journal of neuroscience : the official journal of the Society for Neuroscience*, 23(16), pp.6399–6403.
- Bagley, J.A. et al., 2017. Fused cerebral organoids model interactions between brain regions. *Nature methods*, 14(7), pp.743–751.
- Bak, M. & Fraser, S.E., 2003. Axon fasciculation and differences in midline kinetics between pioneer and follower axons within commissural fascicles. *Development*, 130(20), pp.4999–5008.
- Bar Yaacov, R. et al., 2018. Functional characterization of the ZEB2 regulatory landscape. *Human Molecular Genetics*.
- Barth, K.A. & Wilson, S.W., 1995. Expression of zebrafish nk2.2 is influenced by sonic hedgehog/vertebrate hedgehog-1 and demarcates a zone of neuronal differentiation in the embryonic forebrain. *Development*, 121(6), pp.1755–1768.
- Bavister, B.D., 2012. *The Mammalian Preimplantation Embryo*, Springer Science & Business Media.
- Bäuerlein, F.J.B. et al., 2017. In Situ Architecture and Cellular Interactions of PolyQ Inclusions. *Cell*, 171(1), pp.179–187.
- Beenken, A. & Mohammadi, M., 2009. The FGF family: biology, pathophysiology and therapy. *Nature reviews. Drug discovery*, 8(3), pp.235–253.

- Beltran, M. et al., 2008. A natural antisense transcript regulates Zeb2/Sip1 gene expression during Snail1-induced epithelial-mesenchymal transition. *Genes & development*, 22(6), pp.756–769.
- Ben Pansky, 1982. *Review of Medical Embryology*, Macmillan Publishing Company.
- Ben-Nun, I.F. et al., 2015. Generation of Induced Pluripotent Stem Cells from Mammalian Endangered Species. In P. J. Verma & H. Sumer, eds. *Cell Reprogramming: Methods and Protocols*. Springer New York, pp. 101–109.
- Ben-Nun, I.F. et al., 2011. Induced pluripotent stem cells from highly endangered species. *Nature methods*, 8(10), pp.829–831.
- Betizeau, M. et al., 2013. Precursor diversity and complexity of lineage relationships in the outer subventricular zone of the primate. *Neuron*, 80(2), pp.442–457.
- Bharat, T.A.M., Hoffmann, P.C. & Kukulski, W., 2018. Correlative Microscopy of Vitreous Sections Provides Insights into BAR-Domain Organization In Situ. *Structure*, 26(6), pp.879–886.
- Bielle, F. et al., 2005. Multiple origins of Cajal-Retzius cells at the borders of the developing pallium. *Nature neuroscience*, 8(8), pp.1002–1012.
- Birey, F. et al., 2017 Assembly of functionally integrated human forebrain spheroids. *Nature*, 545, pp.54–59.
- Borello, U. et al., 2008. FGF15 promotes neurogenesis and opposes FGF8 function during neocortical development. *Neural development*, 3, p.17.
- Boyd, J.L. et al., 2015. Human-chimpanzee differences in a FZD8 enhancer alter cell-cycle dynamics in the developing neocortex. *Current biology*, 25(6), pp.772–779.
- Boyden, E.S., 2011. A history of optogenetics: the development of tools for controlling brain circuits with light. *F1000 biology reports*, 3, pp.11.
- Braak, H., 2012. *Architectonics of the Human Telencephalic Cortex*, Springer Science & Business Media, pp.26–48.
- Bridges, D.C. et al., 2018. MEA Viewer: A high-performance interactive application for visualizing electrophysiological data G. Cymbalyuk, ed. *PloS one*, 13(2), p.e0192477.
- Britanova, O. et al., 2008. Satb2 is a postmitotic determinant for upper-layer neuron specification in the neocortex. *Neuron*, 57(3), pp.378–392.
- Bulchand, S. et al., 2001. LIM-homeodomain gene Lhx2 regulates the formation of the cortical hem. *Mechanisms of development*, 100(2), pp.165–175.
- Butler, A. et al., 2018. Integrating single-cell transcriptomic data across different conditions, technologies, and species. *Nature biotechnology*, 36(5), pp.411–420.
- Cabrera-Socorro, A. et al., 2007. Comparative aspects of p73 and Reelin expression in Cajal-Retzius cells and the cortical hem in lizard, mouse and human. *Brain research*, 1132(1), pp.59–70.
- Camp, J.G. et al., 2015. Human cerebral organoids recapitulate gene expression programs of fetal neocortex development. *Proceedings of the National Academy of Sciences of the United States of America*, 112(51), pp.15672–15677.
- Campbell, K. & Götz, M., 2002. Radial glia: multi-purpose cells for vertebrate brain development. *Trends in neurosciences*, 25(5), pp.235–238.

- Carney, R.S.E. et al., 2009. Differential regulation of telencephalic pallial-subpallial boundary patterning by Pax6 and Gsh2. *Cerebral cortex*, 19(4), pp.745–759.
- Caronia-Brown, G. et al., 2014. The cortical hem regulates the size and patterning of neocortex. *Development*, 141(14), pp.2855–2865.
- Caviness, V.S. & Sidman, R.L., 1973. Time of origin or corresponding cell classes in the cerebral cortex of normal and reeler mutant mice: an autoradiographic analysis. *The Journal of comparative neurology*, 148(2), pp.141–151.
- Cárdenas, A. et al., 2018. Evolution of Cortical Neurogenesis in Amniotes Controlled by Robo Signaling Levels. *Cell*, 174(3), pp.590–606.
- Chambers, S.M. et al., 2009. Highly efficient neural conversion of human ES and iPS cells by dual inhibition of SMAD signaling. *Nature biotechnology*, 27(3), pp.275–280.
- Chapouton, P., Gärtner, A. & Götz, M., 1999. The role of Pax6 in restricting cell migration between developing cortex and basal ganglia. *Development*, 126(24), pp.5569–5579.
- Charvet, C.J., Owerkowicz, T. & Striedter, G.F., 2009. Phylogeny of the Telencephalic Subventricular Zone in Sauropsids: Evidence for the Sequential Evolution of Pallial and Subpallial Subventricular Zones. *Brain, Behavior and Evolution*, 73(4), pp.285–294.
- Chen, B. et al., 2008. The Fezf2-Ctip2 genetic pathway regulates the fate choice of subcortical projection neurons in the developing cerebral cortex. *Proceedings of the National Academy of Sciences of the United States of America*, 105(32), pp.11382–11387.
- Chen, B., Schaevitz, L.R. & McConnell, S.K., 2005. Fezl regulates the differentiation and axon targeting of layer 5 subcortical projection neurons in cerebral cortex. *Proceedings of the National Academy of Sciences of the United States of America*, 102(47), pp.17184–17189.
- Chen, I.-P. et al., 2013. Induced Pluripotent Stem Cell Reprogramming by Integration-Free Sendai Virus Vectors from Peripheral Blood of Patients with Craniometaphyseal Dysplasia. *Cellular Reprogramming*, 15(6), pp.503–513.
- Chen, Y.-H. & Pruett-Miller, S.M., 2018. Improving single-cell cloning workflow for gene editing in human pluripotent stem cells. *Stem cell research*, 31, pp.186–192.
- Chesnutt, C. et al., 2004. Coordinate regulation of neural tube patterning and proliferation by TGFbeta and WNT activity. *Developmental biology*, 274(2), pp.334–347.
- Cheung, A.F.P. et al., 2007. Comparative aspects of cortical neurogenesis in vertebrates. *Journal of anatomy*, 211(2), pp.164–176.
- Chiang, C. et al., 1996. Cyclopia and defective axial patterning in mice lacking Sonic hedgehog gene function. *Nature*, 383(6599), pp.407–413.
- Chisholm, A. & Tessier-Lavigne, M., 1999. Conservation and divergence of axon guidance mechanisms. *Current opinion in neurobiology*, 9(5), pp.603–615.
- Chng, Z. et al., 2010. SIP1 mediates cell-fate decisions between neuroectoderm and mesendoderm in human pluripotent stem cells. *Cell stem cell*, 6(1), pp.59–70.
- Cohen, M.A., Itsykson, P. & Reubinoﬀ, B.E., 2010. The role of FGF-signaling in early neural specification of human embryonic stem cells. *Developmental biology*, 340(2), pp.450–458.
- Cohen, N.R. et al., 1998. Errors in corticospinal axon guidance in mice lacking the neural cell adhesion molecule L1. *Current biology*, 8(1), pp.26–33.

- Conidi, A. et al., 2013. Four amino acids within a tandem QxVx repeat in a predicted extended alpha-helix of the Smad-binding domain of Sip1 are necessary for binding to activated Smad proteins. *PloS one*, 8(10), p.e76733.
- Cox, D.B.T. et al., 2017. RNA editing with CRISPR-Cas13. *Science*, 358(6366), pp.1019–1027.
- Cubelos, B. et al., 2008. Cux-1 and Cux-2 control the development of Reelin expressing cortical interneurons. *Developmental neurobiology*, 68(7), pp.917–925.
- Cubelos, B. et al., 2010. Cux1 and Cux2 regulate dendritic branching, spine morphology, and synapses of the upper layer neurons of the cortex. *Neuron*, 66(4), pp.523–535.
- Cullen, D.K. et al., 2018. Three-dimensional Human Axon Tracts Derived From Cerebral Organoids. *SSRN Electronic Journal*.
- Dang, L.T.H. & Tropepe, V., 2010. FGF dependent regulation of *Zfhx1b* gene expression promotes the formation of definitive neural stem cells in the mouse anterior neurectoderm. *Neural development*, 5, p.13.
- Daniszewski, M. et al., 2018. Single-Cell Profiling Identifies Key Pathways Expressed by iPSCs Cultured in Different Commercial Media. *iScience*, 7, pp.30–39.
- Davis, B.N. et al., 2008. SMAD proteins control DROSHA-mediated microRNA maturation. *Nature*, 454(7200), pp.56–61.
- Daza, R.A.M., Englund, C. & Hevner, R.F., 2007. Organotypic slice culture of embryonic brain tissue. *CSH protocols*, 2007, p.pdb.prot4914.
- DeAzevedo, L.C. et al., 2003. Cortical radial glial cells in human fetuses: Depth-correlated transformation into astrocytes. *Journal of Neurobiology*, 55(3), pp.288–298.
- Delaune, E., Lemaire, P. & Kodjabachian, L., 2005. Neural induction in *Xenopus* requires early FGF signalling in addition to BMP inhibition. *Development*, 132(2), pp.299–310.
- Demyanenko, G.P., Tsai, A.Y. & Maness, P.F., 1999. Abnormalities in neuronal process extension, hippocampal development, and the ventricular system of L1 knockout mice. *The Journal of neuroscience : the official journal of the Society for Neuroscience*, 19(12), pp.4907–4920.
- Dickson, B.J., 2002. Molecular mechanisms of axon guidance. *Science*, 298(5600), pp.1959–1964.
- Dong, J. et al., 2018. Single-cell RNA-seq analysis unveils a prevalent epithelial/mesenchymal hybrid state during mouse organogenesis. *Genome biology*, 19(1), p.31.
- Dono, R. et al., 1998. Impaired cerebral cortex development and blood pressure regulation in FGF-2-deficient mice. *The EMBO journal*, 17(15), pp.4213–4225.
- Dufour, A. et al., 2003. Area specificity and topography of thalamocortical projections are controlled by ephrin/Eph genes. *Neuron*, 39(3), pp.453–465.
- Dugas-Ford, J. & Ragsdale, C.W., 2015. Levels of homology and the problem of neocortex. *Annual review of neuroscience*, 38, pp.351–368.
- Eckert, J.J. & Fleming, T.P., 2008. Tight junction biogenesis during early development. *Biochimica et biophysica acta*, 1778(3), pp.717–728.
- Eckler, M.J. et al., 2015. Cux2-Positive Radial Glial Cells Generate Diverse Subtypes of Neocortical Projection Neurons and Macroglia. *Neuron*, 86(4), pp.1100–1108.

- Eiraku, M. et al., 2008. Self-Organized Formation of Polarized Cortical Tissues from ESCs and Its Active Manipulation by Extrinsic Signals. *Cell stem cell*, 3(5), pp.519–532.
- Eiraku, M. et al., 2011. Self-organizing optic-cup morphogenesis in three-dimensional culture. *Nature*, 472, pp.51–56.
- Eisaki, A. et al., 2000. XSIP1, a Member of Two-Handed Zinc Finger Proteins, Induced Anterior Neural Markers in *Xenopus laevis* Animal Cap. *Biochemical and Biophysical Research Communications*, 271(1), pp.151–157.
- El-Kasti, M.M., Wells, T. & Carter, D.A., 2012. A novel long-range enhancer regulates postnatal expression of Zeb2: implications for Mowat-Wilson syndrome phenotypes. *Human molecular genetics*, 21(26), pp.5429–5442.
- Erwin, G.D. et al., 2014. Integrating Diverse Datasets Improves Developmental Enhancer Prediction U. Ohler, ed. *PLoS Computational Biology*, 10(6), p.e1003677.
- Falk, J. et al., 2005. Dual functional activity of semaphorin 3B is required for positioning the anterior commissure. *Neuron*, 48(1), pp.63–75.
- Fame, R.M., MacDonald, J.L. & Macklis, J.D., 2011. Development, specification, and diversity of callosal projection neurons. *Trends in neurosciences*, 34(1), pp.41–50.
- Fan, X. et al., 2018. Spatial transcriptomic survey of human embryonic cerebral cortex by single-cell RNA-seq analysis. *Cell Research*, 28(7), pp.730–745.
- Faux, C.H. et al., 2001. Interactions between fibroblast growth factors and Notch regulate neuronal differentiation. *The Journal of neuroscience : the official journal of the Society for Neuroscience*, 21(15), pp.5587–5596.
- Fenko, L., Yizhar, O. & Deisseroth, K., 2011. The Development and Application of Optogenetics. *Annual review of neuroscience*, 34(1), pp.389–412.
- Ferguson, E.L. & Anderson, K.V., 1992. Decapentaplegic acts as a morphogen to organize dorsal-ventral pattern in the *Drosophila* embryo. *Cell*, 71(3), pp.451–461.
- Fernandes, M. et al., 2007. Mutations in the BMP pathway in mice support the existence of two molecular classes of holoprosencephaly. *Development*, 134(21), pp.3789–3794.
- Fernández, V., Llinares-Benadero, C. & Borrell, V., 2016. Cerebral cortex expansion and folding: what have we learned? *The EMBO journal*, 35(10), pp.1021–1044.
- Fietz, S.A. et al., 2010. OSVZ progenitors of human and ferret neocortex are epithelial-like and expand by integrin signaling. *Nature neuroscience*, 13(6), pp.690–699.
- Findlay, S.D. et al., 2016. A Digital PCR-Based Method for Efficient and Highly Specific Screening of Genome Edited Cells. *PloS one*, 11(4), pp.e0153901–e0153901.
- Finlay, B.L. & Darlington, R.B., 1995. Linked regularities in the development and evolution of mammalian brains. *Science*, 268(5217), pp.1578–1584.
- Flanagan, J.G. & Vanderhaeghen, P., 1998. THE EPHRINS AND EPH RECEPTORS IN NEURAL DEVELOPMENT. *Annual review of neuroscience*, 21(1), pp.309–345.
- Florio, M. et al., 2015. Human-specific gene ARHGAP11B promotes basal progenitor amplification and neocortex expansion. *Science*, 347(6229), pp.1465–1470.
- Förster, E. et al., 2002. Reelin, Disabled 1, and beta 1 integrins are required for the formation of the

- radial glial scaffold in the hippocampus. *Proceedings of the National Academy of Sciences of the United States of America*, 99(20), pp.13178–13183.
- Frantz, G.D. & McConnell, S.K., 1996. Restriction of late cerebral cortical progenitors to an upper-layer fate. *Neuron*, 17(1), pp.55–61.
- Frantz, G.D. et al., 1994. Otx1 and Otx2 define layers and regions in developing cerebral cortex and cerebellum. *The Journal of neuroscience : the official journal of the Society for Neuroscience*, 14(10), pp.5725–5740.
- Fukumitsu, H. et al., 2006. Brain-derived neurotrophic factor participates in determination of neuronal laminar fate in the developing mouse cerebral cortex. *The Journal of neuroscience : the official journal of the Society for Neuroscience*, 26(51), pp.13218–13230.
- Gadisieux, J.F. & Evrard, P., 1985. Glial-neuronal relationship in the developing central nervous system. A histochemical-electron microscope study of radial glial cell particulate glycogen in normal and reeler mice and the human fetus. *Developmental neuroscience*, 7(1), pp.12–32.
- Garavelli, L. et al., 2017. Neuroimaging findings in Mowat-Wilson syndrome: a study of 54 patients. *Genetics in medicine : official journal of the American College of Medical Genetics*, 19(6), pp.691–700.
- Gertz, C.C. et al., 2014. Diverse behaviors of outer radial glia in developing ferret and human cortex. *The Journal of neuroscience : the official journal of the Society for Neuroscience*, 34(7), pp.2559–2570.
- Geschwind, D.H. & Rakic, P., 2013. Cortical evolution: judge the brain by its cover. *Neuron*, 80(3), pp.633–647.
- Giandomenico, S.L. & Lancaster, M.A., 2017. Probing human brain evolution and development in organoids. *Current opinion in cell biology*, 44, pp.36–43.
- Giandomenico, S.L. et al., 2019. Cerebral organoids at the air-liquid interface generate diverse nerve tracts with functional output. *Nature neuroscience*, 22(4), pp.669–679.
- Godbole, G. et al., 2018. Hierarchical genetic interactions between FOXG1 and LHX2 regulate the formation of the cortical hem in the developing telencephalon. *Development*, 145(1).
- Gold, C., Henze, D.A. & Koch, C., 2007. Using extracellular action potential recordings to constrain compartmental models. *Journal of Computational Neuroscience*, 23(1), pp.39–58.
- Götz, M. & Huttner, W.B., 2005. The cell biology of neurogenesis. *Nature Reviews Molecular Cell Biology*, 6, pp.777–788.
- Greber, B. et al., 2010. Conserved and divergent roles of FGF signaling in mouse epiblast stem cells and human embryonic stem cells. *Cell stem cell*, 6(3), pp.215–226.
- Gregory, P.A. et al., 2011. An autocrine TGF-beta/ZEB/miR-200 signaling network regulates establishment and maintenance of epithelial-mesenchymal transition. *Molecular biology of the cell*, 22(10), pp.1686–1698.
- Greig, L.C. et al., 2013. Molecular logic of neocortical projection neuron specification, development and diversity. *Nature reviews. Neuroscience*, 14(11), pp.755–769.
- Grunz, H., 2013. *The Vertebrate Organizer*, Springer Science & Business Media, pp.55–71.
- Grunz, H. & Tacke, L., 1989. Neural differentiation of *Xenopus laevis* ectoderm takes place after disaggregation and delayed reaggregation without inducer. *Cell differentiation and development*,

28(3), pp.211–217.

- Guo, C. et al., 2013. Fezf2 expression identifies a multipotent progenitor for neocortical projection neurons, astrocytes, and oligodendrocytes. *Neuron*, 80(5), pp.1167–1174.
- Hagen, W.J.H., Wan, W. & Briggs, J.A.G., 2017. Implementation of a cryo-electron tomography tilt-scheme optimized for high resolution subtomogram averaging. *Journal of Structural Biology*, 197(2), pp.191–198.
- Hanashima, C. et al., 2007. The role of Foxg1 and dorsal midline signaling in the generation of Cajal-Retzius subtypes. *The Journal of neuroscience : the official journal of the Society for Neuroscience*, 27(41), pp.11103–11111.
- Hansen, D.V. et al., 2010. Neurogenic radial glia in the outer subventricular zone of human neocortex. *Nature*, 464(7288), pp.554–561.
- Hatta, K. et al., 1987. Spatial and temporal expression pattern of N-cadherin cell adhesion molecules correlated with morphogenetic processes of chicken embryos. *Developmental biology*, 120(1), pp.215–227.
- Haubensak, W. et al., 2004. Neurons arise in the basal neuroepithelium of the early mammalian telencephalon: a major site of neurogenesis. *Proceedings of the National Academy of Sciences of the United States of America*, 101(9), pp.3196–3201.
- Haubst, N. et al., 2006. Basement membrane attachment is dispensable for radial glial cell fate and for proliferation, but affects positioning of neuronal subtypes. *Development*, 133(16), pp.3245–3254.
- Hegarty, S.V., Sullivan, A.M. & O'Keefe, G.W., 2015. Zeb2: A multifunctional regulator of nervous system development. *Progress in neurobiology*, 132, pp.81–95.
- Hemmati-Brivanlou, A. & Melton, D.A., 1992. A truncated activin receptor inhibits mesoderm induction and formation of axial structures in *Xenopus* embryos. *Nature*, 359(6396), pp.609–614.
- Hemmati-Brivanlou, A. & Melton, D.A., 1994. Inhibition of activin receptor signaling promotes neuralization in *Xenopus*. *Cell*, 77(2), pp.273–281.
- Hemmati-Brivanlou, A., Kelly, O.G. & Melton, D.A., 1994. Follistatin, an antagonist of activin, is expressed in the Spemann organizer and displays direct neuralizing activity. *Cell*, 77(2), pp.283–295.
- Herculano-Houzel, S., 2012. Neuronal scaling rules for primate brains: the primate advantage. *Progress in brain research*, 195, pp.325–340.
- Herculano-Houzel, S., 2009. The human brain in numbers: a linearly scaled-up primate brain. *Frontiers in human neuroscience*, 3, p.31.
- Herculano-Houzel, S., Manger, P.R. & Kaas, J.H., 2014. Brain scaling in mammalian evolution as a consequence of concerted and mosaic changes in numbers of neurons and average neuronal cell size. *Frontiers in neuroanatomy*, 8, p.77.
- Hirata, T. et al., 2002. Mosaic development of the olfactory cortex with Pax6-dependent and independent components. *Brain research. Developmental brain research*, 136(1), pp.17–26.
- His, W., 1889. *Die neuroblasten und deren entstehung im embryonalen mark*, S. Hirzel.
- Houart, C. et al., 2002. Establishment of the telencephalon during gastrulation by local antagonism of Wnt signaling. *Neuron*, 35(2), pp.255–265.

- Houart, C., Westerfield, M. & Wilson, S.W., 1998. A small population of anterior cells patterns the forebrain during zebrafish gastrulation. *Nature*, 391(6669), pp.788–792.
- Howard, B., Chen, Y.H. & Zecevic, N., 2006. Cortical progenitor cells in the developing human telencephalon. *Glia*, 53(1), pp.57–66.
- Hu, Z. et al., 2003. Corpus callosum deficiency in transgenic mice expressing a truncated ephrin-A receptor. *The Journal of neuroscience : the official journal of the Society for Neuroscience*, 23(34), pp.10963–10970.
- Huber, A.B. et al., 2003. Signaling at the growth cone: ligand-receptor complexes and the control of axon growth and guidance. *Annual review of neuroscience*, 26, pp.509–563.
- Huttner, W.B. & Kosodo, Y., 2005. Symmetric versus asymmetric cell division during neurogenesis in the developing vertebrate central nervous system. *Current opinion in cell biology*, 17(6), pp.648–657.
- Imayoshi, I. et al., 2008. Hes genes and neurogenin regulate non-neural versus neural fate specification in the dorsal telencephalic midline. *Development*, 135(15), pp.2531–2541.
- Jerison, H., 1973. Evolution of The Brain and Intelligence. *Academic Press*, New York.
- Johnson, M.B. et al., 2018. Aspm knockout ferret reveals an evolutionary mechanism governing cerebral cortical size. *Nature*, 556(7701), pp.370–375.
- Jossin, Y. et al., 2004. The central fragment of Reelin, generated by proteolytic processing in vivo, is critical to its function during cortical plate development. *The Journal of neuroscience : the official journal of the Society for Neuroscience*, 24(2), pp.514–521.
- Judas, M. et al., 2003. Complex patterns and simple architects: molecular guidance cues for developing axonal pathways in the telencephalon. *Progress in molecular and subcellular biology*, 32, pp.1–32.
- Kalchauer, C., 2015. Epithelial-Mesenchymal Transitions during Neural Crest and Somite Development. *Journal of clinical medicine*, 5(1), p.1.
- Kalil, K., Li, L. & Hutchins, B.I., 2011. Signaling mechanisms in cortical axon growth, guidance, and branching. *Frontiers in neuroanatomy*, 5, p.62.
- Kawada, J. et al., 2017. Generation of a Motor Nerve Organoid with Human Stem Cell-Derived Neurons. *Stem cell reports*, 9(5), pp.1441–1449.
- Kawakami, Y. et al., 2009. Impaired neurogenesis in embryonic spinal cord of Phgdh knockout mice, a serine deficiency disorder model. *Neuroscience research*, 63(3), pp.184–193.
- Kawasaki, H. et al., 2000. Induction of midbrain dopaminergic neurons from ES cells by stromal cell-derived inducing activity. *Neuron*, 28(1), pp.31–40.
- Keeble, T.R. et al., 2006. The Wnt receptor Ryk is required for Wnt5a-mediated axon guidance on the contralateral side of the corpus callosum. *The Journal of neuroscience : the official journal of the Society for Neuroscience*, 26(21), pp.5840–5848.
- Kelava, I. & Lancaster, M.A., 2016. Stem Cell Models of Human Brain Development. *Cell stem cell*, 18(6), pp.736–748.
- Kennedy, T.E. et al., 1994. Netrins are diffusible chemotropic factors for commissural axons in the embryonic spinal cord. *Cell*, 78(3), pp.425–435.

- Kidd, T., Brose, K., et al., 1998a. Roundabout controls axon crossing of the CNS midline and defines a novel subfamily of evolutionarily conserved guidance receptors. *Cell*, 92(2), pp.205–215.
- Kidd, T., Russell, C., et al., 1998b. Dosage-sensitive and complementary functions of roundabout and commissureless control axon crossing of the CNS midline. *Neuron*, 20(1), pp.25–33.
- Kiecker, C. & Niehrs, C., 2001. A morphogen gradient of Wnt/beta-catenin signalling regulates anteroposterior neural patterning in *Xenopus*. *Development*, 128(21), pp.4189–4201.
- Kikuma, K. et al., 2017. Extended Synaptotagmin Localizes to Presynaptic ER and Promotes Neurotransmission and Synaptic Growth in *Drosophila*. *Genetics*, 207(3), pp.993–1006.
- Kim, A.S. et al., 2001. Pax-6 regulates expression of SFRP-2 and Wnt-7b in the developing CNS. *The Journal of neuroscience : the official journal of the Society for Neuroscience*, 21(5), p.RC132.
- Kimelman, D. & Kirschner, M., 1987. Synergistic induction of mesoderm by FGF and TGF-beta and the identification of an mRNA coding for FGF in the early *Xenopus* embryo. *Cell*, 51(5), pp.869–877.
- Klein, R., 2001. Excitatory Eph receptors and adhesive ephrin ligands. *Current opinion in cell biology*, 13(2), pp.196–203.
- Kogut, I. et al., 2018. High-efficiency RNA-based reprogramming of human primary fibroblasts. *Nature communications*, 9(1), p.745.
- Kohtz, J.D. et al., 1998. Regionalization within the mammalian telencephalon is mediated by changes in responsiveness to Sonic Hedgehog. *Development*, 125(24), pp.5079–5089.
- Konermann, S. et al., 2015. Genome-scale transcriptional activation by an engineered CRISPR-Cas9 complex. *Nature*, 517(7536), pp.583–588.
- Konermann, S. et al., 2018. Transcriptome Engineering with RNA-Targeting Type VI-D CRISPR Effectors. *Cell*, 173(3), pp.665–676.
- Kornack, D.R. & Rakic, P., 1995. Radial and Horizontal Deployment of Clonally Related Cells in the Primate Neocortex - Relationship to Distinct Mitotic Lineages. *Neuron*, 15(2), pp.311–321.
- Krebs, A.M. et al., 2017. The EMT-activator Zeb1 is a key factor for cell plasticity and promotes metastasis in pancreatic cancer. *Nature cell biology*, 19(5), pp.518–529.
- Kremer, J.R., Mastronarde, D.N. & McIntosh, J.R., 1996. Computer visualization of three-dimensional image data using IMOD. *Journal of Structural Biology*, 116(1), pp.71–76.
- Kriegstein, A.R. & Götz, M., 2003. Radial glia diversity: a matter of cell fate. *Glia*, 43(1), pp.37–43.
- Kriegstein, A.R. & Noctor, S.C., 2004. Patterns of neuronal migration in the embryonic cortex. *Trends in neurosciences*, 27(7), pp.392–399.
- Krubitzer, L. & Kaas, J., 2005. The evolution of the neocortex in mammals: how is phenotypic diversity generated? *Current opinion in neurobiology*, 15(4), pp.444–453.
- Kwan, K.Y. et al., 2008. SOX5 postmitotically regulates migration, postmigratory differentiation, and projections of subplate and deep-layer neocortical neurons. *Proceedings of the National Academy of Sciences of the United States of America*, 105(41), pp.16021–16026.
- Lagutin, O.V. et al., 2003. Six3 repression of Wnt signaling in the anterior neuroectoderm is essential for vertebrate forebrain development. *Genes & development*, 17(3), pp.368–379.

- Lai, T. et al., 2008. SOX5 controls the sequential generation of distinct corticofugal neuron subtypes. *Neuron*, 57(2), pp.232–247.
- Lake, B.B. et al., 2016. Neuronal subtypes and diversity revealed by single-nucleus RNA sequencing of the human brain. *Science*, 352(6293), pp.1586–1590.
- Lamb, T.M. et al., 1993. Neural induction by the secreted polypeptide noggin. *Science*, 262(5134), pp.713–718.
- LaMonica, B.E. et al., 2013. Mitotic spindle orientation predicts outer radial glial cell generation in human neocortex. *Nature communications*, 4, p.1665.
- Lamouille, S. et al., 2013. Regulation of epithelial-mesenchymal and mesenchymal-epithelial transitions by microRNAs. *Current opinion in cell biology*, 25(2), pp.200–207.
- Lamouille, S., Xu, J. & Derynck, R., 2014. Molecular mechanisms of epithelial-mesenchymal transition. *Nature Reviews Molecular Cell Biology*, 15(3), pp.178–196.
- Lancaster, M.A. & Knoblich, J.A., 2014. Generation of cerebral organoids from human pluripotent stem cells. *Nature protocols*, 9(10), pp.2329–2340.
- Lancaster, M.A. et al., 2017. Guided self-organization and cortical plate formation in human brain organoids. *Nature biotechnology*, 35(7), pp.659–666.
- Lancaster, M.A. et al., 2013. Cerebral organoids model human brain development and microcephaly. *Nature*, 501(7467), pp.373–379.
- Lavdas, A.A. et al., 1999. The medial ganglionic eminence gives rise to a population of early neurons in the developing cerebral cortex. *The Journal of neuroscience : the official journal of the Society for Neuroscience*, 19(18), pp.7881–7888.
- Le Dréau, G. & Martí, E., 2012. Dorsal-ventral patterning of the neural tube: a tale of three signals. *Developmental neurobiology*, 72(12), pp.1471–1481.
- Lee, J.G., Jung, E. & Heur, M., 2018. Fibroblast growth factor 2 induces proliferation and fibrosis via SNAI1-mediated activation of CDK2 and ZEB1 in corneal endothelium. *The Journal of biological chemistry*, 293(10), pp.3758–3769.
- Leonavicius, K. et al., 2018. Mechanics of mouse blastocyst hatching revealed by a hydrogel-based microdeformation assay. *Proceedings of the National Academy of Sciences of the United States of America*, 115(41), pp.10375–10380.
- Letinic, K., Zoncu, R. & Rakic, P., 2002. Origin of GABAergic neurons in the human neocortex. *Nature*, 417(6889), pp.645–649.
- Li, X.-J. et al., 2009. Coordination of sonic hedgehog and Wnt signaling determines ventral and dorsal telencephalic neuron types from human embryonic stem cells. *Development (Cambridge, England)*, 136(23), pp.4055–4063.
- Li, Y. et al., 2016. Induction of Expansion and Folding in Human Cerebral Organoids. *Cell stem cell*.
- Lindblad-Toh, K. et al., 2011. A high-resolution map of human evolutionary constraint using 29 mammals. *Nature*, 478, pp.476–482.
- Linker, C. & Stern, C.D., 2004. Neural induction requires BMP inhibition only as a late step, and involves signals other than FGF and Wnt antagonists. *Development*, 131(22), pp.5671–5681.
- Long, J., Zuo, D. & Park, M., 2005. Pc2-mediated sumoylation of Smad-interacting protein 1

- attenuates transcriptional repression of E-cadherin. *The Journal of biological chemistry*, 280(42), pp.35477–35489.
- Long, K. et al., 2016. Integrin signalling regulates the expansion of neuroepithelial progenitors and neurogenesis via Wnt7a and Decorin. *Nature communications*, 7, p.10354.
- Lui, J.H., Hansen, D.V. & Kriegstein, A.R., 2011. Development and evolution of the human neocortex. *Cell*, 146(1), pp.18–36.
- Luo, C. et al., 2016. Cerebral Organoids Recapitulate Epigenomic Signatures of the Human Fetal Brain. *Cell reports*, 17(12), pp.3369–3384.
- Luskin, M.B., Pearlman, A.L. & Sanes, J.R., 1988. Cell lineage in the cerebral cortex of the mouse studied in vivo and in vitro with a recombinant retrovirus. *Neuron*, 1(8), pp.635–647.
- MacDonald, J.L. et al., 2013. *Comprehensive Developmental Neuroscience: Patterning and Cell Type Specification in the Developing CNS and PNS*, Elsevier Inc., Chapter 25. pp.475–497.
- Maden, M., 2007. Retinoic acid in the development, regeneration and maintenance of the nervous system. *Nature reviews. Neuroscience*, 8(10), pp.755–765.
- Mahamid, J. et al., 2016. Visualizing the molecular sociology at the HeLa cell nuclear periphery. *Science*, 351(6276), pp.969–972.
- Mangale, V.S. et al., 2008. Lhx2 selector activity specifies cortical identity and suppresses hippocampal organizer fate. *Science*, 319(5861), pp.304–309.
- Mansour, A.A. et al., 2018. An in vivo model of functional and vascularized human brain organoids. *Nature biotechnology*, 36(5), pp.432–441.
- Marín-Padilla, M., 1992. Ontogenesis of the pyramidal cell of the mammalian neocortex and developmental cytoarchitectonics: a unifying theory. *The Journal of comparative neurology*, 321(2), pp.223–240.
- Martí, E. et al., 1995. Requirement of 19K form of Sonic hedgehog for induction of distinct ventral cell types in CNS explants. *Nature*, 375(6529), pp.322–325.
- Martínez-Cerdeño, V. et al., 2012. Comparative analysis of the subventricular zone in rat, ferret and macaque: evidence for an outer subventricular zone in rodents. *PloS one*, 7(1), p.e30178.
- Martínez-Cerdeño, V. et al., 2016. Evolutionary origin of Tbr2-expressing precursor cells and the subventricular zone in the developing cortex. *The Journal of comparative neurology*, 524(3), pp.433–447.
- Maruhashi, M. et al., 2005. Involvement of SIP1 in positioning of somite boundaries in the mouse embryo. *Developmental dynamics : an official publication of the American Association of Anatomists*, 234(2), pp.332–338.
- Maruoka, Y. et al., 1998. Comparison of the expression of three highly related genes, Fgf8, Fgf17 and Fgf18, in the mouse embryo. *Mechanisms of development*, 74(1-2), pp.175–177.
- Mason, I., 2007. Initiation to end point: the multiple roles of fibroblast growth factors in neural development. *Nature reviews. Neuroscience*, 8(8), pp.583–596.
- Mastronarde, D.N., 2005. Automated electron microscope tomography using robust prediction of specimen movements. *Journal of structural biology*, 152(1), pp.36–51.
- Matsuzaki, F. & Shitamukai, A., 2015. Cell Division Modes and Cleavage Planes of Neural

- Progenitors during Mammalian Cortical Development. *Cold Spring Harbor perspectives in biology*, 7(9), p.a015719.
- Mazaika, E. & Homsy, J., 2014. Droplet digital PCR: CNV Analysis and Other Applications. *Current protocols in human genetics*, 82(1), pp.7.24.1–7.24.13.
- McConnell, S.K. & Kaznowski, C.E., 1991. Cell cycle dependence of laminar determination in developing neocortex. *Science*, 254(5029), pp.282–285.
- McConnell, S.K., Ghosh, A. & Shatz, C.J., 1989. Subplate neurons pioneer the first axon pathway from the cerebral cortex. *Science*, 245(4921), pp.978–982.
- McKinsey, G.L. et al., 2013. Dlx1&2-dependent expression of Zfhx1b (Sip1, Zeb2) regulates the fate switch between cortical and striatal interneurons. *Neuron*, 77(1), pp.83–98.
- McWhirter, J.R. et al., 1997. A novel fibroblast growth factor gene expressed in the developing nervous system is a downstream target of the chimeric homeodomain oncoprotein E2A-Pbx1. *Development (Cambridge, England)*, 124(17), pp.3221–3232.
- Meijering, E., Dzyubachyk, O. & Smal, I., 2012. Methods for cell and particle tracking. *Methods in enzymology*, 504, pp.183–200.
- Meyer, G., 2010. Building a human cortex: the evolutionary differentiation of Cajal-Retzius cells and the cortical hem. *Journal of anatomy*, 217(4), pp.334–343.
- Meyer, G. et al., 2002. Expression of p73 and Reelin in the developing human cortex. *The Journal of neuroscience : the official journal of the Society for Neuroscience*, 22(12), pp.4973–4986.
- Miquelajauregui, A. et al., 2007. Smad-interacting protein-1 (Zfhx1b) acts upstream of Wnt signaling in the mouse hippocampus and controls its formation. *Proceedings of the National Academy of Sciences of the United States of America*, 104(31), pp.12919–12924.
- Mire, E. et al., 2018. Developmental Upregulation of Ephrin-B1 Silences Sema3C/Neuropilin-1 Signaling during Post-crossing Navigation of Corpus Callosum Axons. *Current biology : CB*, 28(11), pp.1768–1782.e4.
- Mitchell, B.D. & Macklis, J.D., 2005. Large-scale maintenance of dual projections by callosal and frontal cortical projection neurons in adult mice. *The Journal of comparative neurology*, 482(1), pp.17–32.
- Miyaoka, Y. et al., 2014. Isolation of single-base genome-edited human iPS cells without antibiotic selection. *Nature methods*, 11(3), pp.291–293.
- Miyata, T. et al., 2004. Asymmetric production of surface-dividing and non-surface-dividing cortical progenitor cells. *Development*, 131(13), pp.3133–3145.
- Miyoshi, T. et al., 2006. Complementary expression pattern of Zfhx1 genes Sip1 and deltaEF1 in the mouse embryo and their genetic interaction revealed by compound mutants. *Developmental dynamics : an official publication of the American Association of Anatomists*, 235(7), pp.1941–1952.
- Molnár, Z. & Cheung, A.F.P., 2006. Towards the classification of subpopulations of layer V pyramidal projection neurons. *Neuroscience research*, 55(2), pp.105–115.
- Molnár, Z. & Pollen, A., 2014. How unique is the human neocortex? *Development*, 141(1), pp. 11–16.
- Molnár, Z. et al., 2006. Comparative aspects of cerebral cortical development. *European Journal of Neuroscience*, 23(4), pp.921–934.

- Molyneaux, B.J. et al., 2007. Neuronal subtype specification in the cerebral cortex. *Nature reviews. Neuroscience*, 8(6), pp.427–437.
- Molyneaux, B.J. et al., 2009. Novel subtype-specific genes identify distinct subpopulations of callosal projection neurons. *The Journal of neuroscience : the official journal of the Society for Neuroscience*, 29(39), pp.12343–12354.
- Montiel, J.F. & Aboitiz, F., 2015. Pallial patterning and the origin of the isocortex. *Frontiers in Neuroscience*, 9(38), p.377.
- Montiel, J.F. et al., 2016. From sauropsids to mammals and back: New approaches to comparative cortical development. *The Journal of comparative neurology*, 524(3), pp.630–645.
- Monuki, E.S., Porter, F.D. & Walsh, C.A., 2001. Patterning of the dorsal telencephalon and cerebral cortex by a roof plate-Lhx2 pathway. *Neuron*, 32(4), pp.591–604.
- Mora-Bermúdez, F. et al., 2016. Differences and similarities between human and chimpanzee neural progenitors during cerebral cortex development. *Elife*, 5.
- Moriwaki, K., Tsukita, S. & Furuse, M., 2007. Tight junctions containing claudin 4 and 6 are essential for blastocyst formation in preimplantation mouse embryos. *Developmental biology*, 312(2), pp.509–522.
- Mowat, D.R. et al., 1998. Hirschsprung disease, microcephaly, mental retardation, and characteristic facial features: Delineation of a new syndrome and identification of a locus at chromosome 2q22-q23. *Journal of Medical Genetics*, 35(8), pp.617–623.
- Munji, R.N. et al., 2011. Wnt signaling regulates neuronal differentiation of cortical intermediate progenitors. *The Journal of neuroscience : the official journal of the Society for Neuroscience*, 31(5), pp.1676–1687.
- Murray, S.A. & Gridley, T., 2006. Snail family genes are required for left-right asymmetry determination, but not neural crest formation, in mice. *Proceedings of the National Academy of Sciences of the United States of America*, 103(27), pp.10300–10304.
- Nakai, J. & Fujita, S., 1994. Early events in the histo- and cytogenesis of the vertebrate CNS. *The International journal of developmental biology*, 38(2), pp.175–183.
- Nakamura, F., Kalb, R.G. & Strittmatter, S.M., 2000. Molecular basis of semaphorin-mediated axon guidance. *Journal of Neurobiology*, 44(2), pp.219–229.
- Niehrs, C., 2004. Regionally specific induction by the Spemann-Mangold organizer. *Nature reviews. Genetics*, 5(6), pp.425–434.
- Nieto, M. et al., 2004. Expression of Cux-1 and Cux-2 in the subventricular zone and upper layers II–IV of the cerebral cortex. *The Journal of comparative neurology*, 479(2), pp.168–180.
- Niquille, M. et al., 2009. Transient neuronal populations are required to guide callosal axons: a role for semaphorin 3C. *PLoS biology*, 7(10), p.e1000230.
- Nitta, K.R. et al., 2007. The N-terminus zinc finger domain of *Xenopus* SIP1 is important for neural induction, but not for suppression of *Xbra* expression. *The International journal of developmental biology*, 51(4), pp.321–325.
- Nitta, K.R. et al., 2004. XSIP1 is essential for early neural gene expression and neural differentiation by suppression of BMP signaling. *Developmental biology*, 275(1), pp.258–267.
- Noctor, S.C. et al., 2004. Cortical neurons arise in symmetric and asymmetric division zones and

- migrate through specific phases. *Nature neuroscience*, 7(2), pp.136–144.
- Nomura, T. et al., 2016. The evolution of basal progenitors in the developing non-mammalian brain. *Development*, 143(1), pp.66–74.
- Nowakowski, T.J. et al., 2017. Spatiotemporal gene expression trajectories reveal developmental hierarchies of the human cortex. *Science*, 358(6368), pp.1318–1323.
- Nowakowski, T.J. et al., 2016. Transformation of the Radial Glia Scaffold Demarcates Two Stages of Human Cerebral Cortex Development. *Neuron*, 91(6), pp.1219–1227.
- Nurcombe, V. et al., 1993. Developmental Regulation of Neural Response to Fgf-1 and Fgf-2 by Heparan-Sulfate Proteoglycan. *Science*, 260(5104), pp.103–106.
- O'Leary, D.D.M. & Nakagawa, Y., 2002. Patterning centers, regulatory genes and extrinsic mechanisms controlling arealization of the neocortex. *Current opinion in neurobiology*, 12(1), pp.14–25.
- Oberst, P. et al., 2018. Apical progenitors remain multipotent throughout cortical neurogenesis. *bioRxiv*, p.478891.
- Ohnuki, M. & Takahashi, K., 2015. Present and future challenges of induced pluripotent stem cells. *Philosophical transactions of the Royal Society of London. Series B, Biological sciences*, 370(1680), pp.20140367–20140367.
- Oikonomou, C.M., Chang, Y.-W. & Jensen, G.J., 2016. A new view into prokaryotic cell biology from electron cryotomography. *Nature reviews. Microbiology*, 14(4), pp.205–220.
- O'Leary, D.D.M., Stocker, A.M. & Zembrzycki, A., 2013. *Comprehensive Developmental Neuroscience: Patterning and Cell Type Specification in the Developing CNS and PNS*, Elsevier Inc., Chapter 4. pp.61–81.
- Olson, E.C., 2014. Analysis of preplate splitting and early cortical development illuminates the biology of neurological disease. *Frontiers in pediatrics*, 2, p.121.
- Ortega, S. et al., 1998. Neuronal defects and delayed wound healing in mice lacking fibroblast growth factor 2. *Proceedings of the National Academy of Sciences of the United States of America*, 95(10), pp.5672–5677.
- Ostrem, B., Di Lullo, E. & Kriegstein, A., 2017. oRGs and mitotic somal translocation - a role in development and disease. *Current opinion in neurobiology*, 42, pp.61–67.
- Otani, T. et al., 2016. 2D and 3D Stem Cell Models of Primate Cortical Development Identify Species-Specific Differences in Progenitor Behavior Contributing to Brain Size. *Cell stem cell*, 18(4), pp.467–480.
- Ozair, M.Z. et al., 2018. hPSC Modeling Reveals that Fate Selection of Cortical Deep Projection Neurons Occurs in the Subplate. *Cell stem cell*, 23(1), pp.60–73.e6.
- Paek, H., Gutin, G. & Hebert, J.M., 2009. FGF signaling is strictly required to maintain early telencephalic precursor cell survival. *Development*, 136(14), pp.2457–2465.
- Park, J.E. et al., 2016. Generation of transgenic marmosets expressing genetically encoded calcium indicators. *Scientific reports*, 6.
- Park, S., Frisén, J. & Barbacid, M., 1997. Aberrant axonal projections in mice lacking EphA8 (Eek)

- tyrosine protein kinase receptors. *The EMBO journal*, 16(11), pp.3106–3114.
- Parthasarathy, S. et al., 2014. Ntf3 acts downstream of Sip1 in cortical postmitotic neurons to control progenitor cell fate through feedback signaling. *Development*, 141(17), pp.3324–3330.
- Pastushenko, I. & Blanpain, C., 2018. EMT Transition States during Tumor Progression and Metastasis. *Trends in cell biology*. 29(3), pp.212–226.
- Paşca, S.P., 2018. The rise of three-dimensional human brain cultures. *Nature*, 553, pp.437–445.
- Paul-Gilloteaux, P. et al., 2017. eC-CLEM: flexible multidimensional registration software for correlative microscopies. *Nature methods*, 14(2), pp.102–103.
- Pei, D. et al., 2019. Mesenchymal-epithelial transition in development and reprogramming. *Nature cell biology*, 21(1), pp.44–53.
- Peinado, H., Olmeda, D. & Cano, A., 2007. Snail, ZEB and bHLH factors in tumour progression: an alliance against the epithelial phenotype? *Nature Reviews Cancer*, 7(6), pp.415–428.
- Peterson, E.R. & Crain, S.M., 1981. Preferential growth of neurites from isolated fetal mouse dorsal root ganglia in relation to specific regions of co-cultured spinal cord explants. *Brain research. Developmental brain research*, 2(3), pp.363–382.
- Piccolo, S. et al., 1996. Dorsoventral patterning in *Xenopus*: inhibition of ventral signals by direct binding of chordin to BMP-4. *Cell*, 86(4), pp.589–598.
- Pilz, G.-A. et al., 2013. Amplification of progenitors in the mammalian telencephalon includes a new radial glial cell type. *Nature communications*, 4, p.2125.
- Pini, A., 1993. Chemorepulsion of axons in the developing mammalian central nervous system. *Science*, 261(5117), pp.95–98.
- Piper, M. et al., 2009. Neuropilin 1-Sema signaling regulates crossing of cingulate pioneering axons during development of the corpus callosum. *Cerebral cortex*, 19 Suppl 1, pp.i11–21.
- Pollard, K.S. et al., 2006. An RNA gene expressed during cortical development evolved rapidly in humans. *Nature*, 443(7108), pp.167–172.
- Pollen, A.A. et al., 2014. Low-coverage single-cell mRNA sequencing reveals cellular heterogeneity and activated signaling pathways in developing cerebral cortex. *Nature biotechnology*, 32(10), pp.1053–1058.
- Pollen, A.A. et al., 2015. Molecular identity of human outer radial glia during cortical development. *Cell*, 163(1), pp.55–67.
- Pollerberg, G.E. et al., 2013. The role of cell adhesion molecules for navigating axons: density matters. *Mechanisms of development*, 130(6-8), pp.359–372.
- Postigo, A.A. & Dean, D.C., 1999. ZEB represses transcription through interaction with the corepressor CtBP. *Proceedings of the National Academy of Sciences of the United States of America*, 96(12), pp.6683–6688.
- Preissl, S. et al., 2018. Single-nucleus analysis of accessible chromatin in developing mouse forebrain reveals cell-type-specific transcriptional regulation. *Nature neuroscience*, 21(3), pp.432–439.
- Qian, X. et al., 2016. Brain-Region-Specific Organoids Using Mini-bioreactors for Modeling ZIKV Exposure. *Cell*, 165(5), pp.1238–1254.

- Qiao, Y. et al., 2015. AP-1-mediated chromatin looping regulates ZEB2 transcription: new insights into TNF α -induced epithelial-mesenchymal transition in triple-negative breast cancer. *Oncotarget*, 6(10), pp.7804–7814.
- Quadrato, G. et al., 2017. Cell diversity and network dynamics in photosensitive human brain organoids. *Nature*, 545(7652), pp.48–53.
- Quintes, S. et al., 2016. Zeb2 is essential for Schwann cell differentiation, myelination and nerve repair. *Nature neuroscience*. 19(8), pp.1050–1059.
- Raab, S. et al., 2014. A Comparative View on Human Somatic Cell Sources for iPSC Generation. *Stem cells international*, 768391.
- Raballo, R. et al., 2000. Basic fibroblast growth factor (Fgf2) is necessary for cell proliferation and neurogenesis in the developing cerebral cortex. *The Journal of neuroscience : the official journal of the Society for Neuroscience*, 20(13), pp.5012–5023.
- Radakovits, R. et al., 2009. Regulation of radial glial survival by signals from the meninges. *The Journal of neuroscience : the official journal of the Society for Neuroscience*, 29(24), pp.7694–7705.
- Rakic, P., 2009. Evolution of the neocortex: a perspective from developmental biology. *Nature reviews. Neuroscience*, 10(10), pp.724–735.
- Rakic, P., 1972. Mode of cell migration to the superficial layers of fetal monkey neocortex. *The Journal of comparative neurology*, 145(1), pp.61–83.
- Rakic, P., 1978. Neuronal migration and contact guidance in the primate telencephalon. *Postgraduate medical journal*, 54 Suppl 1, pp.25–40.
- Rakic, P., 1974. Neurons in Rhesus-Monkey Visual-Cortex - Systematic Relation Between Time of Origin and Eventual Disposition. *Science*, 183(4123), pp.425–427.
- Rakic, P., 1988. Specification of Cerebral Cortical Areas. *Science*, 241(4862), pp.170–176.
- Rallu, M. et al., 2002. Dorsoventral patterning is established in the telencephalon of mutants lacking both Gli3 and Hedgehog signaling. *Development*, 129(21), pp.4963–4974.
- Ran, F.A. et al., 2013. Genome engineering using the CRISPR-Cas9 system. *Nature Protocols*, 8(11), pp.2281–2308.
- Rash, B.G. & Grove, E.A., 2007. Patterning the dorsal telencephalon: a role for sonic hedgehog? *The Journal of neuroscience : the official journal of the Society for Neuroscience*, 27(43), pp.11595–11603.
- Remacle, J.E. et al., 1999. New mode of DNA binding of multi-zinc finger transcription factors: deltaEF1 family members bind with two hands to two target sites. *The EMBO journal*, 18(18), pp.5073–5084.
- Renner, M. et al., 2017. Self-organized developmental patterning and differentiation in cerebral organoids. *The EMBO journal*, 36(10), pp.1316–1329.
- Rezakhaniha, R. et al., 2012. Experimental investigation of collagen waviness and orientation in the arterial adventitia using confocal laser scanning microscopy. *Biomechanics and modeling in mechanobiology*, 11(3-4), pp.461–473.
- Rogers, C.D., Saxena, A. & Bronner, M.E., 2013. Sip1 mediates an E-cadherin-to-N-cadherin switch during cranial neural crest EMT. *The Journal of cell biology*, 203(5), pp.835–847.

- Rosenberg, A.B. et al., 2018. Single-cell profiling of the developing mouse brain and spinal cord with split-pool barcoding. *Science*, 360(6385), pp.176–182.
- Rosselló, R.A. et al., 2013. Mammalian genes induce partially reprogrammed pluripotent stem cells in non-mammalian vertebrate and invertebrate species. *Elife*, 2.
- Roth, G. & Dicke, U., 2005. Evolution of the brain and intelligence. *Trends in cognitive sciences*, 9(5), pp.250–257.
- Rouaux, C. & Arlotta, P., 2010. Fezf2 directs the differentiation of corticofugal neurons from striatal progenitors in vivo. *Nature neuroscience*, 13(11), pp.1345–1347.
- Sadoul, R. et al., 1983. Adult and embryonic mouse neural cell adhesion molecules have different binding properties. *Nature*, 304(5924), pp.347–349.
- Sahara, S. & O'Leary, D.D.M., 2009. Fgf10 regulates transition period of cortical stem cell differentiation to radial glia controlling generation of neurons and basal progenitors. *Neuron*, 63(1), pp.48–62.
- Sahara, S. et al., 2012. The fraction of cortical GABAergic neurons is constant from near the start of cortical neurogenesis to adulthood. *The Journal of neuroscience : the official journal of the Society for Neuroscience*, 32(14), pp.4755–4761.
- Sakane, F. & Miyamoto, Y., 2013. N-cadherin regulates the proliferation and differentiation of ventral midbrain dopaminergic progenitors. *Developmental neurobiology*, 73(7), pp.518–529.
- Sasai, Y. et al., 1995. Regulation of neural induction by the Chd and Bmp-4 antagonistic patterning signals in *Xenopus*. *Nature*, 376, pp.333–336.
- Sato, T. et al., 2009. Single Lgr5 stem cells build crypt villus structures in vitro without a mesenchymal niche. *Nature*, 459, pp. 262–265.
- Sauer, F.C., 1935. Mitosis in the neural tube. *The Journal of comparative neurology*, 62(2), pp.377–405.
- Sauka-Spengler, T. & Bronner-Fraser, M., 2008. Evolution of the neural crest viewed from a gene regulatory perspective. *Genesis*, 46(11), pp.673–682.
- Schenk, J. et al., 2009. Myosin II Is Required for Interkinetic Nuclear Migration of Neural Progenitors. *Proceedings of the National Academy of Sciences of the United States of America*, 106(38), pp.16487–16492.
- Schmid, R.S., Pruitt, W.M. & Maness, P.F., 2000. A MAP kinase-signaling pathway mediates neurite outgrowth on L1 and requires Src-dependent endocytosis. *The Journal of neuroscience : the official journal of the Society for Neuroscience*, 20(11), pp.4177–4188.
- Schmierer, B. & Hill, C.S., TGF β –SMAD signal transduction: molecular specificity and functional flexibility. *Nature Reviews Molecular Cell Biology*, 8 (12), pp.970–982.
- Schoenwolf, G.C. et al., 2014. *Larsen's Human Embryology E-Book*, Elsevier Health Sciences. pp.14–131.
- Schuermans, C. & Guillemot, F., 2002. Molecular mechanisms underlying cell fate specification in the developing telencephalon. *Current opinion in neurobiology*, 12(1), pp.26–34.
- Schwank, G. et al., 2013. Functional repair of CFTR by CRISPR/Cas9 in intestinal stem cell organoids of cystic fibrosis patients. *Cell stem cell*, 13(6), pp.653–658.

- Sclip, A. et al., 2016. Extended Synaptotagmin (ESyt) Triple Knock-Out Mice Are Viable and Fertile without Obvious Endoplasmic Reticulum Dysfunction. C. Beh, ed. *PloS one*, 11(6), p.e0158295.
- Serafini, T. et al., 1994. The netrins define a family of axon outgrowth-promoting proteins homologous to *C. elegans* UNC-6. *Cell*, 78(3), pp.409–424.
- Seuntjens, E. et al., 2009. Sip1 regulates sequential fate decisions by feedback signaling from postmitotic neurons to progenitors. *Nature neuroscience*, 12(11), pp.1373–1380.
- Shadrach, J.L. & Pierchala, B.A., 2018. Semaphorin3A Signaling Is Dispensable for Motor Axon Reinnervation of the Adult Neuromuscular Junction. *eNeuro*, 5(3).
- Sheppard, A.M. & Pearlman, A.L., 1997. Abnormal reorganization of preplate neurons and their associated extracellular matrix: an early manifestation of altered neocortical development in the reeler mutant mouse. *The Journal of comparative neurology*, 378(2), pp.173–179.
- Shimamura, K. & Rubenstein, J.L., 1997. Inductive interactions direct early regionalization of the mouse forebrain. *Development*, 124(14), pp.2709–2718.
- Shimogori, T. et al., 2004. Embryonic signaling centers expressing BMP, WNT and FGF proteins interact to pattern the cerebral cortex. *Development*, 131(22), pp.5639–5647.
- Sidman, R.L. & Rakic, P., 1973. Neuronal migration, with special reference to developing human brain: a review. *Brain research*, 62(1), pp.1–35.
- Siegenthaler, J.A. et al., 2009. Retinoic acid from the meninges regulates cortical neuron generation. *Cell*, 139(3), pp.597–609.
- Slack, J. et al., 1987. Mesoderm Induction in Early *Xenopus* Embryos by Heparin-Binding Growth-Factors. *Nature*, 326(6109), pp.197–200.
- Smart, I. et al., 2002. Unique morphological features of the proliferative zones and postmitotic compartments of the neural epithelium giving rise to striate and extrastriate cortex in the monkey. *Cerebral cortex*, 12(1), pp.37–53.
- Smart, I.H., 1973. Proliferative characteristics of the ependymal layer during the early development of the mouse neocortex: a pilot study based on recording the number, location and plane of cleavage of mitotic figures. *Journal of anatomy*, 116(1), pp.67–91.
- Smart, I.H., 1972. Proliferative characteristics of the ependymal layer during the early development of the spinal cord in the mouse. *Journal of anatomy*, 111(3), pp.365–380.
- Smith, W.C. & Harland, R.M., 1992. Expression cloning of noggin, a new dorsalizing factor localized to the Spemann organizer in *Xenopus* embryos. *Cell*, 70(5), pp.829–840.
- Smukler, S.R. et al., 2006. Embryonic stem cells assume a primitive neural stem cell fate in the absence of extrinsic influences. *The Journal of cell biology*, 172(1), pp.79–90.
- Solnica-Krezel, L., 2005. Conserved patterns of cell movements during vertebrate gastrulation. *Current biology*, 15(6), pp.213–228.
- Soo, K. et al., 2002. Twist function is required for the morphogenesis of the cephalic neural tube and the differentiation of the cranial neural crest cells in the mouse embryo. *Developmental biology*, 247(2), pp.251–270.
- Spemann, H., 1938. Embryonic Development and Induction, by Hans Spemann, *Oxford University Press*.

- Squire, L. et al., 2012. *Fundamental Neuroscience*, Academic Press. pp.287–382.
- Srivatsa, S. et al., 2015. Sip1 downstream Effector ninein controls neocortical axonal growth, ipsilateral branching, and microtubule growth and stability. *Neuron*, 85(5), pp.998–1012.
- Stahl, R. et al., 2013. Trnp1 regulates expansion and folding of the mammalian cerebral cortex by control of radial glial fate. *Cell*, 153(3), pp.535–549.
- Stemmler, M.P. et al., 2019. Non-redundant functions of EMT transcription factors. *Nature cell biology*, 21(1), pp.102–112.
- Stoeckli, E.T., 2018. Understanding axon guidance: are we nearly there yet? *Development*, 145(10).
- Storm, E.E. et al., 2006. Dose-dependent functions of Fgf8 in regulating telencephalic patterning centers. *Development*, 133(9), pp.1831–1844.
- Stoykova, A. et al., 1997. Pax6-dependent regulation of adhesive patterning, R-cadherin expression and boundary formation in developing forebrain. *Development*, 124(19), pp.3765–3777.
- Streit, A., 2007. The preplacodal region: an ectodermal domain with multipotential progenitors that contribute to sense organs and cranial sensory ganglia. *The International journal of developmental biology*, 51(6-7), pp.447–461.
- Streit, A. et al., 2000. Initiation of neural induction by FGF signalling before gastrulation. *Nature*, 406(6791), pp.74–78.
- Streit, J., Spenger, C. & Luscher, H.-R., 1991. An Organotypic Spinal Cord-Dorsal Root Ganglion-Skeletal Muscle Coculture of Embryonic Rat. II. Functional Evidence for the Formation of Spinal Reflex Arcs In Vitro. *European Journal of Neuroscience*, 3(11), pp.1054–1068.
- Stryjewska, A. et al., 2016. Zeb2 Regulates Cell Fate at the Exit from Epiblast State in Mouse Embryonic Stem Cells. *Stem cells (Dayton, Ohio)*, 35(3), pp.611–625.
- Suárez, R. et al., 2018. A pan-mammalian map of interhemispheric brain connections predates the evolution of the corpus callosum. *Proceedings of the National Academy of Sciences of the United States of America*, 115(38), pp.9622–9627.
- Subramanian, L. et al., 2017. Dynamic behaviour of human neuroepithelial cells in the developing forebrain. *Nature communications*, 8, p.14167.
- Suzuki, I.K. et al., 2018. Human-Specific NOTCH2NL Genes Expand Cortical Neurogenesis through Delta/Notch Regulation. *Cell*, 173(6), pp.1370–1384.
- Takagi, T. et al., 2015. De novo inbred heterozygous Zeb2/Sip1 mutant mice uniquely generated by germ-line conditional knockout exhibit craniofacial, callosal and behavioral defects associated with Mowat–Wilson syndrome. *Human Molecular Genetics*, 24(22), pp.6390–6402.
- Takagi, T. et al., 1998. DeltaEF1, a zinc finger and homeodomain transcription factor, is required for skeleton patterning in multiple lineages. *Development*, 125(1), pp.21–31.
- Tamagnone, L. & Comoglio, P.M., 2000. Signalling by semaphorin receptors: cell guidance and beyond. *Trends in cell biology*, 10(9), pp.377–383.
- Tanaka, D.H. & Nakajima, K., 2012. Migratory pathways of GABAergic interneurons when they enter the neocortex. *The European journal of neuroscience*, 35(11), pp.1655–1660.
- Tanaka, D.H. et al., 2006. Multidirectional and multizonal tangential migration of GABAergic interneurons in the developing cerebral cortex. *Development*, 133(11), pp.2167–2176.

- Taverna, E. & Huttner, W.B., 2010. Neural progenitor nuclei IN motion. *Neuron*, 67(6), pp.906–914.
- Thelen, K. et al., 2012. Translation of the cell adhesion molecule ALCAM in axonal growth cones - regulation and functional importance. *Journal of cell science*, 125(Pt 4), pp.1003–1014.
- Tole, S. & Hébert, J., 2013. *Comprehensive Developmental Neuroscience: Patterning and Cell Type Specification in the Developing CNS and PNS*, Elsevier Inc., Chapter 1, pp.3–20.
- Tole, S., Ragsdale, C.W. & Grove, E.A., 2000. Dorsoventral patterning of the telencephalon is disrupted in the mouse mutant extra-toes(J). *Developmental biology*, 217(2), pp.254–265.
- Torii, M. & Levitt, P., 2005. Dissociation of corticothalamic and thalamocortical axon targeting by an EphA7-mediated mechanism. *Neuron*, 48(4), pp.563–575.
- Toyoda, R. et al., 2010. FGF8 acts as a classic diffusible morphogen to pattern the neocortex. *Development*, 137(20), pp.3439–3448.
- Tremblay, M.G. & Moss, T., 2016. Loss of all 3 Extended Synaptotagmins does not affect normal mouse development, viability or fertility. *Cell cycle*, 15(17), pp.2360–2366.
- Tropepe, V. et al., 2001. Direct neural fate specification from embryonic stem cells: a primitive mammalian neural stem cell stage acquired through a default mechanism. *Neuron*, 30(1), pp.65–78.
- Tsankov, A.M. et al., 2015. A qPCR ScoreCard quantifies the differentiation potential of human pluripotent stem cells. *Nature biotechnology*, 33(11), pp.1182–1192.
- Tsuda, H. et al., 2002. Dorsalization of the neural tube by *Xenopus* tiarin, a novel patterning factor secreted by the flanking nonneural head ectoderm. *Neuron*, 33(4), pp.515–528.
- Uziel, D. et al., 2002. Miswiring of limbic thalamocortical projections in the absence of ephrin-A5. *The Journal of neuroscience : the official journal of the Society for Neuroscience*, 22(21), pp.9352–9357.
- Vaccarino, F., Schwartz, M., Raballo, R., Nilsen, J., et al., 1999. Changes in cerebral cortex size are governed by fibroblast growth factor during embryogenesis. *Nature neuroscience*, 2(9), p.848.
- Vaccarino, F.M., Schwartz, M.L., Raballo, R., Rhee, J., et al., 1999. Fibroblast growth factor signaling regulates growth and morphogenesis at multiple steps during brain development. *Current topics in developmental biology*, 46, pp.179–200.
- Vallier, L., Reynolds, D. & Pedersen, R.A., 2004. Nodal inhibits differentiation of human embryonic stem cells along the neuroectodermal default pathway. *Developmental biology*, 275(2), pp.403–421.
- Van De Putte, T. et al., 2003. Mice lacking ZFHX1B, the gene that codes for Smad-interacting protein-1, reveal a role for multiple neural crest cell defects in the etiology of Hirschsprung disease-mental retardation syndrome. *American journal of human genetics*, 72(2), pp.465–470.
- van den Berghe, V. et al., 2013. Directed migration of cortical interneurons depends on the cell-autonomous action of Sip1. *Neuron*, 77(1), pp.70–82.
- van Grunsven, L.A. et al., 2007. XSip1 neuralizing activity involves the co-repressor CtBP and occurs through BMP dependent and independent mechanisms. *Developmental biology*, 306(1), pp.34–49.
- van Grunsven, L.A. et al., 2006. δ EF1 and SIP1 are differentially expressed and have overlapping activities during *Xenopus* embryogenesis. *Developmental dynamics*, 235(6), pp.1491–1500.

- Vasistha, N.A. et al., 2015. Cortical and Clonal Contribution of Tbr2 Expressing Progenitors in the Developing Mouse Brain. *Cerebral cortex*, 25(10), pp.3290–3302.
- Verschueren, K. et al., 1999. SIP1, a novel zinc finger/homeodomain repressor, interacts with Smad proteins and binds to 5'-CACCT sequences in candidate target genes. *The Journal of biological chemistry*, 274(29), pp.20489–20498.
- Verstappen, G. et al., 2008. Atypical Mowat-Wilson patient confirms the importance of the novel association between ZFH1B/SIP1 and NuRD corepressor complex. *Human molecular genetics*, 17(8), pp.1175–1183.
- Vonica, A. & Gumbiner, B.M., 2007. The Xenopus Nieuwkoop center and Spemann-Mangold organizer share molecular components and a requirement for maternal Wnt activity. *Developmental biology*, 312(1), pp.90–102.
- Wang, L., Hou, S. & Han, Y.-G., 2016. Hedgehog signaling promotes basal progenitor expansion and the growth and folding of the neocortex. *Nature neuroscience*, 19(7), pp.888–896.
- Watanabe, K. et al., 2005. Directed differentiation of telencephalic precursors from embryonic stem cells. *Nature neuroscience*, 8(3), pp.288–296.
- Watanabe, M. et al., 2012. BMP4 Sufficiency to Induce Choroid Plexus Epithelial Fate from Embryonic Stem Cell-Derived Neuroepithelial Progenitors. *The Journal of neuroscience : the official journal of the Society for Neuroscience*, 32(45), pp.15934–15945.
- Weimann, J.M. et al., 1999. Cortical neurons require Otx1 for the refinement of exuberant axonal projections to subcortical targets. *Neuron*, 24(4), pp.819–831.
- Weng, Q. et al., 2012. Dual-mode modulation of Smad signaling by Smad-interacting protein Sip1 is required for myelination in the central nervous system. *Neuron*, 73(4), pp.713–728.
- Wharton, K.A., Ray, R.P. & Gelbart, W.M., 1993. An activity gradient of decapentaplegic is necessary for the specification of dorsal pattern elements in the Drosophila embryo. *Development*, 117(2), pp.807–822.
- White, T.D. et al., 2009. Ardipithecus ramidus and the paleobiology of early hominids. *Science*, 326(5949), pp.75–86.
- Whitmarsh, A.J. & Davis, R.J., 2001. Analyzing JNK and p38 mitogen-activated protein kinase activity. *Methods in enzymology*, 332, pp.319–336.
- Wong, F.K. et al., 2015. Sustained Pax6 Expression Generates Primate-like Basal Radial Glia in Developing Mouse Neocortex. P. Khaitovich, *PLoS Biology*, 13(8), p.e1002217.
- Wu, L.M.N. et al., 2016. Zeb2 recruits HDAC-NuRD to inhibit Notch and controls Schwann cell differentiation and remyelination. *Nature neuroscience*. 19(8), pp.1060–1072.
- Wunderlich, S. et al., 2014. Primate iPS cells as tools for evolutionary analyses. *Stem cell research*, 12(3), pp.622–629.
- Xiang, Y. et al., 2019. hESC-Derived Thalamic Organoids Form Reciprocal Projections When Fused with Cortical Organoids. *Cell stem cell*, 24(3), pp.487–497.
- Xie, Z. et al., 2007. Cep120 and TACCs control interkinetic nuclear migration and the neural progenitor pool. *Neuron*, 56(1), pp.79–93.
- Xuan, S. et al., 1995. Winged helix transcription factor BF-1 is essential for the development of the cerebral hemispheres. *Neuron*, 14(6), pp.1141–1152.

- Yasumi, T. et al., 2016. Regulation of trunk neural crest delamination by deltaEF1 and Sip1 in the chicken embryo. *Development, growth & differentiation*, 58(2), pp.205–214.
- Yoon, S.-J. et al., 2019. Reliability of human cortical organoid generation. *Nature methods*, 16(1), pp.75–78.
- Yuzwa, S.A. et al., 2017. Developmental Emergence of Adult Neural Stem Cells as Revealed by Single-Cell Transcriptional Profiling. *Cell reports*, 21(13), pp.3970–3986.
- Zhang, S.C. et al., 2001. In vitro differentiation of transplantable neural precursors from human embryonic stem cells. *Nature biotechnology*, 19(12), pp.1129–1133.
- Zhang, X. et al., 2009. SUN1/2 and Syne/Nesprin-1/2 complexes connect centrosome to the nucleus during neurogenesis and neuronal migration in mice. *Neuron*, 64(2), pp.173–187.
- Zheng, Y. et al., 2018. CRISPR interference-based specific and efficient gene inactivation in the brain. *Nature neuroscience*, 21(3), pp.447–454.
- Zhong, S. et al., 2018. A single-cell RNA-seq survey of the developmental landscape of the human prefrontal cortex. *Nature*, 555(7697), pp.524–528.
- Zoltewicz, J.S. & Gerhart, J.C., 1997. The Spemann organizer of *Xenopus* is patterned along its anteroposterior axis at the earliest gastrula stage. *Developmental biology*, 192(2), pp.482–491.
- Zou, Y. & Lyuksyutova, A.I., 2007. Morphogens as conserved axon guidance cues. *Current opinion in neurobiology*, 17(1), pp.22–28.
- Zou, Y. et al., 2000. Squeezing axons out of the gray matter: a role for slit and semaphorin proteins from midline and ventral spinal cord. *Cell*, 102(3), pp.363–375.

Appendix 1

Table of oligos used in the study

Oligo name	Sequence (5'-3')	Application and reaction mix
CAG_F	GCTTCTGGCGTGTGACGG	Outsourced sequence validation
CuO_seq	CACCTGGCCGATCTGGCC	Outsourced sequence validation
CuO_ZEB2_seq_1	CACCCCTGGCACACAAC	Outsourced sequence validation
CuO_ZEB2_seq_2	GAGGAACGCGATGGTCATGC	Outsourced sequence validation
CuO_ZEB2_seq_3	TTTGCCTACCGCACCCAG	Outsourced sequence validation
CuO_ZEB2_seq_4	TGCTCAGAGTCCAATGCAGCA	Outsourced sequence validation
CuO_ZEB2_seq_5	TCAAGGCGTCTGCGAGC	Outsourced sequence validation
CuO_ZEB2_seq_6	AGGAGCTCCAGGCTGAGC	Outsourced sequence validation
CuO_ZEB2_seq_7	ACAAGACTACATGTCAGGCCTAG	Outsourced sequence validation
ffusionRed_R	GAGGTTTCAGCTTACTCAGCGTGATTACCTCCATCACCAGCGC	Cloning FusionRed into pT2-CAG-Ct-Farnesyl/ Q5 Mmix
ffusionRed_F	GTGCTGTCTCATCTTTGGCAAGAAATTCATGGTGAGCGCTGATTAAAGGAG	Cloning FusionRed into pT2-CAG-Ct-Farnesyl/ Q5 Mmix
pJET1.2 forward sequencing primer	CGACTCACTATAGGGAGAGCGGC	Outsourced sequence validation
RT-ddPCR_E-Cadherin_F	CGAGAGCTACACGTTTCACGG	RT-ddPCR absolute quantification/ ddPCR EvaGreen Supermix
RT-ddPCR_E-Cadherin_R	GGGTGTCGAGGGAAAAAATAGG	RT-ddPCR absolute quantification/ ddPCR EvaGreen Supermix
RT-ddPCR_EIF2B2_F	TCCGGGAGGAGTATGGCAG	RT-ddPCR absolute quantification/ ddPCR EvaGreen Supermix
RT-ddPCR_EIF2B2_R	AATGGAAGCTGAATCTCTCG	RT-ddPCR absolute quantification/ ddPCR EvaGreen Supermix
RT-ddPCR_FGF2_F	AGAAGAGCGACCCCTCACATCA	RT-ddPCR absolute quantification/ ddPCR EvaGreen Supermix
RT-ddPCR_FGF2_R	CGGTTAGCACACACTCCTTTG	RT-ddPCR absolute quantification/ ddPCR EvaGreen Supermix
RT-ddPCR_GLAST_F	AGCAGGGAGTCCGTAAACG	RT-ddPCR absolute quantification/ ddPCR EvaGreen Supermix
RT-ddPCR_GLAST_R	AGCATTCCGAAACAGGTAACCTTT	RT-ddPCR absolute quantification/ ddPCR EvaGreen Supermix
RT-ddPCR_HES1_F	TCAACACGACACCGGATAAAC	RT-ddPCR absolute quantification/ ddPCR EvaGreen Supermix
RT-ddPCR_HES1_R	GCCGCGAGCTATCTTCTTCA	RT-ddPCR absolute quantification/ ddPCR EvaGreen Supermix
RT-ddPCR_N-Cadherin_F	AGCCAACCTTAACCTGAGGAGT	RT-ddPCR absolute quantification/ ddPCR EvaGreen Supermix
RT-ddPCR_N-Cadherin_R	GGCAAGTTGATTGGAGGATG	RT-ddPCR absolute quantification/ ddPCR EvaGreen Supermix
RT-ddPCR_Ocludin_F	ACAAGCGGTTTATCCAGAGTC	RT-ddPCR absolute quantification/ ddPCR EvaGreen Supermix
RT-ddPCR_Ocludin_R	GTCATCCACAGCGGAAGTTAAT	RT-ddPCR absolute quantification/ ddPCR EvaGreen Supermix
RT-ddPCR_ZEB2_F	TTACCTGCTCTTGGGTTAG	RT-ddPCR absolute quantification/ ddPCR EvaGreen Supermix
RT-ddPCR_ZEB2_R	CACAAGCCAGGGACAGATCAG	RT-ddPCR absolute quantification/ ddPCR EvaGreen Supermix
RT-PCR_ZEB2-agarose-gel_F	CGCTTGACATCACTGAAGGA	RT-PCR and agarose gel electrophoresis/ GoTaq Green
RT-PCR_ZEB2-agarose-gel_R	GCTCCTGGTTAGCATTTG	RT-PCR and agarose gel electrophoresis/ GoTaq Green
U6_F	GACTATCATATGCTTACCGT	Outsourced sequence validation
ZEB2_Cas9n_screening_R	GAAGAAGTTTGGTTCGGGCTG	Amplification of the edited site/ Q5 Mmix
ZEB2_Cas9n_screening_F	CCACATTGCTGCTGTTTG	Amplification of the edited site/ Q5 Mmix
ZEB2_CuO_cloning_R	ACCGTAGCGCGCCTTACATGCCATCTTCCATATTGTTCTCTCG	Cloning ZEB2 ORF/ Q5 Mmix
ZEB2_CuO_cloning_F	ACCGTAGCTAGCGCGCCACCATGAAGCAGCGCATCATGCGC	Cloning ZEB2 ORF/ Q5 Mmix
ZEB2_DNA_PAGE_F	GCCATCTGATCGCTCTTAT	Genotyping analysis of ZEB2 mutants/ GoTaq Green
ZEB2_DNA_PAGE_R	GGTTCGGGCTGCTTCTTAC	Genotyping analysis of ZEB2 mutants/ GoTaq Green
ZEB2_drop-off_primer_F	CCACATTGCTGCTGTTTG	ddPCR drop-off assay/ ddPCR SuperMix for probes
ZEB2_drop-off_primer_R	GAAGAAGTTTGGTTCGGGCTG	ddPCR drop-off assay/ ddPCR SuperMix for probes
ZEB2_drop-off_probe	(HEX)-TCTGGGATTGGCTGTTGTTGCG-(BHQ1)	ddPCR drop-off assay/ ddPCR SuperMix for probes
ZEB2_iso-2_R	TGGACCATCTACAGAGGCTGTGA	Cloning ZEB2 isoform-2 ORF/ Q5 Mmix
ZEB2_iso-2_F	TGAAGAATGCAAAATGCACATCAGATTTT	Cloning ZEB2 isoform-2 ORF/ Q5 Mmix
ZEB2_reference_probe	(FAM)-AGGCGCGGAGTCCATGc-(BHQ1)	ddPCR drop-off assay/ ddPCR SuperMix for probes
ZEB2_sgRNA_A	ATCCGCCATGATCGGCTGC	ZEB2 CRISPR-Cas9n editing
ZEB2_sgRNA_B	TCCTGGGATTGGCTGTTGTTGCG	ZEB2 CRISPR-Cas9n editing
ZEB2_Splicing analysis_F	AGCTAGTGTGCCCAACCAT	Splicing analysis of ZEB2 isoforms-1 & 2/ GoTaq Green
ZEB2_Splicing analysis_FR	ATGACCATCGCGTTCCTCCA	Splicing analysis of ZEB2 isoforms-1 & 2/ GoTaq Green

Appendix 2

Whole-cell patch-clamp recording data

Cell	RMP (mV)	Ra (MΩ)	Ri (MΩ)	AP-threshold (mV)	AP amplitude (mV)	AP half width (ms)	AHP amplitude (mV)	AHP width (ms)
1	-52.0	26.0	2057.3	-45.0	52.1	3.4	-11.4	120.1
2	-62.0	33.2	1030.6	-	-	-	-	-
3	-75.0	40.6	1149.9	-	-	-	-	-
4	-53.0	28.9	1035.0	-43.4	65.8	6.2	-4.0	145.0
5	-57.0	51.7	1059.5	-43.8	57.4	6.6	-12.0	109.0
6	-61.8	22.9	1018.8	-46.7	67.1	4.3	-9.5	104.0
7	-65.2	38.0	1423.6	-45.6	35.7	4.5	-4.6	84.2
8	-58.7	37.3	1244.7	-42.8	65.0	2.1	-13.1	71.4
9	-60.1	53.7	1033.3	-	-	-	-	-
10	-62.0	31.2	1079.9	-	-	-	-	-
11	-58.3	44.2	1679.9	-	-	-	-	-
12	-65.2	29.2	3816.9	-43.1	61.3	3.8	-2.2	48.0
13	-67.0	28.0	1013.7	-	-	-	-	-
14	-81.1	24.7	1761.0	-	-	-	-	-
15	-66.6	26.6	2354.4	-44.6	60.1	3.6	-3.9	100.7
16	-61.3	23.4	1589.5	-35.1	79.0	2.1	-11.5	63.9
17	-66.4	40.0	1522.5	-43.6	71.3	2.9	-5.9	105.1
18	-60.1	23.2	1018.4	-40.1	73.7	2.2	-7.2	144.9
19	-60.0	23.1	2150.8	-	-	-	-	-
20	-57.0	25.4	2752.3	-	-	-	-	-
21	-65.4	34.8	1888.2	-	-	-	-	-
22	-62.9	33.9	1029.9	-43.7	57.1	3.7	-12.5	62.0
23	-61.3	22.2	1977.8	-42.5	63.9	5.3	-11.2	121.4
Average ± SEM	-62.5 ± 1.3	32.3 ± 1.9	1595.5 ± 146.2	-43.1 ± 0.8	62.3 ± 3.0	3.9 ± 0.4	-8.4 ± 1.1	98.4 ± 8.6